# NON-INVASIVE DETECTION OF THE ELECTROMYOGRAPHIC ACTIVITY OF THE DEEP EXTRINSIC THUMB MUSCLES USING SURFACE ELECTRODES


**Prepared by:** **Jeremy David Pitman**
BScEng: Mechanical Engineering
PTMJER001

**Supervised by:** **Dr. Lester John**
Division of Biomedical Engineering
Department of Human Biology
Faculty of Health Sciences
University of Cape Town

## June 2015

Submitted to the University of Cape Town in partial fulfilment of the requirements for the degree of MSc(Med):Biomedical Engineering

# ABSTRACT

**Motivation:** Conventional surface electromyography (EMG) methods cannot be used to detect deep muscle activation. A new non-invasive superficial and deep muscle EMG (sdEMG) technique has recently been used to derive the EMG activity of Brachialis and Tibialis Posterior muscles in the upper and lower limb respectively. The aim of the present study was to apply a modified version of sdEMG to the forearm to detect EMG activity of the deep extrinsic thumb muscles Flexor Pollicis Longus (FPL), Extensor Pollicis Longus (EPL), Extensor Pollicis Brevis (EPB) and Abductor Pollicis Longus (APL) using surface electrodes.

**Methods**: High density monopolar EMG was detected from 2 concentric rings, each consisting of 20 custom designed and manufactured silver electrodes, placed at the distal and proximal thirds of the right forearm of 15 healthy male participants. The EMG signals were recorded by a custom synthesised from open source components, EMG amplifier system interfacing with a custom designed LabVIEW® program. The participants performed 10 repetitions of isometric thumb flexion (TFl), thumb extension (TEx), thumb abduction (TAb), thumb adduction (TAd), index finger flexion (IFFl) and index finger extension (IFEx). Each isometric contraction was performed in a randomized order at a standardized effort level of 30% of the participant's maximum voluntary contraction (verified by a custom designed and built thumb dynamometer). The Independent Component Analysis (ICA) algorithm, fastICA, was used to un-mix the 40 monopolar EMG waveforms (containing EMG activity attributable to both superficial and deep muscles) into 40 constitutive components, known as the Independent Components (ICs). The activation envelope of the ICs was found using a 250ms RMS smoothing filter and normalized between 0 and 1. A contraction sequence specific predicted EMG waveform based on intramuscular measurements (from existing studies in the literature) was created for each deep muscle and correlated with the processed ICs using Pearson's Correlation Coefficient (r). The ICs were ranked according to the corresponding r value and the highest r ranked IC for each muscle was considered to represent the recovered EMG activity from that particular muscle. Finally, a per sample basis accuracy, sensitivity and specificity analysis was conducted between each deep muscle's predicted EMG and highest r ranked IC at different activation thresholds. A linear mixed-effects statistical model was used to find the overall accuracy, sensitivity and specificity values over all the thresholds for each deep muscle.

**Results:** Overall correlations of 0.81 for FPL (D), 0.88 for EPL (D), 0.92 for EPB (D) and 0.83 for APL (D) ($p<0.001$ for all muscles) were found between the predicted EMG waveforms and ICs. Using an activation threshold of 3 standard deviations above a resting baseline level, statistically significant ($p<0.001$) accuracy, sensitivity and specificity measures were found between the predicted EMG waveforms and top r ranked ICs for each of the deep muscles. The values of the 3 statistical measures (accuracy, sensitivity, specificity) for each of the deep muscles were: FPL (0.76, 0.88, 0.70); EPL (0.87, 0.85, 0.91); EPB (0.94, 0.93, 0.94); APL (0.80, 0.87, 0.87).

**Conclusions:** The results indicate that this is the first non-invasive detection of the EMG activity of FPL (D), EPL (D), EPB (D) and APL (D). The ability to detect movement intention as a result of activation from these muscles may be of use for robot based targeted rehabilitation of the hand or in the control of prosthetic hand devices.

# Declaration

I, Jeremy David Pitman, hereby declare that the work upon which this dissertation is based is my own original work (except where acknowledgements indicate otherwise) and that neither the whole work, nor any part of it, has been, is being, or is to be submitted for another degree in this or any other university. I empower the University of Cape Town to reproduce, for the purpose of research, either the whole or any portion of the contents in any manner whatsoever.

The Harvard referencing style was used for citation and referencing. Each contribution to, and quotation from the work(s) of other people has been cited and referenced.

Signature of Author:

signature removed

Signed by candidate

Date: 11/06/2015

# Acknowledgements

I would like to thank my supervisor, Dr Lester John, for his guidance throughout the study; Kylie de Jager, for her invaluable advice and assistance in reviewing the many drafts; and my office mate, Cara Swanepoel, for her invaluable assistance and advice throughout the study.

I would like to acknowledge the Medical Research Council, the National Research Foundation and the University of Cape Town for their financial assistance of the study.

I would also like to gratefully acknowledge the contributions towards the development and use of the various pieces of experimental equipment by Susalele Moroaswi, Nikhil Divekar, Stefan Stoeckigt, Anees Sayed, Raphael Smith, Charles Harris, Yasheen Brijlal, and Gokul Nair. I would also to thank Katya Mauff and Ushma Galal of the UCT Statistical Consulting service for their excellent advice and assistance.

To my fellow biomedical engineering friends, Kieran Duggan, Tim Perks and Shaun Fickling, thank you for the lunch breaks, coffee breaks and great times we had together. I would also like to thank all my friends, particularly Dirk Snoeck-Henkemans, Marc Brighton, Bianca Amos-Brown, and Ansune van der Merwe for their unwavering support and encouragement throughout the project.

Finally, I would like to thank my wonderful family for proof reading various chapters as well as their love and support throughout this journey. I would like to especially thank my incredible parents for supporting and believing in me through everything. I am truly astounded at the depth of your love and support.

*(And here's to you, Mrs Robinson…)*

# Table of Contents

# List of Figures

# List of Tables

# List of abbreviations

| Abbreviation | Definition |
|---|---|
| MU | Motor Unit |
| MUAP | Motor Unit Action Potential |
| EMG | Electromyography |
| BSS | Blind Source Separation. |
| ICA | Independent Component Analysis. |
| IC | Independent Component |
| MVC | Maximal Voluntary Contraction |
| FPL | Flexor Pollicis Longus |
| EPL | Extensor Pollicis Longus |
| EPB | Extensor Pollicis Brevis |
| APL | Abductor Pollicis Longus |
| FD | Flexor Digitorum |
| ED | Extensor Digitorum |
| SENIAM | Surface Electromyography for the Non-Invasive Assessment of Muscles |
| RMS | Root Mean Square |
| TFl | Thumb Flexion |
| TEx | Thumb Extension |
| TAb | Thumb Abduction |
| TAd | Thumb Adduction |
| IFFl | Index Finger Flexion |
| IFEx | Index Finger Extension |
| PDF | Probability Density Function |
| r | Pearson's sample correlation coefficient |
| ρ | Pearson's population correlation coefficient |
| ThC | Threshold Combination |
| IP | Interphalangeal |

# Chapter 1 Introduction

The upper limb (and the hand in particular) plays an integral role in many different activities of daily living (ADLs) such as eating, washing and dressing. The hand is an extremely dextrous appendage whose natural movements involve both superficial[1] and deep[2] muscles working closely together. Partial or complete loss of motor function of the hand as a result of cardiovascular accident (stroke) or amputation considerably reduces the affected person's ability to perform these everyday tasks, and often impairs their ability to live independently. Researchers in the field of rehabilitation engineering have sought to develop advanced orthotic[3] and prosthetic[4] devices that emulate the functionality of the hand as closely as possible to assist in rehabilitation protocols to either regain functionality or replace the functionality of the amputated hand (Gopura et al. 2013; Merril et al. 2013; Asghari Oskoei & Hu 2007). Active orthotic and prosthetic devices incorporating bio-signal features such as surface Electromyography (sEMG) are one such example, since sEMG can provide real-time muscle activation feedback for the wearer as well as being used as a control input for the device. However, conventional sEMG methods are unable to differentiate between the activation of superficial muscles and deep muscles. Consequently, the control inputs for many sEMG triggered orthotic and prosthetic devices for the hand are limited to interpreting movement intention from superficial muscles.

The research presented in this thesis sought to improve upon existing EMG detection techniques; specifically detecting EMG activity from the deep muscles responsible for thumb function using electrodes placed on the surface of the skin. A pilot study to assess the viability of modifying an existing technique (John 2009) for the detection of deep muscle EMG to the forearm muscles of 15 healthy participants was conducted. The capability of measuring EMG activity of these muscles may be beneficial in the development of myoelectric prostheses or rehabilitation devices targeting specific movements, such as a lateral pinch grip, for stroke patients in an acute or chronic setting.

To provide context for the study, a description of EMG signal generation and measurement theory is provided in section 1.1 followed by a description of the application of EMG for orthotic and prosthetic control in section 1.2. The theory behind the sdEMG technique and preceding work in developing the technique is presented in section 1.3. Finally, an overview of the aim, research objectives, hypothesis and scope of the study are provided in section 1.4.

## 1.1 EMG signal generation and measurement

The descriptions of the biophysics of EMG generation and detection in this section have primarily been sourced from *Electromyography- Physiology, Engineering and Noninvasive Applications* (Merletti & Parker 2004) and the *ABC of EMG* (Konrad 2005). Additional sources have been cited where applicable.

EMG signals are generated as a result of the contraction of muscles, coordinated by the firing of individual muscle units (MUs), the smallest functional unit of the muscle. A motor unit consists of an α-motoneuron (originating in the spinal column) and the individual muscle fibres the motoneuron

[1] An anatomical term referring to muscles located directly below the skin
[2] An anatomical term referring to muscles lying below the first muscle layer (Gilroy et al. 2008)
[3] Devices to augment and assist a body part to perform a particular function
[4] Devices to replace the function of an amputated body part

innervates (shown in Figure 1-1, see Figure A-1 in APPENDIX A.1 for a description of the organizational structure of skeletal muscle). The neuron invaginates into the muscle fibres near its midpoint, creating a neuromuscular junction, known as the motor end plate. The motor unit is so named because all the individual muscle fibres act as one upon innervation from their α-motoneuron.

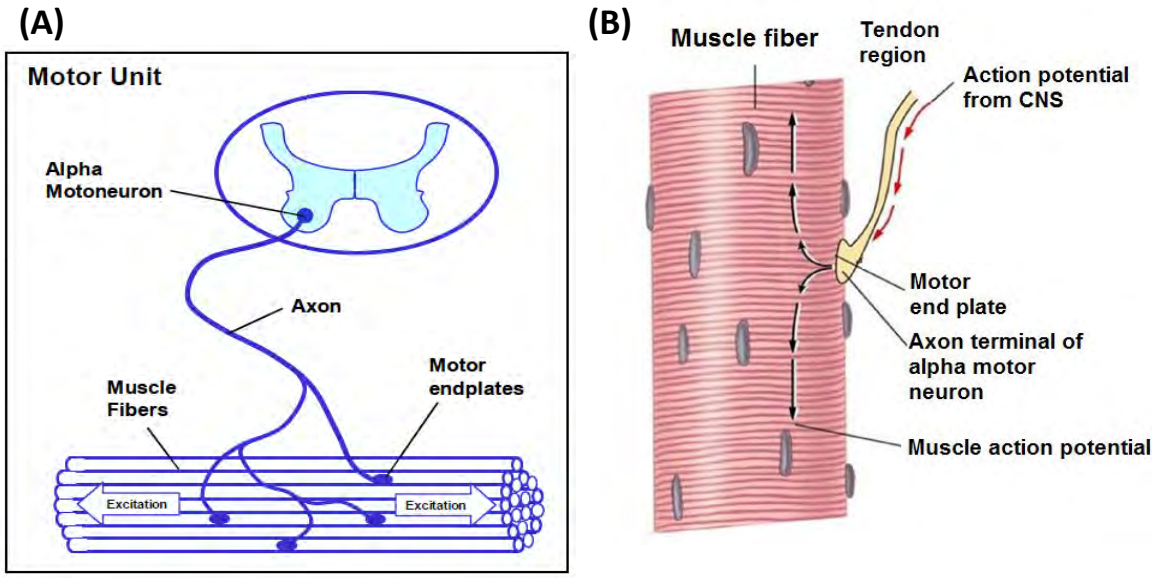


**Figure 1-1**: Structure of a single motor unit (Image A, from (Konrad 2005)) and action potential propagation (Image B, from (Guyton & Hall 2006)).

Upon the arrival of a neuronal action potential at the motor end plate, the α-motoneuron elicits an action potential in the muscle fibres, which propagates axially (away from the motor end plate and towards the tendons) on both sides of the motor end plate (see APPENDIX A.1 for a description of the biophysics of the muscle fibre action potential generation). The muscle fibre action potential creates a local depolarisation zone as it travels along the fibre, which creates a potential difference between suitably placed electrodes (either inserted into the muscle or placed on the surface of the skin). A simplified illustration of the bipolar detection of a travelling action potential from a single muscle fibre at different time points is shown in Figure 1-2:

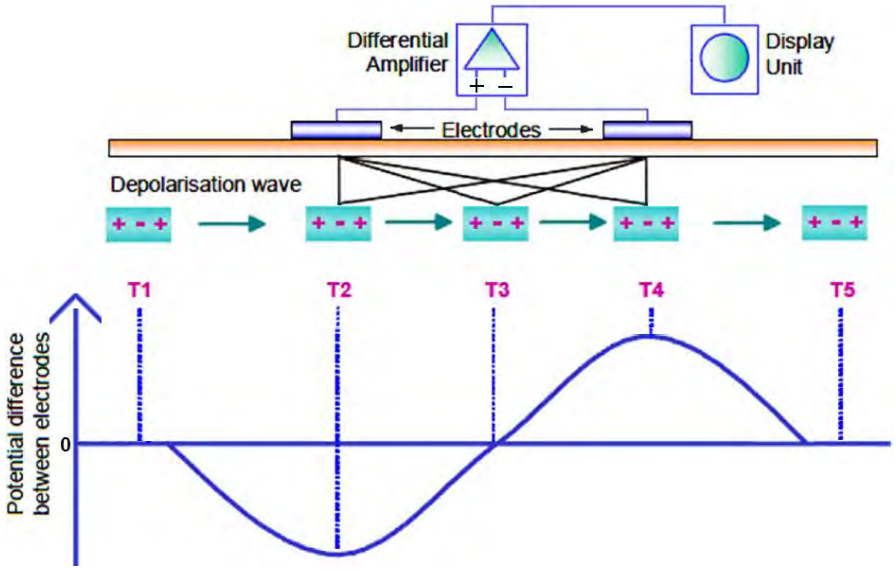


**Figure 1-2**: Simplified illustration of the detection of an action potential travelling along a muscle fibre by electrodes in a bipolar configuration. Image from (Konrad 2005)

A decreasing potential is measured at the positive electrode reaching a maximum at T2, when the wave is directly beneath the positive electrode (since the negative electrode does not detect any change in fibre potential). When the wave is equidistant from the positive and negative electrodes (T3), the differential amplifier detects a zero potential difference. The potential then increases to a maximum at T4, when the wave is directly beneath the negative electrode.

In reality, α-motoneurons synapse with multiple muscle fibres which summate to form a triphasic motor unit action potential (MUAP), see Figure 1-3. An electrode pair measuring the activity from a particular motor unit detects the summated magnitude of all these innervated fibres. The form and size of the MUAP depends on the geometric orientation of the individual fibres and their motor end plates in relation to the electrode detection site. In other words, the electrodes detect different components of the MUAP according to their distance from each fibre's motor end plate, as shown in Figure 1-3:

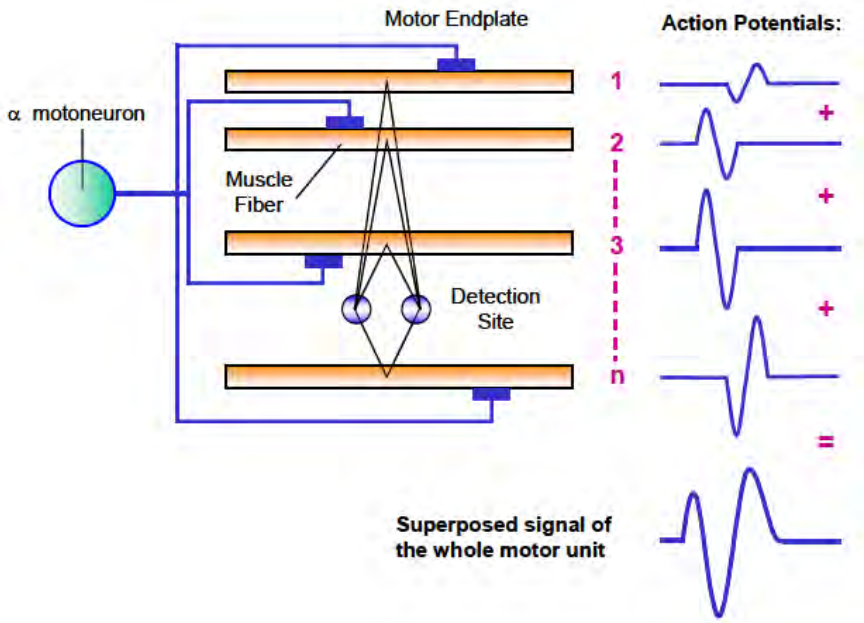


**Figure 1-3**: Formation of a triphasic motor unit action potential from the summation of individual muscle fibre action potentials. Image from (Konrad 2005)

The number of muscle fibres served by a single α-motoneuron, and the number of motor units present in a muscle, varies depending on the size of the muscle and its native function. Muscles responsible for very fine movements (such as muscles in the eye, ear and larynx) tend to contain few (~120) motor units interacting with 3-100 muscle fibres per motor unit. Large muscles responsible for coarse (limb) movements have up to 2000 muscle fibres per motor unit and ~600 motor units (Basmajian 1974; Jones et al. 2004).

EMG activity is most commonly measured using 2 electrodes (positive and negative) placed close together in a bipolar configuration, with a reference electrode placed at an electrically inert location (for instance, the bony surface of the olecranon). EMG may also be measured in a monopolar configuration, where the negative electrode is neither intramuscular nor superficial to the muscle. EMG electrodes can either be placed intramuscularly using a hypodermic needle, or non-invasively placed on the skin surface with a self-adhesive pad and conductive gel. Due to the small distance between their measuring points, intramuscular electrodes provide very precise, localized information from individual MUs near the electrode tip. Intramuscular electrodes have important applications in myopathy diagnosis and are required for recording of activity from deep muscles and the assessment of fine movement (Winter 2005). However, the insertion of needle electrodes into a muscle is often a painful, invasive process and difficult to repeat. Electrodes placed on the skin surface detect MUAPs in large volumes and provide a global picture of the muscle's MUAP activity. EMG measurements using surface electrodes (sEMG) are easily applied and widely used in applications such as sport and rehabilitation environments where whole muscle characterisation is more important than individual MU activity monitoring.

## 1.2 EMG applied to robotic devices

### 1.2.1 EMG in robot-aided neurorehabilitation

The development of EMG-based active orthotic devices has mainly focussed around exoskeleton devices for the rehabilitation of the stroke affected hand, as part of a broader treatment approach known as robot-aided neurorehabilitation. Robot-aided neurorehabilitation has been suggested as an alternate treatment approach to increase the quality of care therapists provide to their patients by taking over the more labour intensive aspects of the session (Richards et al. 2008; Krebs et al. 2000). Therapists may then spend more time engaging the patient with their therapy during the session to facilitate important natural neurological recovery processes such as cortical reorganisation[5] (Danzl et al. 2012; Krupinski et al. 2014; Blank et al. 2014).

Various EMG triggered devices have been proposed for neurorehabilitation of the hand, a comprehensive survey of which was conducted by Maciejasz et al. (2014). The majority of EMG-driven neurorehabilitation devices detect the EMG activity using surface electrodes (sEMG) since many of them are designed to be used multiple times by the stroke patients during the various rehabilitation sessions. Overall, the design focus for many of these devices has been toward facilitating the movements to be rehabilitated correctly and ensuring the device is safe to use, rather than developing the EMG control strategy. The main reason for doing so has been to avoid triggering inadvertent movements by the robot due to abnormal, uncoordinated activation and crosstalk interference from different muscles (Marchal-Crespo & Reinkensmeyer 2009; Farina et al. 2004). Therefore many of these devices use simple EMG control strategies, targeting a limited group of muscles that are easily detectable with sEMG to avoid interference from neighbouring muscles.

Three examples of current EMG-driven exoskeleton orthotic devices for stroke rehabilitation are shown in Figure 1-4. A 4 degree of freedom (DoF) device was developed by (Wege & Zimmermann (2007) (image A in Figure 1-4) for rehabilitation of the fingers and thumb. The device used 10 bipolar surface electrode pairs to detect the wearer's intention from the EMG activity of muscles in the forearm involved in movements of the hand and thumb (Flexor Digitorum Superficialis, Flexor Pollicis Longus[6], Extensor Digitorum, Extensor Pollicis Longus[6] and Extensor Indicis). When the EMG activity crossed a certain threshold, the device would move the fingers and thumb with a motor and cable system. Wege & Zimmermann (2007) found that it was not possible to discern the activation of each of the target muscle under investigation as there was a large of coupling (multiple muscles active during some movements). They also found that the placement of the electrodes was critical for the device to function properly and the correct placement was a very time consuming procedure.

Kline et al. (2005) developed a simple rehabilitation glove (image B in Figure 1-4) which flexed and extended the fingers using a pneumatic bladder system in response to EMG activity from the Flexor Digitorum Superficialis and Extensor Digitorum muscles (muscles responsible for flexion and extension of the fingers). The device operated in a very similar manner to the device by Wege &

[5] A key mechanism by which the stroke affected brain recovers functional ability (Westlake & Byl 2013; Kleim & Jones 2008; Warraich & Kleim 2010)

[6] No standardized details were provided by Wege & Zimmermann (2007) as to the exact electrode locations for these deep extrinsic thumb muscles nor how well the orthotic device detection system detected the activity of these muscles.

Zimmermann (2007) and was relatively easy to don and doff by participants with severe impairment and showed promise for reducing the impairment in the user's hand.

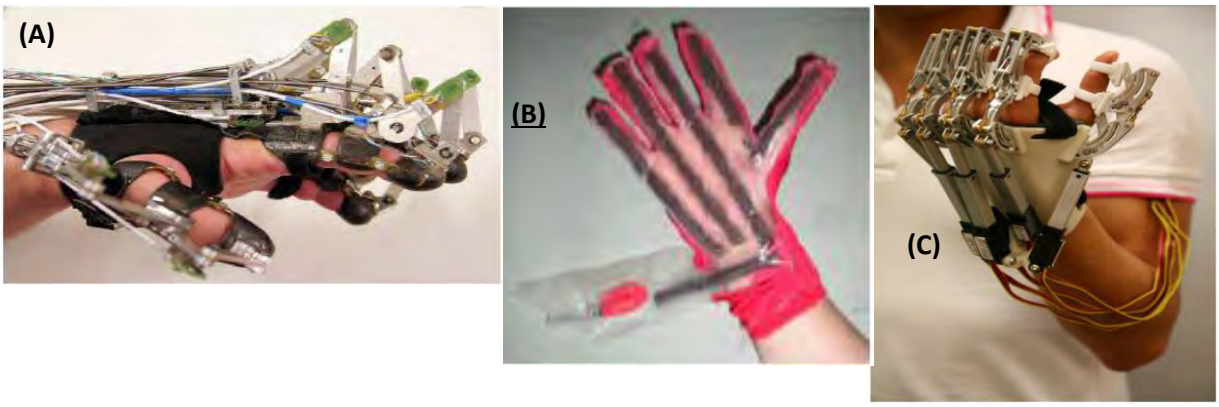


**Figure 1-4**: A 4 DoF orthotic device developed by Wege & Zimmermann (2007) uses a cable and motor actuation system triggered by EMG signals from muscles in the forearm responsible for movements of the thumb and fingers (Image A). A rehabilitation glove developed by Kline et al. (2005) using a pneumatic bladder system in response to EMG measurements from Flexor Digitorum Superficialis and Extensor Digitorum (Image B). The *Hand of Hope* developed by Tong et al. (2010) detects EMG activity from Abductor Pollicis Brevis in the hand and Extensor Digitorum in the forearm to open and close the hand using linear actuators (Image C). .

The *Hand of Hope* developed by Tong et al. (2010) uses EMG activity from the Abductor Pollicis Brevis muscle in the hand and Extensor Digitorum in the forearm as control signals to flex the fingers and thumb (close the hand) and extend the fingers and thumb (open the hand) respectively. *Hand of Hope* uses linear actuators to move the fingers and thumb and has shown promise for functional rehabilitation after stroke in two follow up studies (Ho et al. 2011; Ockenfeld et al. 2013).

The devices developed by Kline et al. (2005) and Tong et al. (2010) both use simple actuation and measurement systems for rehabilitation systems, but are limited in the number of movements from which intention can be detected, since they are only measuring activity from a few muscles. More complex and sophisticated devices such as the device developed by Wege & Zimmermann (2007) are able to provide more functionality, but are not able to detect clear control signals for each movement due to muscle activation ambiguity in the measured signals. Thus there is a need to develop new ways to detect movement intention from different muscles in order to expand the capabilities of robot-aided neurorehabilitation devices to provide targeted movement rehabilitation.

### 1.2.2 EMG applied to prosthetic device control

In contrast to EMG-driven orthotic devices, far more attention has been applied to the signal acquisition systems for EMG-driven prosthetic devices. EMG-driven prosthetic devices typically detect muscle activity from the residual stump using surface electrodes embedded in the socket of the prosthetic device. Devices such as the *i-limb™-ultra* (shown in Figure 1-5) measure EMG activity from only two separate sites on the stump of the arm, yet is capable of performing 14 highly dextrous hand movements (Touch Bionics Inc. 2015).

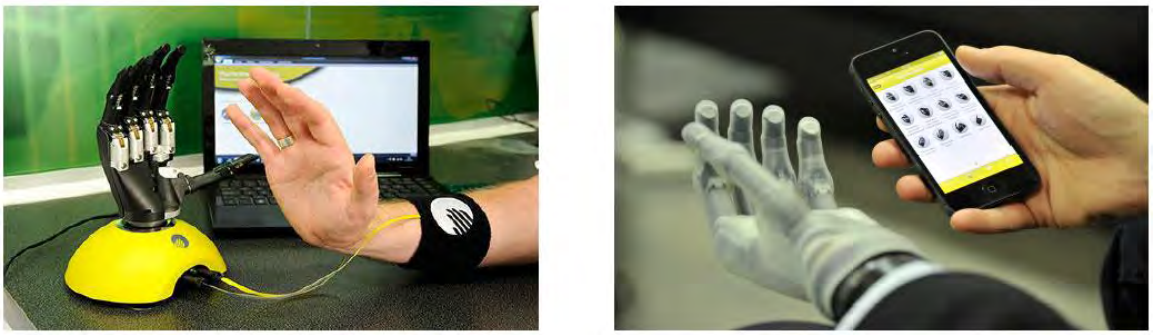

**Figure 1-5**: The *i-limb™-ultra* measures EMG activity from just 2 detection sites, yet is capable of performing 14 highly dextrous hand movements.

Due to the susceptibility of surface EMG measurements to crosstalk, the number of EMG measurement sites is limited, which hinders the degrees of control for prosthetic hand devices. The ability to detect EMG from a greater number of sites on the residual stump may be beneficial towards increasing the available degrees of control for the prosthetic device to provide the equivalent functionality of the amputated hand.

## 1.3 Superficial and deep muscle EMG (sdEMG) technique

The theoretical framework and prior work towards the development of sdEMG is described in this section. First, the concept of volume conduction of the EMG signal is described in section 1.3.1 to provide the physiological background of sdEMG's source separation ability from monopolar EMG measurements. The signal processing theory behind sdEMG is then described in section 1.3.2 followed by a description of the considerations specific to the choice of separation algorithm used in the present study, ICA, in section 1.3.3. Finally, prior work in developing sdEMG is described in section 1.3.4.

### 1.3.1 Volume conduction

Biological tissues between the muscle fibres and the measuring electrodes act as electrical volume conductors (Merletti & Parker 2004). Local volume conductors play an important role in assisting MUAP propagation, by providing an area external to the muscle fibre through which the ionic currents of the MUAP can travel and thereby help to extend the propagating MUAP. Volume conduction has a spatial low pass filtering (blurring) effect on the EMG signal, which is more pronounced in sEMG measurements than intramuscular measurements due to the greater distance between the detection site and the source. This filtering phenomenon mainly affects the frequency content of the signal, filtering out the higher frequency components, resulting in flatter looking waveforms (shown in Figure 1-6).

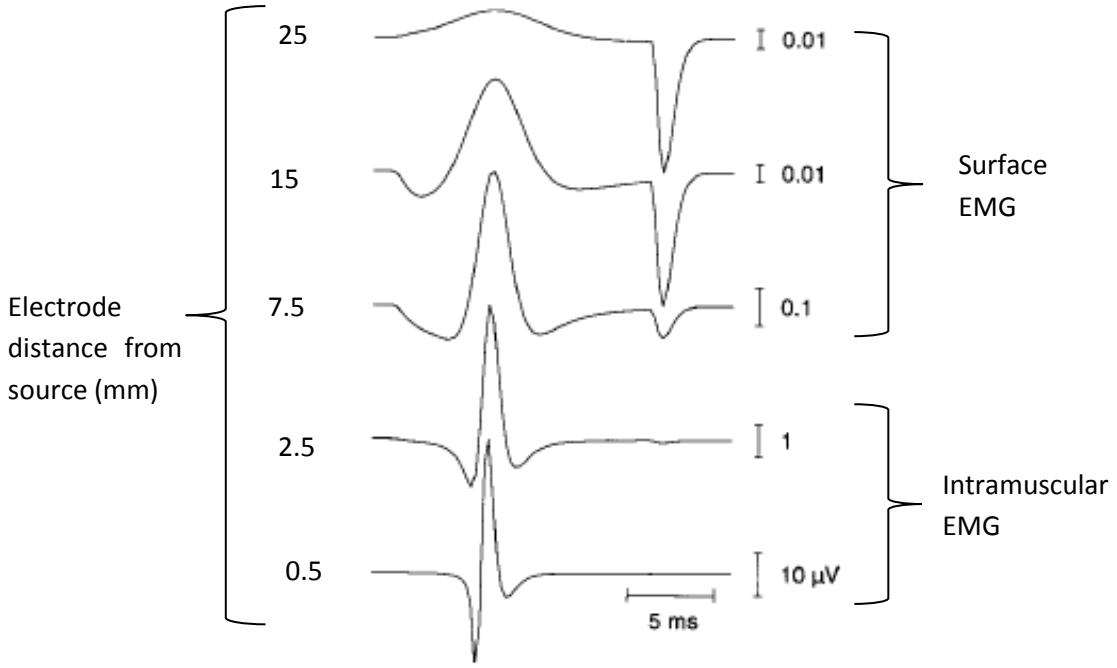


**Figure 1-6**: Single fibre action potentials from the same muscle fibre for varying distances between the electrode detection site and source. Adapted from (Blok et al. 2002)

Two separate studies by Roeleveld et al. ((1997) and (1997a)) investigated the effect of volume conduction on the recorded surface EMG potential from individual MUs at different depths and radial distances from the electrodes during voluntary isometric contractions of the biceps brachii muscle. The experiment combined 36 surface electrodes arranged in 2 rows of 18 electrodes each as well as concentric needle (CN) and single fibre (SF) intramuscular electrodes to determine the depth and position of the individual MUs (represented as dots over the biceps brachii muscle in Figure 1-7).

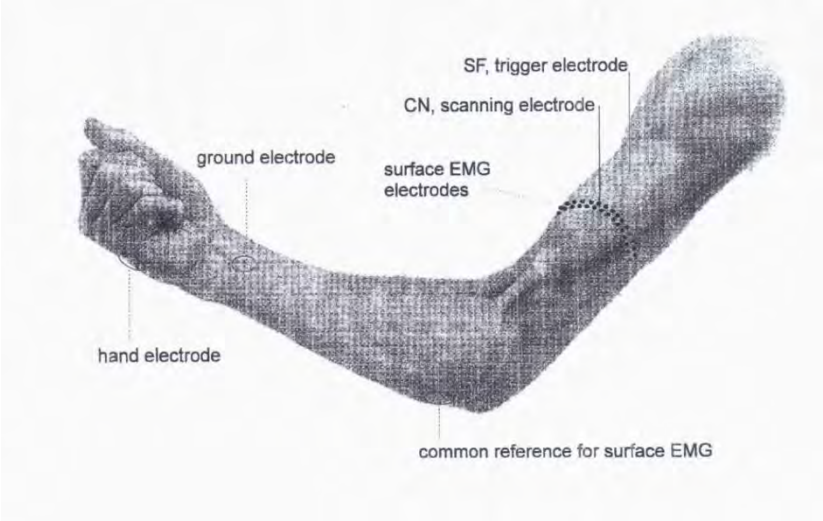


**Figure 1-7**: Experimental electrode configuration used by Roeleveld et al. (1997). The experiment combined 36 surface electrodes arranged in 2 rows of 18 electrodes each as well as concentric needle (CN) and single fibre (SF) intramuscular electrodes to determine the depth and position of the individual MUs (represented as dots over the biceps brachii muscle)

The studies found that the bipolar surface signals' amplitude decreased faster, as the radial distance between the MU and the electrodes increased, compared with the monopolar signals' amplitude (Roeleveld et al., 1997a). This is because volume conduction broadens the distribution of the surface potentials from deep MUs more than surface potentials from MUs closer to the skin surface due to the further distance the deep MU potentials have to travel to reach the surface electrodes. The broader distribution of the surface potentials results in greater spatial overlap of the signal across adjacent electrodes and thus the potentials start to appear as common mode signals. When detected by a bipolar electrode pair, common mode signals are cancelled out by the differential amplifier (Roeleveld et al.,1997). In the case of monopolar electrodes, the common mode signal is retained as part of the recorded signal (Merletti & Parker 2004).

Figure 1-8 provides a graphical representation of the distributed electrical potentials from deep (b, d) and superficial (a, c) MUs during the monopolar (a, b) and bipolar (c, d) recordings conducted by Roeleveld et al. (1997). The surface potential distributions in images (a) and (c) are highly peaked in the area directly above the MU due to the short distance between the superficial MU to the electrodes at that point. Volume conduction disperses the potential of the deep MU over a broader area (b) and causes the potential from the deep MU activity to appear as a common mode signal on multiple electrodes, which is cancelled out by the differential amplifier when measured in a bipolar configuration (d).

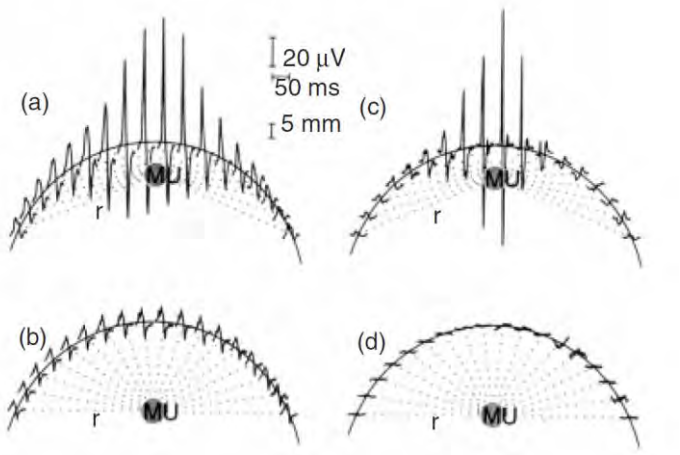


**Figure 1-8**: Model of the MUAP potential distribution on the skin surface of a superficial (a, c) and deep (b, d) MU. Images (a, b) are representative of a monopolar measurement and images (c, d) are representative of a bipolar measurement. Image from (Roeleveld et al., 1997). The surface potential distributions in images (a) and (c) are highly peaked in the area directly above the MU due to the short distance between the superficial MU to the electrodes at that point. Volume conduction disperses the potential of the deep MU over a broader area (b) and causes the potential from the deep MU activity to appear as a common mode signal on multiple electrodes, which is cancelled out by the differential amplifier when measured in a bipolar configuration (d)

This observation implies that monopolar EMG measurements contain a larger portion of the actual muscle activity (by virtue of the electrodes detecting contributions from both deep and superficial MUs) than bipolar measurements. By the same measure, the signal overlap from deep MUs on adjacent electrodes indicates that the bipolar electrode configuration is unable to detect deep MU activity. This is an essential aspect for the development of sdEMG.

### 1.3.2 Signal processing theory of sdEMG

The sdEMG technique was proposed by Dr Lester John and patented in 2009[7]. During movements in which deep and superficial muscles are both active, the extent to which the muscles are active is dependent on the muscle function and specific movement being executed. sdEMG is based on the postulation that monopolar EMG recorded from rings of electrodes, may be considered as a linear mixture of the muscle's activity associated with the muscles encircled by the rings during movements in which the muscles are active. Since each muscle has its own innervation characteristics during different movements, they may, initially, be considered as independent sources contributing towards the mixture. An estimation of the sources constituting this mixture may then be calculated by a suitable statistical separation algorithm such as, but not limited to, Independent Component Analysis (ICA) (John 2009).

ICA is an algorithm that separates sources within a linear mixture according to their statistical independence which can be summarised by the "cocktail party" analogy shown in Figure 1-9.

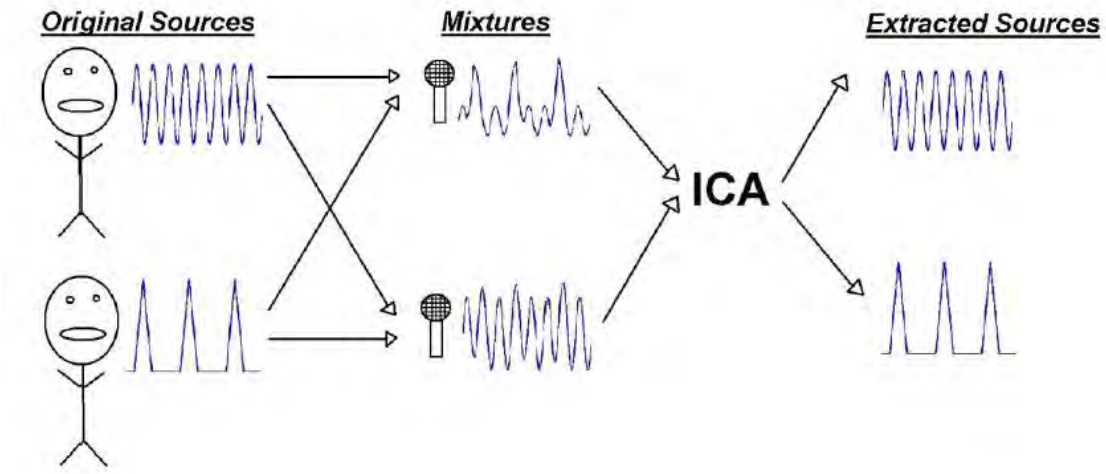


**Figure 1-9**: Illustration of the decomposition process by ICA represented by the "cocktail party" analogy. Image from (Langlois et al. 2010). If a group of people are speaking in a room with an equal number of microphones as people placed around the periphery, each microphone will (by virtue of its spatial position relative to the group) record a linear combination of each person in the group's voice. Assuming each person's voice is unique, ICA separates each voice from the linear mixture based on each voice's unique characteristics.

Consider a group of people speaking simultaneously in a room, with an equal number of microphones as people placed around the periphery. Each microphone will, by virtue of its position in the room relative to the group, record a different linear combination of the people's voices. Since each source (a person's voice) is unique to that person and independent of anyone else's in the group, ICA extracts the individual sources from the mixtures recorded by the microphones on the basis of their un-relatedness or independence to each other. ICA separates the sources by assuming the recordings from the microphones (x) are a linear mixture of the people's voices (s) such that:

[7] The technique is patented (priority date: 30 July 2009) in South Africa (2011/09523) and China (201080030787.6) and patent-pending in the USA (13/387,897), Europe (10803972.8), Japan (J2012-522271) and India (2823/MUMNP/2011).

$$x = As$$

Where A is a linear mixing matrix. ICA calculates an un-mixing matrix (the inverse of the mixing matrix, A) W to estimate the original source activity (s), known as the independent components (ICs):

$$s = Wx$$

This process can be represented graphically in Figure 1-10:

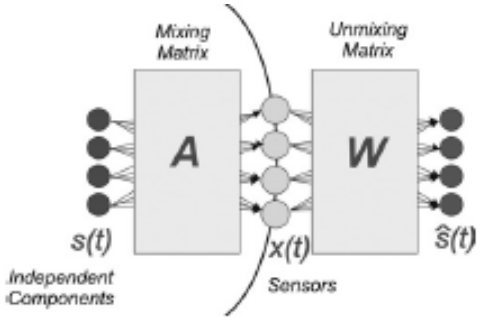


**Figure 1-10**: Mathematical representation of ICA decomposition from multiple sensors. Image from (James & Hesse 2005). Measurements from x sensors are considered as a linear mixture of s independent sources under the action of a linear mixing matrix A. ICA calculates an un-mixing matrix W (the inverse of A) to estimate the original source activity, known as the independent components (ICs).

ICA can be applied in an electrophysiology application if the voices in the cocktail party analogy are replaced with biological signals and the microphones with electrodes. An example of this which has been extensively used, is as an artefact removal tool in recorded Electroencephalography (EEG) data: ICA pools together fragments of signals and artefacts present on adjacent electrodes. This can be performed since the random processes creating the artefacts and the cortical potentials are independent from each other (Delorme et al. 2007; James & Hesse 2005; T. Jung et al. 2000).

### 1.3.3 ICA applied to surface EMG measurements

Using a similar approach, ICA (or another suitable separation algorithm) could theoretically be used to extract the sources present in a monopolar mixture of sEMG potentials. ICA is a Blind Source Separation (BSS) algorithm that does not rely on any prior information about the signals or their spatial location. It does, however, rely on a number of assumptions for the un-mixing matrix estimation (Djuwari et al. 2005; James & Hesse 2005; Stone 2004):

1. The sources must be statistically independent (the random processes generating the sources are independent of each other). Mathematically, statistical independence is defined by the non-Gaussianity of a signal (how dissimilar the probability density function (PDF) of the signal is to a normal, Gaussian distribution). ICA separates out sources from mixtures based on their non-Gaussianity and cannot separate mixtures of Gaussian sources (since Gaussian sources have a non-Gaussianity measure of 0).
2. The number of sensors (recording devices) is at least the same as the number of sources (voices or muscles making up the mixture to be separated). ICA algorithms assume a square-

mixing matrix (where the number of sources equals the number of measurement channels) in order to make the separation process more manageable

3. The sources are linearly and noiselessly mixed in order for ICA to find a linear un-mixing matrix.
4. The sources are stationary and do not change position with time.
5. There is no propagation delay of the signal.

The assumptions for ICA are satisfied by sdEMG according to the following arguments (Naik & Kumar 2012; James & Hesse 2005):

1. EMG activity is made up of motor unit action potentials (MUAPs) from individual motor units (MUs) firing in each muscle during a contraction. Force production in the muscle is related to the number of active MUs as well as the rate at which the active MUs fire (Merletti & Parker 2004). At low contraction levels, the signal is made up of few MUAPs from a small number of MUs recruited independently of other muscles, thus each muscle can be assumed to be an independent source. A study by Nazarpour et al. (2013) confirmed this observation and found that as the percentage MVC effort level increased (and more MUs were recruited), the PDF of the recorded signal became more similar to a normal distribution, as shown in Figure 1-11.

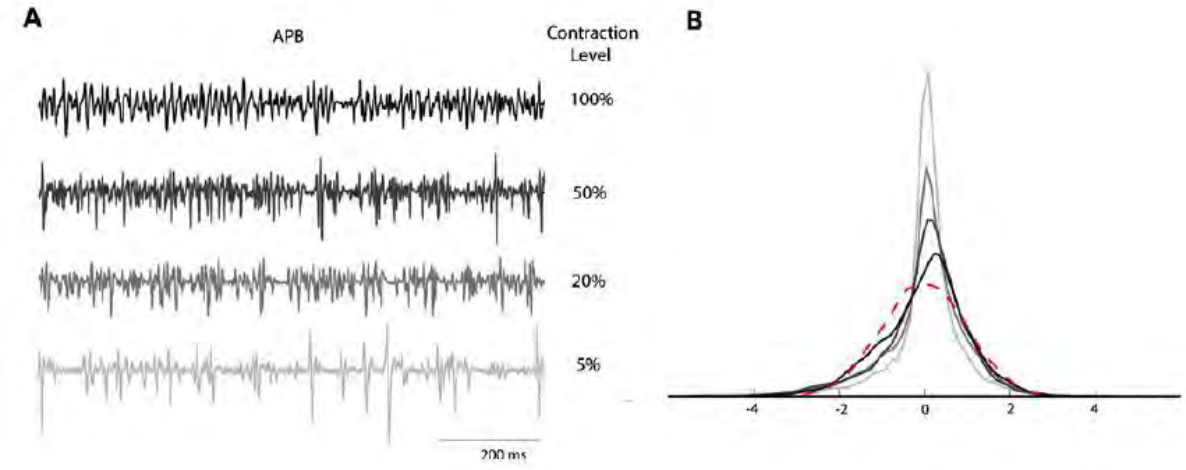


**Figure 1-11**: Probability density function (PDF, in image B) of an EMG signal at different contraction levels (represented as percentage MVCs, shaded from light to dark as the contraction level increase) and sections of the representative EMG measurements (image A) from the Abductor Pollicis Longus (APB) muscle at each contraction level. Image from Nazarpour et al. (2013)

2. At least the same number of recording electrodes (sensors) as muscles (sources) must be used so that the activity is not under-sampled.
3. Linear mixing assumes that the monopolar EMG signal measured at the electrodes is composed by linear superposition of the underlying muscle activity. Since the surface EMG activity is already a superposition of individual MUs firing (in the form of MUAPs), this is a reasonable assumption make.
4. During low levels of muscle contractions and isometric contractions, the length and position of the muscles does not change very much relative to the recording electrodes.

5. Volume conduction in tissue is essentially instantaneous (T.-P. Jung et al. 2000; Makeig et al. 1996)

There are two main limitations associated with ICA decomposition for EMG (Djuwari et al. 2006; Nakamura et al. 2004):

1. The amplitude of the ICs is no longer related to the original EMG activity. The relative amplitude within the ICs is maintained, however the amplitude cannot be compared between ICs[8]
2. The order in which the ICs are returned cannot be linked back to an electrode or particular area of the skin and may differ with each estimate. However, once the source activity estimation and un-mixing matrix has been found, the source activity associated with a particular electrode does not change (provided the electrodes remain in their original positions).

These limitations are due to one of the pre-processing steps in the ICA algorithm implementation to make the source activity estimation easier, known as signal whitening. Whitening is a process where a matrix of vectors is transformed to be uncorrelated, by forcing all elements to have unit variance using Principal Component Analysis (Hyvärinen & Oja 1997). In the context of EMG measurement, signal whitening removes the link between the electrode location and the EMG activity measured at that location. The relative amplitude between ICs is also lost because whitening scales the uncorrelated mixture (Stone 2004).

When dealing with the separation of the EMG signals, these limitations have considerable implications for the source separation and identification: the deep muscles from which the EMG signals originate cannot easily be determined by inspection of the electrode locations from which the surface measurements were recorded and the purpose of separating the monopolar EMG data is to find the original muscle source activity. Thus an independent method to identify which IC represented the muscle activity for each muscle was required for sdEMG (described in more detail in section 3.4).

### 1.3.4 Prior development of sdEMG technique

The technique was first tested in a proof of concept investigation to isolate the brachialis muscle in the upper arm by a fellow MSc student, Susalele Moroaswi (2009, unpublished results). Monopolar EMG was recorded from 12 electrodes arranged in 2 rings of 6 electrodes each placed in the appropriate locations according to the SENIAM placement guidelines[9] for measuring EMG activity from biceps brachii. The choice of using 12 electrodes for detecting the monopolar EMG activity was based on ensuring there were twice as many electrodes (12) as muscle bellies in the upper arm (6): so that the electrodes in the two bands would detect the MUAP on both sides of the motor end

[8] This limitation is also true for sEMG recordings: amplitude values from sEMG measurements between different muscles cannot be compared to each other, therefore the amplitudes are normalised relative to their MVC value.

[9] The 'Surface Electromyography for the Non-Invasive Assessment of Muscles (SENIAM)' guidelines are the result of collaboration between 16 European research institutions to develop a standardized framework for measuring, recording and reporting surface muscle EMG signals (Hermens et al. 1999). These guidelines have become the accepted standard of practice within the EMG field.

plates, as it propagates towards the muscle tendons. The common reference electrode was placed on the point of the elbow, shown in Figure 1-12.

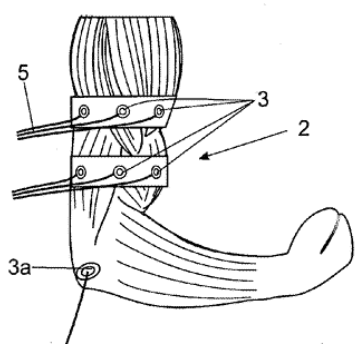


**Figure 1-12**: Electrode placement on upper arm for proof of concept investigation by Moroaswi & John (2010). Two rings of 6 electrodes each were placed around the upper arm. The common reference electrode (3a) was placed on the point of the elbow. Image adapted from (John 2009)**.**

The testing procedure involved 5 movements of the upper arm (shown in Figure 1-13). The brachialis muscle is primarily involved in flexion of the arm during pronation of the forearm (movements B and D in Figure 1-13), a function shared with the biceps brachii muscle. However, during flexed supination (movement C in Figure 1-13), biceps brachii takes over from brachialis, the latter becoming inactive (Hislop & Montgomery 2007). The monopolar EMG recordings from the two rings of electrodes were separated by fastICA, an ICA algorithm developed by Aapo Hyvärinen & Errki Oja (1997). The source signal of the brachialis was identified by observing which IC contained activity during flexed pronation but not during flexed supination (IC-V in Figure 1-13, highlighted by the red ellipses).

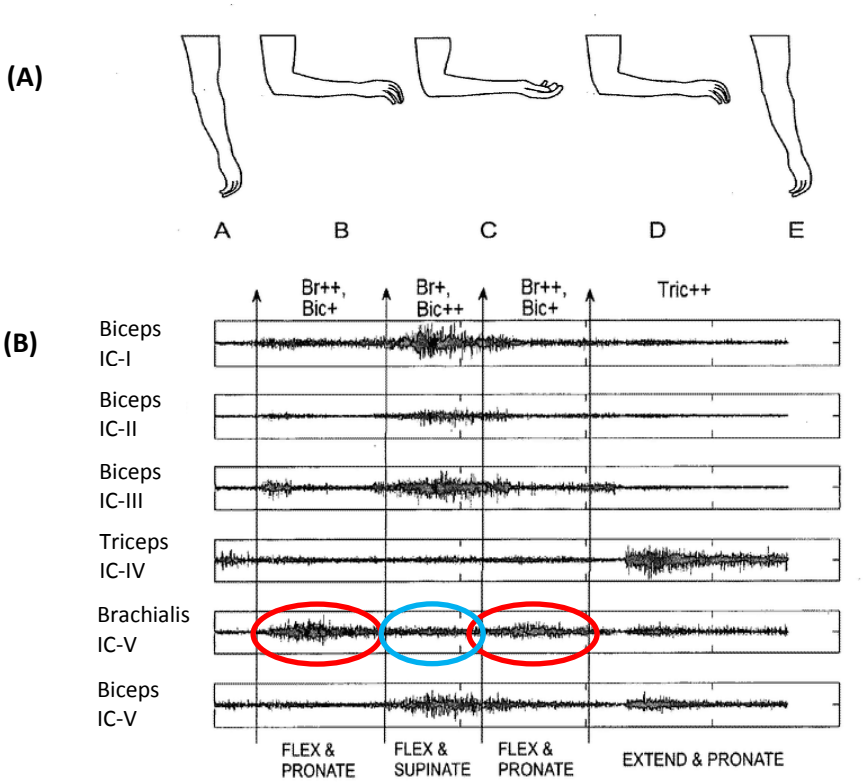


**Figure 1-13**: Movements used in proof of concept investigation (image A). Provisional RMS values for each ICA-EMG components during each of the five movements and first six ICA-EMG components derived from the EMG recordings of (Moroaswi & John 2010, unpublished results) (image B). The red ellipses highlight activity found during pronated flexion, which was subsequently absent during supinated flexion (highlighted by the blue ellipse). Images adapted from (John 2009).

Moroaswi & John (2010)'s preliminary results crossed the first hurdle by demonstrating the technique is able to detect deep muscle EMG using surface electrodes. Moroaswi & John (2010)'s findings were confirmed by a similar study by Mulligan et al. (2014), in which a genetic algorithm was used in conjunction with fastICA in a modified version of Moroaswi & John (2010)'s implementation of sdEMG to determine the minimum number of electrodes needed to detect the activity of brachialis. The choice of ICA for the monopolar EMG decomposition was an initial step. There are also a number of different ICA algorithms available (Stone 2004), however fastICA was the first algorithm used in the monopolar EMG data analysis and produced favourable results.

A second study was conducted by (Sayed et al. 2014) to detect the activity of Tibialis Posterior (TP), a deep muscle in the calf region of the leg. The experiment was conducted on 15 healthy participants performing 6 repetitions of 6 isometric contractions (plantar flexion, plantar extension, inversion, eversion, toe flexion, and toe extension) with the knee flexed and extended. Monopolar EMG was recorded from two rings of 10 electrodes each for all experimental runs. FastICA was used to un-mix the 20 monopolar EMG signals from each experiment and returned 20 ICs: the equivalent of 20 superficial and deep EMG measurements. The number of electrodes used by Sayed et al. (2014)'s application of sdEMG followed the same convention for the ratio of electrodes to muscles as

Moroaswi & John (2010): twice as many electrodes as muscles to ensure the electrodes detect the MUAP on both sides of the motor end plate as it propagates toward the muscle tendons. The ICs were full wave rectified using a moving average filter with a 250ms window and normalised. TP is active during inversion and plantar flexion and inactive during plantar extension, eversion, toe flexion and toe extension (Hislop & Montgomery 2007).

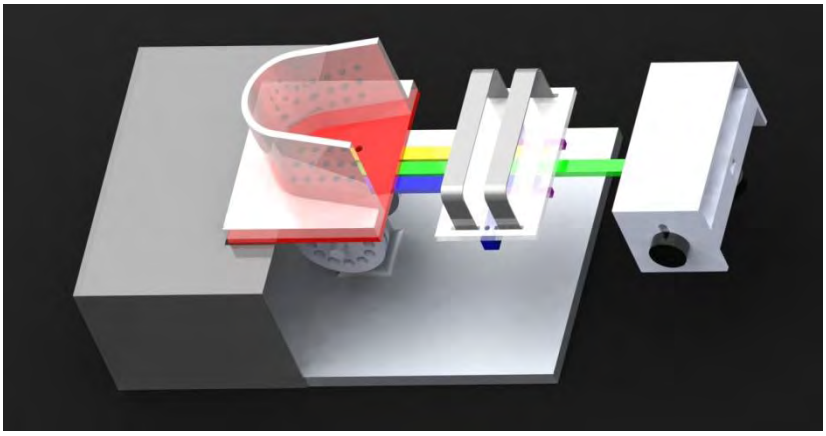

**Figure 1-14**: Movement platform used by Sayed et al. (2014) for the independent timing measurement for each isometric contraction

The isometric contractions were performed with the aid of a force measuring foot movement platform (shown in Figure 1-14), which served as an independent mechanism for timing each isometric contraction. A predicted EMG waveform for TP was created using the timing information from the movement platform and correlated with the ICs for each experimental run (shown in Figure 1-15). The correlated ICs were then ranked from highest to lowest, the highest ranked IC was considered to represent the activity of TP.

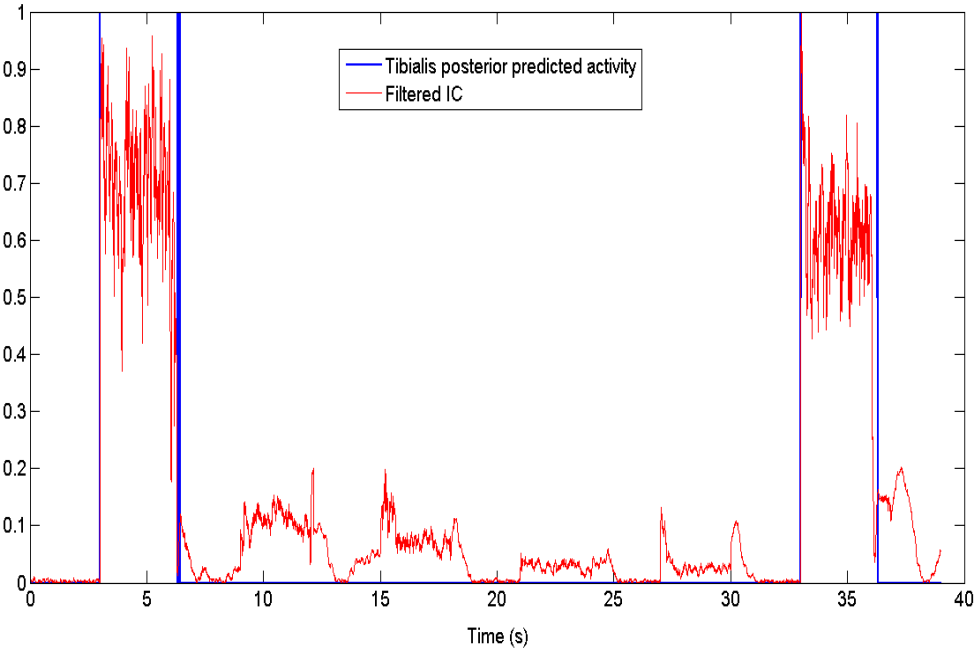


**Figure 1-15**: Filtered, rectified IC and predicted EMG waveform for TP. Image from (Sayed et al. 2014)

A mean correlation of 0.78 (0.6-0.86) and 0.78 (0.42-0.87) was found between the TP IC and the predicted EMG in the knee flexed and knee extended conditions respectively. The preliminary results indicated the technique was able to detect the activity of TP using surface electrodes.

## 1.4 Study overview

### 1.4.1 Opportunity for further development of sdEMG

The opportunity exists to broaden the degrees of control for robot-aided neurorehabilitation devices for the stroke affected hand as well as for the control of prosthetic hand devices by applying a modified version of sdEMG to the forearm to detect activity from the deep forearm muscles:

- Flexor Pollicis Longus (FPL)
- Extensor Pollicis Longus (EPL)
- Extensor Pollicis Brevis (EPB)
- Abductor Pollicis Longus (APL)

### 1.4.2 Hypothesis

It is hypothesized that sdEMG can detect the activity from the extrinsic deep (D) muscles FPL, EPL, EPB, APL.

### 1.4.3 Study aim

The aim of the present study was thus to investigate whether sdEMG can detect EMG activity of the deep extrinsic thumb muscles FPL, EPL, EPB and APL.

### 1.4.4 Research objectives

To test the study aim, sdEMG was applied to EMG activity recorded from the forearms of 15 participants during movements in which FPL, EPL, EPB and APL are known to be active: thumb flexion (TFl), thumb extension (TEx), thumb abduction (TAb) and thumb adduction (TAd). The research objectives for this process were thus defined as:

1. To develop an algorithm for determining the predicted EMG for each deep extrinsic thumb muscle.
2. To develop an algorithm for identifying the IC most likely to correspond to the activity of the deep extrinsic thumb muscles[10]:
    a. Flexor Pollicis Longus (FPL)
    b. Extensor Pollicis Longus (EPL)
    c. Extensor Pollicis Brevis (EPB)
    d. Abductor Pollicis Longus (APL)
3. Quantitatively determine how well the predicted EMG matched the ICs
4. Develop a statistical method for quantifying sdEMG's detection ability

As a secondary methodological objective, sdEMG's ability to detect activity from the superficial muscles Flexor Digitorum (FD)[11] and Extensor Digitorum (ED) using the electrode rings intended for deep muscles EMG detection (i.e., not optimised for superficial muscle detection) was also tested.

[10] The activity identification was also considered as a physiological objective

[11] The activation of Flexor Digitorum Superficialis and Flexor Digitorum Profundus were assumed to be acting together as a unit, see APPEDIX A.3.2

To test for these muscles, isometric index finger flexion (IFFl) and index finger extension (IFEx) were added to the experimental protocol. A description of the anatomy for each of the muscles under investigation may be found in APPENDIX A.3.

The choice of muscles to investigate as well as the isometric contractions in the present study was informed by a preliminary test, prior to conducting the main study, to determine which muscles and movements to target. The results of this test can be found in APPENDIX A.2. In order to conduct the experiment in the current study, a number of different pieces of experimental apparatus had to be developed by the researcher:

- An attenuation system to ensure the custom-built EMG amplifier system functioned as anticipated, as well as to calibrate the recorded EMG to millivolt values for reporting purposes.
- A thumb dynamometer was designed and built to ensure each thumb isometric contraction was performed at a standardized effort level
- A customised LabVIEW® application to coordinate the various data acquisition processes
- An electrode punch was built to construct the electrodes used in the present study from silver plate.
- Elasticised bands into which the electrodes were arranged for placement on the forearm of the participants had to be constructed.

### 1.4.5 Research value

The present study may be the first non-invasive EMG detection of the deep extrinsic muscles FPL, EPL, EPB and APL. The signal processing method in which this activity was identified is also novel.

It is possible that the ability to non-invasively detect activity in the extrinsic thumb muscles may provide additional degrees of control for myoelectric prosthetic devices or neurorehabilitation devices providing targeted movement rehabilitation of the thumb.

### 1.4.6 Scope of the present study

The present study is limited to investigating whether the method may be applied to healthy male subjects. This is a proof of concept investigation: if the method was unable to identify the muscles listed in section 1.4.4 in healthy subjects, it will be impossible to identify them in neurologically impaired subjects or persons with amputated limbs. Only isometric movements at an exertion level of 30% of the participant's Maximal Voluntary Contraction (MVC) were tested[12].

### 1.4.7 Thesis outline

Chapter 2 (Experimental Apparatus) describes the development and calibration of the apparatus used. Chapter 3 (Experimental Methodology) describes the experiment carried out to test the research objectives, the data processing procedures and statistical analysis performed on the experimental data. The results of the experiment and statistical analysis are presented in Chapter 4 (Results). Chapter 5 (Discussion) critically reviews the results and identifies possible shortcomings. Finally, the conclusions, limitations of the current study and recommendations for future work are presented in Chapter 6 (Conclusions).

[12] The choice of 30% MVC was related to ICA's separation ability of the monopolar EMG signals, see section 1.3.2 and APPENDIX A.5

[This page is intentionally blank]

# Chapter 2 Experimental apparatus

Chapter 2 describes the design, construction and calibration of the experimental equipment required to test the research objectives defined in 1.4.4. The experimental equipment facilitated the measurement and recording of forearm EMG activity using surface electrodes during isometric contractions of the thumb and index finger. The individual sub-components and their corresponding sub-sections are shown in Figure 2-1.

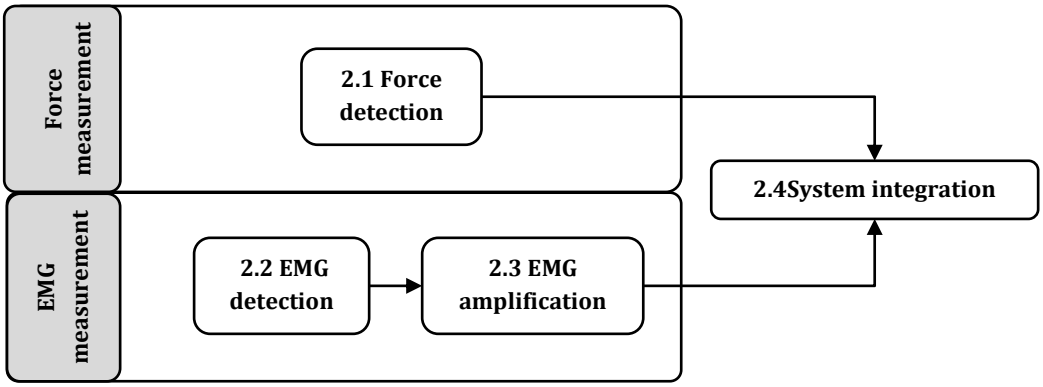


**Figure 2-1**: Experimental apparatus sub-components and associated section numbers

## 2.1 Force Detection

Two devices were used for force measurement during the experiment:

1. A dynamometer to measure forces during isometric Thumb Flexion (TFl), Thumb Extension (TEx), Thumb Abduction (TAb) and Thumb Adduction (TAd) was developed.
2. A finger load cell to measure forces during isometric Index Finger Flexion (IFF) and Index Finger Extension (IFE) was designed by another MSc student, R. Smith.

The design, force detection, force amplification and calibration of the two devices are described below.

### 2.1.1 Thumb dynamometer

The thumb dynamometer was designed in SolidWorks® by the researcher and constructed in the Department of Human Biology workshop by Mr. Charles Harris. A SolidWorks rendering and picture of the constructed dynamometer is shown in Figure 2-2. Full engineering drawings of the dynamometer may be found in APPENDIX F.

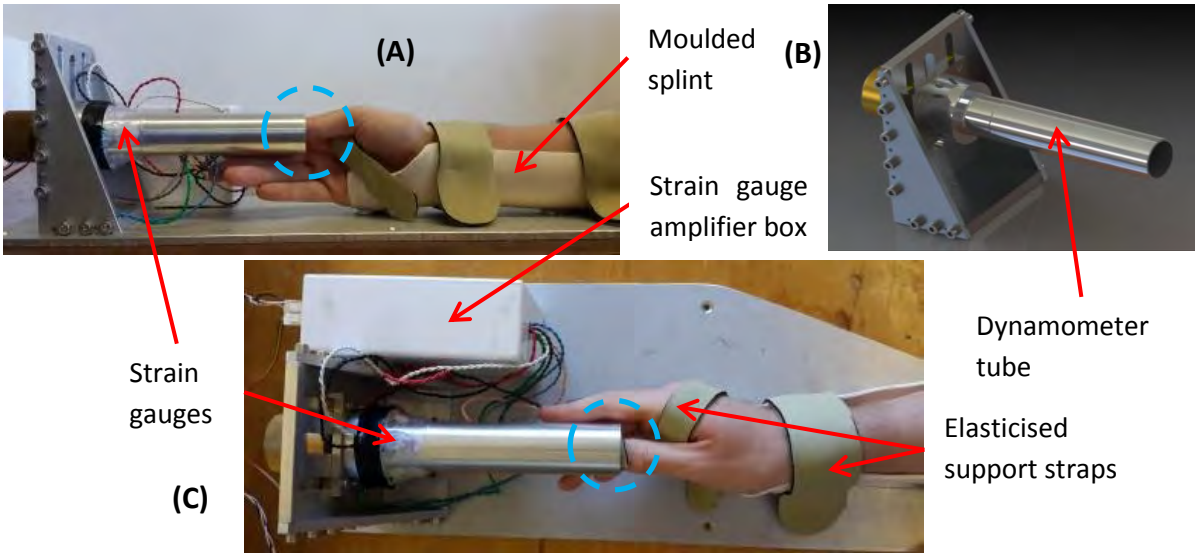


**Figure 2-2**: Left side and top views of the completed dynamometer in use (image A and C). SolidWorks rendering of dynamometer during design phase (image A). Note the thumb is inserted into the dynamometer tube (blue dashed circle). The hand is supported in a fixed position (30$^{o}$ extension), mid-way between pronation and supination by a moulded gutter splint and secured by elasticised bands. Other visible features are the strain gauges and their corresponding amplifier box.

### Design considerations

A primary design requirement was for the device to discern between the 4 different thumb isometric contractions, without having to change the hand's position. This was to allow for the selective activation of the muscles under investigation during each of the isometric contractions (see APPENDIX A.3 for an examination of each deep extrinsic thumb muscle's functional roles).

Studies by Bourbonnais & Duval (1991) and Kaufman et al. (1999) (both investigating the relationship between force and EMG activity contributions from extrinsic and intrinsic thumb muscles during thumb contractions) used thumb measurement devices capable of measuring forces in multiple directions without changing positions (Bourbonnais & Duval 1991; Kaufman et al. 1999). However the device used by Kaufman et al. was made by a third party company (NK Biotechnical Engineering Co., Minneapolis, USA) and no diagrams or dimensions of the design were provided. The device developed by Bourbonnais and Duval was based on a simple end loaded cantilever beam design with a solid cylinder as the cantilever. Two separate strain gauge bridges on the top-bottom and left-right surfaces of the cylindrical bar allowed for the measurement of forces during isometric TFl, TEx, TAd and TAb in the vertical and horizontal directions respectively (shown in Figure 2-3).

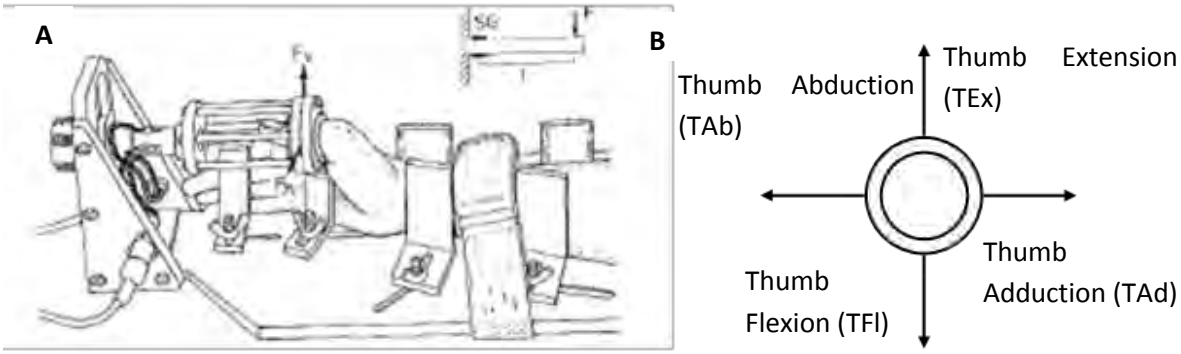


**Figure 2-3**: Diagram of dynamometer used in a study by Bourbonnais & Duval (1991) (A). Schematic representation of the isometric thumb contractions associated with the horizontal and vertical directions applied to the cylindrical cantilever, as viewed from the thumb cage element end (B).

The height of the strain gauge dynamometer tube was made adjustable to account for different sized hands (as indicated in Figure 2-4). The dynamometer design for the present study was a simplified version from that of Bourbonnais and Duval in that the cage elements (see Figure 2-3) were replaced with a cylindrical cantilever tube, into which the thumb is inserted. The cage structure was replaced with a tube to reduce the number of components to manufacture whilst allowing the participants thumb to apply forces in multiple directions without having to change the hand's position. The primary purpose of the cage structure in Bourbonnais & Duval (1991)'s study was to ensure there was only one point of application of the force on the strain gauge instrumented cylinder. A padded 3D printed ring placed inside the end of the dynamometer tube (shown in Figure 2-4) served as the single point of force application for the dynamometer in the present study. The 3D printed ring also served to accommodate for different sized thumbs (2 different spacer rings were used to account for different sized thumbs) as well as securing the thumb in the dynamometer tube.

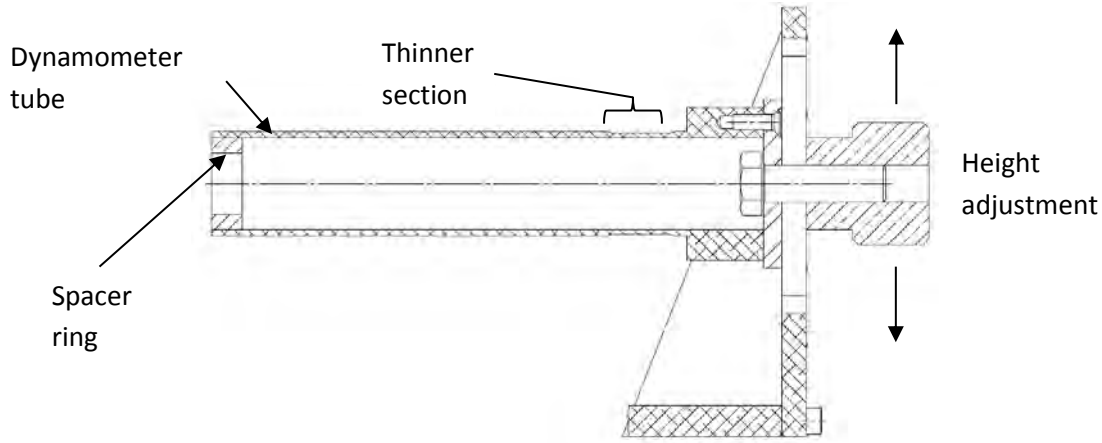


**Figure 2-4**: Cross section of dynamometer tube designed for this study

In simplifying the design, the length of the dynamometer tube as well as the inner and outer diameters of the tube were identified as important dimensions as they would have a direct effect on the dynamometer's sensitivity: a tube too thick (>3 mm) would be too stiff; a tube too thin (< 1 mm) would be at risk of plastic deformation and thus be unusable. Thus an analytical stress analysis was conducted in Microsoft Excel® to determine the appropriate inner and outer tube diameter, and

tube length dimensions for the dynamometer prior to its construction (described in APPENDIX B.1.2).

Finally, the mechanical strain was further concentrated into a specific zone (in which the strain gauges were placed) by cutting a thinner gauge section into the dynamometer tube, close to the fixed end (shown in Figure 2-4). A mechanical stress simulation of the dynamometer tube was conducted in SolidWorks to determine effect of the gauge section as well as verifying the analytical stress analysis results. The results of the mechanical stress analysis in SolidWorks may be found in APPENDIX B.1.2.

### Force amplification

Two separate full Wheatstone bridges (5mm gauge length, Aluminium, GF = 2, 120Ω) were placed at 90° intervals around the dynamometer tube to measure forces produced in the horizontal and vertical directions respectively (connected as shown in Figure 2-5).

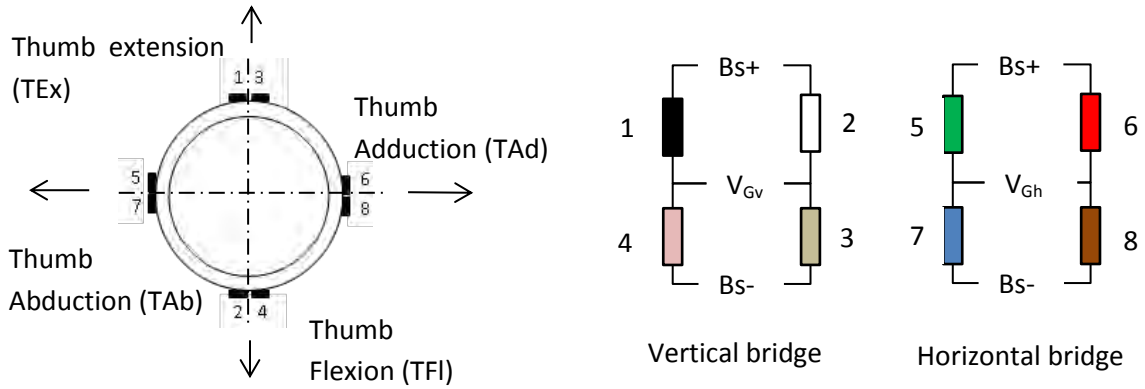


**Figure 2-5**: Strain gauge positions for vertical and horizontal bridges on the dynamometer tube (as viewed from end in which the thumb is inserted). The colours of the gauges in the image on the right indicate the wire colour going to that particular gauge.

The voltage differences between the arms (points $V_{Gv}$ and $V_{Gh}$ in Figure 2-5) of the two bridges were each amplified using identical, commercial amplifiers (RS components, stock code 435-692). Both amplifiers had a high common mode rejection ratio (CMMR) (> 120dB), a bandwidth of 450 kHz and used high precision resistors (1% tolerance) (see APPENDIX F for datasheet and circuit schematic). The supply voltage for both bridges (points Bs+ and Bs- in Figure 2-5) was set to 3.0V. The gain for the dynamometer and finger load cell was set to 1001 by choosing appropriate resistor values ($R_1$ = 100kΩ; $R_2$ = 100Ω) according to the equation:

$$Gain = \frac{R_1}{R_2} + 1 \qquad \textbf{Equation 2-1}$$

A full datasheet and schematic layout of the amplifier printed circuit boards is provided in APPENDIX F. A calculation of the theoretical output voltages from the strain gauges is included in APPENDIX B.1.2. Voltage outputs from each bridge circuit were measured as positive or negative voltages depending on the direction of the applied force (see Table 2-1).

**Table 2-1**: Direction definitions for vertical and horizontal dynamometer directions (isometric contraction abbreviations defined in sections 1.4.4 and 2.1)

| Measurement direction | Applied force direction | Wheatstone bridge voltage polarity | Isometric contraction |
|---|---|---|---|
| Vertical: | Down | Negative | TFl |
| | Up | Positive | TEx |
| Horizontal: | Left | Positive | TAb |
| | Right | Negative | TAd |

### Calibration

The dynamometer was calibrated in each of the four directions indicated in Figure 2-5 separately. This was to verify the linearity of each direction and mechanical decoupling of the two measurement systems. Hanging weights were used to apply increasing forces, from 0 to 109 N in 10 N intervals, to the dynamometer tube from the same point of application as the 3D printed spacer ring. The output voltages from both strain gauge measurement systems were recorded at each force application point by a National Instruments Data Acquisition (DAQ) device. Linear regression trend lines were calculated for the recorded voltage and force values for each tested direction and are shown in Figure 2-6 and Figure 2-7 respectively.

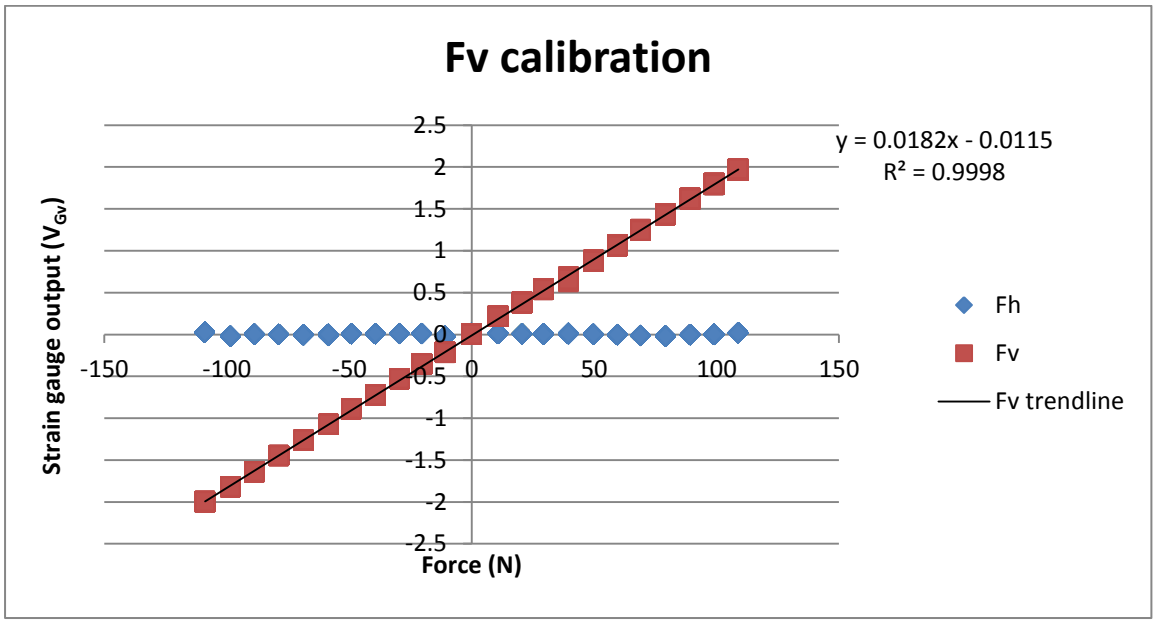


**Figure 2-6**: Calibration curve of the vertical dynamometer measurement system during the application of hanging weights to the dynamometer tube in the vertical direction. The output of the horizontal measurement system was also recorded for each hanging mass to determine whether there was mechanical decoupling of the measurement systems.

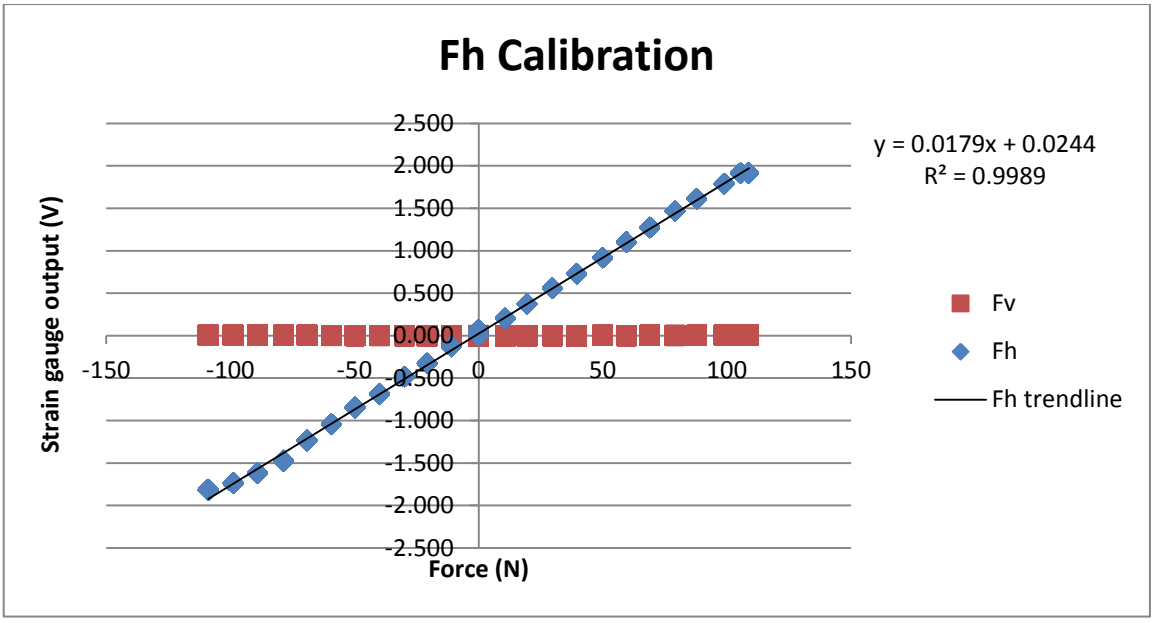


**Figure 2-7**: Calibration curve of the horizontal dynamometer measurement system during the application of hanging weights to the dynamometer tube in the horizontal direction. The output of the vertical strain gauge measurement system was also recorded for each hanging mass to determine whether there was mechanical decoupling of the measurement systems.

The trend line slope represented the horizontal (Fh) and vertical (Fv) strain gauge measurement systems' voltage output per unit of force applied (V/N) at the 3D printed spacer ring end of the tube (into which the thumb is inserted). Figure 2-6 and Figure 2-7 clearly show a mechanical decoupling between the two strain gauge systems. The Fv and Fh regression slopes for the vertical and horizontal measurement systems were found to be 0.018 V/N and 0.018 V/N respectively. For a complete description of the calibration procedure see APPENDIX B.2.

### 2.1.2 Finger Load Cell

#### Design considerations

The load cell (shown in Figure 2-8) was designed to fit the proximal interphalangeal (IP) joint of the index finger in a comfortable position (as individually found for each participant) between flexion and extension. The device was constructed from Perspex. (See APPENDIX F for engineering drawings).

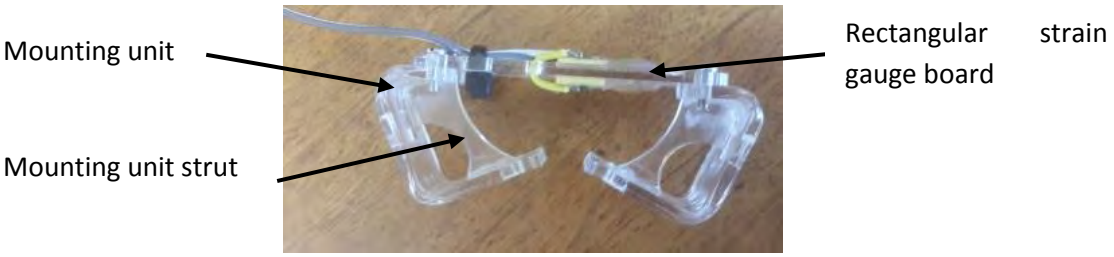


**Figure 2-8**: Finger load cell position during testing (left). Side (centre) and isometric views of the device (right)

The device was designed around a flat rectangular board upon which the strain gauge is mounted (shown in Figure 2-9). During IFFl the board bends negatively (as defined in Figure 2-9), according to the bending definition by Hearn (1985)) and in the opposite manner during IFEx. The mount unit is reinforced with a strut to ensure that all the force applied is transferred to the strain board.

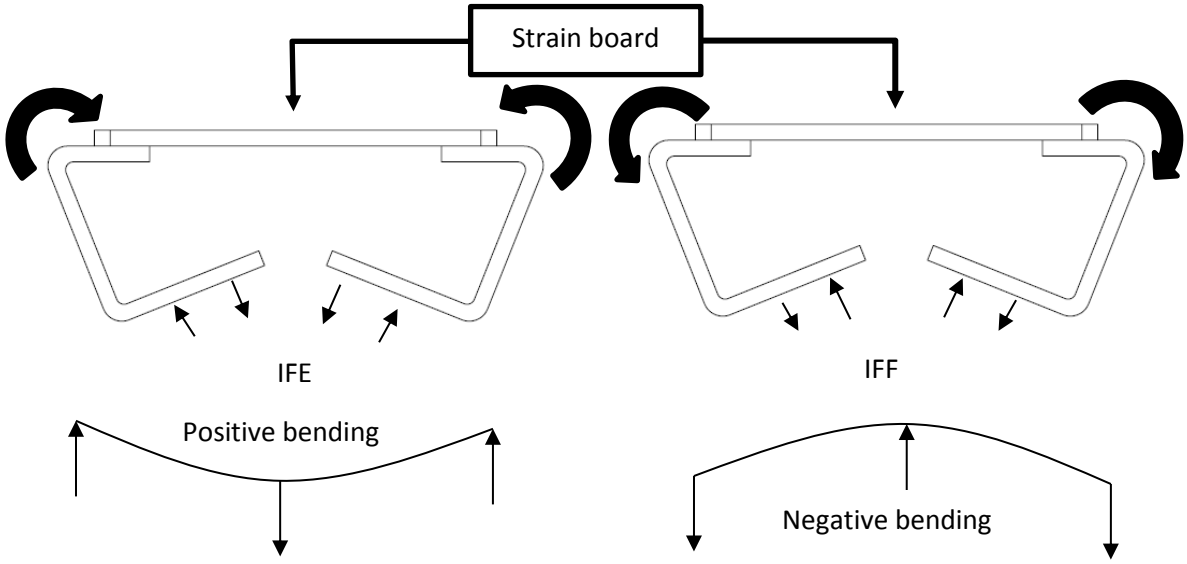


**Figure 2-9**: Free body diagram of the finger load cell operation during index finger extension (left) and flexion (right)

### Force amplification

Two foil strain gauges (2mm gauge length, Aluminium, Gauge Factor = 2, 120Ω) were mounted in a half-Wheatstone bridge configuration on the strain board. Perspex is far more flexible than steel, thus any losses in resolution as a result of using fewer active gauges is mitigated by the larger strains measured by the remaining active gauges during flexion and extension of the finger. The bridge was completed using two high precision (1%) 120Ω resistors as dummy gauges. The gauges were connected as shown in Figure 2-10:

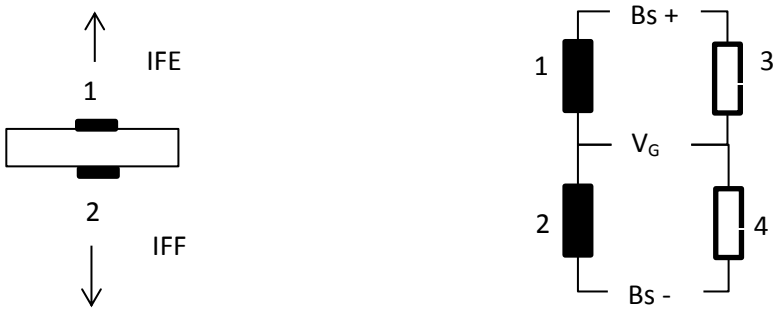


**Figure 2-10**: Strain gauge configuration for the finger load cell. Gauges 1 and 2 were placed on the strain board (see Figure 2-9) while gauges 3 and 4 were dummy gauges.

An identical amplifier (with the same gain value) to that of the dynamometer was used to amplify the finger load cell strain signals. The bridge supply for the finger load cell strain gauge amplifier was set to 0.3V. As was the case for the thumb dynamometer, the voltage output was measured as

positive or negative depending on the direction of the applied force. The polarity of the Wheatstone bridge and the associated directions is defined in Table 2-2:

**Table 2-2**: Direction definitions for the finger load cell (isometric contraction abbreviations defined in section 1.4.4 and 2.1)

| Contraction plane | Wheatstone bridge voltage | Isometric contraction |
|---|---|---|
| Finger | Positive | IFEx |
| | Negative | IFFl |

### Calibration

The finger load cell was calibrated by applying forces in the flexion and extension directions using a spring gauge from 0-10N in increments of 1N. The output voltage from the finger load cell was recorded at each force loading point and is shown in Figure 2-11. A best fit line of the plotted output voltage and force plots was found for both directions using linear regression. The slope for the finger load cell (F_finger) was found to be 0.15 V/N. See APPENDIX B.3 for a full description of the finger load cell calibration

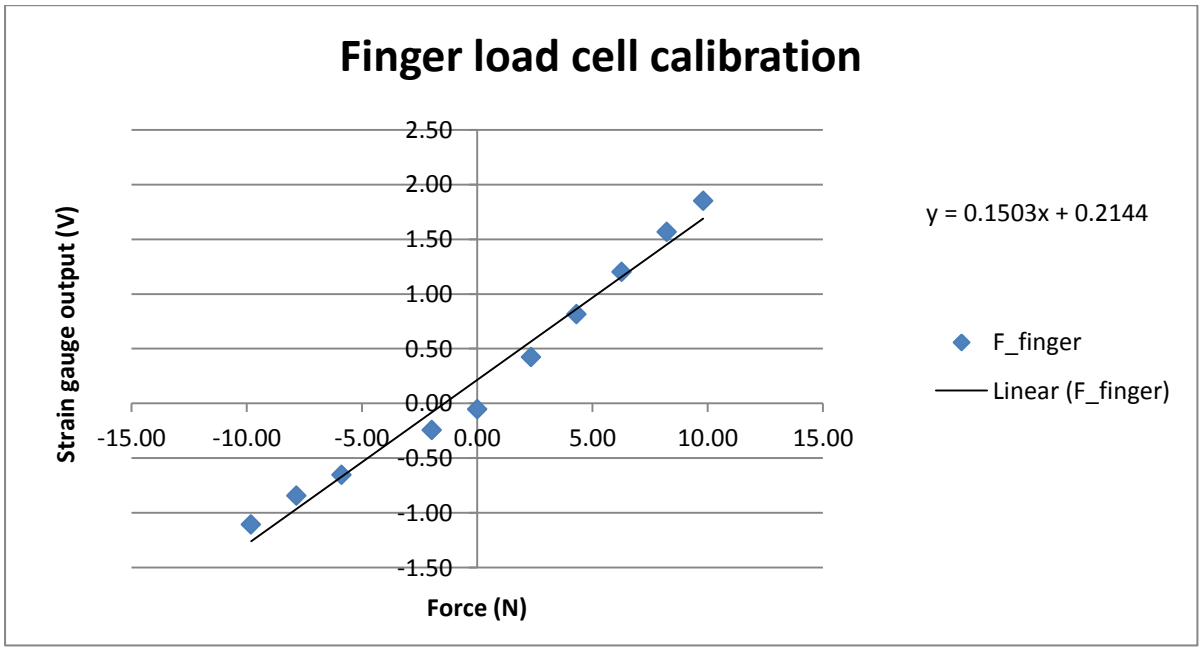


**Figure 2-11**: Calibration curve of finger load cell during forces applied in flexion (negative) and extension (positive) direction

## 2.2 EMG Detection

The design of the electrodes were based on that of EEG electrodes produced by Nihon Kohden (Nihon Kohden, Japan) and in accordance with the size and shape recommendations of SENIAM[13] (Hermens et al. 2000). Sterling silver was chosen as the material for the electrodes in accordance

[13] The Surface Electromyography for the Non-Invasive Assessment of Muscles (SENIAM) guidelines is the result of collaboration between 16 European research institutions to develop a standardized framework for measuring, recording and reporting surface muscle EMG. These guidelines have become the accepted standard of practice within the EMG field.

with the SENIAM recommendations as silver “provides a very stable transition with low noise” (Stegeman & Hermens 1999). Engineering drawings of the electrode and individual components for the electrode punch may be found in APPENDIX F.

Forty-two silver cup-type electrodes (diameter = 10mm) were punched out of 2mm thick sterling silver sheet using a custom-made electrode press shown in Figure 2-12. The electrodes were made to be used with Elefix conductive electrode paste from Nihon Kohden (see section 3.2.1), establishing the Ag-AgCl ion transfer bridge required for bio-signal acquisition. Forty electrodes were used for the monopolar EMG detection, one for the Driven Right Leg (DRL) (see section 2.3.1) electrode and another for the common reference electrode. The number of electrodes was limited to 40 in accordance with the principles applied in the previous sdEMG studies of Moroaswi & John (2010) and Sayed et al. (2014): to ensure that approximately twice as many electrodes as muscles (there are 19 muscles in the forearm, see APPENDIX A.2.1) were used so that the electrodes could be placed on either side of the motor end plate of the muscles under investigation (see 1.3.4 for description of previous sdEMG studies). Oversubscribing the number of electrodes to muscles also allows for the detection and elimination of non-muscle activity related artefacts that might have been introduced during recording by ICA (Naik et al. 2006; Delorme et al. 2007)

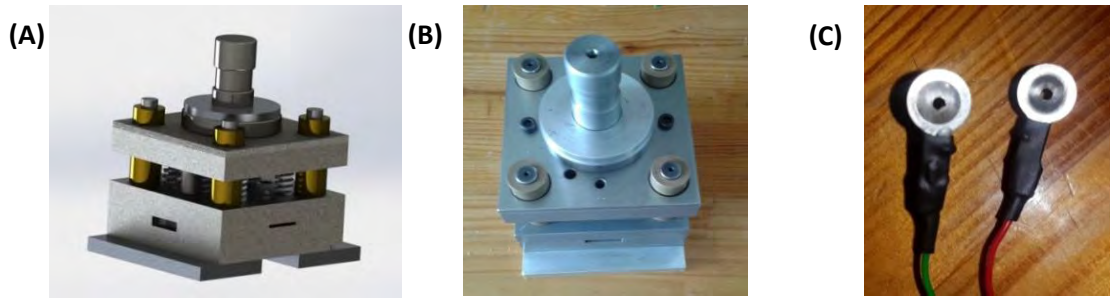


**Figure 2-12**: Electrode punch rendering in SolidWorks (image A), the actual punch (image B), sample electrodes made by punch (image C).

The electrodes were arranged into 2 elasticized bands of 20 electrodes each (forming a ring of electrodes when placed around the forearm), based on the design used by Mulligan et al. (2014) (see section 1.3.4).The electrodes were arranged into rings so as to have the best chance of detecting the distributed deep muscle activity on the surface from as many locations as possible. This was to enable ICA to pool together activity from all the electrodes in its estimation of the source activity. The bands maintained a consistent inter-electrode distance of 20mm and reduce the setup time applying and removing the electrodes between tests. The bands were elasticized to accommodate differing arm sizes. The electrodes were arranged diametrically opposite each other according to the diagram shown in Figure 2-13: each number corresponds to the amplifier channel with which the electrode interfaced.

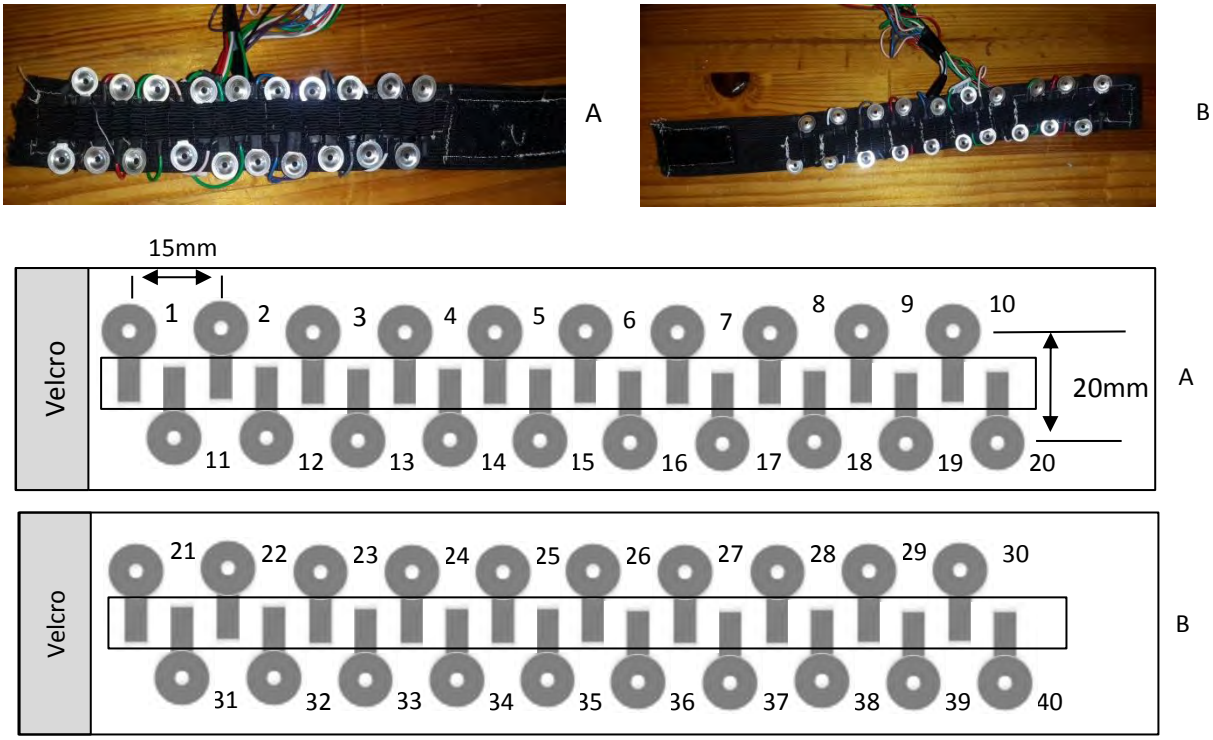


**Figure 2-13**: Electrode bands A and B (top) and electrode numbering for each band (bottom)

## 2.3 EMG amplification

The EMG signals were amplified by a 40ch EMG system. Figure 2-14 provides a schematic breakdown of the system sub-components.

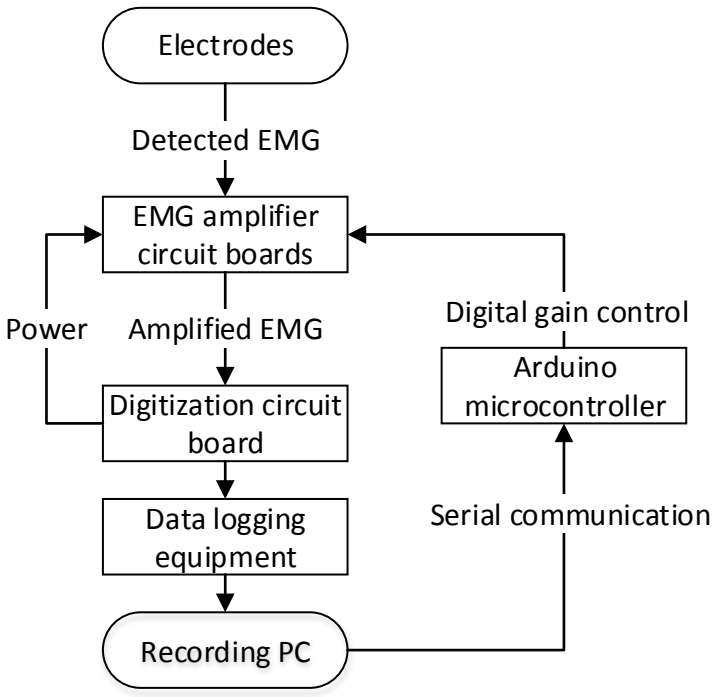


**Figure 2-14**: Flow diagram of 40ch EMG amplification process

The EMG system used in the present study was synthesised from open source components by R Smith[14]. Photos and circuit diagrams of the EMG system may be found in APPENDIX C.1.

### 2.3.1 EMG amplifier boards

ModularEEG bio-amplifier boards were modified for amplification of the EMG signal. The circuit boards were designed by the OpenEEG project (Griffiths et al. 2002); consists of an analogue amplifier board and digital communication board; are open source, inexpensive and modularly scalable. The analogue boards contained the primary amplification, filtering and noise cancellation circuitry for a maximum of 2 channels (see APPENDIX C.1.1. Thus 20 analogue amplifier boards were used to achieve the 40 channels required for the present study.

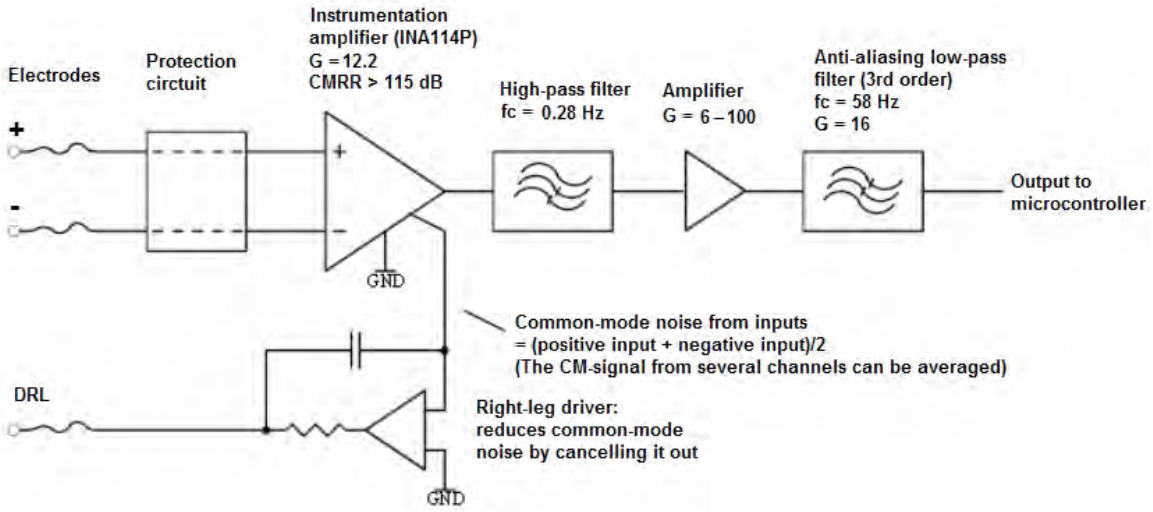


**Figure 2-15**: Operational schematic of a single OpenEEG channel, analogue amplifier board (Griffiths et al. 2002). The circuit is grounded to earth (GND in the diagram above)

OpenEEG amplifiers were originally designed for the measurement of EEG signals in the range of 0.28-58Hz (shown schematically in Figure 2-15). However, EMG signals exist in the range of 10–500Hz (Merletti & Parker 2004), thus the bandwidth of the amplifier boards was modified by replacing specific capacitor values according to a technical note compiled by AM McNaught and LR John (the technical note may be found in APPENDIX F).

The OpenEEG amplifiers were designed for bipolar (differential) measurement of bio-signals between the positive and negative electrodes, with an active ground electrode, known as the Driven Right Leg (DRL in Figure 2-15), placed on an electrically inert area of the head. The DRL reduces common mode noise such as 50Hz buzz by injecting an averaged, inverted current back into the body, thus actively cancelling the common mode out. However, for the purposes of the present study, monopolar EMG and not bipolar EMG was required. To achieve this recording configuration using the OpenEEG boards, the negative electrode terminals from all the amplifier boards were tied

[14] The EMG system used in the present study was the most recent iteration of a series of incremental open source EMG system designs with concept and ongoing contributions by L.R John and incremental contributions by SP Moroaswi, A McNaught, N Divekar, S Stoeckigt, A Sayed, J Pitman, and C Swanepoel.

together to form a single common reference electrode. The DRL and common reference electrodes were arranged in a separate band and placed on the bony prominence of the olecranon, a commonly used location for the reference electrode (shown in Figure 2-16).

**Figure 2-16**: Ground (black wire) and DRL (blue wire) electrode band (right). The ground and DRL electrode band placed on the olecranon as used during the experiment.

The output of the OpenEEG amplifiers were designed to contain a 2V 'Virtual Ground' DC offset as a means of creating a dual supply with a single supply voltage (Griffiths et al. 2002). The amplified signals were thus recorded at this voltage level swinging between 0 and 4V.

### 2.3.2 Digitization Board

The ModularEEG digital communication board provided power to the analogue amplifier circuit boards, a final low pass filter stage, and digitized the signal to enable communication with a PC. However, the digital communication board is designed for a maximum of 6 inputs (3 analogue amplifier boards), so a digitization circuit board was constructed as a substitute (see APPENDIX C.1.2 for schematic and board layout diagrams of the digitization board).

The electronic design of the digitization board was closely based on the design of the ModularEEG digital communication board. It provided power to the EMG amplifiers and a final ≈1000 Hz low pass filtering stage to remove any high frequency components from the amplified signals. Due to the increased number of amplifiers for which the digitization board provided power, higher rated power components were used in place of the original digital communication board. Additionally, a National Instruments Data Acquisition (DAQ) device was used to digitize the signals, see section 2.4.1.

### 2.3.3 Digital gain control

The standard OpenEEG amplifier board design uses a variable resistor (potentiometer) for final gain adjustment. It was decided to standardize the gain across all the amplifier boards by replacing the gain potentiometers with digital potentiometers. The AD5235 microchip (Analog Devices), a 25kΩ digital potentiometer, was selected as its resistive range closely matched the potentiometer it replaced. Each EMG amplifier board was fitted with a daughter board (designed by S Stoeckigt, N Divekar, and LR John. See APPENDIX C.2.1 for schematic and board layout diagrams) designed around the AD5235 digital potentiometer chip (relevant pages of the datasheet may be found in APPENDIX F); the daughter boards acted as replacements for the analogue potentiometers.

The digital potentiometers were controlled by an Arduino® Mega 2560 microcontroller. The Arduino microcontroller communicated with the LabVIEW® (2012, National Instruments, Dallas TX) software

via Universal Serial Bus (USB). A description of the amplifier gain setting procedure is provided in APPENDIX C.3.6.

### 2.3.4 EMG amplifier system calibration

As mentioned in section 2.3.1, the bandwidth of the amplifier boards was modified to enable the detection of EMG signals. Additionally, the standards for reporting EMG data (Merletti 1999) require that EMG waveforms are reported in their original, unamplified form[15]. Thus it was important to determine the EMG system's transfer function (amplification gain and phase shift characteristics) to:

- Ensure the amplifiers functioned as anticipated after modification
- Calibrate the amplitude of the amplified monopolar EMG signals back to their original form as measured at the electrodes.

The calibration procedure involved passing a known, reference signal through the EMG amplifiers and comparing between the recorded input and output signals. A full description of the hardware and software used for this process is provided in APPENDIX C.4. A flow chart summary of the steps undertaken in the calibration process is shown in Figure 2-17.

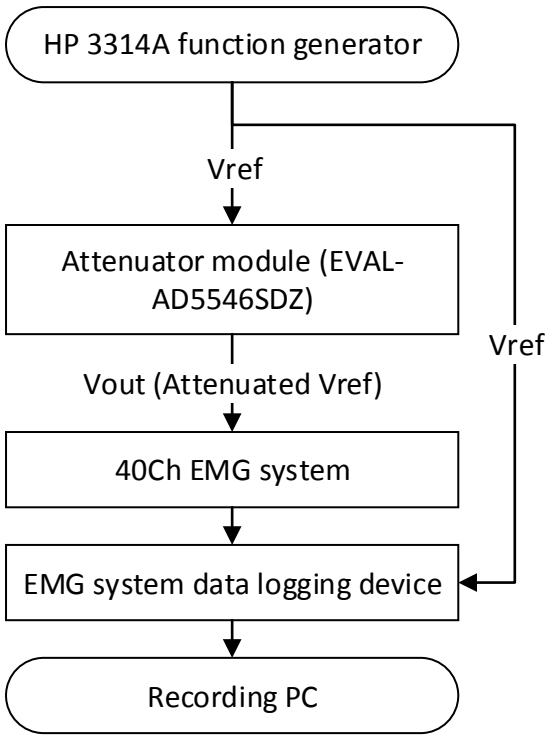


**Figure 2-17**: Calibration procedure for determining the transfer function of the amplifiers

Since the amplifiers were designed to amplify EMG signals, the reference signal had to be of similar amplitude and bandwidth to an EMG waveform (amplitude = 50-5000µV, bandwidth=10-500Hz (Konrad 2005)). A sinusoidal reference waveform (Vref), with fixed amplitude of 100mV pk-pk sweeping from 0.2-2 kHz, was produced by a HP 3314A signal generator. The frequency range for Vref was specifically chosen outside the range of the EMG amplifiers' high and low pass filters to find the upper and lower 3dB amplifier rolloff points and ensure they were filtering out the correct

[15] Reporting EMG measurements in their original, unamplified format is also the norm for all commercial amplifier systems.

frequencies. Vref was simultaneously sent to an attenuation module and a spare 'analogue in' port of the data logging device used for the EMG amplifier system. The attenuator module consisted of an Analog Devices evaluation board, the EVAL-AD5546SDZ (see APPENDIX F for datasheet) and an auxiliary power circuit board. The EVAL-AD5546 evaluation board is built around the AD5546 chip: a low power, high precision Digital to Analogue Converter (DAC) (see APPENDIX F for datasheet). The DAC chip can be used to attenuate a reference signal between 0 and 1 times Vref with a resolution of Vref/$2^{16}$, according to the equation (see AD5546 chip datasheet in APPENDIX F):

$$V_{out} = \frac{D}{2^{16}} * V_{ref} \qquad \textbf{Equation 2-2}$$

where D is the attenuation coefficient. The attenuation coefficient value was set in LabVIEW® through a specific communication protocol in a task-specific LabVIEW® application (see APPENDIX C.4.3). For the calibration process described herein, D was set to 655, to give an attenuated Vout = 1mV pk-pk. The attenuated voltage was fed to all 40 EMG amplifier channels simultaneously and the amplified outputs were digitized and recorded together with Vref from the signal generator by the EMG system Data Acquisition (DAQ) device (see section 2.4.1).

The recorded amplifier output signals and the un-attenuated reference signal were then compared using the MATLAB® function 'tfestimate' to find the amplifiers' transfer function. The transfer function of the attenuator itself was calculated prior to calculating the amplifiers' transfer function according to the procedure shown in Figure 2-18.

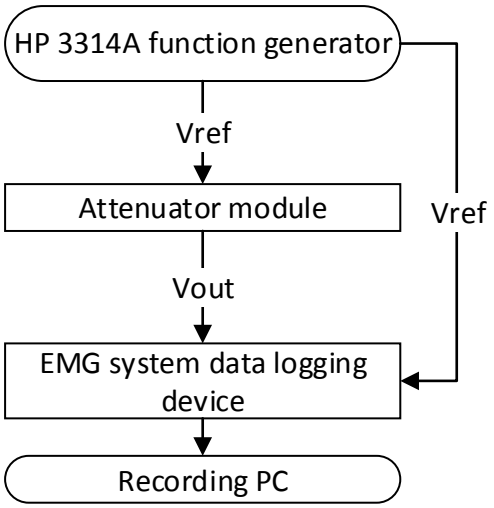


**Figure 2-18**: Schematic breakdown of attenuator module calibration

The attenuator transfer function was found to be 0.009. Figure 2-19 and Figure 2-20 show the gain and phase plots of all the EMG amplifier channels. The passband gain was approximately 66 dB (1995 V/V), the low -3dB rolloff was ~5 Hz and the upper -3dB rolloff was ~425 Hz.

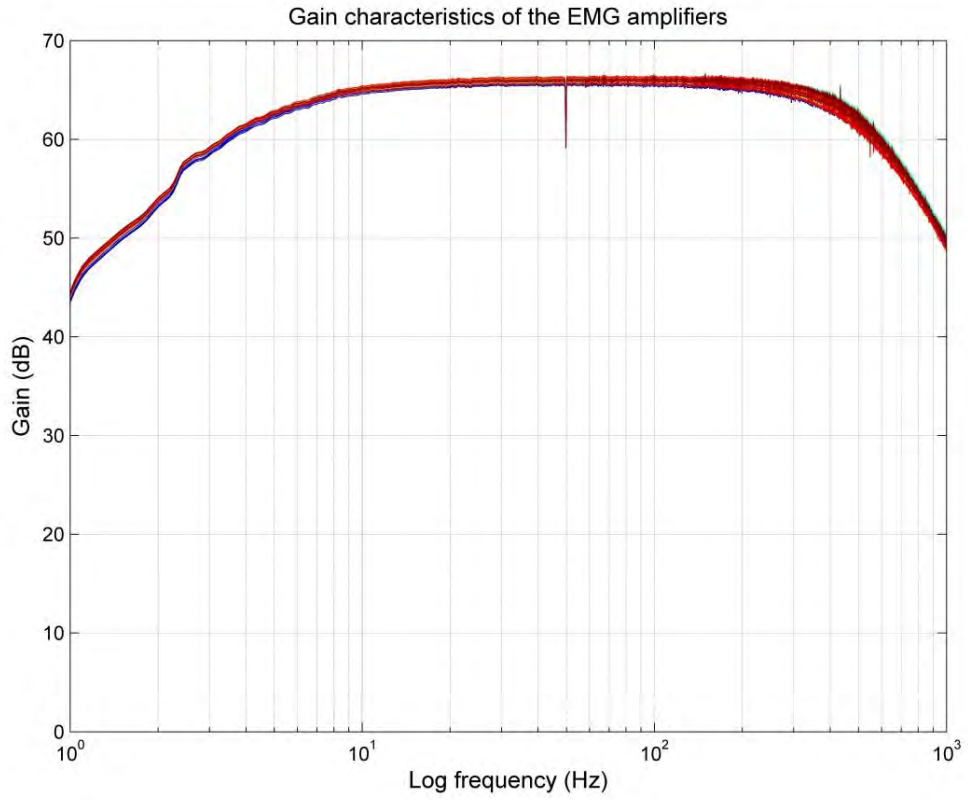


**Figure 2-19**: Gain characteristics for all 40 EMG amplifiers over the range 1-1kHz.

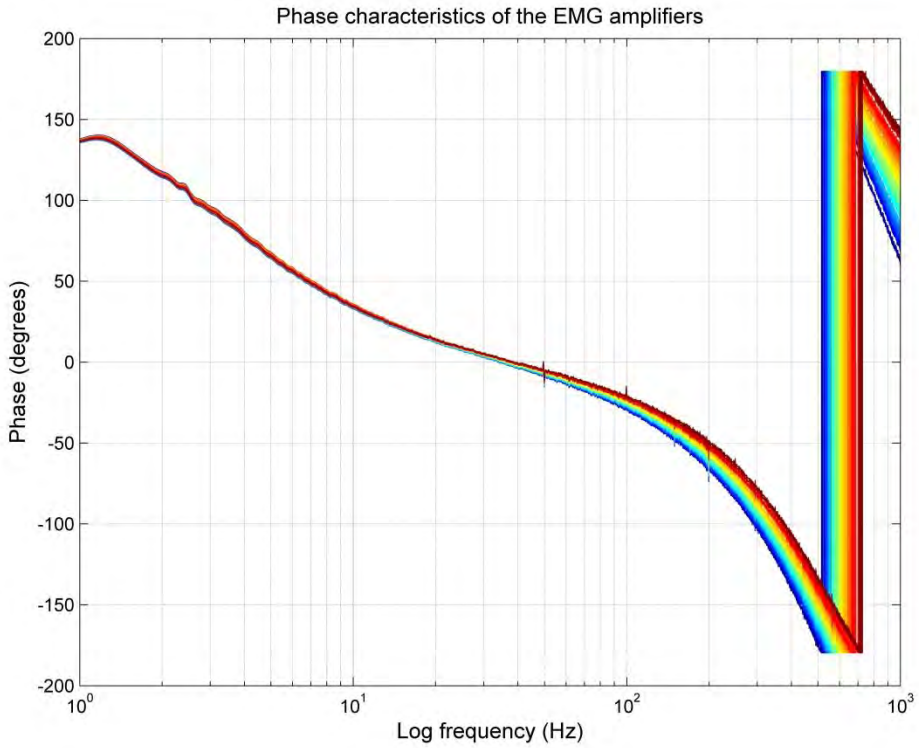


**Figure 2-20**: Phase-shift characteristics of the EMG amplifiers over the range 1-1kHz

As can be seen from Figure 2-19 and Figure 2-20, the gain and phase characteristics from all the amplifiers are very similar and individual differences are likely due to component tolerances of the resistors and capacitors.

## 2.4 System integration

A National Instruments USB-6225 DAQ device was used as the data logging equipment. The DAQ device was chosen due to the high number of analogue input channels available (80 in total), its high resolution (16 bits) and a fast sampling rate (maximum of 250 kS/s). The DAQ device was also ideally suited to interface with LabVIEW®, the program in which the experimental acquisition application was written.

LabVIEW® is a graphical programming application designed for developing Virtual Instruments (VIs) for measurement or monitoring tasks. Each VI consists of a Front Panel and a Block Diagram. The Front Panel is a Graphical User Interface (GUI) to facilitate user interaction with the program during the measurement application, while the Block Diagram contains the various sub-functions required for the application. Screen shots of the data acquisition VI Front Panel and Block Diagram are shown in APPENDIX C.3. The LabVIEW® application coordinated the data logging operations of the DAQ device, provided the randomized visual feedback for the participant and saved the data for analysis in MATLAB®.

### 2.4.1 Data logging operations

Each experimental run lasted for 65 seconds and all data was sampled simultaneously at 1 kHz (satisfying the Nyquist frequency for EMG Acquisition (Merletti 1999)). Thus each channel of EMG data contained ~65000 samples, equivalent to a sample every 0.001 seconds. To ensure that no data was lost, the LabVIEW® application held the samples from all channels in a software buffer for the duration of each experimental run prior to saving the data.

### 2.4.2 Visual feedback

Visual feedback provided to the participant consisted of an image depicting the required contraction and 3 effort level gauges for each isometric contraction, shown in Table 2-3 below. The randomization process was performed in the LabVIEW® acquisition programme by assigning each movement a number. The numbers corresponding used for each movement in the LabVIEW® programme are shown in Table 2-3. The vertical and horizontal gauges indicated forces applied to the dynamometer in the corresponding contraction planes shown in Figure 2-5 according to the directions defined in Table 2-1. Similarly, the finger gauge indicated forces applied to the finger load cell (as shown in Figure 2-3); according to the directions defined in Table 2-2. The applied forces were displayed as a percentage of the participant's MVC.

For each experimental run, the LabVIEW® application prompted the participant to perform the required contraction using the image combinations shown in Table 2-3. The participants were blinded to the order of isometric contraction, i.e. no indication of the next required contraction was given during the preceding rest period.

**Table 2-3**: Visual feedback provided in the LabVIEW® acquisition programme for each isometric contraction. The four images were presented together as a combination in a randomized order (the randomization procedure was performed by the LabVIEW® programme). The effort level gauge images shown in the table also indicate the required positions for the needles during each of the isometric contractions (i.e. the participant force application direction and effort level instructions for each isometric contraction). The target effort level for each isometric contraction is indicated as a green section on the dial with a width of 10% on either side of the target.

| Contraction | Visual feedback | | | |
|---|---|---|---|---|
| | Contraction prompt image | Effort level gauges | | |
| | | Vertical | Horizontal | Finger |
| Rest |  | 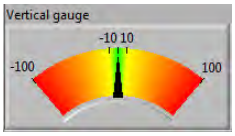 | 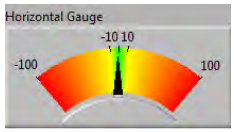 | 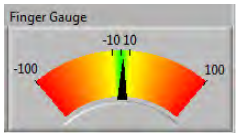 |
| TFl |  | 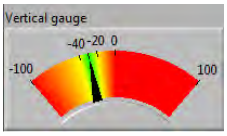 | 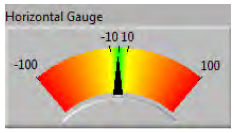 | 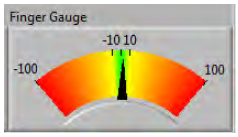 |
| TEx |  | 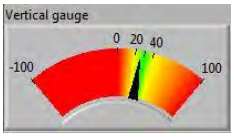 | 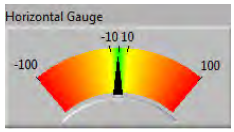 | 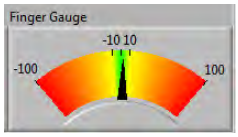 |
| TAb |  | 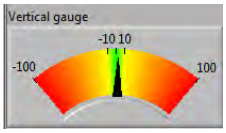 | 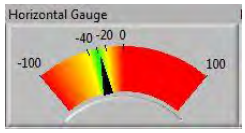 | 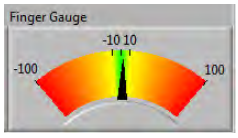 |
| TAd |  | 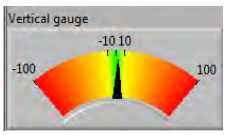 | 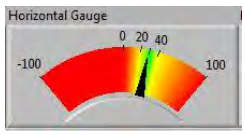 | 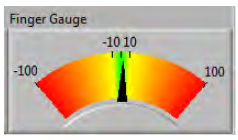 |
| IFFl |  | 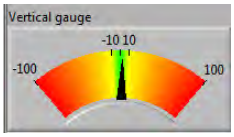 | 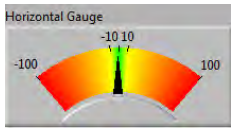 | 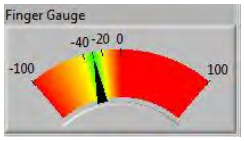 |
| IFEx |  | 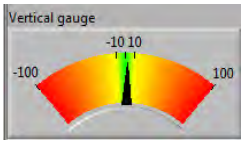 | 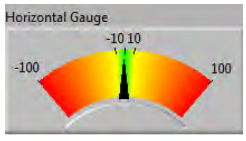 | 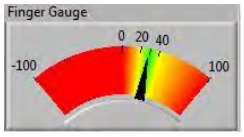 |

## 2.5 Technical specifications of experimental apparatus

A summary of the specifications for all the experimental equipment sub-components is shown in Table 2-4:

**Table 2-4:** Technical specifications of all equipment used for the present study

| Apparatus | Sub-component | Parameter | Value | Unit |
|---|---|---|---|---|
| **Thumb dynamometer** | Strain gauges: | Gauge length: | 5 | mm |
| | | Gauge factor: | 2 | |
| | | Nominal resistance: | 120 | Ω |
| | | Bridge configuration: | Full | |
| | Strain gauge amplifiers: | CMMR | >120 | dB |
| | | Bandwidth | 450 | kHz |
| | | Gain | 1001 | V/V |
| **Finger load cell** | Strain gauges | Gauge length | 2 | mm |
| | | Gauge factor | 2 | |
| | | Nominal resistance | 120 | Ω |
| | | Bridge configuration | Half | |
| | Amplifier: | CMMR | >120 | dB |
| | | Bandwidth | 450 | kHz |
| | | Gain | 1001 | V/V |
| **EMG detection** | Electrodes | Number of electrode bands | 2 | |
| | | Number of electrodes in each band | 20 | |
| | | Electrode material | Sterling silver | |
| | | Electrode paste composition | ref: Bio-medical Instruments (2015) | |
| **EMG amplification** | Amplifiers | CMMR | 115 | dB |
| | | Bandwidth | 5-450 | Hz |
| | | Gain | 1995 | V/V |
| | | Channels | 40 | |
| | Calibration | Attenuator resolution | 16 bits | |
| **System integration** | DAQ device | Acquisition resolution | 16 | bits |
| | | Sampling rate | 1000 | S/s |

[This page is left intentionally blank]

# Chapter 3 Experimental Methodology

Chapter 3 describes the experiment carried out to test the research objectives (described in section 1.4.4). Details of the study participants are provided in section 3.1. A description of the data capture and processing procedures are provided in section 3.2 and section 3.3 respectively. A description of the muscle identification algorithm is provided in section 3.4, followed by a description of the statistical analysis method in section 3.5.

## 3.1 Participants

Ethics approval for the study was granted by the Health Sciences Human Research Ethics Committee (reference number: 546/2011), in accordance with the declaration of Helsinki (World Medical Association 2013). Fifteen healthy, right-handed, male participants (25 ±2.9 years of age), without any history of neurological disease were recruited for the study. Participants gave informed consent before testing (A blank copy of the Informed Consent Form may be found in APPENDIX F).

## 3.2 Data capture methodology

The following steps were implemented prior to experimental data recording:

- To standardize the electrode band placeme0nt across participants, the forearm length from the elbow to the wrist was measured and recorded.
- Using a non-toxic permanent marker, two parallel lines were drawn along the ulnar and radial aspects of the right forearm from the elbow to the wrist.
- Two transverse lines, encircling the forearm, were drawn. These lines were perpendicular to the above mentioned parallel lines and, divided the forearm into thirds as indicated in Figure 3-1. These lines were used to locate the positions for the electrode bands[16]. These particular sites were chosen to ensure the electrode rings encircle as large a volume of the target muscles as possible.
- The skin found in a 6cm wide band (3cm on either side of the transverse lines) and a patch on the bony point of the elbow (as shown in Figure 3-1), was prepared using an emery board and sterile alcohol swabs to remove dead skin cells.

[16] The SENIAM electrode placement guidelines (Hermens et al. 2000) were consulted prior to choosing the electrode locations, however no placement guidelines were available for the deep muscles under investigation. Nor were any guidelines for intramuscular or surface sensor locations provided in The ABC of EMG (Konrad 2005).

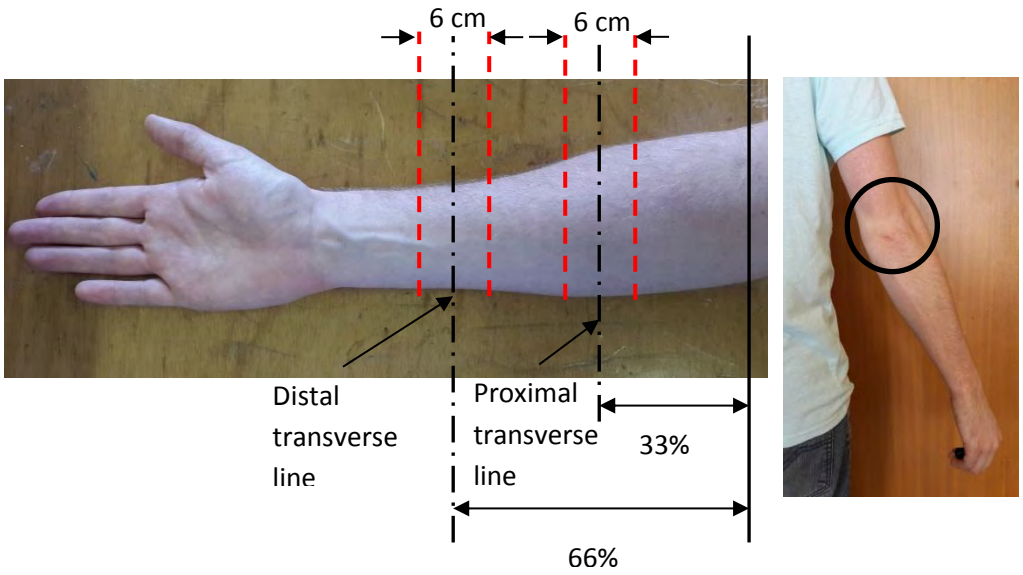


**Figure 3-1**: Approximate locations for electrode bands and skin preparation area (left). The point of the elbow was also prepared for placement of the ground and DRL electrodes (right).

- Approximately 5mm$^3$ of Elefix conductive paste (Nihon Kohden, Japan) was applied to each electrode cup to improve skin-electrode conductivity.
- The common reference and DRL electrodes were placed on the point of the elbow.
- The electrode bands (see section 2.2) were placed on the forearm. Band A in Figure 2-13 was placed 19.6 ± 1.1 cm from the elbow. Band B (also in Figure 2-13) was placed 9.8 ± 0.5 cm from the elbow.
- Electrical impedance measurements between the common reference and measurement electrodes were taken using a Checktrode model 1089 Electrode Impedance device (excitation frequency = 30 Hz, UFI systems, USA). The impedance of the electrode pair was deemed acceptable if it was below 10 kΩ[17], based on the recommendations of the Checktrode user manual (UFI, 2013). If the measured impedance was greater than 10 kΩ, the electrode in question was removed, the skin preparation process repeated and the electrode reapplied, until the desired impedance was achieved[18].
- The finger load cell (see section 2.1.2) was fitted to the proximal interphalangeal joint of the index finger for each participant. The flat mount unit surfaces were placed on the dorsal side of the index finger and secured using cable ties as shown in Figure 3-2. The cable ties were tightened by the test participant to a comfortable level that did not restrict blood flow but was still secure. This was verified by gently pinching the fingertip and visually verifying colour returning to the fingertip.

[17] UFI systems recommendation for a good impedance measurement from the Checktrode user manual (*www.ufiservingscience.com/datasheets/1089MKIII_manual.pdf)*

[18] A low electrode-skin impedance measurement (relative to the amplifier impedance, see Table 2-4 for amplifier specifications) was necessary to ensure the potential measured by the electrode would be an accurate reflection of the activity below the skin (Merletti & Parker 2004; Dimitrov & Dimitrova 1998; Farina et al. 2002; Merletti et al. 2008).

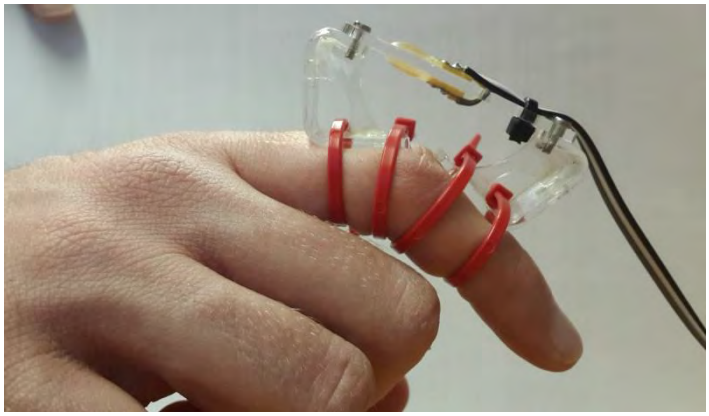

**Figure 3-2**: Finger load cell in place on the proximal interphalangeal joint of the index finger

- The participant's right hand was placed in a moulded hand and forearm splint, which was bolted to the thumb dynamometer base plate (shown in Figure 2-12 in section 2.1.1) and secured to a table. The splint maintained the wrist at a fixed position of $30^{o}$ in extension, mid-way between pronation and supination.
- Stretchable Velcro straps over the top of the splint secured the forearm in place. This prevented any movement of the forearm relative to the wrist.
- Finally, the 3D printed spacer ring (see section 2.1.2) was placed over the IP joint of the thumb and placed inside the dynamometer tube.

### 3.2.1 Experimental procedure

Once the hand had been placed in the dynamometer splint, participants were given an opportunity to become familiar with the experimental procedure.

As mentioned in 2.4.2, participants were required to perform a randomized sequence of thumb flexion (TFl), thumb extension (TEx), thumb abduction (TAb), thumb adduction (TAd), Index finger flexion (IFFl) and index finger extension (IFEx). MVC measurements were taken for each contraction prior to recording (see section 3.2.2 for measurement procedure). During the experiment, participants were required to maintain each contraction at an effort level of 30 ± 10% MVC for 5s. The target effort level was indicated as a "target effort zone" on each of the 3 gauges (shown in Table 2-3); the 30% MVC target was indicated on the gauges as a green section with the upper and lower bounds (20-40%) indicated in yellow. During each contraction, the participant was required to maintain the needle indicator within the target effort zone on the appropriate gauge, whilst keeping the needles of the other two gauges at 0%. During the rest condition, the participant was instructed to relax and maintain all three needle gauges at 0%.

The randomization procedure for each contraction was performed by the LabVIEW® application (see section 2.4.2 and APPENDIX C.3.5 for more details of the visual cues and LabVIEW® code for this function) and interspersed with rest periods. Additional rest periods at the beginning and end of each test made for a total experimental run time of 65s. A schematic representation of a typical experimental isometric contraction sequence is shown in Table 3-1. Each sequence was repeated 10 times for each participant. The isometric sequence was commenced by clicking the 'Perform Movement Sequence' button in the LabVIEW® application (highlighted in the yellow box in Figure 3-3).

**Table 3-1**: Typical isometric contraction sequence during testing

| Time(s) | | 0 | 5 | 10 | 15 | 20 | 25 | 30 | 35 | 40 | 45 | 50 | 55 | 60 |
|---|---|---|---|---|---|---|---|---|---|---|---|---|---|---|
| Contraction | Rest | | | | | | | | | | | | | |
| | TFl | | | | | | | | | | | | | |
| | TEx | | | | | | | | | | | | | |
| | TAb | | | | | | | | | | | | | |
| | TAd | | | | | | | | | | | | | |
| | IFF | | | | | | | | | | | | | |
| | IFE | | | | | | | | | | | | | |

### 3.2.2 MVC measurement procedure

Prior to recording, MVC measurements were taken for each contraction using the thumb dynamometer (screen shots of the LabVIEW® performing this function may be found in APPENDIX C.3.3). The effort level gauges were first zeroed and the scales reset by clicking the "Zero gauges" and "Reset" buttons respectively in the LabVIEW® program (highlighted by the violet box in Figure 3-3).

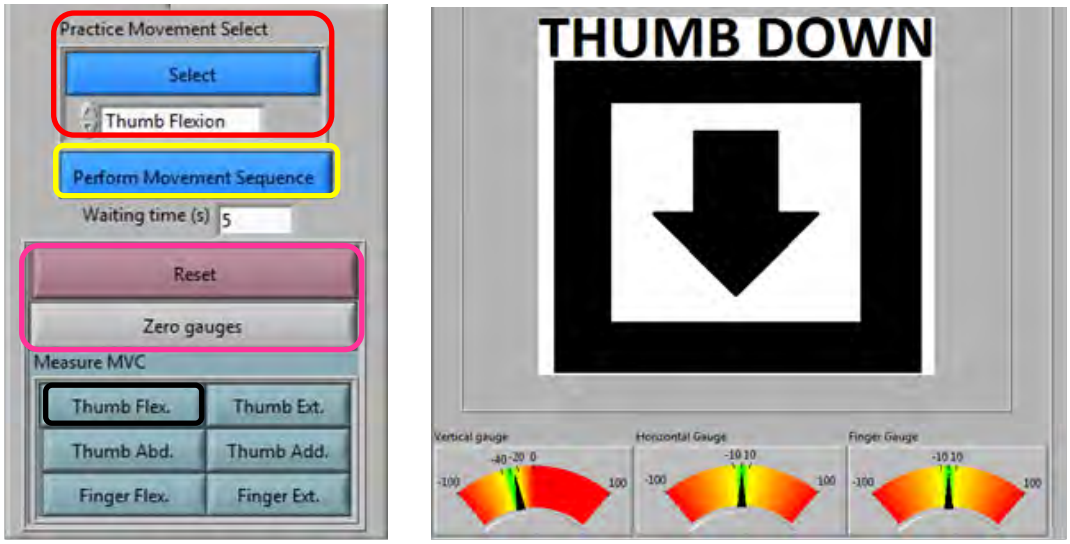


**Figure 3-3:** Movement selection and MVC value storage tab in LabVIEW® acquisition program. The Practice Movement Select (red box) and Measure MVC (black box). The visual feedback depicted above was used for indicating thumb flexion.

The procedure for measuring the Thumb Flexion MVC is described below, and was replicated for each contraction's MVC measurement:

1. The visual feedback for each contraction was individually selected using the scroll buttons in the "Practice Movement Select" box (highlighted in red in Figure 3-3) and clicking "Select" in the LabVIEW® data capture application.
2. Upon command from the researcher, participants were instructed to push downwards against the thumb dynamometer with their thumb, as hard as they could.
3. Once the maximum value on the vertical effort gauge was reached, the researcher saved the MVC value by clicking the "Thumb Flex." button (highlighted black box in Figure 3-3).

4. The output of the Vertical effort gauge was then scaled according to the new MVC value. The output of the horizontal and finger gauge scales were scaled to a value just above their zero value (the LabVIEW® code performing this function is shown in APPENDIX C.3.4). This forced the gauges in the non-intended directions (i.e. the horizontal and finger gauges) to be more sensitive during thumb flexion, so that the participant could be more precise in applying the downward force during thumb flexion.

## 3.3 Data processing methodology

The monopolar EMG, strain data (acquired by the DAQ device) and experimental data (isometric contraction sequence and participant information from the LabVIEW® program) were recorded and analysed offline. All analysis was conducted in MATLAB® (2008a, MathWorks, Natick, MA) and a flow diagram of the main MATLAB® functions may be found in D.5.1. This section describes the steps undertaken to process the raw monopolar EMG data for use in the Muscle-IC identification algorithm described in section 3.4.

The raw EMG waveforms were processed according to the flow diagram presented in Figure 3-4.

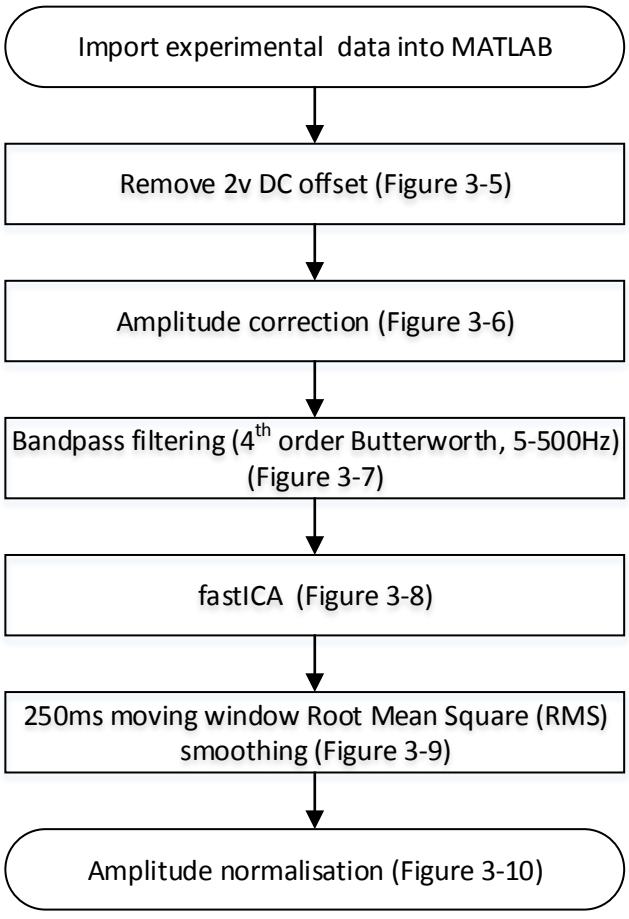


**Figure 3-4**: Flow diagram of processing steps applied to the monopolar EMG data in MATLAB®.

Subsequent figures from each process described in Figure 3-4 are derived from a single experimental run; the procedure was repeated for all other experimental runs. The monopolar EMG waveforms were recorded with a 2V DC offset (see section 2.3.1), as shown in Figure 3-5.

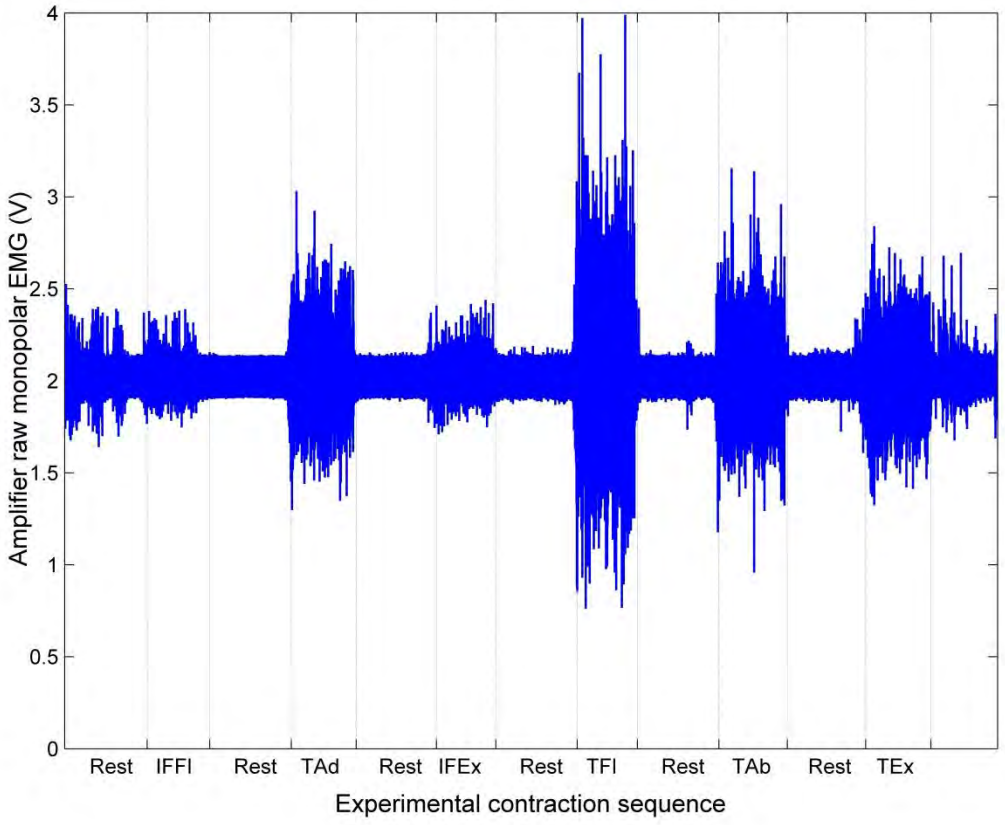


**Figure 3-5**: An illustrative example of a raw monopolar EMG waveform, as recorded. The vertical dotted lines represent the strain gauge derived timing intervals for the respective isometric contractions. The waveform shown here is divided into segments, each 5s long, according to the isometric contraction performed during that segment.

The DC offset was removed and the waveforms' amplitudes were corrected from their recorded values to the original values detected by the electrodes (Figure 3-6) by dividing each time point in the waveforms by 1995 V/V (the average amplifier gain between the upper and lower 3dB rolloff points in Figure 2-19).

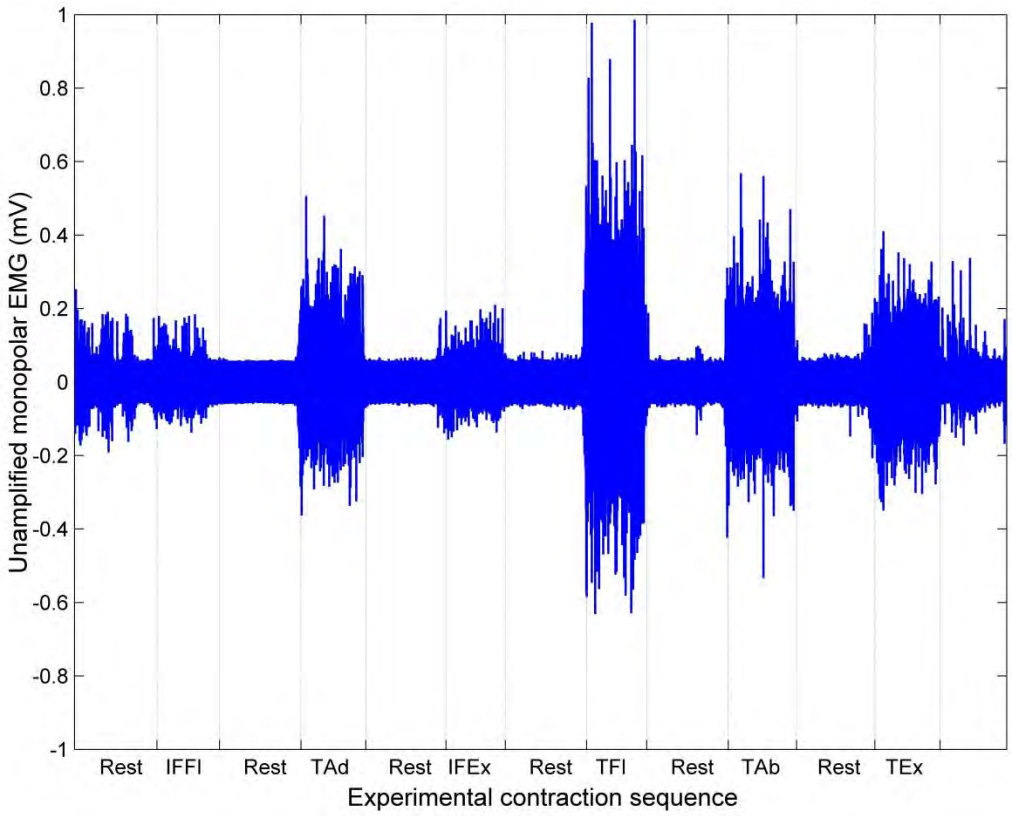


**Figure 3-6**: An illustrative example of the raw monopolar EMG recording shown in Figure 3-5 after amplitude correction. The vertical dotted lines represent the strain gauge derived timing intervals for the respective isometric contractions. The waveform shown here is divided into segments, each 5s long, according to the isometric contraction performed during that segment.

The amplitude corrected waveforms were digitally filtered from 5-500Hz using a 4$^{th}$ order Butterworth bandpass filter function in MATLAB® (shown in Figure 3-7). This was to remove any artefacts outside the EMG frequency range (according to the ISEK[19] Standards for Reporting EMG Data (Merletti 1999)) that may have been introduced during recording.

[19] ISEK: International Society for Electromyography and Kinesiology

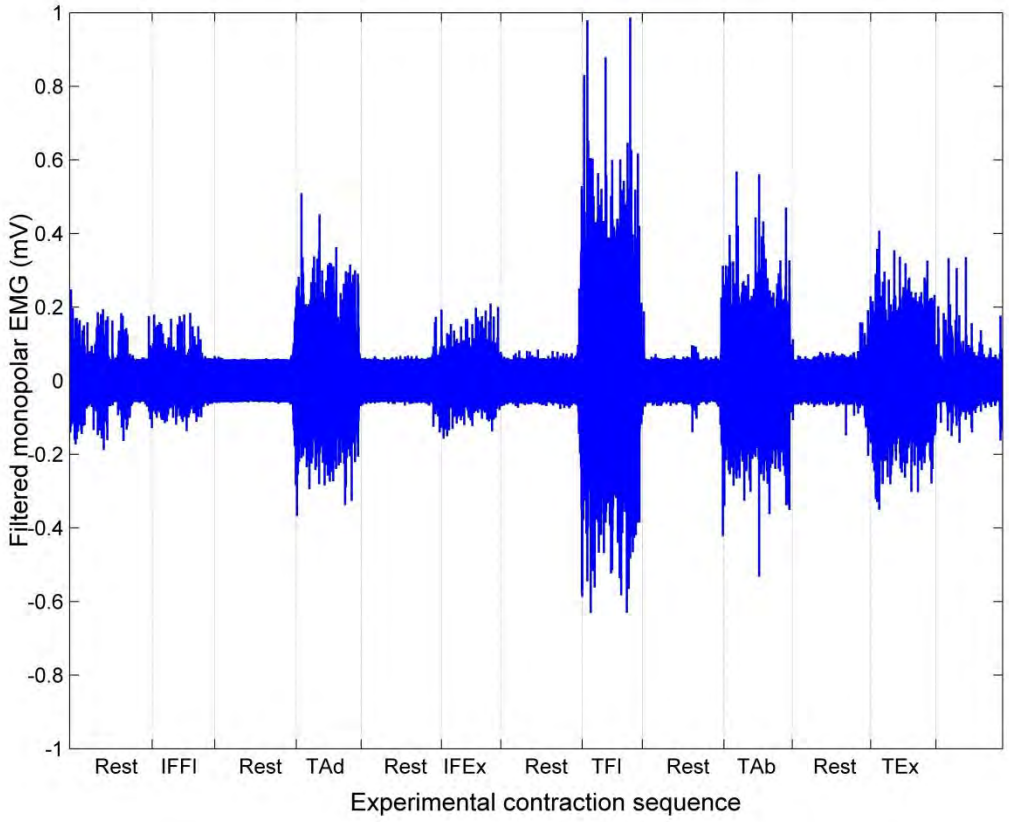


**Figure 3-7:** An illustrative example of the raw monopolar EMG recording shown in Figure 3-5 after amplitude correction and bandpass ($4^{th}$ order Butterworth, 5-500Hz) filtering. The vertical dotted lines represent the strain gauge derived timing intervals for the respective isometric contractions. The waveform shown here is divided into segments, each 5s long, according to the isometric contraction performed during that segment.

The underlying source activity, known as the Independent Components (ICs), was estimated from the filtered EMG waveforms by fastICA (Gävert et al. 2005), a function from the MATLAB® Independent Component Analysis toolbox. All 40 of the filtered EMG channels were passed through the fastICA function, which then returned the same number of ICs.

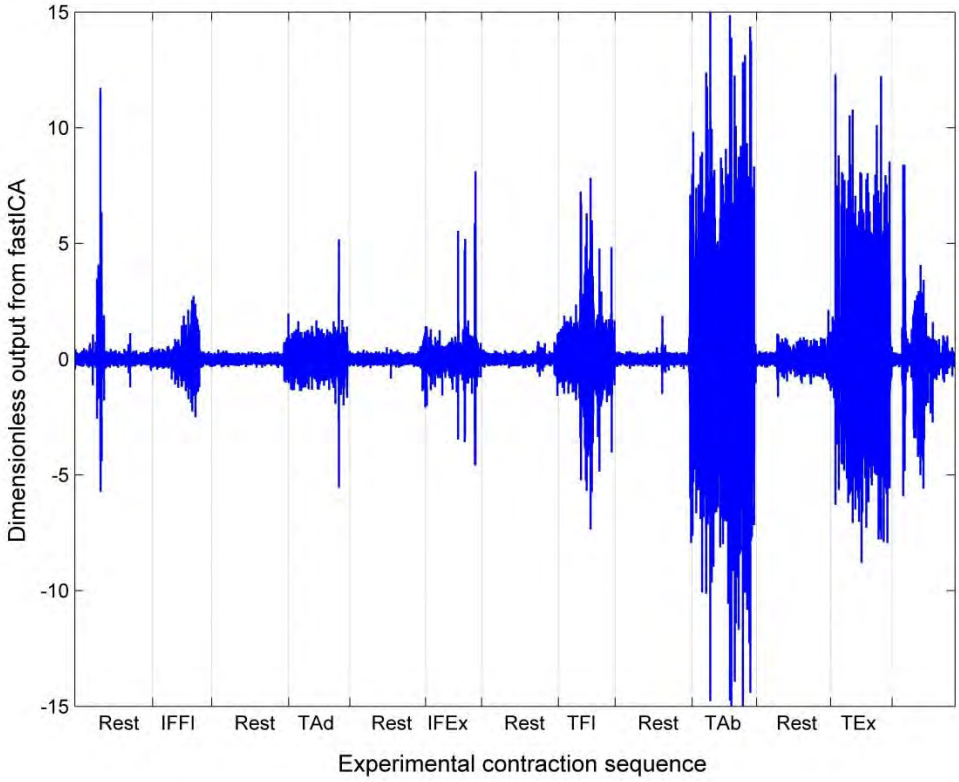


**Figure 3-8:** An illustrative example of an Independent Component (IC) derived from the amplitude corrected and filtered monopolar EMG dataset shown in Figures 3-5 to 3-7. The vertical dotted lines represent the strain gauge derived timing intervals for the respective isometric contractions. The waveform shown here is divided into segments, each 5s long, according to the isometric contraction performed during that segment.

Each IC was full wave rectified and the RMS computed using a 250ms moving window to find the positive activation "envelope[20]" of the signal (shown in Figure 3-9).

[20] A term used to describe the RMS or moving average smoothing of an EMG burst waveform (Winter 2005)

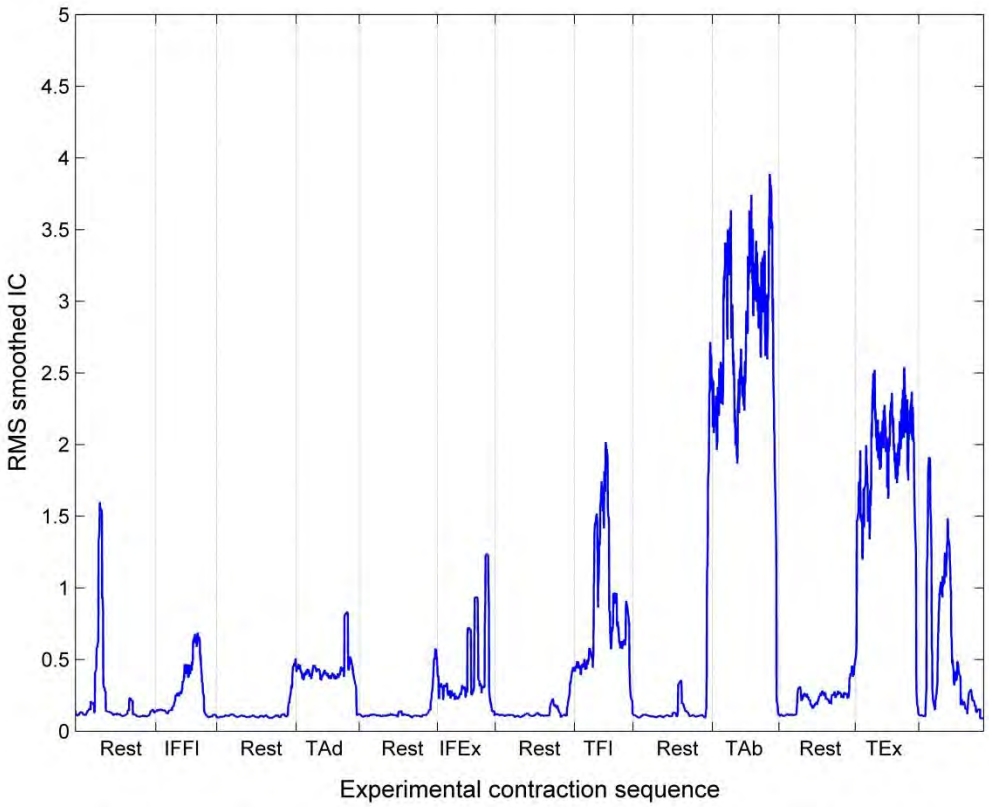


**Figure 3-9:** An illustrative example of the full wave rectification and RMS smoothing process applied to the IC in Figure 3-8. The vertical dotted lines represent the strain gauge derived timing intervals for the respective isometric contractions. The waveform shown here is divided into segments, each 5s long, according to the isometric contraction performed during that segment.

Finally, the enveloped waveforms were normalised from 0-1. An example of a rectified and normalised IC is shown below in Figure 3-10:

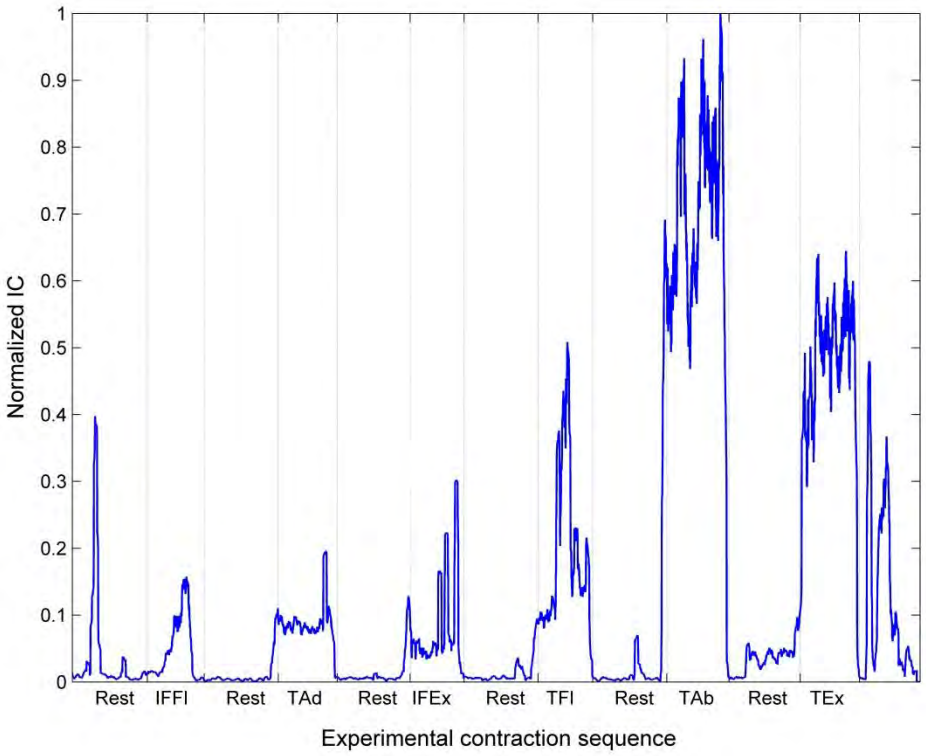


**Figure 3-10:** An illustrative example of the normalization process applied to the full-wave rectified and RMS smoothed IC shown in Figure 3-9. The vertical dotted lines represent the strain gauge derived timing intervals for the respective isometric contractions. The waveform shown here is divided into segments, each 5s long, according to the isometric contraction performed during that segment.

## 3.4 Muscle-IC identification algorithm

As mentioned in 1.3.3, the order in which the ICs are returned from fastICA is no longer related to the original electrodes from which the measurement was taken and therefore cannot easily be linked back to a particular area in which the activity was detected. Thus an independent reference signal had to be constructed to identify which ICs represented the activity of the different muscles under investigation. Since the temporal arrival of the EMG potentials at the electrodes is maintained after separation of the monopolar EMG by fastICA, the ICs could only be matched to the predicted EMG in the temporal domain. The temporal measurement at the electrode is directly related to the muscle activity since this information is a function of the distance from the source to the electrode, as well as the source's contribution to a particular movement (Stone 2004). I.e. fastICA would interpret two signals arriving at different times as independent sources. Thus to determine whether a particular IC corresponds to a particular muscle, the ICs were quantitatively compared with a predicted EMG waveform for each muscle in the temporal domain using Pearson's correlation coefficient (r). The IC selection algorithm is summarised in flow chart form in Figure 3-11:

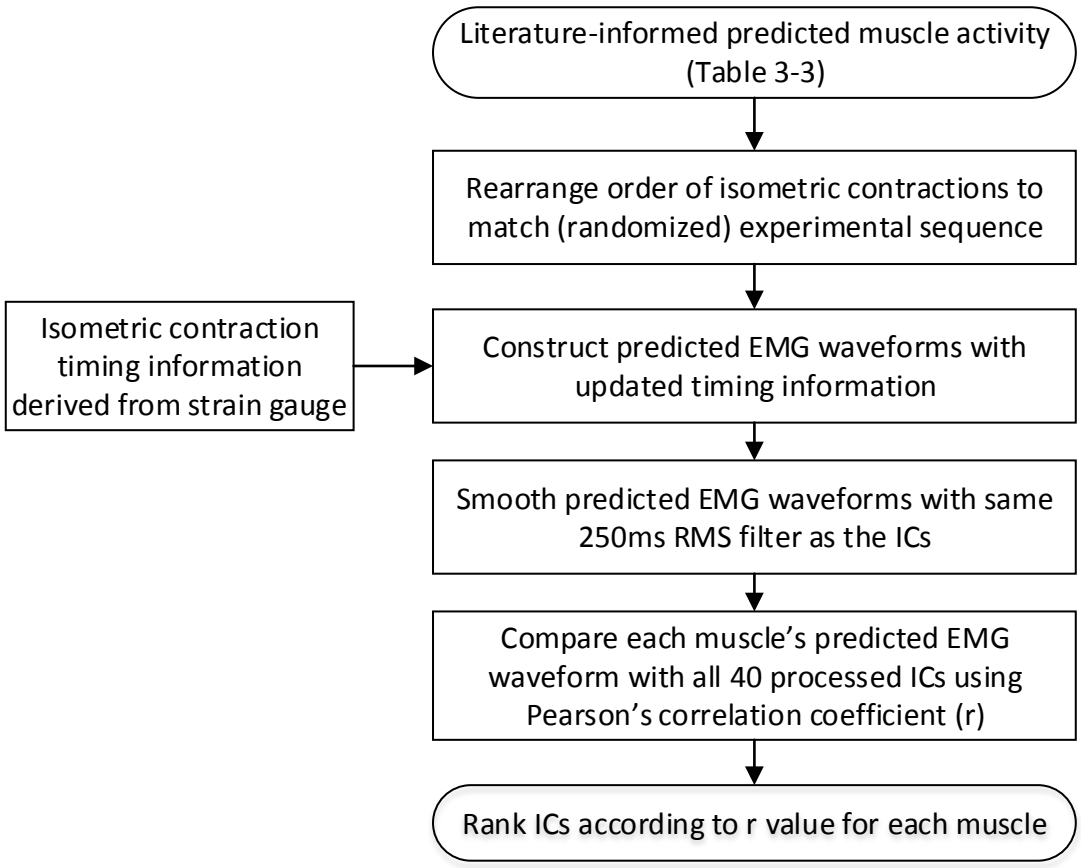


**Figure 3-11**: Muscle-IC selection algorithm flowchart

Since participant and experimental run specific time lags between the execution of the required isometric contraction and the visual instruction cue were expected, an accurate measure of the timing of each isometric contraction had to be found to build a reliable estimation of the muscle activity. The contraction timing was derived from the force measurements from the strain gauges, the procedure of which is described in section 3.4.1. The timing information for each contraction was then used to create predicted EMG waveforms; the procedure followed is described in section 3.4.2. The comparison using Pearson's correlation coefficient was performed to obtain an objective measure of identifying which IC was most likely to correspond to the predicted activation waveform for a particular deep muscle. Examples of the Pearson's correlation coefficient comparison waveforms are shown in section 3.4.3

### 3.4.1 Contraction timing extraction

The strain gauge contraction timing extraction procedure was based on the postulation that if a force is applied by the thumb or index finger in a particular direction, the muscles known to be responsible for producing that force in healthy individuals (Hislop & Montgomery 2007; Hollister & Giurintano 1995; Johnston et al. 2011; Gilroy et al. 2008), must be active.

A Schmitt-trigger function was used to find the data points at which each contraction commenced and terminated, summarised graphically in Figure 3-12.

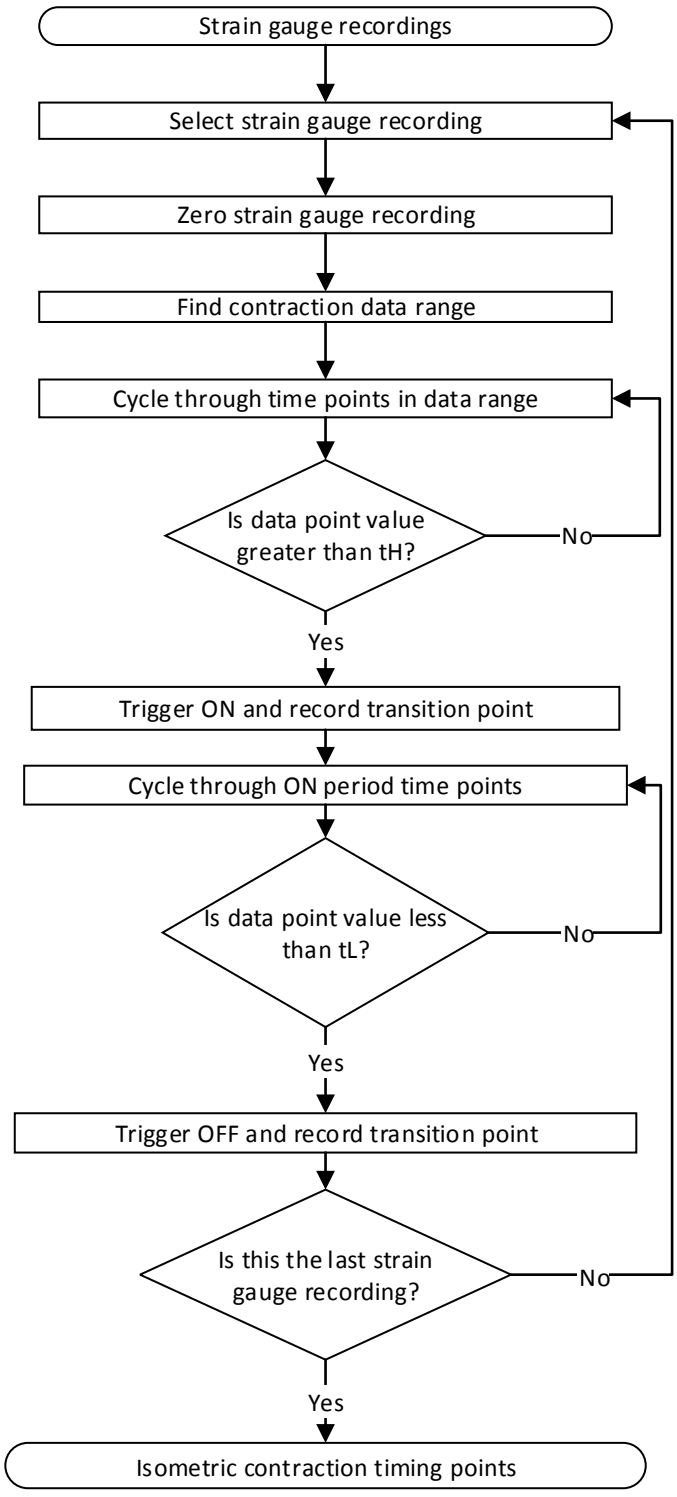


**Figure 3-12**: Flow diagram for extracting the commencing and terminating points for each isometric contraction. The function searched for the timing points within a 6.5s segment of data in which the contraction was expected to occur. If the data points was greater than 10% of the MVC value (tH) the function triggered high and the position of the transition point was recorded. If the data point was then less than 5% of the MVC value (tL) the function triggered low and the position of the transition point was recorded.

The function triggered 'ON' when the strain signal exceeded 10% of the MVC value (tH) and the position of the transition data point was recorded (red circles in Figure 3-13). The function remained ON until the signal dropped below 5% of the MVC value (tL), at which point it triggered OFF and the position of the transition point was recorded (black circles in Figure 3-13). To reduce the processing time, the function searched for the transition points within a data range in which each contraction was expected to occur. The data range consisted of a 6.5s segment of data: since each contraction was to be maintained for 5s and an additional 1.5s into the rest period to allow for participants that didn't terminate the contraction within the 5s period.

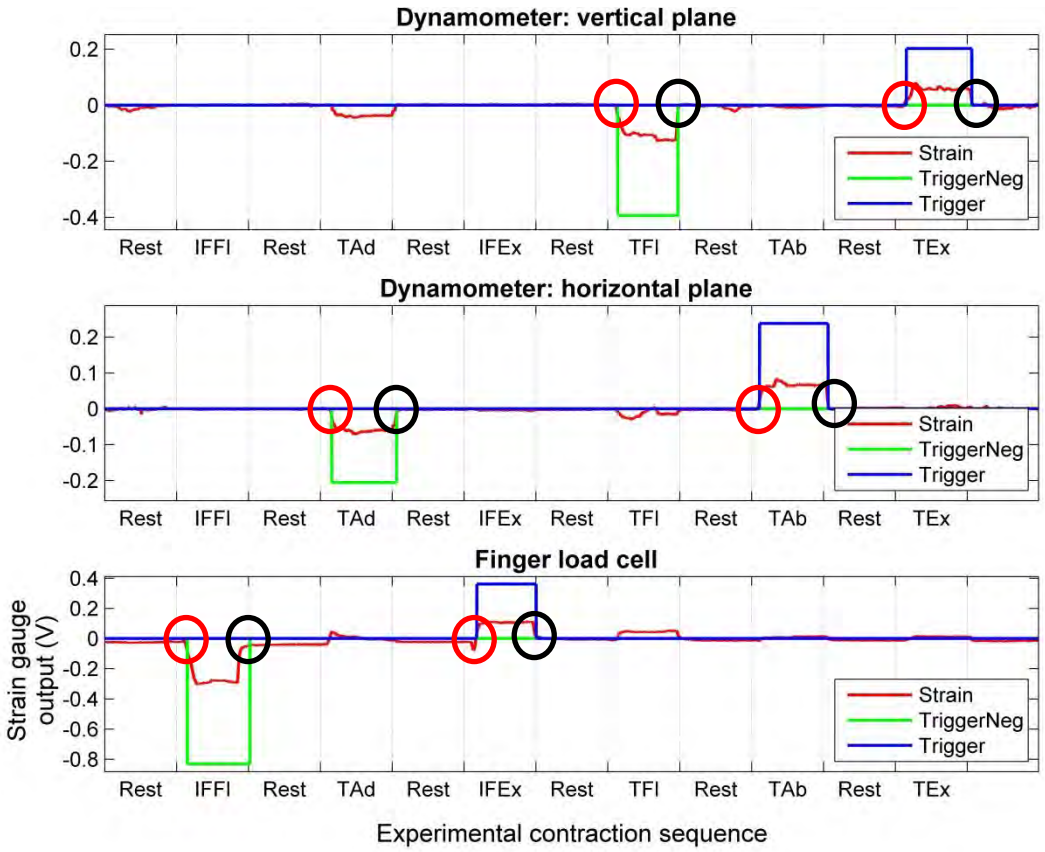


**Figure 3-13:** Strain gauge measurements from which the timing of each isometric contraction was extracted using a Schmitt-trigger function. The red circles highlight the points at which the Schmitt-trigger function triggered 'ON', (i.e. the strain signal exceeded the tH value. tH was defined as 10% of the corresponding isometric contraction's MVC value). The black circles highlight the points at which the Schmitt-trigger function triggered 'OFF' (i.e. the strain signal dropped below the tL value. tL was defined as 5% of the corresponding isometric contraction's MVC value). The waveform 'Trigger' refers to the Schmitt-trigger function examining the strain gauge values >0; the waveform 'TriggerNeg' refers to the Schmitt-trigger function examining the strain gauge values <0. The vertical dotted lines represent the strain gauge derived timing intervals for the respective isometric contractions. The waveforms shown here are divided into segments, each 5s long, according to the isometric contraction performed during that segment

As indicated in Table 3-2, the polarity of each strain signal indicated which isometric contraction was being performed. The positive and negative Schmitt trigger functions shown in Figure 3-13 used these relationships to find the activation timing points for each contraction.

**Table 3-2:** Strain gauge signal polarity and isometric contraction relationships

| Isometric contraction | Strain gauge voltage polarity | Strain gauge channel |
|---|---|---|
| TFl | Negative | Vertical dynamometer |
| TEx | Positive | |
| TAb | Positive | Horizontal dynamometer |
| TAd | Negative | |
| IFFl | Negative | Finger load cell |
| IFEx | Positive | |

### 3.4.2 Predicted EMG algorithm

Predicted EMG waveforms were derived for each deep (D) muscle from the investigations by Birdwell et al. (2013), Kaufman et al. (1999) and An et al. (1983) into the roles of FPL (D), EPL (D), EPB (D) and APL (D) during isometric TFl, TEx, TAb and TAd. The investigations attempted to quantify the activity of each muscle during different isometric thumb contractions using intramuscular EMG to determine each muscle's role during the isometric contractions. The role identification of the muscles from these studies was used in the present study to determine each muscle's level of activity for the predicted EMG waveforms during the randomized sequence of isometric contractions. The activation for each muscle in the study was modelled as a positive activation envelope (such as the waveforms shown in Figure 3-9 and Figure 3-10). Since there are multiple muscles responsible for thumb function and a high degree of co-activity between them, three activation thresholds were used to model the contributions of the research objective muscles during the various contractions:

- Primary muscles for a particular contraction were considered as fully active (*fa*).
- Muscles providing a significant supporting role during a contraction were considered partially active (*pa*).
- Muscles found to have negligible roles or known to be inactive during one of the contractions used in the experiment were considered as inactive (0).

The predicted activity for each of the muscles was modelled according to Table 3-3:

**Table 3-3:** Expected muscle activity during the 6 contractions, according to the experimental isometric contraction sequence presented in Figure 3-5 to Figure 3-10. *fa* = full activation; *pa* = partial activation; *0* = inactive.

| | Isometric contractions | | | | | |
|---|---|---|---|---|---|---|
| **Muscles** | **IFFl** | **TAd** | **IFEx** | **TFl** | **TAb** | **TEx** |
| FPL (D) | *0* | *0* | *0* | *fa* | *pa* | *0* |
| EPL (D) | *0* | *pa* | *0* | *pa* | *p* | *fa* |
| EPB (D) | *0* | *pa* | *0* | *pa* | *pa* | *pa* |
| APL (D) | *0* | *fa* | *0* | *0* | *pa* | *fa* |
| FD (S) | *fa* | *0* | *0* | *0* | *0* | *0* |
| ED (S) | *0* | *0* | *fa* | *0* | *0* | *0* |

Using Table 3-3 as a template, the contraction order in which the predicted activity was modelled was matched to the isometric contraction sequence order (including rest periods) for each experimental run. An illustration of a typical expected waveform (rest periods omitted for simplicity) for FPL is shown in Figure 3-14.

**Figure 3-14:** Sample predicted EMG waveform of the deep (D) muscle, FPL's, activation during the experimental contraction sequence presented in Figure 3-5 to Figure 3-10. Each muscle is modelled as fully active (fa), partially active (pa) or inactive (0). Each threshold is represented by a unique line style.

| | **Isometric contractions** | | | | | |
|---|---|---|---|---|---|---|
| **Muscle** | **IFFl** | **TAd** | **IFEx** | **TFl** | **TAb** | **TEx** |
| FPL (D) | | *pa* | *0* | *fa* | *0* | *0* |

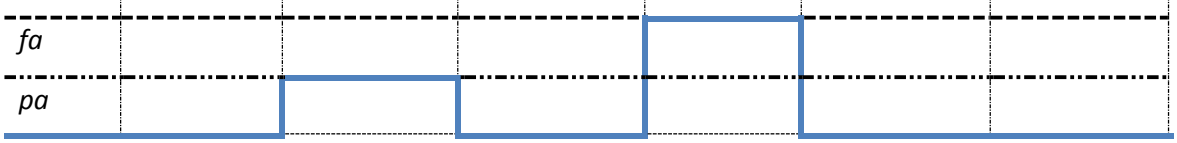


The predicted EMG waveforms were expanded into full waveforms with rest periods using the isometric contraction timing information (see section 3.4.1). A sample waveform for EPL is shown in Figure 3-15.

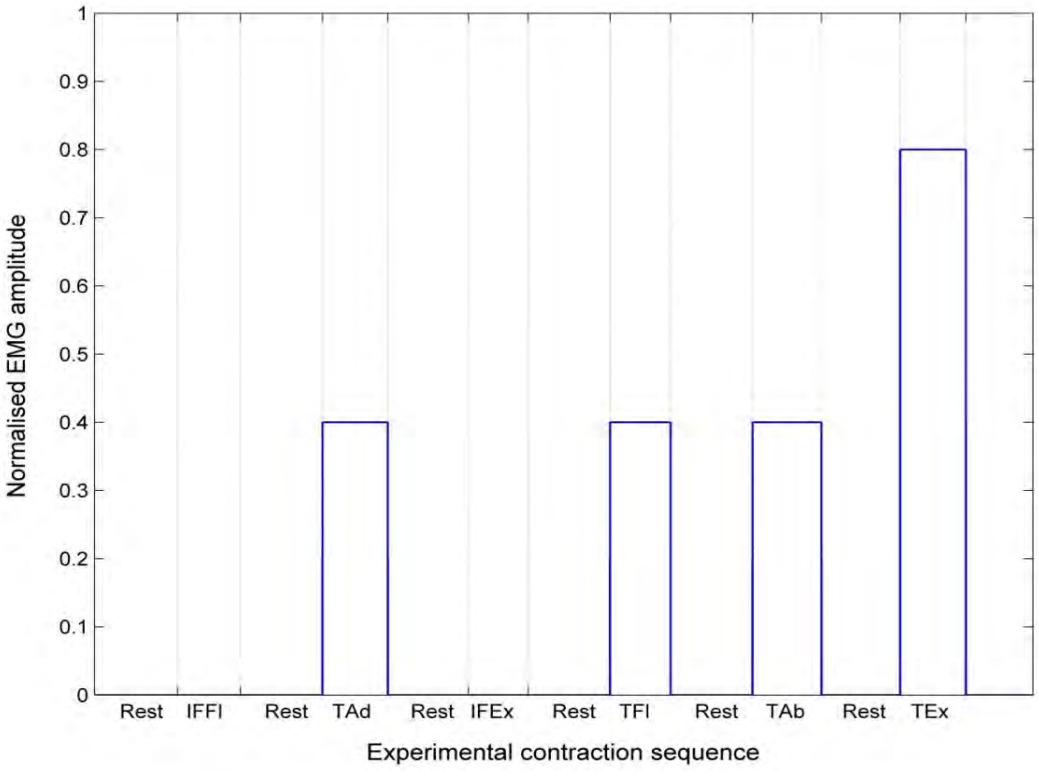


**Figure 3-15:** An illustrative example of a predicted EMG waveform for EPL (D) using the literature based activation patterns defined in Table 3-3. The vertical dotted lines represent the strain gauge derived timing intervals for the respective isometric contractions. The waveform shown here is divided into segments, each 5s long, according to the isometric contraction performed during that segment. Note that here *fa* = 0.8 and *pa* = 0.4.

Finally, the predicted EMG waveforms for each muscle were smoothed using the same 250ms RMS filter used for rectifying the IC waveforms. This was to ensure the same delay (inherent to filters) was introduced into both the enveloped IC and predicted waveforms prior to the correlation coefficient comparison described in section 3.4.3. An example of a smoothed predicted activation waveforms are shown in Figure 3-16:

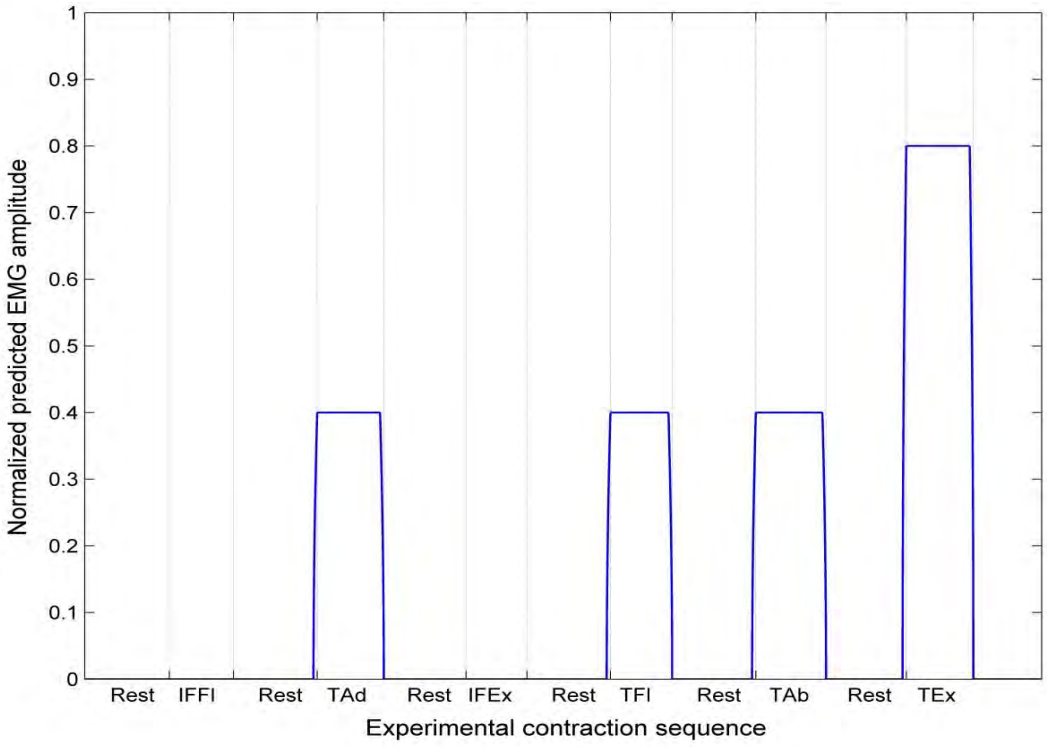


**Figure 3-16:** An illustrative example of a predicted EMG waveform for EPL (D) after applying the 250ms RMS filter previously used to obtain the linear activation envelopes of the ICs. The reason for doing so was to introduce the same filter delay effects to the ICs and the predicted EMG waveforms to ensure an even comparison between the two with Pearson's correlation coefficient (see section 3.4.3). The RMS filter effectively rounds out the vertical sides of the predicted EMG waveform shown in Figure 3-15. The vertical dotted lines represent the strain gauge derived timing intervals for the respective isometric contractions. The waveform shown here is divided into segments, each 5s long, according to the isometric contraction performed during that segment.

### 3.4.3 Pearson's correlation coefficient (r) comparison

The r value provided an indication of how closely the shapes of the predicted and enveloped waveforms match. The MATLAB® function "*corrcoef*" was used to compare the two waveforms. The waveforms were ranked from highest to lowest according to the r value; the highest ranked IC best represented the predicted activation for a particular muscle. This process was repeated for each muscle, thereby identifying the top ranked IC for each muscle (shown in Figure 3-17).

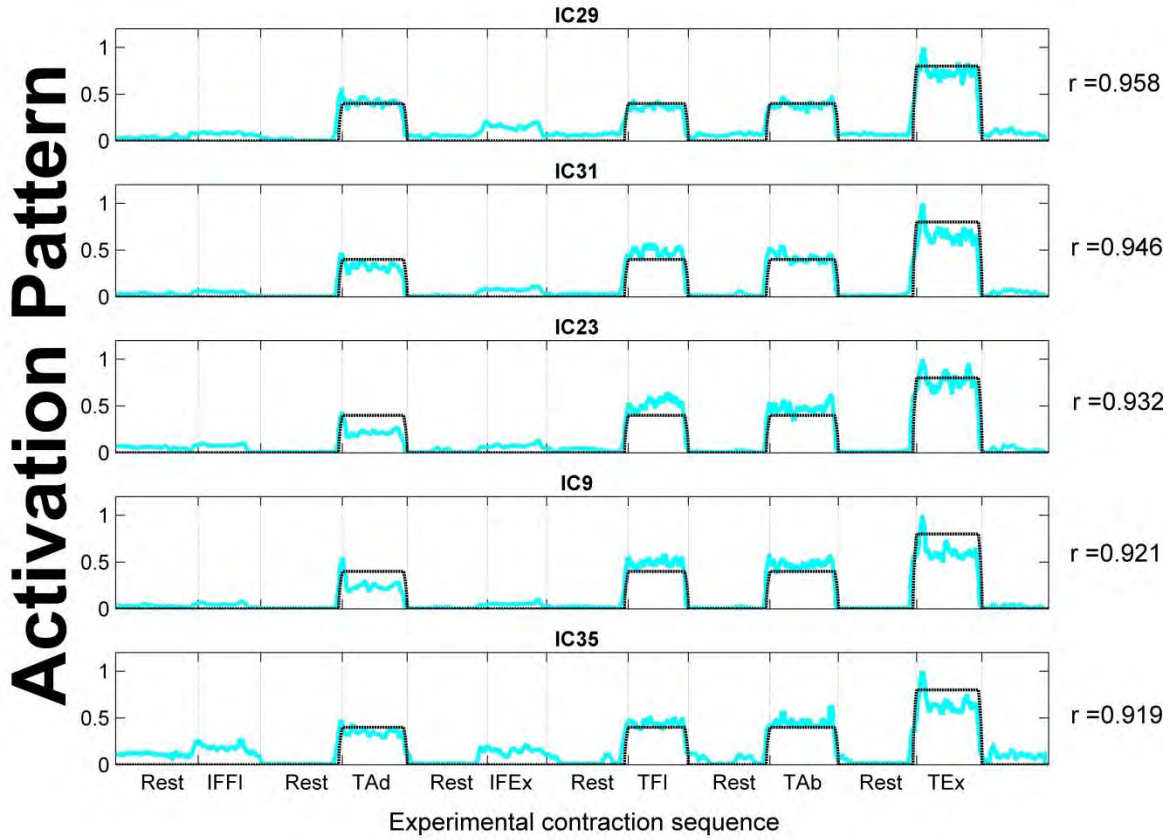


**Figure 3-17:** An illustrative example of the Pearson's correlation coefficient comparison between the enveloped IC (turquoise line) and predicted EMG (black line) for EPL. The 5 highest ranked ICs (according to Correlation Coefficient (r), shown on the right of each waveform) are presented here. The vertical dotted lines represent the strain gauge derived timing intervals for the respective isometric contractions. The waveforms shown here are divided into segments, each 5s long, according to the isometric contraction performed during that segment.

### 3.4.4 Resolving IC duplication

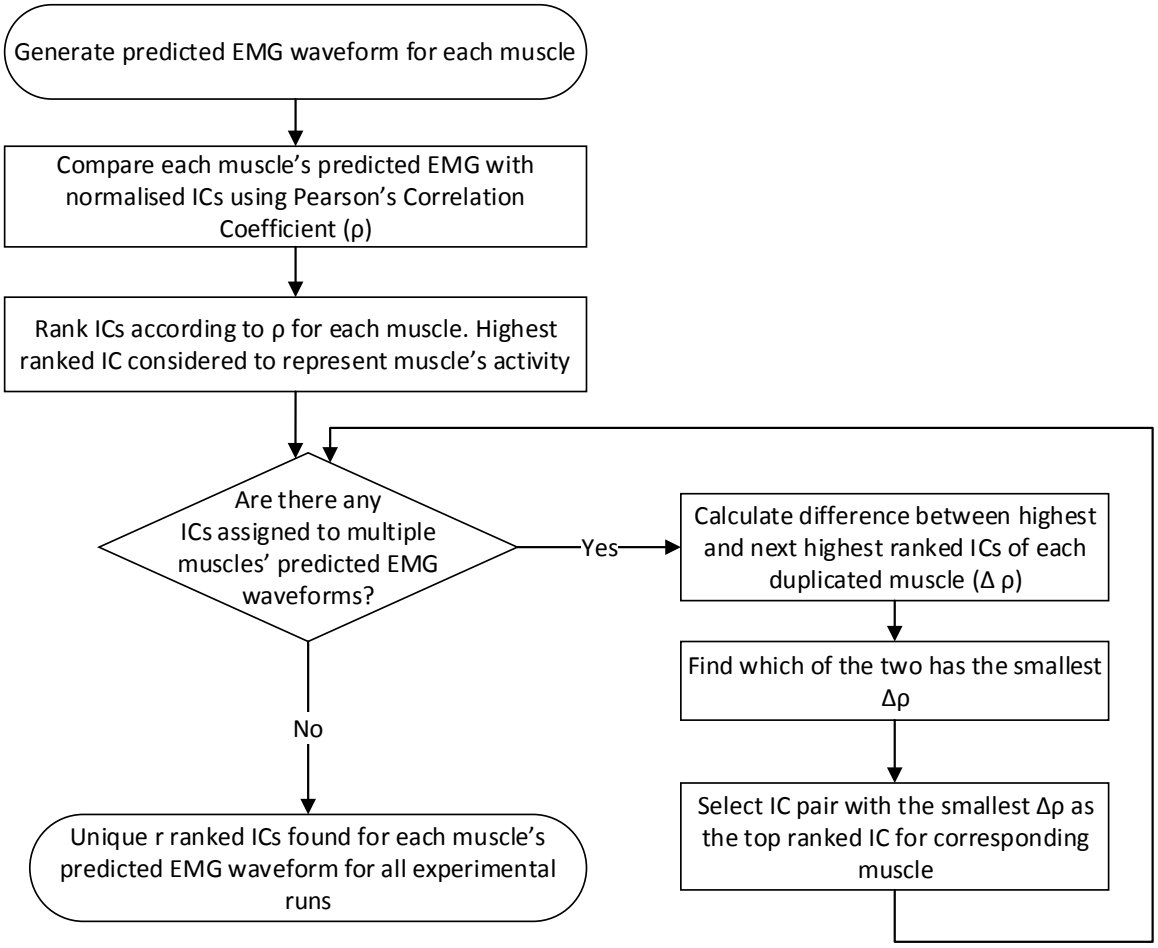


**Figure 3-18:** Selection process flow chart for deciding on the top r ranked IC when more than one muscle's predicted EMG waveform correlate best with the same IC

In their investigation into the activation of individual finger and thumb muscles, both Birdwell et al. (2013) and Li et al. (2008) and found that the activity of EPL and EPB during thumb movements were very similar and difficult to individually isolate. Thus there were instances in the present study where the same IC correlated with the predicted activity of these two muscles in particular. To account for this, the top IC selection function compared the difference in r values between the top and the second or third highest ranked ICs to find the highest ranked unique IC. The muscle pair (predicted EMG and IC) with the smallest change in r providing a unique IC number was chosen as the IC top r ranked IC for that muscle. This process is summarised graphically in Figure 3-18.

## 3.5 Statistical analysis

This analysis sought a diagnostic measure of how well the predicted EMG matched the top r ranked ICs for each muscle across multiple experimental runs and was performed in 2 main steps:

1. A per time point basis accuracy, sensitivity and specificity (psASS) analysis was conducted at different partial (*pa*) and full (*fa*) activation threshold combinations (ThCs) for each experimental run (see section 3.5.1).
2. A mixed effects linear regression model was fitted to the psASS data to find the overall accuracy between the predicted EMG and enveloped ICs for the different threshold combinations. Details of the mixed effects model are described in section 3.5.3.

The statistical analysis methodology is summarised by the flow chart shown in Figure 3-19.

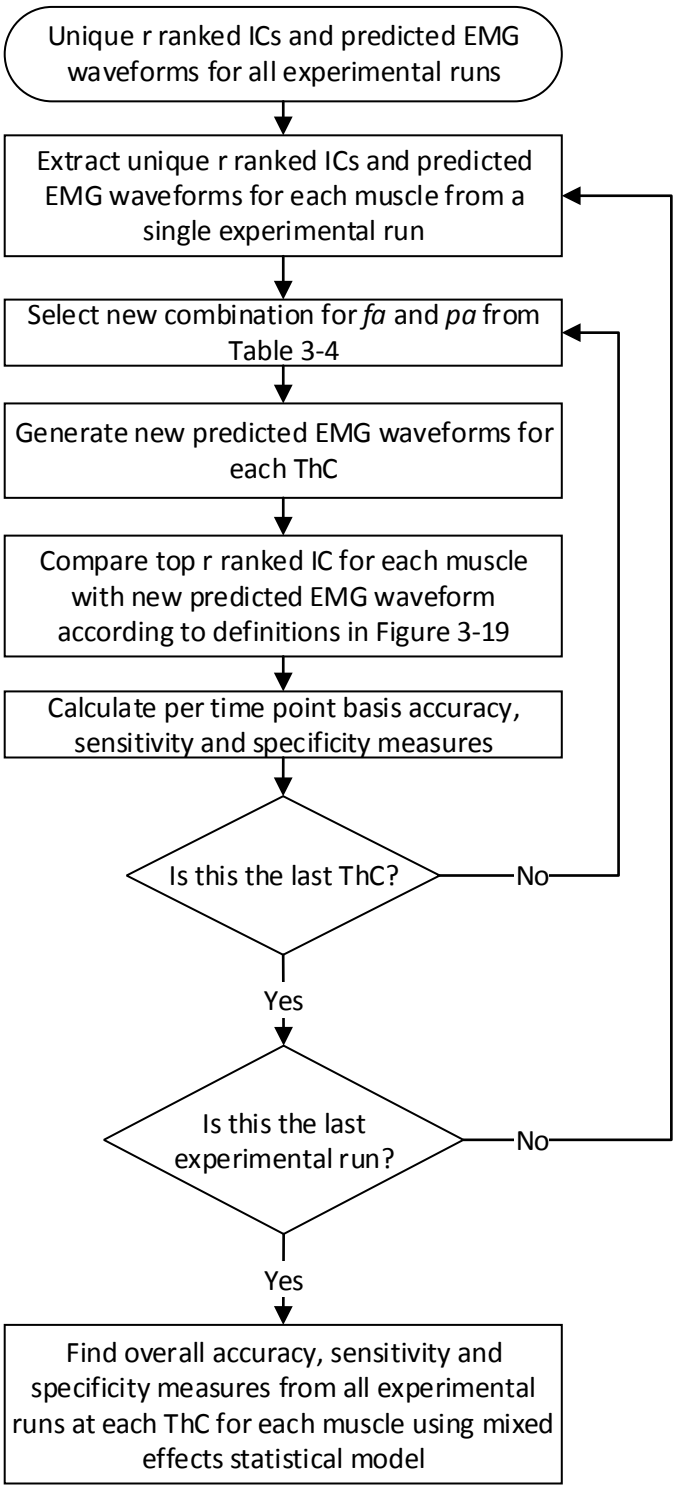


**Figure 3-19:** Flow chart of statistical analysis methodology.

### 3.5.1 psASS analysis

The psASS analysis measured the level of agreement between the top-ranked IC and predicted EMG waveform for each experimental run. The waveforms were compared on a per sample basis (i.e. at individual time points) during each isometric contraction. Agreement was measured by classifying the samples as True Positives (TPs), True Negatives (TNs), False Positives (FPs) and False Negatives (FNs) according to the following definitions:

- Where the IC was greater or equal to the predicted EMG when the predicted EMG was non-zero, a True TP was registered.
- Where the IC was less than the predicted EMG when the predicted EMG was non-zero, a False Negative FN was registered.
- Where the IC was less than or equal to the predicted EMG when the predicted EMG was at its minimum value, a True Negative TN was registered.
- Where the IC was greater than the predicted EMG when the predicted EMG was at its minimum value or a partial activation, a False Positive FP was registered.

A simplified, visual representation of the definitions for the TPs, TNs, FNs, FPs is shown in Figure 3-20:

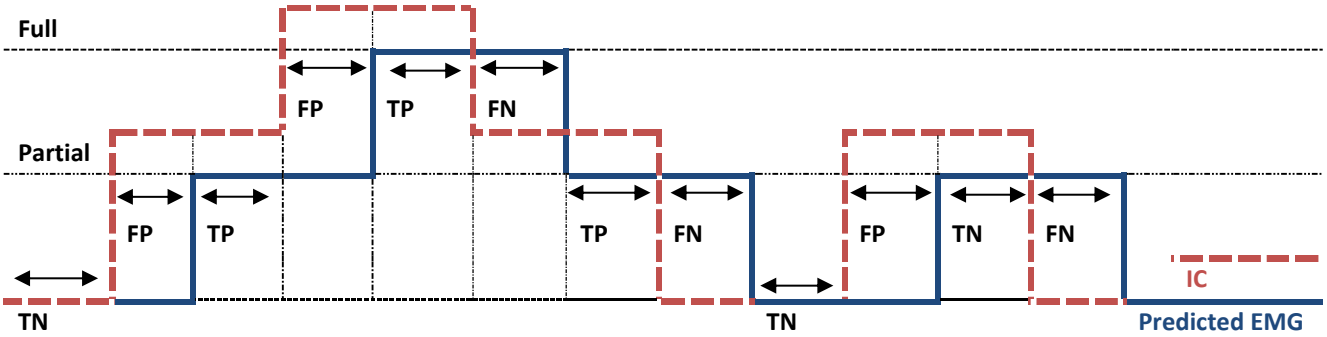


**Figure 3-20:** Conceptual definitions for True Positives (TPs), True Negatives (TNs), False Positives (FPs) and False Negatives (FNs) used in the psASS analysis. The blue line represents the predicted EMG waveform and the dashed red line represents the IC

Experimentally, the top r ranked ICs were far more jagged (see Figure 3-10) than depicted in Figure 3-20, thus small blips of activity in the IC incorrectly indicated the muscle was active when compared to a flat predicted EMG waveform (see Figure 3-15). An activation threshold of 3 standard deviations (3σ) above a resting baseline was used as a standardized measure for determining whether the muscle was active or not. 3σ above a resting baseline is a widely used value in biomechanics for defining muscle activation from sEMG measurements (Konrad 2005; Krebs et al. 2003). Any samples above the 3σ threshold were considered TPs or FPs depending on the predicted EMG waveform at the corresponding time points. Likewise, any samples below the 3σ threshold were considered TNs or FNs depending on the predicted EMG activity at the corresponding time points. The mean activity level during the rest periods between the isometric contractions was considered as the baseline activity value. To ensure the predicted EMG and top r ranked ICs were compared to the same reference, the minimum value of the predicted EMG was matched to this resting baseline value. A visual representation of this comparison is shown for a single experimental run in Figure 3-21.

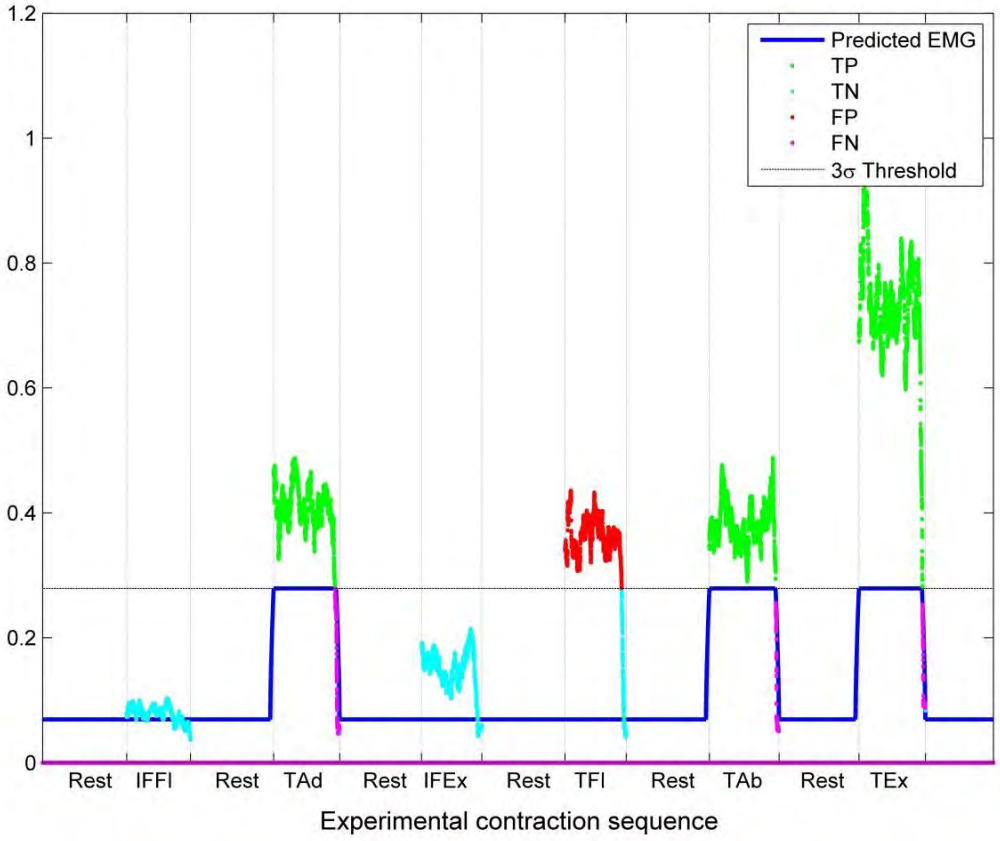


**Figure 3-21:** An illustrative example of True Positives (TPs - green dots), True Negative (TNs -blue dots), False Positives (FPs) - red dots) and False Negatives (FNs - purple dots) found for APL using the 3 standard deviations from a resting baseline activation threshold for both *pa* and *fa*. In this example, very few FNs were registered, which is why there appears to be a purple line on the bottom of the figure. The minimum value of the predicted waveform for APL was matched to the resting baseline value of the IC (the mean activity during the rest periods of the IC most likely to represent the activity of APL). Where the IC was greater or equal to the predicted EMG when the predicted EMG was greater than the resting baseline value, a TP was registered. Where the IC was less than or equal to the predicted EMG when the predicted EMG was at the resting baseline value, a TN was registered. Where the IC was greater than the predicted EMG when the predicted EMG was at the resting baseline value or a partial activation, a FP was registered. Where the IC was less than the predicted EMG when the predicted EMG was greater than the resting baseline value, a FN was registered. The vertical dotted lines represent the strain gauge derived timing intervals for the respective isometric contractions. The waveform shown here is divided into segments, each 5s long, according to the isometric contraction performed during that segment.

Since the choice of threshold can affect the number of TPs, TNs, FNs and FPs detected, the psASS analysis was repeated for different combinations of the partial and full activation threshold values (ThCs), shown in Table 3-4. The analysis was first conducted using the 3σ activation threshold value for both the partial and full thresholds for comparison purposes with the different threshold combinations in Table 3-4 (an example of this comparison using the 3σ value for both the full and partial thresholds is shown in Figure 3-21). The values in Table 3-4 were specifically chosen to find any patterns in the data by varying the partial threshold for fixed full thresholds. New predicted EMG waveforms were generated for each ThC and used solely for comparison with each muscle's top r

ranked IC, for each experimental run. These waveforms were smoothed with the same RMS filter with a 250ms window function used for producing the predicted EMG waveforms (see section 3.4.2).

**Table 3-4:** Full (*fa*) and partial (*pa*) activation threshold combinations (ThC) used in psASS analysis

| Threshold Combination (ThC) | Full activation (fa) threshold | Partial activation (pa) threshold |
|---|---|---|
| Ref | 3σ | 3σ |
| ThC1 | 1 | 0.5 |
| ThC2 | 1 | 0.4 |
| ThC3 | 1 | 0.3 |
| ThC4 | 1 | 0.2 |
| ThC5 | 1 | 0.1 |
| ThC6 | 0.9 | 0.5 |
| ThC7 | 0.9 | 0.4 |
| ThC8 | 0.9 | 0.3 |
| ThC9 | 0.9 | 0.2 |
| ThC10 | 0.9 | 0.1 |
| ThC11 | 0.8 | 0.5 |
| ThC12 | 0.8 | 0.4 |
| ThC13 | 0.8 | 0.3 |
| ThC14 | 0.8 | 0.2 |
| ThC15 | 0.8 | 0.1 |
| ThC16 | 0.7 | 0.5 |
| ThC17 | 0.7 | 0.4 |
| ThC18 | 0.7 | 0.3 |
| ThC19 | 0.7 | 0.2 |
| ThC20 | 0.7 | 0.1 |
| ThC21 | 0.6 | 0.5 |
| ThC22 | 0.6 | 0.4 |
| ThC23 | 0.6 | 0.3 |
| ThC24 | 0.6 | 0.2 |
| ThC25 | 0.6 | 0.1 |
| ThC26 | 0.5 | 0.5 |
| ThC27 | 0.5 | 0.4 |
| ThC28 | 0.5 | 0.3 |
| ThC29 | 0.5 | 0.2 |
| ThC30 | 0.5 | 0.1 |

An example of a psASS comparison between a top r ranked IC for APL and a predicted EMG waveform using *fa* = 0.6 and *pa* = 0.4 in Figure 3-22.

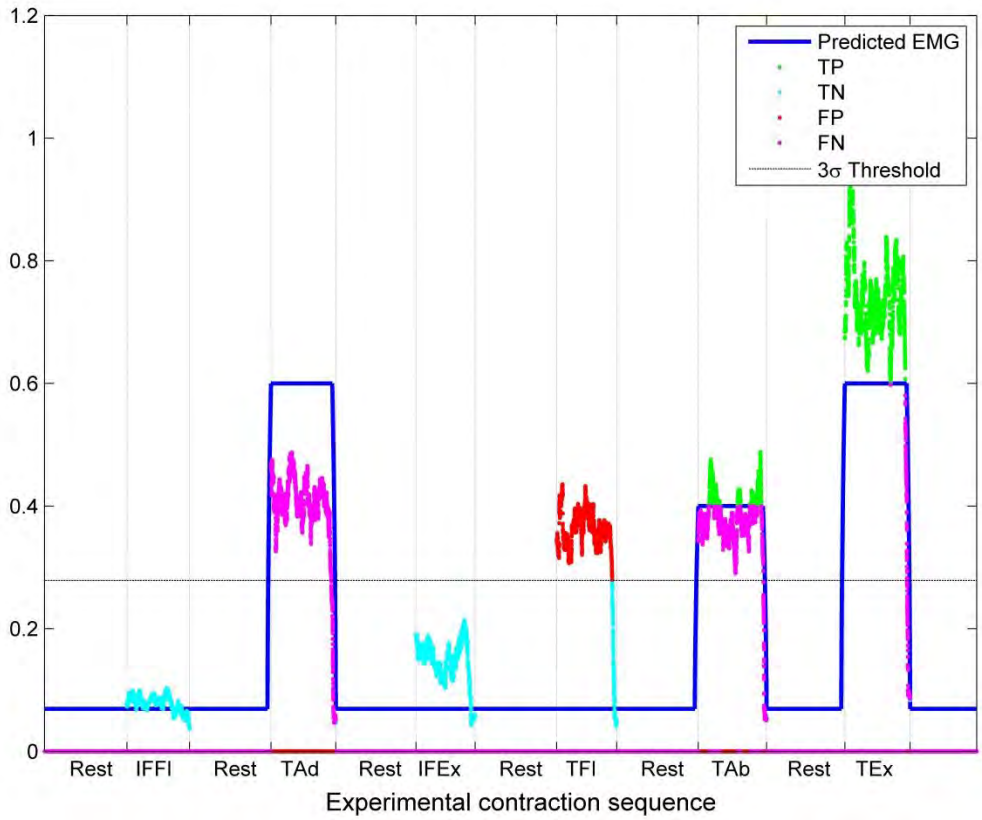


**Figure 3-22**: An illustrative example of the psASS comparison between a predicted EMG waveform (*fa* = 0.6, *pa* = 0.4) and top r ranked IC for APL. The minimum value of the predicted waveform for APL was matched to the resting baseline value (the mean activity value during the rest periods of the IC most likely to represent the activity of APL).

The TNs, TPs, FNs and FPs from each ThC were tallied to calculate sensitivity, specificity and accuracy measures according to the following equations (Merrill 2013):

$$Accuracy = \frac{TP + TN}{TP + TN + FP + FN} \qquad \textbf{Equation 3-3}$$

$$Sensitivity = \frac{TP}{TP + FN} \qquad \textbf{Equation 3-4}$$

$$Specificity = \frac{TN}{TN + FP} \qquad \textbf{Equation 3-5}$$

Accuracy (Equation 3-3) gives an indication of the time points that were correctly identified or rejected relative to the total population of time points. Sensitivity (Equation 3-4) indicates the classification performance when activity was expected (the ratio of correctly identified and incorrectly rejected time points); specificity (Equation 3-5) indicates the classification performance when activity is not expected (the ratio of correctly rejected and incorrectly identified time points). The tallying and calculation of accuracy, sensitivity and specificity measures was repeated for each muscle under investigation and each experimental run. This resulted in a total of 4650 accuracy,

sensitivity, and specificity values for each target muscle (15 participants x 10 experimental runs per participant x 31 ThCs).

### 3.5.2 Exclusion of experimental data for statistical analysis by ThC

Since the 3σ threshold for each experimental run was derived from the baseline activity of that experimental run, the 3σ threshold value was not necessarily the same for all experimental runs. Thus the possibility existed that the *fa* or *pa* values for a particular ThC in Table 3-4 was smaller than the 3σ threshold. In this event, any experimental run whose 3σ threshold value was greater than the *pa* or *fa* value for a particular ThC was excluded from the statistical analysis. The justification for doing so was due to the fact that, as mentioned in section 3.5.1, the choice for the value of the 3σ threshold is considered an accepted value for determining whether a muscle is active or not. The 3σ threshold value was thus considered a minimum level of IC activity that could be classified as 'ON' or 'OFF'. Thus only experimental runs which might have influenced the psASS analysis above that of the 3σ activation threshold were considered for the statistical analysis

### 3.5.3 Mixed effects statistical analysis

The following statistical analysis was formulated through consultations with Dr Katya Mauff and Ms Ushma Galal of the University of Cape Town's statistics consultancy service. The aim of the analysis was to:

1. Find the overall accuracy, sensitivity and specificity of the fit between each muscle's predicted EMG and top r ranked IC for each ThC across all experimental runs.
2. Determine whether quantifying the IC activity (by the *fa* and *pa* thresholds) above a single clinical activation threshold value would result in a statistically significant improvement in the fit between the predicted EMG waveforms and the top r ranked IC for each muscle.

To this end, a mixed effects model calculated the overall accuracy for each threshold combination, while taking the variation between participants as well as the within participant variation (variation between experimental repetitions performed by the same participant) into account.

Mixed effects models are often used to predict outcomes in studies where repeated measurements from the same participant are taken. This is due to the assumption of independence between observations for simple linear regression being violated: multiple observations from the same participant are inherently correlated and are thus inter-dependent (as opposed to independent). Mixed effects models are so-named since the models calculate the influence of the variables manipulated by the examiner during the analysis (the ThCs) on the predicted variables or 'fixed effects' (Accuracy, Sensitivity and Specificity) while resolving the independence assumption by clustering the data to be modelled according to the repeated measurement similarity (grouping the data by participant) using the random effect (Winter 2013).

The mixed effects model nlme developed by Pinheiro et al. (2014) (part of the statistical modelling package, R (R Core Team 2014)) was fitted to the psASS data from section 3.5.1 to test the effect 'Accuracy' (dependent variable) as a result of each ThC. The model fitting was repeated for each muscle with 'Accuracy' set as the fixed effect in each instance. To account for the correlated data structure due to the experimental repetitions performed by each participant, the participant identifier 'SID' was set as the random effect to improve the model fit for each muscle.

The ‘Accuracy’ mixed effects model was fitted to the sensitivity and specificity psASS data for each muscle. Sensitivity and specificity values calculated from corresponding ‘Sensitivity’ and ‘Specificity’ mixed effects models were reported according to the ThC with which the highest accuracy was calculated.

A major assumption inherent in any linear regression model is that the data to be modelled is normally distributed. Examination of the residuals (error function of the statistical model fit to the data) for each ‘Accuracy’ model showed the assumptions were not violated. Scatterplots and histograms investigating these effects for each muscle under investigation’s ‘Accuracy’ model can be found in APPENDIX D.2 -D.4.

[This page is left intentionally blank]

# Chapter 4 Results

Chapter 4 presents the results of the experiment carried out to test the research objectives defined in 1.4.4. Sample waveforms produced by the final predicted EMG algorithm for each of the muscles are presented in section 4.1. Qualitative and quantitative results of the algorithm identifying the IC most likely to correspond to the activity of each muscle are shown in section 4.2 and 4.3 respectively. Finally, the results of the statistical analysis are shown in section 4.4

## 4.1 Results of the final predicted EMG activation algorithm

The initial predicted EMG envelope shape for each of the deep (D) and superficial (S) muscles (for the same experimental run depicted in Figures 3-5 to 3-20) are shown in Figure 4-1 (see section 3.4.2 for derivation of the initial predicted EMG). These initial predicted waveforms were expanded into final predicted waveforms, including rest periods and RMS smoothing, by adjusting the start and end of each contraction to match the corresponding timing information derived from the strain gauges (see section 3.4.1 for details of contraction timing extraction procedure) in combination with Figure 4-1. The isometric contraction sequence order of the initial predicted EMG was matched to that of the experimental run. Ideally, the initial predicted EMG considered the muscles under investigation as fully active (*fa*) or partially active (*pa*) if the activity was 100% or 50%, respectively, of their normalized value (ie *fa* = 1.0 and *pa* = 0.5). However, through visual inspection of the ICs during the analysis, it was seen that values of 0.8 and 0.4 (for *fa* and *pa* respectively) were found to better represent the IC activity.

| | Experimental contraction sequence | | | | | |
|---|---|---|---|---|---|---|
| | **IFFl** | **TAd** | **IFEx** | **TFl** | **TAb** | **TEx** |
| **FPL (D)** | *0* | *0* | *0* | *fa* | *pa* | *0* |
| *fa* | | | | | | |
| *pa* | | | | | | |
| *0* | | | | | | |
| **EPL (D)** | *0* | *pa* | *0* | *pa* | *pa* | *fa* |
| *fa* | | | | | | |
| *pa* | | | | | | |
| *0* | | | | | | |
| **EPB (D)** | *0* | *pa* | *0* | *pa* | *pa* | *pa* |
| *fa* | | | | | | |
| *pa* | | | | | | |
| *0* | | | | | | |
| **APL (D)** | *0* | *fa* | *0* | *0* | *pa* | *fa* |
| *fa* | | | | | | |
| *pa* | | | | | | |
| *0* | | | | | | |
| **FD (S)** | *fa* | *0* | *0* | *0* | *0* | *0* |
| *fa* | | | | | | |
| *pa* | | | | | | |
| *0* | | | | | | |
| **ED (S)** | *0* | *0* | *fa* | *0* | *0* | *0* |
| *fa* | | | | | | |
| *pa* | | | | | | |
| *0* | | | | | | |

**Figure 4-1**: Initial predicted EMG envelope shapes for each of the deep (D) and superficial (S) muscles based upon Table 3-3 (see section 3.4.2). The muscles are modelled as fully active (*fa*), partially active (*pa*) or inactive (*0*). Each threshold is represented by a unique line style. The horizontal axis is labelled according to the isometric contraction order performed during the experiment. Each muscle's predicted EMG waveform is shown on the vertical axis.

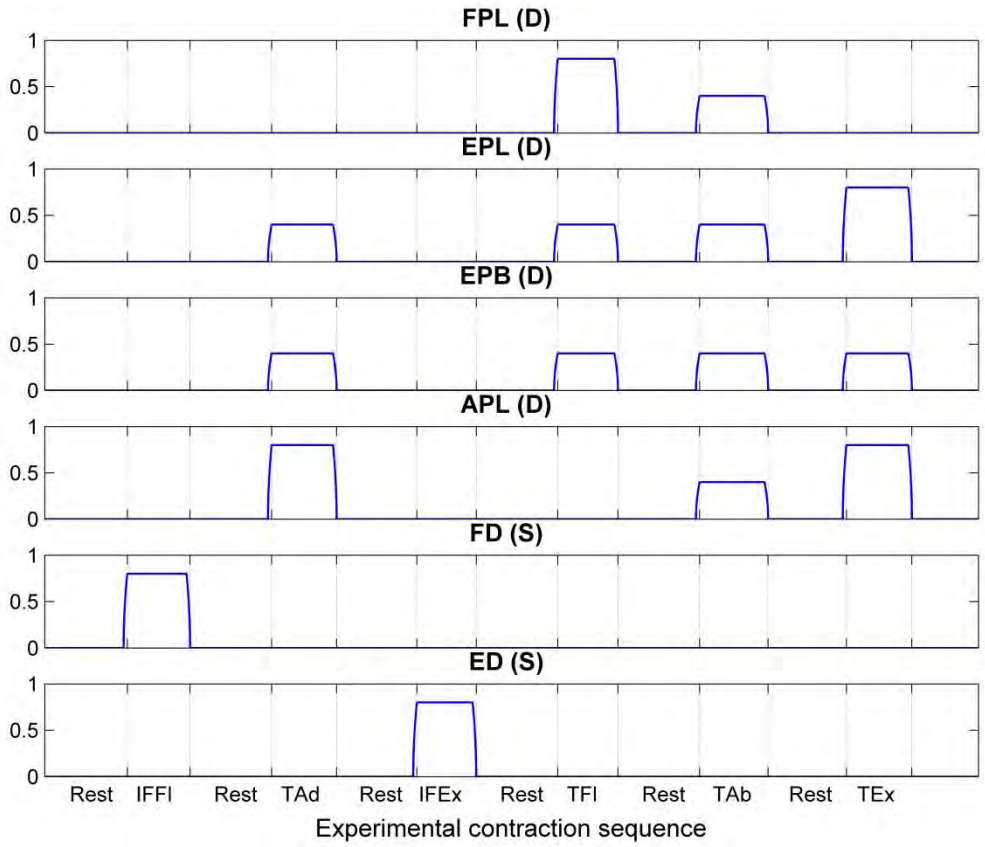


**Figure 4-2**: An illustrative example of the final predicted waveforms for each of the deep (D) and superficial (S) muscles with RMS filtering and rest periods included for a single experimental run. Each final predicted EMG waveform is normalised with values of 0.8 and 0.4 used for the *fa* and *pa* thresholds respectively. The vertical dotted lines represent the strain gauge derived timing intervals for the respective isometric contractions. The waveforms shown here are divided into segments, each 5s long, according to the isometric contraction performed during that segment.

## 4.2 Qualitative results of IC identification algorithm

### 4.2.1 Top r ranked ICs

Top r ranked ICs for each deep (D) and superficial (S) muscle with their final predicted waveforms for a single experimental run are shown in Figure 4-3. For the sake of consistency, since the order in which each isometric contraction was performed was randomized for each experimental run, the top r ranked ICs presented in Figure 4-3 originate from the same experimental run as Figure 3-5 to Figure 3-10. Best and worst top r ranked ICs for each of the muscles under investigation are presented in APPENDIX A.4 for a more representative view of the experimental data. Note that the final predicted EMG waveforms shown in Figure 4-3 are slightly more curved than those depicted in Figure 4-2: this is due to the application of the 250ms RMS smoothing filter to the final predicted EMG waveform to more closely match the IC (see section 3.4.2 for more details on the predicted EMG RMS smoothing and final predicted EMG generation procedure). The peak correlation coefficient value (r) for each comparison between the predicted EMG and enveloped IC is shown on the right of the waveforms.

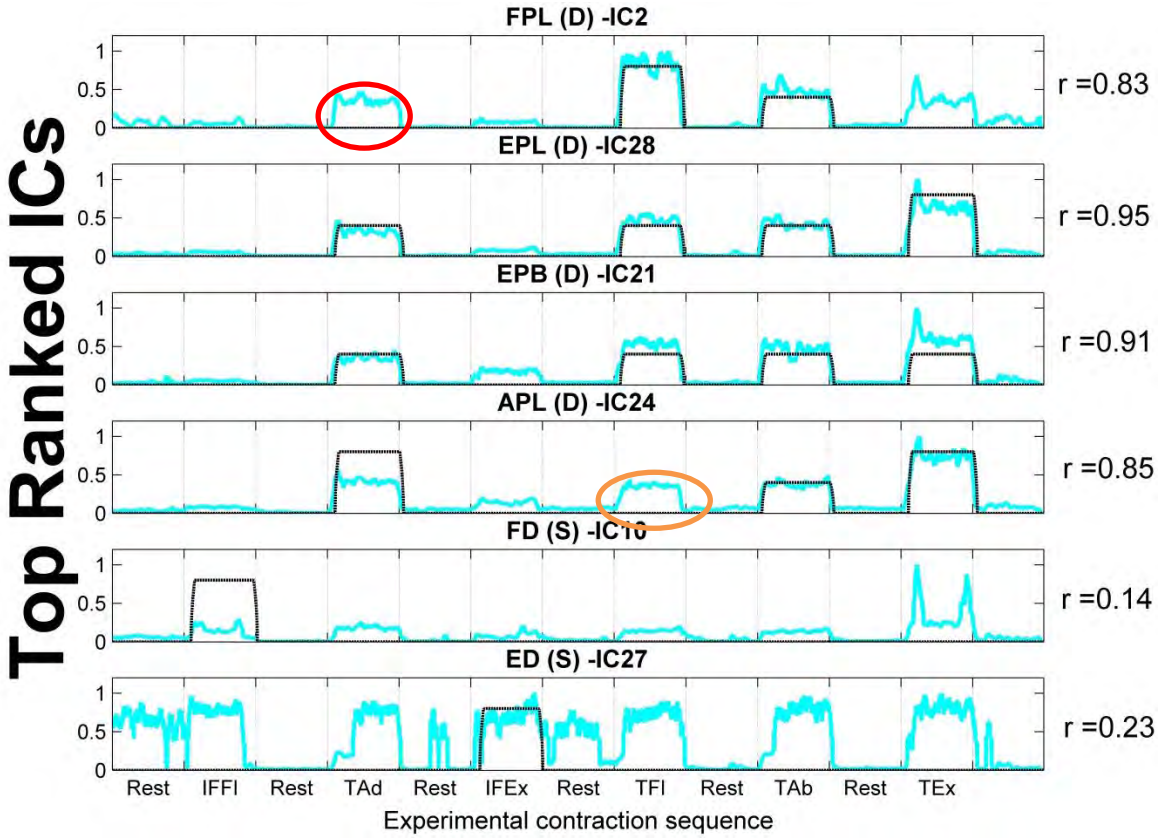


**Figure 4-3**: An illustrative example of the top r ranked ICs (blue line) with the corresponding final predicted EMG waveform (black line) for the deep (D) and superficial (S) muscles from a single experimental run. The correlation coefficient (r) value for the comparison between each enveloped IC and final predicted EMG is shown on the right of each waveform. A more representative set of figures for each of the muscles under investigation may found in APPENDIX A.4. The vertical dotted lines represent the strain gauge derived timing intervals for the respective isometric contractions. The waveforms shown here are divided into segments, each 5s long, according to the isometric contraction performed during that segment. The red and orange ellipses during TAd for FPL (D) and TFl for APL (D) highlight EMG activity that was detected but unaccounted for by the final predicted EMG.

### 4.2.2 Co-contraction evaluation

The red and orange ellipses in Figure 4-3 highlight EMG activity derived from the recorded monopolar EMG detected by the electrodes, but which was unaccounted for in the final predicted EMG. Corresponding red and orange ellipses in Figure 4-4 highlight forces detected by the strain gauges on the dynamometer in additional directions to the required direction for the isometric contraction (see Table 2-1 in section 2.1.1 for details on the direction definitions for the thumb dynamometer strain gauge system). The red ellipse in Figure 4-3 and Figure 4-4 indicates the participant applied a downward force (shown by the negative voltage dip on the vertical plane dynamometer trace in Figure 4-4) during TAd when the applied force was expected to be solely in the horizontal plane. The orange ellipse indicates the participant applied a force to the right (shown by the negative voltage dip on the horizontal plane dynamometer strain gauge trace) during TFl when the applied force was expected to be solely in the vertical plane. Both ellipses show the

participant did not comply fully with the required isometric contraction and that there was co-activation of muscles other than the target muscles during some of the isometric contractions.

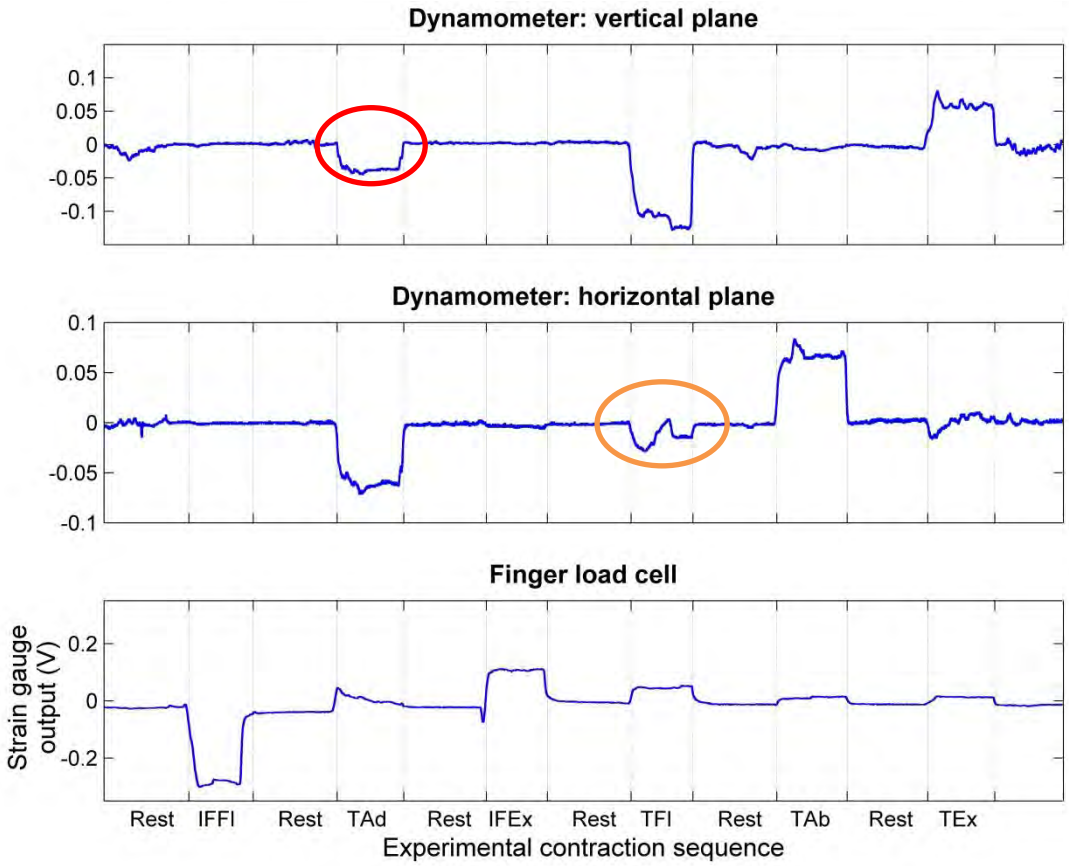


**Figure 4-4**: Strain gauge measurements from the thumb dynamometer and finger load cell from the same experimental run as Figure 4-3. The vertical dotted lines represent the strain gauge derived timing intervals for the respective isometric contractions. The waveforms shown here are divided into segments, each 5s long, according to the isometric contraction performed during that segment. The red and orange ellipses highlight forces detected as a result of unanticipated movements by the participant. Corresponding red and orange ellipses in Figure 4-3 indicate EMG activity during the same isometric contraction that was unaccounted for by the final predicted EMG. The red ellipse indicates the participant was pushing downwards (shown by the negative voltage dip on the vertical plane dynamometer trace in Figure 4-4) when the applied force for TAd was expected to be solely in the horizontal plane. The orange ellipse indicates the participant was pushing to the right initially, then attempting to correct the direction of the applied force (shown by the negative voltage dip on the vertical plane dynamometer trace in Figure 4-4) when the applied force for TFl was expected to be solely in the vertical direction. The ellipses indicate the participant did not comply fully with the required isometric contraction and that there was some co-activation of muscles other than those under investigation.

The phenomenon described in Figure 4-3 and Figure 4-4 was seen in the top r ranked waveforms in multiple experimental runs. However, in some instances muscle activity was detected during a particular isometric contraction when no activity was expected, but could not be attributed to a force applied in an unanticipated direction by the strain gauge. An example of this may be seen in Figure 4-5, particularly the activity attributed to FPL (D) during IFEx (highlighted by the orange ellipse

in Figure 4-5). During this contraction, ED (S) was expected to be active (highlighted by the red ellipse in Figure 4-5) and cause a force to be measured by the finger load cell during isometric extension of the index finger (highlighted by the red ellipse in Figure 4-6).

The activity highlighted by the orange ellipse in Figure 4-5 suggests that the participant may have applied a force with the thumb at the same time as extending the index finger. However, no forces were measured by the thumb dynamometer strain gauges during this same time period (highlighted by orange ellipses in Figure 4-6). FPL (D) cannot be expected to be active during index finger extension since the point of insertion for FPL (D) is on the base of the distal thumb phalange (see APPENDIX A.3.1 for a description of FPL (D)'s anatomical structure) and its function is unrelated to index finger extension (Hislop & Montgomery 2007; Gilroy et al. 2008). The activity highlighted by the orange ellipse in Figure 4-5 could possibly be explained by an incomplete separation of the source activity by fastICA.

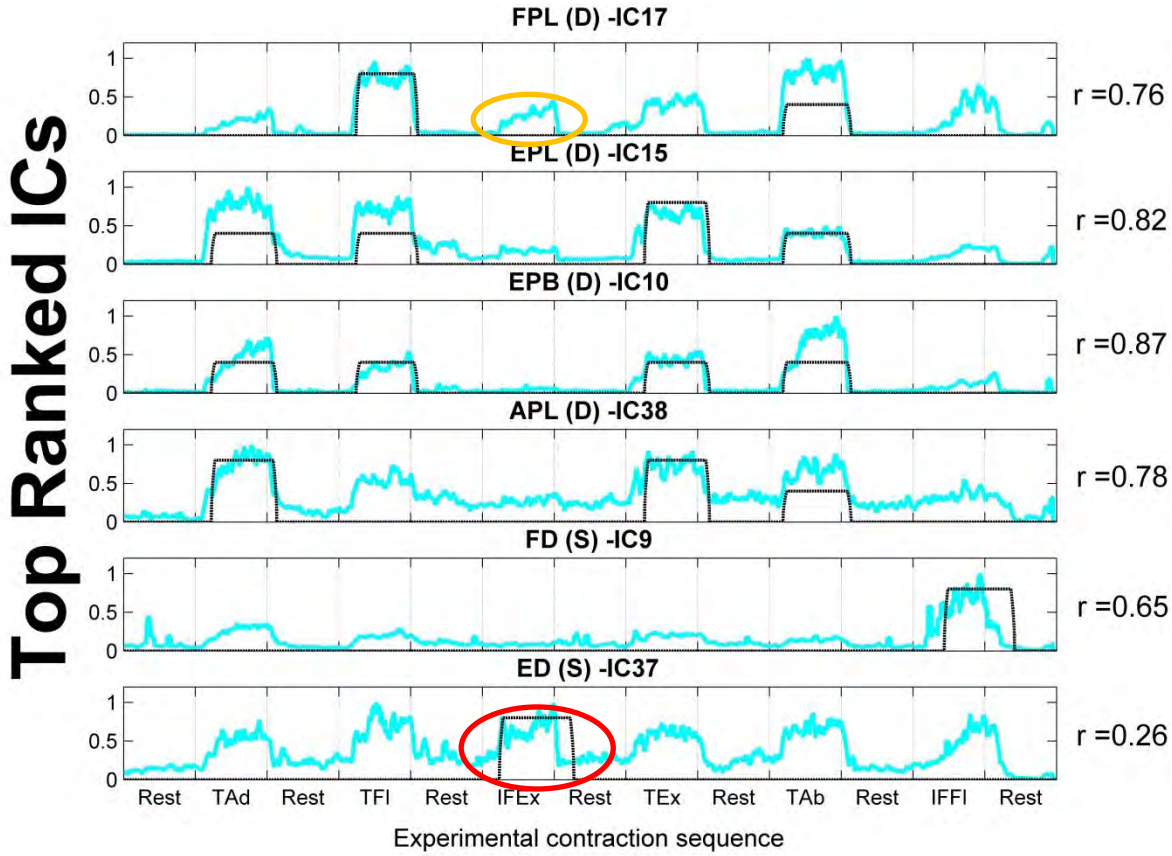


**Figure 4-5**: Top r ranked ICs for an experimental run in which activity was found for FPL (D) during IFEx (highlighted by the orange ellipse). The red ellipse highlights the isometric contraction for which ED (S) was expected to be active. The vertical dotted lines represent the strain gauge derived timing intervals for the respective isometric contractions. The waveforms shown here are divided into segments, each 5s long, according to the isometric contraction performed during that segment.

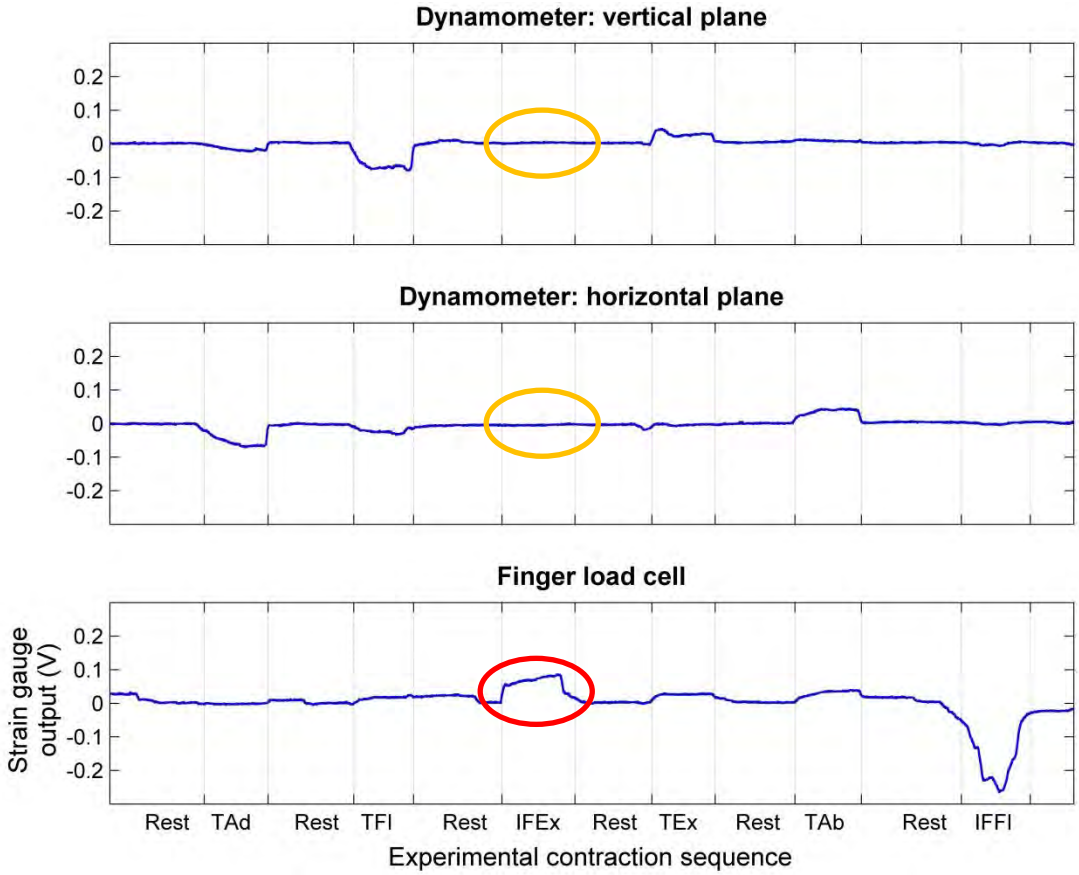


**Figure 4-6**: Strain gauge recordings used to derive the isometric contraction timing information for the top r ranked ICs shown in Figure 4-5. The red ellipse highlights the force measured by the finger load cell during isometric extension of the index finger. The orange ellipses highlight the absence of a force measured by the dynamometer strain gauges during that isometric contraction which may account for the activity found for FPL (D) during the same period (highlighted by corresponding orange ellipse in Figure 4-5). The vertical dotted lines represent the strain gauge derived timing intervals for the respective isometric contractions. The waveforms shown here are divided into segments, each 5s long, according to the isometric contraction performed during that segment.

### 4.2.3 Bipolar equivalent waveforms

Bipolar equivalent waveforms were derived from the original monopolar EMG recordings to verify whether sdEMG correctly detected activity from the superficial muscles FD (S) and ED (S). The waveforms were obtained by subtracting the monopolar EMG recordings from opposing electrode pairs in the electrode bands (e.g. the monopolar EMG measurements from electrode 1 and 11 in Figure 2-13 are considered a bipolar pair). Figure 4-7 shows the bipolar equivalent waveforms from the distal electrode band (derived from monopolar recordings 1-20)[21]. Figure 4-8 the bipolar equivalent waveforms from the proximal electrode band (derived from monopolar recordings 21-40[22]).

The intention in deriving equivalent bipolar plots was to determine whether the original recordings still detected superficial muscle activity when detected in the conventional, bipolar configuration.

[21] See Figure 3-1 in section 3.2.1 for details on the location of the proximal and distal electrode bands.

The superficial muscles under investigation, FD (S) and ED (S), were expected to be solely active during isometric IFFl and IFEx (highlighted by red rectangles in Figure 4-7 and Figure 4-8. Since the distal electrode ring was placed such that the electrode pairs would be orientated fairly closely along the direction of the FD (S) and ED's (S) muscle fibres, the activity of FD (S) and ED (S) was anticipated to be present on the bipolar waveforms derived from 21-40 (shown in Figure 4-8).

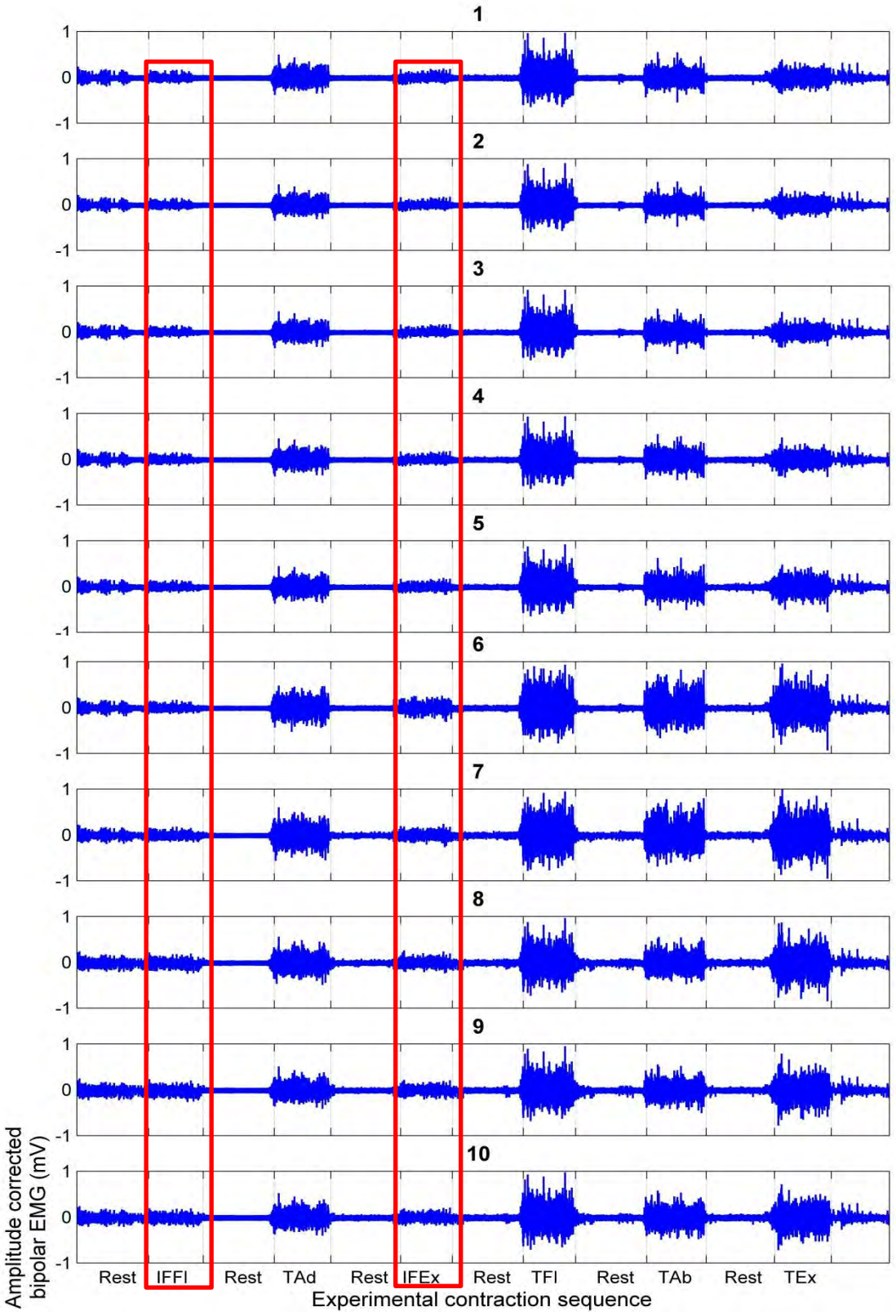


**Figure 4-7**: Equivalent bipolar waveforms derived from monopolar channels 1-20. The red boxes highlight the isometric contractions in which the superficial muscles FD (S) and ED (S) were expected to be active (IFFl and IFEx). The vertical dotted lines represent the strain gauge derived timing intervals for the respective isometric contractions. The waveforms shown here are divided into segments, each 5s long, according to the isometric contraction performed during that segment.

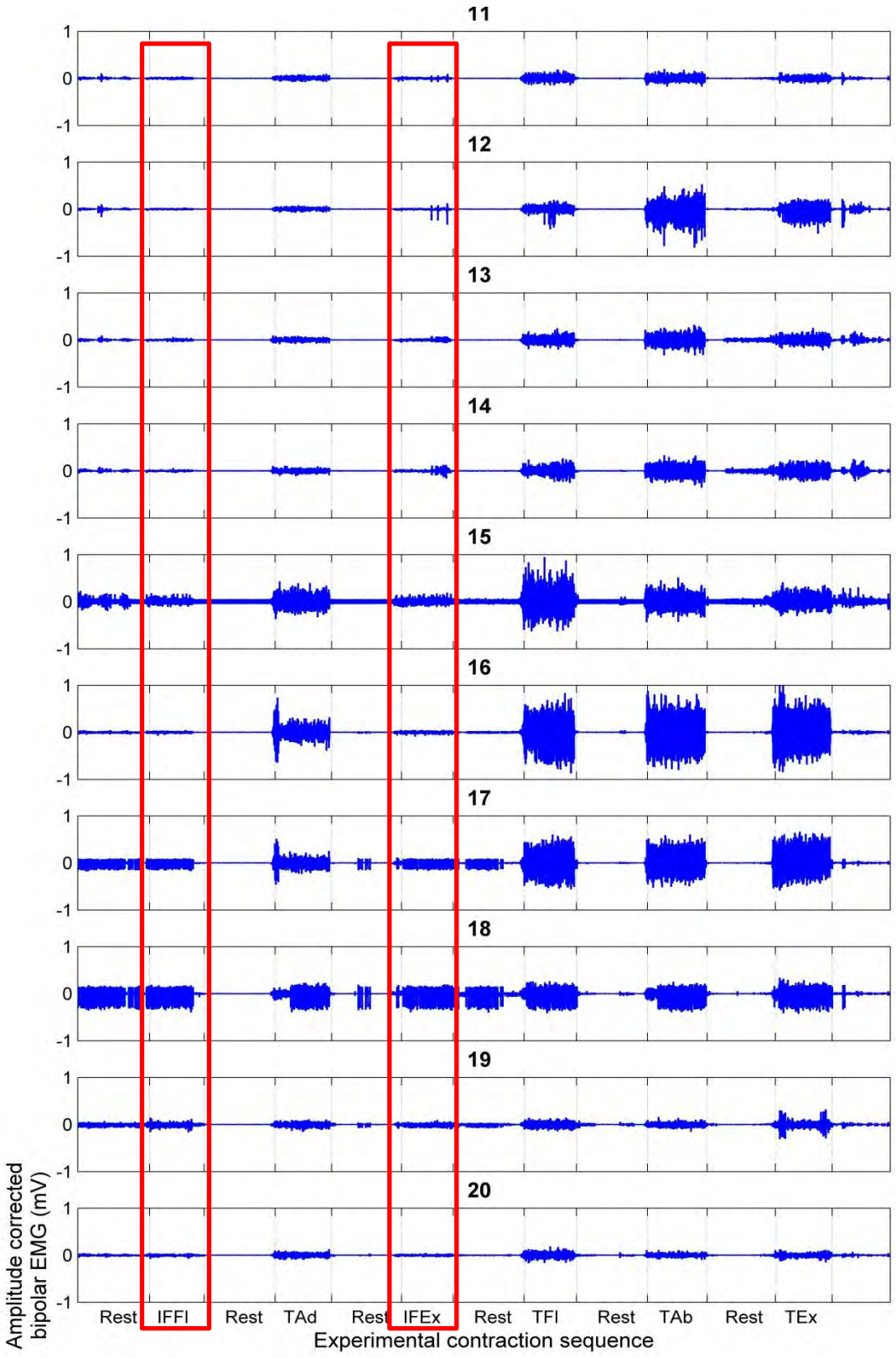


**Figure 4-8**: Equivalent bipolar waveforms derived from monopolar channels 21-40. The red boxes highlight the isometric contractions in which the superficial muscles FD (S) and ED (S) were expected to be active (IFFl and IFEx). The vertical dotted lines represent the strain gauge derived timing intervals for the respective isometric contractions. The waveforms shown here are divided into segments, each 5s long, according to the isometric contraction performed during that segment.

Figure 4-7 and Figure 4-8 show that no clear activity was found for FD (S) during isometric IFFl in either waveform. A subsequent bipolar measurement using a linear electrode array found that this absence of activity was due to the electrode ring not being placed over the appropriate innervation zone for FD (S). However during this bipolar measurement, considerably less activity was found during isometric flexion of the index finger in comparison to isometric flexion of all the fingers together. Thus it is possible that the absence of FD (S) activity in Figure 4-7 and Figure 4-8 is due to generally low EMG signal strength during IFFl or that the positions of the electrode rings were not optimally suited for specifically measuring FD's (S) activity during IFFl (since FD is a multi-tendon muscle, see APPENDIX A.3.2).

In the case of ED (S), some activity during IFEx was detected in bipolar waveforms 5, 6 and 7 (shown in Figure 4-7). The variation in amplitude across these three waveforms suggest that the electrode pairs in waveform 5 and waveform 7 were placed across ED (S) and that the electrode pairs for waveform 5 and 7 were placed slightly off to the side of the muscle whereas waveform 6 was placed close to ED (S). The presence of EMG activity in these waveforms during the different thumb isometric contractions indicates that there was either co-activation of ED (S) during these contractions, or that the detected activity was due to crosstalk from muscles very close to ED (S).

### 4.2.4 Electrode location verification

Following data collection and analysis it became apparent that the electrode ring placement was not ideal for the superficial muscles FD (S) and ED (S). As a result it was not possible to differentiate between crosstalk and co-activity. A post-hoc test was carried out to confirm this using commercial (Skintact™) electrodes placed in the appropriate positions to measure activity from these muscles (by using the linear electrode array to find the innervation zones). Bipolar EMG was recorded from these electrodes during each of the experimental contractions (shown in Figure 4-9). The waveforms for both muscles show that, to different extents, there was co-activity from both FD (S) and ED (S) during the experimental isometric contractions, when it assumed that both these muscles would not be active.

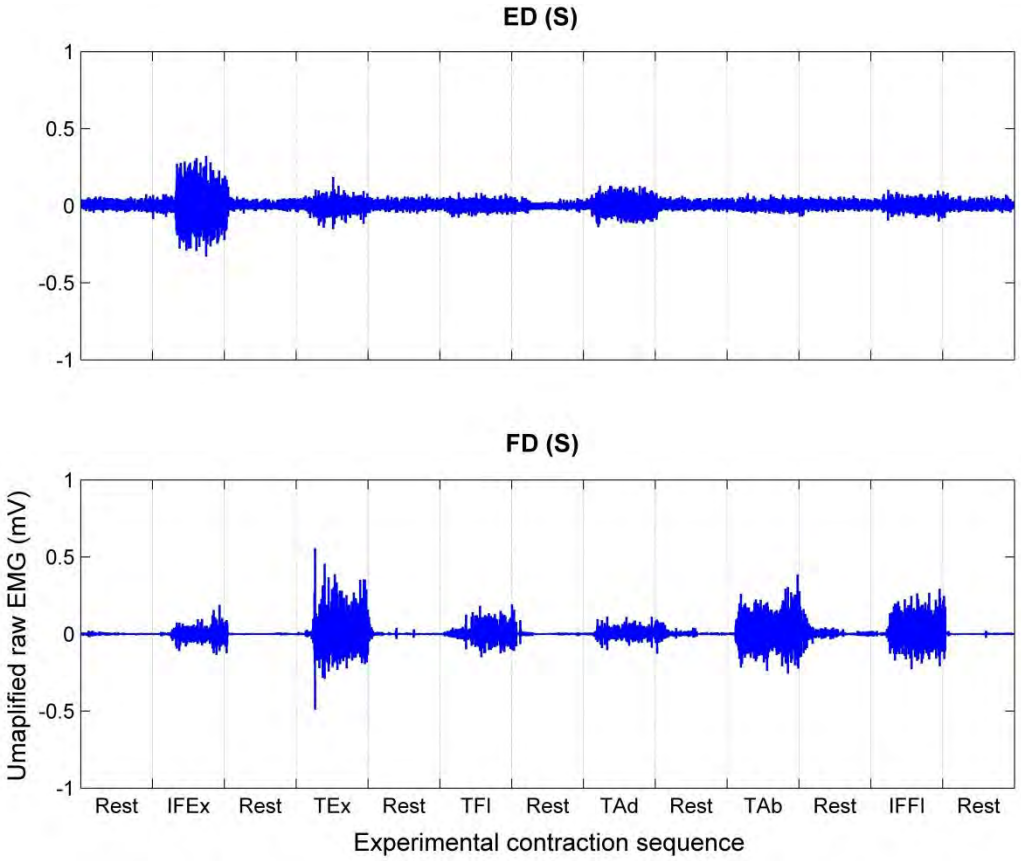


**Figure 4-9**: Bipolar measurement of FD (S) and ED (S) using commercial (Skintact™) placed in the corresponding positions for these two superficial muscles during each experimental isometric contraction. It can be seen in the waveforms above that both FD (S) and ED (S) were active to different extents during each of the experimental isometric contractions. The vertical dotted lines represent the strain gauge derived timing intervals for the respective isometric contractions. The waveforms shown here are divided into segments, each 5s long, according to the isometric contraction performed during that segment.

## 4.3 Quantitative results of IC identification algorithm

Mean values of the correlation coefficient (r) comparison between the top r ranked IC and final predicted EMG waveform for each muscle were found using Fisher's Transform. Fisher's Z transform corrects for averaging and confidence interval distortions since sample correlation coefficients tend to underestimate the population correlation coefficient (ρ) and thus distort the confidence intervals (Gorsuch & Lehmann 2010; Shen & Lu 2006). The equations used for the Fisher transform correction procedure were drawn from Gorsuch & Lehmann (2010) and Shen & Lu (2006), unless otherwise stated. r values from each experimental run were converted to a standardized *z* score using the Fisher Transform equation:

$$z = \frac{1}{2}\ln\left(\frac{1+r}{1-r}\right) \qquad \textbf{Equation 4-1}$$

The mean z ($\bar{z}$) score was found for each of the muscles and converted to a mean correlation coefficient (population correlation coefficient, ρ) using the Inverse Fisher Transform (Gorsuch & Lehmann 2010):

$$\rho = \frac{e^{2\bar{z}} - 1}{e^{2\bar{z}} + 1} \qquad \textbf{Equation 4-2}$$

Lower ($\bar{z}_l$) and upper ($\bar{z}_u$) 95% confidence intervals were calculated from the $\bar{z}$ value using the equations:

$$\bar{z}_l = \bar{z} - 1.96 \times SE \qquad \textbf{Equation 4-3}$$

$$\bar{z}_u = \bar{z} + 1.96 \times SE \qquad \textbf{Equation 4-4}$$

where SE is the standard error and 1.96 is the approximate *z* score used to calculate 95% confidence intervals[22] and calculated by the equation:

$$SE = \left(\sqrt{\frac{1}{N-3}}\right) \qquad \textbf{Equation 4-5}$$

Finally, $\bar{z}_l$ and $\bar{z}_u$ were converted to upper and lower confidence intervals using Equation 4-2. Overall Fisher transform corrected r values (ρ) for each of the deep (D) and superficial (S) muscles is shown in Table 4-5. In general, good correlation was found between the final predicted EMG waveforms and the enveloped ICs for the deep (D) muscles FPL, EPL, EPB and APL. In general, poor correlation was found for the two superficial (S) muscles FD and ED.

**Table 4-5**: Fisher corrected average r values over all 150 (15 participants x 10 repetitions) comparisons between the predicted EMG and top r ranked ICs for each of the deep (D) and superficial (S) muscles and their corresponding 95% confidence intervals.

| Muscles | Mean r (ρ) | (95% CI) |
|---|---|---|
| FPL (D) | 0.81 | (0.74, 0.86) |
| EPL (D) | 0.88 | (0.84, 0.91) |
| EPB (D) | 0.92 | (0.90, 0.94) |
| APL (D) | 0.83 | (0.77, 0.87) |
| FD (S) | 0.38 | (0.23,0.51) |
| ED (S) | 0.36 | (0.22,0.50) |

A box plot of the r values confirms the high correlation finding since the median value (red horizontal line inside each box) for FPL (D), EPL (D), EPB (D)and APL (D) is above 0.8. It may also be observed that, for the deep muscles, the data outside of the 25$^{th}$ and 75$^{th}$ percentile (upper and lower boundaries of the boxes) is not very widely scattered (shown by the short whiskers for each of the deep muscles). This shows there was consistently high correlation between the final predicted EMG and processed ICs for the deep muscles.

[22] Since 95% of the area under a normal distribution curve is distributed 1.96σ from the mean (Merrill 2013)

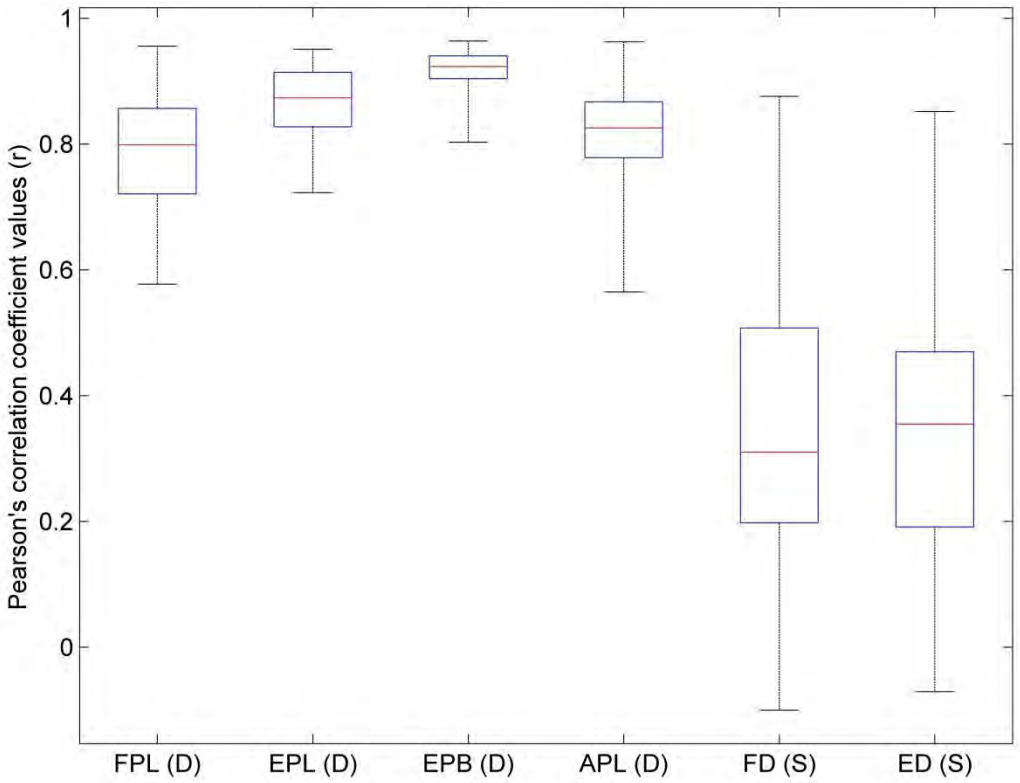


**Figure 4-10**: Box and whisker plot of r values from all 150 (15 participants x 10 repetitions) experimental runs for the deep (D) and superficial (S) muscles.

From Table 4-5, it can be seen that poor correlation was found for FD (S) and ED (S) respectively. The large spread of the r values in Table 4-5 and the long whiskers in Figure 4-10 indicates the correlation was consistently poor across experimental runs.

## 4.4 Statistical analysis results

Linear mixed effects models were individually applied to the accuracy, sensitivity and specificity results from the psASS analysis to find the overall accuracy (and corresponding sensitivity and specificity) from each threshold combination (ThC) (see section 3.5.1 for more details on the psASS analysis methodology). The results of the 'Accuracy' model are presented herein, the results for 'Sensitivity' and 'Specificity' may be found in APPENDIX D.5.

As one of the first steps, the mixed effects model conducted an Analysis of Variance (ANOVA) to determine which variables significantly contributed to each model's output: it calculated the influence of using the 3σ activation threshold for both the *fa* and *pa* on the model (represented as a reference case, Ref), then the effect of the changing ThCs on the model. A summary of the results of the ANOVA for each muscle are shown in Table 4-6. The p-values in the ANOVA section of Table 4-6 are all <0.0001, which implies that the changing ThC had a statistically significant effect on the accuracy for each of the muscles under investigation

**Table 4-6**: Table of results from the ANOVA from the 'Accuracy' model, to determine which variables significantly contribute towards the model output. The ANOVA initially calculated the influence of using the 3σ activation threshold for both *fa* and *pa* on the model (represented as a reference case, Ref), then the effect of the changing ThCs on the model. It can be seen that the p values are <0.0001 for all muscles, implying the changing ThCs have a highly statistically significant effect on the output.

| | **'Accuracy' model ANOVA results** | | | |
|---|---|---|---|---|
| | **numDF** | | **p-value** | |
| **Muscles** | **Ref** | **ThC** | **Ref** | **ThC** |
| **FPL (D)** | 1 | 30 | <0.0001 | <0.0001 |
| **EPL (D)** | 1 | 30 | <0.0001 | <0.0001 |
| **EPB (D)** | 1 | 30 | <0.0001 | <0.0001 |
| **APL (D)** | 1 | 30 | <0.0001 | <0.0001 |
| **FD (S)** | 1 | 30 | <0.0001 | <0.0001 |
| **ED (S)** | 1 | 30 | <0.0001 | <0.0001 |

Overall accuracy values from all the ThCs and their statistical significance (p) are shown in Table 4-7. The first row (3σ) shows the average accuracy for each muscle and across all experimental runs when using the 3σ activation threshold for both *fa* and *pa*. All subsequent rows beneath are difference measures representing the effect on the overall accuracy due to each ThC relative to the 3σ condition's accuracy measure. Peak values for each ThC are highlighted in yellow. Statistically non-significant results (p>0.05) imply that the difference in accuracy as a result of a particular ThC relative to the accuracy due to the 3σ activation threshold for both *fa* and *pa* is not statistically significant. All statistically non-significant ThCs in Table 4-7 are highlighted in grey.

Table 4-7 is interpreted as follows: the overall accuracy for FPL (D) across all participants and experimental runs, when using the 3σ activation threshold for both *fa* and *pa,* is 0.76. When using ThC 1 (*fa* = 1, *pa* = 0.5, see Table 3-4 in section 3.5.1), the overall accuracy of the match between the predicted EMG waveforms and the ICs decreases by 0.22, to 0.54.

**Table 4-7**: Summary of each threshold combination's (ThC) influence on the fixed effect 'Accuracy' for each deep (D) and superficial (S) muscle, relative to using the 3σ activation threshold for both *fa* and *pa* (Ref). Statistically non-significant (p>0.05) results (results for which the difference in accuracy due to a ThC relative to the measure due to the 3σ activation threshold is not statistically significant) are highlighted in grey. The top accuracy results for each muscle are highlighted in yellow.

| | Muscles | | | | | | | | | | | |
|---|---|---|---|---|---|---|---|---|---|---|---|---|
| | FPL (D) | | EPL (D) | | EPLB (D) | | APL (D) | | FD (S) | | ED (S) | |
| | Accuracy | p | Accuracy | p | Accuracy | p | Accuracy | p | Accuracy | p | Accuracy | p |
| 3σ | 0.76 | <0.001 | 0.87 | <0.001 | 0.94 | <0.001 | 0.80 | <0.001 | 0.52 | <0.001 | 0.46 | <0.001 |
| ThC1 | -0.22 | <0.001 | -0.37 | <0.001 | -0.12 | <0.001 | -0.40 | <0.001 | -0.16 | <0.001 | -0.15 | <0.001 |
| ThC2 | -0.20 | <0.001 | -0.29 | <0.001 | -0.05 | <0.001 | -0.37 | <0.001 | -0.16 | <0.001 | -0.15 | <0.001 |
| ThC3 | -0.20 | <0.001 | -0.24 | <0.001 | -0.01 | 0.311 | -0.35 | <0.001 | -0.16 | <0.001 | -0.15 | <0.001 |
| ThC4 | -0.22 | <0.001 | -0.23 | <0.001 | -0.07 | 0.013 | -0.39 | <0.001 | -0.16 | <0.001 | -0.15 | <0.001 |
| ThC5 | -0.29 | 0.001 | -0.23 | <0.001 | -0.11 | 0.017 | -0.51 | <0.001 | -0.16 | <0.001 | -0.15 | <0.001 |
| ThC6 | -0.21 | <0.001 | -0.37 | <0.001 | -0.12 | <0.001 | -0.39 | <0.001 | -0.16 | <0.001 | -0.15 | <0.001 |
| ThC7 | -0.19 | <0.001 | -0.28 | <0.001 | -0.05 | <0.001 | -0.36 | <0.001 | -0.16 | <0.001 | -0.15 | <0.001 |
| ThC8 | -0.19 | <0.001 | -0.23 | <0.001 | -0.01 | 0.311 | -0.33 | <0.001 | -0.16 | <0.001 | -0.15 | <0.001 |
| ThC9 | -0.21 | <0.001 | -0.23 | <0.001 | -0.07 | 0.013 | -0.38 | <0.001 | -0.16 | <0.001 | -0.15 | <0.001 |
| ThC10 | -0.28 | 0.001 | -0.22 | <0.001 | -0.11 | 0.017 | -0.50 | <0.001 | -0.16 | <0.001 | -0.15 | <0.001 |
| ThC11 | -0.18 | <0.001 | -0.35 | <0.001 | -0.12 | <0.001 | -0.36 | <0.001 | -0.15 | <0.001 | -0.14 | <0.001 |
| ThC12 | -0.16 | <0.001 | -0.27 | <0.001 | -0.05 | <0.001 | -0.32 | <0.001 | -0.15 | <0.001 | -0.14 | <0.001 |
| ThC13 | -0.16 | <0.001 | -0.22 | <0.001 | -0.01 | 0.311 | -0.30 | <0.001 | -0.15 | <0.001 | -0.14 | <0.001 |
| ThC14 | -0.18 | <0.001 | -0.21 | <0.001 | -0.07 | 0.013 | -0.34 | <0.001 | -0.15 | <0.001 | -0.14 | <0.001 |
| ThC15 | -0.26 | 0.002 | -0.20 | <0.001 | -0.11 | 0.017 | -0.45 | <0.001 | -0.15 | <0.001 | -0.14 | <0.001 |
| ThC16 | -0.14 | <0.001 | -0.32 | <0.001 | -0.12 | <0.001 | -0.30 | <0.001 | -0.14 | <0.001 | -0.13 | <0.001 |
| ThC17 | -0.12 | <0.001 | -0.24 | <0.001 | -0.05 | <0.001 | -0.27 | <0.001 | -0.14 | <0.001 | -0.13 | <0.001 |
| ThC18 | -0.12 | <0.001 | -0.19 | <0.001 | -0.01 | 0.311 | -0.25 | <0.001 | -0.14 | <0.001 | -0.13 | <0.001 |
| ThC19 | -0.14 | <0.001 | -0.19 | <0.001 | -0.07 | 0.013 | -0.29 | <0.001 | -0.14 | <0.001 | -0.13 | <0.001 |
| ThC20 | -0.23 | 0.005 | -0.18 | 0.001 | -0.11 | 0.017 | -0.37 | <0.001 | -0.14 | <0.001 | -0.13 | <0.001 |
| ThC21 | -0.10 | <0.001 | -0.28 | <0.001 | -0.12 | <0.001 | -0.25 | <0.001 | -0.12 | <0.001 | -0.11 | <0.001 |
| ThC22 | -0.09 | <0.001 | -0.20 | <0.001 | -0.05 | <0.001 | -0.22 | <0.001 | -0.12 | <0.001 | -0.11 | <0.001 |
| ThC23 | -0.09 | <0.001 | -0.15 | <0.001 | -0.01 | 0.311 | -0.20 | <0.001 | -0.12 | <0.001 | -0.11 | <0.001 |
| ThC24 | -0.11 | <0.001 | -0.15 | <0.001 | -0.07 | 0.013 | -0.23 | <0.001 | -0.12 | <0.001 | -0.11 | <0.001 |
| ThC25 | -0.19 | 0.019 | -0.15 | 0.005 | -0.11 | 0.017 | -0.28 | <0.001 | -0.12 | <0.001 | -0.11 | <0.001 |
| ThC26 | -0.08 | <0.001 | -0.24 | <0.001 | -0.12 | <0.001 | -0.19 | <0.001 | -0.10 | <0.001 | -0.08 | 0.002 |
| ThC27 | -0.06 | <0.001 | -0.16 | <0.001 | -0.05 | <0.001 | -0.16 | <0.001 | -0.10 | <0.001 | -0.08 | 0.002 |
| ThC28 | -0.06 | <0.001 | -0.11 | <0.001 | -0.01 | 0.311 | -0.14 | <0.001 | -0.10 | <0.001 | -0.08 | 0.002 |
| ThC29 | -0.08 | <0.001 | -0.11 | <0.001 | -0.07 | 0.013 | -0.18 | <0.001 | -0.10 | <0.001 | -0.08 | 0.002 |
| ThC30 | -0.15 | 0.074 | -0.11 | 0.055 | -0.11 | 0.017 | -0.22 | <0.001 | -0.10 | <0.001 | -0.08 | 0.002 |

For all muscles under investigation, the peak accuracy was found when using the 3σ activation threshold for both *fa* and *pa*. The result implies that changing the *fa* and *pa* levels (over and above an activation threshold of 3σ above a resting baseline level) does not improve the accuracy with

which the ICs match the final predicted EMG waveforms. Similarly, high measures of sensitivity and specificity were found from their respective mixed effects statistical models[23] (shown in Table 4-8) when using the threshold combination corresponding to the peak accuracy measures (3σ for both *fa* and *pa*) for all the muscles under investigation.

**Table 4-8**: Sensitivity and specificity results at the ThC corresponding to the peak Accuracy values are also shown for each of the deep (D) and superficial (S) results. High accuracy, sensitivity and accuracy values were found for FPL (D), EPL (D), EPB (D) and EPB (D) while low values were found for FD (S) and ED (S).

| Muscles | ThC | *pa* | *fa* | Sensitivity (95% CI) | p | Specificity (95% CI) | p |
|---|---|---|---|---|---|---|---|
| FPL (D) | Ref | 3σ | 3σ | 0.88 (0.80, 0.96) | <0.001 | 0.70 (0.63, 0.78) | <0.001 |
| EPL (D) | Ref | 3σ | 3σ | 0.85 (0.78, 0.92) | <0.001 | 0.91 (0.82, 1.00) | <0.001 |
| EPB (D) | Ref | 3σ | 3σ | 0.93 (0.90, 0.97) | <0.001 | 0.94 (0.86, 1.02) | <0.001 |
| APL (D) | Ref | 3σ | 3σ | 0.87 (0.83, 0.92) | <0.001 | 0.87 (0.83, 0.92) | <0.001 |
| FD (S) | Ref | 3σ | 3σ | 0.73 (0.66, 0.79) | <0.001 | 0.48 (0.38, 0.58) | <0.001 |
| ED (S) | Ref | 3σ | 3σ | 0.77 (0.71, 0.83) | <0.001 | 0.41 (0.32, 0.50) | <0.001 |

## 4.5 Overview of results

To summarise the results from the present study (also available in tabular form in Table 4-9):

- Overall correlation values greater than 0.80 were found between the predicted EMG waveforms and top r ranked ICs for all the deep muscles, while overall correlations less than 0.40 were found between the predicted EMG waveforms for FD (S) and ED (S).
- When using an activation threshold of 3σ above a resting baseline level, consistently higher accuracy, sensitivity and specificity measures were found between the predicted EMG waveforms and top r ranked ICs for the deep muscles than for the superficial muscles.

**Table 4-9**: Summary of results for the average correlation ρ, between the ICs and final predicted EMG waveform for the deep (D) and superficial (S) muscles. Overall accuracy, sensitivity and specificity results from the statistical analysis are also shown.

| Muscles | ρ (95% CI) | Accuracy (95% CI) | Sensitivity (95% CI) | Specificity (95% CI) |
|---|---|---|---|---|
| FPL (D) | 0.81 (0.74, 0.86) | 0.76 (0.70, 0.81) | 0.88 (0.80, 0.96) | 0.70 (0.63, 0.78) |
| EPL (D) | 0.88 (0.84, 0.91) | 0.87 (0.83, 0.92) | 0.85 (0.78, 0.92) | 0.91 (0.82, 1.00) |
| EPB (D) | 0.92 (0.90, 0.94) | 0.94 (0.90 ,0.97) | 0.93 (0.90, 0.97) | 0.94 (0.86, 1.02) |
| APL (D) | 0.83 (0.77, 0.87) | 0.80 (0.76 ,0.84) | 0.87 (0.83, 0.92) | 0.87 (0.83, 0.92) |
| FD (S) | 0.38 (0.23,0.51) | 0.52 (0.44 , 0.60) | 0.73 (0.66, 0.79) | 0.48 (0.38, 0.58) |
| ED (S) | 0.36 (0.22,0.50) | 0.47(0.40 , 0.54) | 0.77 (0.71, 0.83) | 0.41 (0.32, 0.50) |

[23] Sensitivity and specificity were modelled as fixed effects using a modified version of the 'Accuracy' model from the psASS analysis. The full accuracy, sensitivity and specificity statistical results may be found in APPENDIX D.5.

[This page is left intentionally blank]

# Chapter 5 Discussion

The first main finding from the present study was the strong correlation (ρ>0.80) between the predicted EMG waveforms modelling the activity of the deep muscles FPL (D), EPL (D), EPB (D) and APL (D) and the ICs derived from the monopolar EMG recordings. The second main finding follows on from the first since the statistical analysis was conducted between each muscle's predicted EMG waveforms and top r ranked ICs. The analysis was indicative of how well the predicted EMG waveforms fitted the ICs selected to represent the activity of the muscles under investigation on a deeper level than the similarity comparison used in the Muscle-IC selection algorithm. The accuracy results from the statistical analysis show that, using an activation threshold of 3σ above a resting baseline level, the final predicted EMG waveforms correctly predicted the time points for FPL (D), EPL (D), EPB (D) and APL (D) as active or inactive more than 77% of the time during the time periods of interest. The sensitivity and specificity results for these muscles show that, during the intervals in which the ICs were predicted to be active or inactive, the predicted EMG waveforms correctly classified the time points as active 85% of the time and correctly classified as inactive 70% of time respectively.

In the case of FD (S) and ED (S), weak correlation (ρ<0.40) was found between the predicted EMG waveforms and the ICs. The accuracy values from the psASS analysis for FD (S) and ED (S) show that, when using an activation threshold of 3σ above a resting baseline level, their final predicted EMG waveforms correctly classified the time points as active or inactive less than 55% of the time over all the time periods of interest. The sensitivity and specificity results show that, during the intervals in which the muscles were predicted to be active or inactive, the predicted EMG waveforms for FD (S) and ED (S) correctly classified the time points as active approximately 75% of the time and correctly classified as inactive less than 50% of the time respectively.

A number of potential factors may have influenced the results of the study and are discussed in section 5.1. The clinical relevance of the study is described in section 5.2.

## 5.1 Potential factors influencing the investigation

Figure 4-3 to Figure 4-6 show that in some instances, the predicted EMG waveforms did not fully account for the activity found in the ICs selected as being representative of the deep muscle activity. Activity un-accounted for in the predicted EMG was one of the main reasons for the reduced correlation between the predicted EMG waveforms and the ICs for each muscle. There were four possible reasons for this mismatch:

1. Incomplete un-mixing of the monopolar EMG signals by fastICA (described in section 5.1.1).
2. Reduced sensitivity of the thumb dynamometer due to modifications of the design from that of (Bourbonnais & Duval 1991) (described in section 5.1.2)
3. The biomechanical model from which the predicted EMG waveforms were derived was inadequate and incorrectly accounted for the activity of the deep muscles during the experimental isometric contractions (described in section 5.1.3).
4. The isometric contractions performed by the participants with the thumb dynamometer and finger load cell did not selectively activate the deep muscles to the extent that their activity could be sufficiently isolated (described in section 5.1.4).

Other factors possibly affecting the investigation include not accounting for strain gauge derived muscle activation when generating the predicted EMG waveforms (described in section 5.1.5); the use of Pearson's correlation coefficient to quantify the match between the ICs and the predicted EMG waveforms (described in section 5.1.6); the electrode locations for detecting activity from FD (S) and ED (S) (described in section 5.1.7 and ) and, finally, the weak signal strength as a result of using isometric index finger flexion and extension rather than mass isometric finger flexion and extension (described in section 5.1.8).

### 5.1.1 Incomplete un-mixing by fastICA

The underlying concept of sdEMG is that monopolar surface EMG measurements from arrays of electrodes encircling a particular part of the body contain potentials from both deep and superficial muscles. During natural movements in which the muscles encircled by the electrodes are known to be active, the monopolar measurements represent a linear mixture of the underlying muscle activity which can be separated by a suitable Blind Source Separation (BSS) algorithm (John 2009). Despite known limitations (described in 1.3.3), ICA was utilised as the BSS algorithm in the present study since favourable results had been found using fastICA in the previous sdEMG studies by Moroaswi & John (2010) and Sayed et al. (2014). sdEMG is not limited to ICA exclusively: another suitable blind source separation technique could be used in a future study to estimate the source activity from the monopolar measurements.

Figure 4-5 show that in some instances, activity was found in the top r ranked ICs for some muscles during isometric contractions for which the muscles are known to not have a role (i.e. FPL (D) during IFEx). The activity attributed to the muscle could also not be accounted for by the strain gauge measurements (shown in Figure 4-6). It was suspected that this unaccounted for activity was due to fastICA failing to completely un-mix the original monopolar EMG recordings and attributing some of the activity from unrelated muscles to the IC in question. The forearm contains many muscles packed into a relatively small volume (see APPENDIX A.2.1 for a description of the anatomy of the forearm). Consequently their small size provides ample opportunity for mixing of the signals. As the name implies, fastICA is a fast and simple ICA algorithm and may not be optimally suited to decomposing the monopolar EMG activity from the deep forearm muscles under investigation. fastICA is one of many different ICA algorithms such as InfoMax, JADE, ICA Projection Pursuit (Bell & Sejnowski 1995; James & Hesse 2005); any one of which may be better suited to separate out the source activity from the muscles under investigation instead of fastICA.

An alternate ICA algorithm, Weights-Adjusted Second Order Blind source Identification (WASOBI) (Tichavský et al. 2006; Tichavsky et al. 2008), was applied to the monopolar EMG data from which the top r ranked ICs in Figure 4-5 were derived to determine whether it would separate the source activity better than fastICA. Slightly better separation was found using WASOBI, however the separation process took approximately 9 minutes for a single experimental run compared to approximately 30 seconds when using fastICA. The top r ranked ICs from this test may be found in APPENDIX A.6.

### 5.1.2 Reduced sensitivity of the thumb dynamometer

It is also possible that the activity found in Figure 4-5 was correctly accounted for by fastICA but the dynamometer was not sensitive enough to detect the applied force, since the design was changed from that of Bourbonnais & Duval (1991) (see section 2.1.1). Determining the effect on the

sensitivity between the two dynamometer designs is difficult since the diameter of the strain gauge instrumented cylinder and the distance between the strain gauges and the load bearing ring from the cage structure dimensions were not provided in Bourbonnais & Duval (1991)'s paper. There are a few instances in which a tube is stronger than a solid rod: for a constant cross sectional area, a cylindrical tube is considerably stronger than a solid rod, due to the force being distributed over a larger area. However, for a constant outer diameter, a solid rod is stronger than a cylindrical tube since there is more material to bear the load (a mathematical proof of these two situations is provided in APPENDIX B.1.1).

Additionally, Bourbonnais & Duval (1991) used strain gauges with a gauge resistance of 350Ω, whereas 120Ω strain gauges were used in the present study. Strain gauges with higher gauge resistance are less susceptible to circuit desensitisation due to increased resistance from long lead wires and have higher signal to noise ratios in the gauge circuit (Micro-Measurements 2010). Using 350Ω strain gauges may have increased the sensitivity of the dynamometer developed in the present study.

### 5.1.3 Biomechanical model for constructing the predicted EMG waveforms

The mismatch highlighted between the predicted EMG waveforms and the ICs in Figure 4-3 and Figure 4-4 may be attributed to incorrect assumptions of the roles of the deep muscles under investigation during the different isometric contractions. The assumptions were first approximations in predicting the extent to which each deep muscle would be active during the different isometric contractions, based on the intramuscular needle EMG measurements of Birdwell et al. (2013), Kaufman et al. (1999) and An et al. (1983). However, intramuscular needle EMG measurements only represent the activity of a small number of MUs in the immediate area surrounding the electrode tip, whereas surface EMG measurements represent an aggregated measure of the activity of the whole muscle. Nevertheless, the needle EMG measurements of Kaufman et al. (1999), Birdwell et al. (2013), An et al. (1983) were the most reliable measurements of the activity of the deep muscles under investigation. Therefore, the intramuscular measurements were utilised for the predicted EMG biomechanical model despite this limitation.

The results of the statistical analysis conducted in the present study suggest that quantifying the extent to which the muscles might be active in the predicted EMG waveforms had very little influence on determining how well the predicted EMG waveforms matched the top r ranked ICs. Instead, it would seem that the detection of IC activity above the 3σ activation threshold (i.e. muscle activation) during the isometric contractions had a greater influence than matching the amplitude of the IC activity with the predicted EMG waveform when determining the accuracy of the fit between the predicted EMG and the ICs. Thus the biomechanical model for constructing the predicted EMG waveform should possibly have taken stronger consideration of the muscle activation when identifying the IC most likely to represent the activity of each deep muscle.

Methods such as needle EMG could be used to experimentally verify the activation and timing of the different muscles under investigation during each of the experimental isometric contractions: if the activity detected by the needle and the surface electrodes is detected simultaneously, it is very likely that the activity originated from the same muscle. However needle EMG is an invasive procedure and the intention behind sdEMG is for the non-invasive measurement of deep and superficial muscle

activity. The use of needle EMG would therefore only be a once-off application in order to better inform the biomechanical model used to construct the predicted EMG waveforms.

### 5.1.4 Inadequate isolation of muscle activity by the isometric contractions

The mismatch highlighted in Figure 4-3 and Figure 4-4 could also indicate that the four thumb and two finger isometric contractions performed with the thumb dynamometer and finger load cell in the present study did not adequately isolate the activity of the muscles under investigation. In contrast, Kaufman et al. (1999)'s investigation into the functional roles of FPL (D), EPL (D) and APL (D) involved eight different thumb isometric contractions (TFl, TEx, TAb, TAd and combinations thereof) to gauge each muscle's contribution during different isometric thumb contractions. The number of isometric contractions in the present study was limited to 6 due to two main reasons:

1. The physical memory capabilities of the recording PC constrained the length of each experimental run to ~65s. In this time period, the LabVIEW® acquisition programme held the samples from 40 monopolar EMG channels and 3 strain gauge channels acquired simultaneously at 1 kHz in a software buffer before saving the data to the recording PC. The handling of such a large amount of data placed considerable strain on the recording PC and it was found that the LabVIEW® data acquisition programme missed an unacceptably high number of samples during experimental runs that ran longer than 65s. The time taken for each isometric contraction and rest period could have been shortened to accommodate more isometric contractions; however it was found that not all participants were able to completely relax their forearm muscles during the 5s rest period. Incorporating more isometric contractions for shorter time periods would also increase the complexity of the experiment for the participant since the order in which each isometric contraction is presented is randomized.
2. The isometric contractions in the present study were chosen such that the forces applied to the thumb dynamometer would be mapped to separate force measurement directions. The reasons for doing so was to ensure the least number of muscles were active during each isometric contraction: isometric contractions such TFl/TAb involves the muscles from both isometric contractions being active simultaneously. The present study actively sought to avoid co-activation of the muscles under investigation and simplify the predicted EMG waveforms by utilising established isometric thumb contractions for the experiment.

A greater variety of isometric contractions to better isolate the activity of the different muscles should be investigated in a future study.

### 5.1.5 Not accounting for strain gauge derived muscle activation when generating the predicted EMG waveforms

The similarly timed activity found in some of the top r ranked ICs and the corresponding strain gauge measurements (highlighted in Figure 4-4 and Figure 4-5 in section 4.2.2) suggest that the strain gauge measurements could be used to inform the predicted EMG waveforms of muscle activation when the participants did not solely apply forces in the required directions. In these instances, the participants did not perform the required isometric contraction correctly and activated muscles which were expected to be inactive during the required isometric contraction. The biomechanical model used for generating the predicted EMG waveforms in the present study was largely static and only changed to suit each experimental run's randomized isometric contraction sequence.

Consequently, muscle activation as a result of the participants not performing the movement correctly was not accounted for by the biomechanical model.

Informing the predicted EMG waveforms with the strain gauge measurements was not performed in the present study because the primary purposes of the thumb dynamometer and finger load cell were to provide real-time feedback on whether the participant performed the isometric contractions correctly. Deriving the timing information of the isometric contractions from the strain gauge measurements was considered a secondary requirement to ensure the predicted EMG waveforms were accurately timed representations of the original EMG activity. Future studies should investigate accounting for unanticipated IC activity as a result of participants not performing the isometric contractions correctly as a means of reducing the mismatch between the predicted EMG and ICs.

### 5.1.6 Pearson's correlation coefficient for correlating the predicted EMG to the ICs

Pearson's Correlation Coefficient appears to place greater importance upon matching the IC with the *fa* and *pa* values of the predicted EMG (amplitude matching between the IC and the predicted EMG) than when activity and inactivity was predicted (muscle activation timing). For example, it can be seen in Figure 3-17 in section 3.4.3 that there is less activity during IFEx in IC31 and IC9 than in the current highest ranked IC (IC29), yet both IC31 and IC9 are ranked lower than IC29. If the comparison was based upon the presence of muscle activity and inactivity, then IC31 and IC9 appear to be better matches. Thus an alternative metric which places greater importance on the muscle timing would be more appropriate for quantifying the match between the predicted EMG and the ICs in a future study.

### 5.1.7 Electrode placement for FD (S) and ED (S)

The bipolar measurements shown in Figure 4-9 highlight the importance of electrode placement for detecting the activity of FD (S) and ED (S). The choice of location for the electrode rings in the current study was based on encircling the largest possible volume in which all the muscles under investigation would be found, because the distribution of the potentials from the deep muscles on the surface of the skin was unknown. The number of electrodes was limited to 40 in accordance with the principles applied in the previous sdEMG studies of Moroaswi & John (2010) and Sayed et al. (2014), to ensure that approximately twice as many electrodes as muscles (19) were used so that the electrodes could be placed on either side of the motor end plate of the muscles under investigation (see 1.3.4 for description of previous sdEMG studies). Since the muscles in the forearm are small and tightly packed into a relatively small space, the electrodes were arranged into two bands of 20 electrodes each to account for the different anatomical positions of the muscles (and their corresponding motor end plates) from as many locations on the skin as possible.

The standard method of acquiring superficial muscle surface activity is the use of a bipolar electrode pair with optimised placement to avoid inclusion of the innervation zone. However, the option of locating the innervation zones for measuring deep muscle surface activity is not available. When a pair of sdEMG electrodes is superimposed on the standard bipolar locations for measuring superficial muscle activity, the preliminary results of Moroaswi & John (2010) indicate that sdEMG may be used to derive the bipolar waveforms through the subtraction of monopolar measurements from the superimposed electrode pair. The preliminary results of Moroaswi & John (2010) also

indicate that, for large superficial muscles, small deviations in electrode positions from the standard bipolar locations provide equivalent bipolar waveforms. For the small muscles of the forearm, it is apparent from the present study, that the placement of the sdEMG electrodes is more critical for detecting superficial muscle activity. However, electrode placement was not as critical for the deep muscles, which may be attributed to the electrical properties of the volume conductor and the corresponding lower voltage spatial resolution on the skin surface.

In such cases where the detection of superficial muscle activity is affected by small deviations in electrode location, it is recommended that either an independent bipolar pair be used for detecting the superficial muscle activity; or careful placement of the sdEMG electrode rings be implemented to ensure superimposition of (at least) two monopolar electrodes on the corresponding bipolar locations.

### 5.1.8 Index finger flexion vs mass finger flexion

As mentioned in section 4.3, considerably less bipolar EMG activity was found during isometric flexion of the index finger in isolation than during isometric flexion of all four fingers together. FD (S) is a muscle with multiple insertion points, with tendons responsible for the movement of each of the four fingers (see APPENDIX A.3.2 for a description of the anatomy of FD). The decrease in activity suggests that the use of a single finger isometric contraction may have been an under-simplification of FD's (S) activity and that better results may have been obtained using isometric mass finger flexion.

## 5.2 Clinical relevance of study

The findings of the present study indicate that this is the first non-invasive EMG identification of the activity of FPL (D), EPL (D), EPB (D) and APL (D). The statistical results suggest that the application of sdEMG may have potential in detecting movement intention from the deep extrinsic thumb muscles.

While established methods exist for detecting superficial muscle activity, sdEMG should be able to replicate the functionality of these methods. However, the results from the present study indicate that, in order to detect the superficial muscle activity, greater care must be taken to ensure that the electrode rings are placed in such a way that (at least) two electrodes are placed in the optimum positions to detect superficial muscle activity, as in a standard bipolar sEMG configuration.

[This page is left intentionally blank]

# Chapter 6 Conclusions and recommendations for future work

An algorithm was developed to construct predicted EMG waveforms for the deep muscles FPL (D), EPL (D), EPB (D) and APL (D) during randomized sequences of isometric TFl, TEx, TAb and TAd. An IC-selection algorithm was developed to identify ICs most likely to represent the activity of FPL (D), EPL (D), EPB (D) and APL (D) using the predicted EMG waveforms derived for each of the deep muscles during the randomized isometric contraction sequences. The IC-identification algorithm found strong correlations between the predicted EMG waveforms and the ICs for each of the deep muscles. The statistical analysis found that the ICs considered to represent the activity of each of the deep extrinsic thumb muscles were highly accurate, sensitive and specific matches with their predicted EMG waveforms.

The application of sdEMG for the detection of activity from the superficial muscles FD (S) and ED (S) suggests that the electrode location should be more carefully considered in future studies. The findings of the current study were limited by a number of factors (described in greater detail in section 6.1). Recommendations for improvements of the current study are provided in section 6.2

## 6.1 Limitations of study

### 6.1.1 Investigation into healthy participants

The participant population used in the present study constituted a narrow demographic since the objective was to investigate the feasibility of the sdEMG technique for detecting activity from selected deep muscles in the forearm. A small sample of 15 young, healthy, right handed male participants was chosen since it was assumed that male participants would generally have larger muscles (in contrast to female participants) with good muscle definition and control since the measurements were taken from the dominant hand. It is important in future studies to investigate the efficacy of forearm sdEMG to detect deep muscle EMG from the muscles under investigation in participants outside of this sample if it is be applied in a clinical environment.

### 6.1.2 Contraction protocol

As mentioned in section 1.3.3, the standardisation of the isometric contractions to a fixed effort level of 30% MVC, for each isometric contraction, was done to ensure that the EMG signals were statistically independent in order for fastICA to separate the monopolar EMG recordings. The probability density function (PDF) of a typical monopolar EMG recording from the present study was calculated and found to be very peaked, in accordance with the study by Nazarpour et al., (2013) (the PDF plot of the signal may be found in APPENDIX A.5).

It is also known that the characteristics of isometric and dynamic EMG measurements are different due to the movement of the muscles relative to the electrodes (Burden 2010; De Luca 1997). The lack of movement of the sources relative to the sensors during measurement of the signals is a crucial assumption of ICA (Naik & Kumar 2011), thus it is important to investigate whether dynamic movements would violate this assumption.

Currently, it is not known at what point fastICA ceases to be a suitable algorithm for separating monopolar EMG signals from the forearm for higher MVC levels or during different muscle contraction strategies such as concentric or eccentric loading.

### 6.1.3 Phase correction of recorded EMG data

As mentioned in section 2.3.4, the EMG amplifiers developed for testing the research objectives introduced frequency phase distortion effects into the monopolar EMG signals during the amplification process. A phase distortion of $150^{o}$ to $-180^{o}$ was introduced over a frequency range of 1-500Hz (shown in Figure 2-20), resulting in an equivalent time delay of approximately 0.5s at 1Hz to 0.001s at 500 Hz.

Phase correction was not applied to the monopolar EMG waveforms; however it could potentially have an effect on the decomposition of the monopolar EMG by fastICA. Calhoun et al. (2003) found that the introduction of small delays (~1.5s) into simulated functional Magnetic Resonance Imaging (fMRI) data decreases ICA's source separation accuracy, while bigger delays (~4s) resulted in some signals being split into 2 separate sources by the ICA algorithm, InfoMax (Bell & Sejnowski 1995). The equivalent time delays introduced by the phase shift from the amplification process in the present study were well within these limits and were therefore considered to have a negligible effect on the separation accuracy of the sources by fastICA. In future applications of forearm sdEMG it is necessary to be aware of the phase distortion effects of the recording equipment, to ensure that the equivalent time delay effects are below that of Calhoun et al. (2003)

## 6.2 Recommendations for future work

Based on the limitations and factors affecting the results, a number of different aspects of the current application of sdEMG to the forearm may be improved or should be investigated further in future studies:

- The use of alternative ICA algorithms should also be investigated to determine whether the separation of the monopolar EMG from the forearm would be improved.
- Validation of the current study should investigate the development of a more suitable biomechanical model of muscle activation and timing for each muscle's predicted EMG. In particular, the investigation should incorporate needle EMG measurements in a once-off application to build a better model of muscle activation for the predicted EMG waveforms.
- A study utilising a wider variety of isometric contractions should be conducted to determine whether the activity of the muscles under investigation can be more adequately isolated.
- A study incorporating strain-derived muscle activation information into the predicted EMG model to account for participants not performing the isometric contractions properly should be conducted to determine whether the mismatch between the predicted EMG waveforms and ICs may be reduced.
- An alternate metric (other than Pearson's Correlation Coefficient) for quantifying the correlation between the ICs and the predicted EMG should be investigated so that the muscle activation timing may be incorporated into the similarity measurement for the IC selection.
- A study investigating the optimal locations of the electrode rings to detect activity from both deep and superficial muscles should be conducted to determine the robustness and suitability of forearm sdEMG to applications involving deep and superficial muscle activation.
- A future study using muscle contraction strategies other than isometric contractions and at higher MVC effort levels should be conducted to determine at what point fastICA ceases to be a suitable BSS separation algorithm for sdEMG.

- Future investigations using forearm sdEMG to detect activity from FD (S) and ED (S) should implement isometric mass finger flexion rather than index finger flexion.
- The applicability of forearm sdEMG to participants outside the study sample group, particularly for stroke patients or amputees, should be investigated to determine in which clinical environments sdEMG may be applied.

[This page is left intentionally blank]

# References


An, K.N. et al., 1983. Determination of forces in extensor pollicis longus and flexor pollicis longus of the thumb. *American Physiology Society*, 54(3), pp.714–719.

Asghari Oskoei, M. & Hu, H., 2007. Myoelectric control systems-A survey. *Biomedical Signal Processing and Control*, 2(4), pp.275–294.

Basmajian, J. V, 1974. *Muscles Alive: their function revealed by electromyography* 3rd ed., Baltimore: Waverley Press, Inc.

Bell, a J. & Sejnowski, T.J., 1995. An information-maximization approach to blind separation and blind deconvolution. *Neural computation*, 7(6), pp.1129–59. Available at: http://www.ncbi.nlm.nih.gov/pubmed/7584893.

Bio-medical Instruments, 2015. ELEFIX Conductive EEG Paste. Available at: http://bio-medical.com/products/elefix-conductive-eeg-paste-6-oz-tube.html#product_tabs_more_info_tabbed [Accessed May 31, 2015].

Birdwell, J.A. et al., 2013. Activation of individual extrinsic thumb muscles and compartments of extrinsic finger muscles. *Journal of neurophysiology*, 110(6), pp.1385–92. Available at: http://www.ncbi.nlm.nih.gov/pubmed/23803329 [Accessed November 11, 2013].

Blank, A. a. et al., 2014. Current Trends in Robot-Assisted Upper-Limb Stroke Rehabilitation: Promoting Patient Engagement in Therapy. *Current Physical Medicine and Rehabilitation Reports*. Available at: http://link.springer.com/10.1007/s40141-014-0056-z [Accessed July 1, 2014].

Blok, J.H., Stegeman, D.F. & Van Oosterom, a., 2002. Three-layer volume conductor model and software package for applications in surface electromyography. *Annals of Biomedical Engineering*, 30, pp.566–577.

Bourbonnais, D. & Duval, P., 1991. Static dynamometer for the measurement of multidirectional forces exerted by the thumb. *Medical & biological engineering & computing*, 29, pp.413–418.

Burden, A., 2010. How should we normalize electromyograms obtained from healthy participants? What we have learned from over 25years of research. *Journal of Electromyography and Kinesiology*, 20(6), pp.1023–1035. Available at: http://dx.doi.org/10.1016/j.jelekin.2010.07.004.

Calhoun, V.D. et al., 2003. Latency (in)sensitive ICA: Group independent component analysis of fMRI data in the temporal frequency domain. *NeuroImage*, 20(3), pp.1661–1669.

Cooney, W.P. et al., 1981. The kinesiology of the thumb trapeziometacarpal joint. *Journal of Bone and Joint Surgery*, 63-A(9), pp.1371–1381.

Danzl, M.M. et al., 2012. Facilitating neurorehabilitation through principles of engagement. *Journal of Allied Health*, 41(1), pp.35–41. Available at: http://www.ncbi.nlm.nih.gov/pubmed/22544406.

Delorme, A., Sejnowski, T.J. & Makeig, S., 2007. Enhanced detection of artifacts in EEG data using higher-order statistics and independent component analysis. *Neuroimaging*, 34(4), pp.1443–1449.

Dimitrov, G. V. & Dimitrova, N. a., 1998. Precise and fast calculation of the motor unit potentials detected by a point and rectangular plate electrode. *Medical Engineering and Physics*, 20(5), pp.374–381.

Djuwari, D. et al., 2006. Limitations and Applications of ICA for Surface Electromyogram. *Electromyography and clinical neurophysiology*, 46(5), pp.295–309. Available at: http://europepmc.org/abstract/MED/17059103.

Djuwari, D., Kant Kumar, D. & Palaniswami, M., 2005. Limitations of ICA for Artefact Removal. In *Conference proceedings : 27th Annual International Conference of the IEEE Engineering in Medicine and Biology Society. IEEE Engineering in Medicine and Biology Society. Conference*. Shanghai, China: IEEE, pp. 4685–8. Available at: http://www.ncbi.nlm.nih.gov/pubmed/17281286.

eFunda, 2015. Aluminum Alloy AA 1060. Available at: http://www.efunda.com/materials/alloys/aluminum/show_aluminum.cfm?ID=AA_1060&prop=all&Page_Title=AA 1060 [Accessed January 12, 2015].

Farina, D. et al., 2004. Surface EMG crosstalk evaluated from experimental recordings and simulated signals. *Methods of Information in Medicine*, 43(1), pp.30–35.

Farina, D., Cescon, C. & Merletti, R., 2002. Influence of anatomical, physical, and detection-system parameters on surface EMG. *Biological cybernetics*, 86, pp.445–456.

Gävert, H. et al., 2005. fastica. Available at: http://www.cis.hut.fi/projects/ica/fastica/.

Gilroy, A., MacPherson, B. & Ross, L., 2008. *Atlas of Anatomy* Internatio., Stuttgart, New York: Thieme.

Gopura, R. a R.C. et al., 2013. Recent Trends in EMG-Based Control Methods for Assistive Robots. In *Electrodiagnosis in the New Frontiers of Clinical Research*. InTech. Available at: http://dx.doi.org/10.5772/56174.

Gorsuch, R. & Lehmann, C., 2010. Correlation Coefficients: Mean Bias and Confidence Interval Distortions. *Journal of Methods and Measurement in the Social Sciences*, 1(2), pp.52–65. Available at: https://journals.uair.arizona.edu/index.php/jmmss/article/download/114/118.

Griffiths, D. et al., 2002. OpenEENG design documentation. Available at: http://openeeg.sourceforge.net/doc/modeeg/modeeg_design.html.

Guyton, A. & Hall, J., 2006. *Textbook of medical physiology* 11th ed., Elsevier.

Guyton, A. & Hall, J., 2011. Textbook of Medical Physiology. In *Textbook of Medical Physiology*. Philadelphia, PA: Saunders/Elsevier, pp. 71–82.

Hearn, E., 2005. *Mechanics of materials* 2nd ed., Oxford, UK: Butterworth Heinman.

Hermens, H.J. et al., 2000. Development of recommendations for SEMG sensors and sensor placement procedures. *Journal of Electromyography and Kinesiology*, 10(5), pp.361–374. Available at: http://linkinghub.elsevier.com/retrieve/pii/S1050641100000274.

Hermens, H.J. et al., 1999. European Recommendations for Surface ElectroMyoGraphy. In *SENIAM 8*. pp. 8–11. Available at: http://www.seniam.org/pdf/contents8.PDF.

Hislop, H.J. & Montgomery, J., 2007. *Daniels and Worthington's Muscle Testing: Techniques of Manual Examination* 8th ed., St Louis, Missouri: Saunders-Elsevier.

Ho, N.S.K. et al., 2011. An EMG-driven exoskeleton hand robotic training device on chronic stroke subjects: task training system for stroke rehabilitation. In *IEEE ... International Conference on Rehabilitation Robotics : [proceedings]*. p. 5975340. Available at: http://www.ncbi.nlm.nih.gov/pubmed/22275545.

Hollister, A. & Giurintano, D.J., 1995. Thumb Movements, Motions, and Moments. *Journal of Hand Therapy*, 8(2), pp.106–114. Available at: http://linkinghub.elsevier.com/retrieve/pii/S0894113012803073 [Accessed May 14, 2014].

Hyvärinen, a & Oja, E., 2000. Independent component analysis: algorithms and applications. *Neural networks : the official journal of the International Neural Network Society*, 13(4-5), pp.411–30. Available at: http://www.ncbi.nlm.nih.gov/pubmed/10946390.

Hyvärinen, A. & Oja, E., 1997. A Fast Fixed Point Algorithm for Independent Component Analysis. *Neural Computation*, 9(7), pp.1483–1492. Available at: http://www.mitpressjournals.org.ezproxy.uct.ac.za/doi/abs/10.1162/neco.1997.9.7.1483#.VGJ1E8mnWKI.

Inc., T.B., 2015. i-limb-ultra. Available at: http://www.touchbionics.com/products/active-prostheses/i-limb-ultra [Accessed May 25, 2015].

Instruments, N., 2012. LabVIEW 2012.

James, C.J. & Hesse, C.W., 2005. Independent component analysis for biomedical signals. *Physiological Measurement*, 26(1), pp.R15–R39. Available at: http://stacks.iop.org/0967-3334/26/i=1/a=R02?key=crossref.50acc70869a7c789b1bc0e0bdc83648d [Accessed June 3, 2014].

John, L.R., 2009. NON-INVASIVE DEEP MUSCLE ELECTROMYOGRAPHY. , pp.1–7. Available at: http://www.faqs.org/patents/app/20120184838.

Johnston, J.A., Bobich, L.R. & Santello, M., 2011. Coordination of intrinsic and extrinsic hand muscle activity as a function of wrist joint angle during two digit grasping. *Neuroscience letters*, 474(2), pp.104–108.

Jones, D., Round, J. & de Haan, A., 2004. *Skeletal Muscle from Molecules to Movement: A textbook of Muscle Physiology for Sport, Exercise, Physiotherapy and Medicine* 1st ed., London: Elsevier Science.

Jung, T. et al., 2000. Removing electroencephalographic artifacts by blind source separation. *Psychophysiology*, 37(98-9), pp.163–178.

Jung, T.-P. et al., 2000. Independent component analysis of biomedical signals. In *Proceedings if the 2nd International Workshop on Independent Component Analysis and Blind Source Separation*. pp. 633–644. Available at: internal-pdf:/JUNG_ica_of_biomed_signals_WORKSHOP_ICA_SIGNAL_SEPARATION_2000.pdf.

Kaufman, K.R. et al., 1999. In-vivo function of the thumb muscles. *Clinical biomechanics*, 14(2), pp.141–50. Available at: http://www.ncbi.nlm.nih.gov/pubmed/10619102.

Kleim, J.A. & Jones, T.A., 2008. Principles of experience-dependent neural plasticity: implications for rehabilitation after brain damage. *Journal of speech, language, and hearing research : JSLHR*, 51(1), pp.S225–39. Available at: http://www.ncbi.nlm.nih.gov/pubmed/18230848.

Kline, T., Kamper, D. & Schmit, B., 2005. Control system for pneumatically controlled glove to assist in grasp activities. In *Proceedings of the 2005 IEEE 9th International Conference on Rehabilitation Robotics*. Chicago, Illinois: IEEE, pp. 78–81.

Konrad, P., 2005. *The ABC of EMG: A practical introduction to Kinesiological Electromyography* 1st ed., Noraxon INC. Available at: http://www.google.com/url?sa=t&rct=j&q=&esrc=s&source=web&cd=1&ved=0CB4QFjAAahUKEwiV7c-SuoTGAhVHQBQKHSzoAPI&url=http://www.noraxon.com/?smd_process_download=1&download_id=4277&ei=MdN3VdWQNseAUazQg5AP&usg=AFQjCNGuk2IfJuVoXxFu20Sa-RM2MY6vyw&sig2=JosgKCxXW5g.

Krebs, H.I. et al., 2000. Increasing productivity and quality of care: Robot-aided neuro-rehabilitation. *Journal Of Rehabilitation Research And Development*, 37(6), pp.639–652.

Krebs, H.I. et al., 2003. Rehabilitation Robotics : Performance-Based Progressive Robot-Assisted Therapy. *Autonomous Robots*, 15, pp.7–20.

Krupinski, J., Secades, J. & Shiraliyeva, R.K., 2014. Towards Effective Neurorehabilitation for Stroke Patients. *International Journal of Physical Medicine & Rehabilitation*, 02(02). Available at: http://www.omicsonline.org/open-access/towards-effective-neurorehabilitation-for-stroke-patients-2329-9096.1000183.php?aid=24884 [Accessed April 30, 2014].

Langlois, D., Chartier, S. & Gosselin, D., 2010. An Introduction to Independent Component Analysis : InfoMax and FastICA algorithms. *Tutorial in Quantitative Methods for Psychology*, 6(1), pp.31–38.

Li, Z.-M. et al., 2008. Complex, multidimensional thumb movements generated by individual extrinsic muscles. *Journal of orthopaedic research : official publication of the Orthopaedic Research Society*, 26(9), pp.1289–95. Available at: http://www.ncbi.nlm.nih.gov/pubmed/18404721 [Accessed October 1, 2014].

Lin, H.-T. et al., 2011. The three-dimensional analysis of three thumb joints coordination in activities of daily living. *Clinical biomechanics (Bristol, Avon)*, 26(4), pp.371–6. Available at: http://www.ncbi.nlm.nih.gov/pubmed/21146265 [Accessed October 1, 2014].

De Luca, C.J., 1997. The Use of Surface Electromyography in Biomechanics. *Journal of applied biomechanics*, 13, pp.135–163.

Maciejasz, P. et al., 2014. A survey on robotic devices for upper limb rehabilitation. *Journal of neuroengineering and rehabilitation*, 11(1), p.3. Available at: http://www.ncbi.nlm.nih.gov/pubmed/24401110 [Accessed January 21, 2014].

Makeig, S. et al., 1996. Independent Component Analysis of Electroencephalographic data. In D. Touretzky, M. Mozer, & M. Hasselmo, eds. *Advances in Neural Information Processsing Systems*. Cambridge, Massachusetts: MIT Press, pp. 145–151.

Marchal-Crespo, L. & Reinkensmeyer, D.J., 2009. Review of control strategies for robotic movement training after neurologic injury. *Journal of neuroengineering and rehabilitation*, 6(20). Available at: http://www.pubmedcentral.nih.gov/articlerender.fcgi?artid=2710333&tool=pmcentrez&rendertype=abstract [Accessed May 25, 2014].

MathWorks, T., 2008. MATLAB 2008a.

Measurements, M., 2010. Precision strain gauges. Available at: http://www.google.com/url?sa=t&rct=j&q=&esrc=s&source=web&cd=4&ved=0CDIQFjAD&url=http://www3.nd.edu/~pdunn/www.ame250/straingage.pdf&ei=eiprVcmjEofHsQTUlIO4Bg&usg=AFQjCNGw5nusS1F1zEfWjbbf6UC3DfHInw&sig2=kjpTo805_6vws5rhuJuHFw&bvm=bv.94455598,d.cWc.

Merletti, R., 1999. *Standards for Reporting EMG Data*, Torino, Italy.

Merletti, R., Holobar, A. & Farina, D., 2008. Analysis of motor units with high-density surface electromyography. *Journal of electromyography and kinesiology : official journal of the International Society of Electrophysiological Kinesiology*, 18(6), pp.879–90. Available at: http://www.ncbi.nlm.nih.gov/pubmed/19004645 [Accessed May 15, 2014].

Merletti, R. & Parker, P., 2004. *Electromyography: Physiology, Engineering and Noninvasive Applications*, Hoboken, New Jersey: John Wiley and Sons.

Merril, D. et al., 2013. Development of an implantable myoelectric sensor for advanced prosthesis control. *Artificial Organs*, 35(3), pp.249–252.

Merrill, R.M., 2013. *Fundamentals of Epidemiology and Biostatistics: Combining the basics* 1st ed., Boston: Jones and Bartlett Learning.

Moroaswi, S. & John, L.R., 2010. *The measurement of deep muscle activity using surface Electromyography (unpublished results)*. Cape Town: University of Cape Town.

Mulligan, S.R., John, L.R. & Verrinder, R., 2014. *A Comparison of ICA versus Genetic Algorithm Optimized ICA for use in non-invasive muscle tissue EMG*. University of Cape Town.

Naik, G.R. et al., 2006. Limitations and applications of ICA for surface electromyogram. In *Conference proceedings : ... Annual International Conference of the IEEE Engineering in Medicine and Biology Society. IEEE Engineering in Medicine and Biology Society. Conference*. New York City, New York, pp. 5739–42. Available at: http://www.ncbi.nlm.nih.gov/pubmed/17946718.

Naik, G.R. & Kumar, D.K., 2011. Estimation of independent and dependent components of non-invasive EMG using fast ICA : validation in recognising complex gestures. *Computer Methods in*

*Biomechanics and Biomedical Engineering*, 14(12), pp.1105–1111. Available at: http://dx.doi.org/10.1080/10255842.2010.515211.

Naik, G.R. & Kumar, D.K., 2012. Identification of hand and finger movements using multi run ICA of surface electromyogram. *Journal of medical systems*, 36(2), pp.841–51. Available at: http://www.ncbi.nlm.nih.gov/pubmed/20703649 [Accessed July 9, 2013].

Nakamura, H. et al., 2004. The application of independent component analysis to the multi-channel surface electromyographic signals for separation of motor unit action potential trains: part II-modelling interpretation. *Journal of electromyography and kinesiology : official journal of the International Society of Electrophysiological Kinesiology*, 14(4), pp.433–41. Available at: http://www.ncbi.nlm.nih.gov/pubmed/15165593 [Accessed June 14, 2014].

Nazarpour, K. et al., 2013. A note on the probability distribution function of the surface electromyogram signal. *Brain research bulletin*, 90, pp.88–91. Available at: http://www.pubmedcentral.nih.gov/articlerender.fcgi?artid=3878385&tool=pmcentrez&rendertype=abstract [Accessed June 5, 2014].

Ockenfeld, C. et al., 2013. Fine finger motor skill training with exoskeleton robotic hand in chronic stroke: Stroke rehabilitation. In *IEEE ... International Conference on Rehabilitation Robotics : [proceedings]*. pp. 1–4. Available at: http://www.ncbi.nlm.nih.gov/pubmed/24187211.

Pinheiro, J. et al., 2014. Linear and Nonlinear Mixed Effects Models. Available at: http://cran.r-project.org/package=nlme.

R Core Team, 2014. R: A language and environment for statistical computing. Available at: http://www.r-project.org/.

Richards, L. et al., 2008. Driving motor recovery after stroke. *Topics in stroke rehabilitation*, 15(5), pp.397–411. Available at: http://www.ncbi.nlm.nih.gov/pubmed/19008201 [Accessed December 11, 2013].

Roeleveld, K., Stegeman, D.F., Vingerhoets, H.M., et al., 1997. Motor unit potential contribution to surface electromyography. *Acta physiologica Scandinavica*, 160, pp.175–183.

Roeleveld, K., Stegeman, D.F. & Vingerhoets, H.M., 1997. The motor unit potential distribution over the skin surface and its use in estimating the motor unit location. *Acta Physiologica Scandenavia*, 161, pp.465–472.

Sayed, A. et al., 2014. The use of surface electromyography (sEMG) to non-invasively measure electrical activity from a deep calf muscle (Tibialis Posterior). In *XX Congress of the International Society for Electrophysiology and Kinesiology (ISEK 2014), 15-18 July 2014*. Rome, Italy.

Shen, D. & Lu, Z., 2006. Computation of Correlation Coefficient and Its Confidence Interval. In *Proceedings of the Thirty-first Annual SAS Users Group International Conference.* San Francisco, California: SAS Institute Inc., pp. 1–6.

Stegeman, D.F. & Hermens, H.J., 1999. Standards for surface electromyography : the European project " Surface EMG for non-invasive assessment of muscles ( SENIAM )." , pp.108–112.

Stone, J. V., 2004. *Independant Component Analysis: A Tutorial Introduction*, Cambridge, Massachusetts: MIT-Press.

Theanatomist, 2008. theanatomist. *Wordpress Blog*. Available at: http://theanatomist.wordpress.com/2008/11/06/who-died/ [Accessed October 17, 2012].

Tichavsky, P. et al., 2008. A hybrid technique for blind separation of non-Gaussian and time-correlated sources using a multicomponent approach. *IEEE Transactions on Neural Networks*, 19(3), pp.421–430.

Tichavský, P. et al., 2006. Blind signal separation by combining two ICA algorithms: HOS-based EFICA and time structure-based WASOBI. *European Signal Processing Conference*.

Tong, K.Y. et al., 2010. An intention driven hand functions task training robotic system. In *Conference proceedings : ... Annual International Conference of the IEEE Engineering in Medicine and Biology Society. IEEE Engineering in Medicine and Biology Society. Conference*. Beunos Aires, Argentina: IEEE, pp. 3406–9. Available at: http://www.ncbi.nlm.nih.gov/pubmed/21097247.

UFI, 2013. MODEL 1089 MK III CHECKTRODE USER MANUAL. , pp.3–6.

Warraich, Z. & Kleim, J. a, 2010. Neural plasticity: the biological substrate for neurorehabilitation. *PM & R : the journal of injury, function, and rehabilitation*, 2(12 Suppl 2), pp.S208–19. Available at: http://www.ncbi.nlm.nih.gov/pubmed/21172683 [Accessed May 24, 2014].

Wege, A. & Zimmermann, A., 2007. Electromyography sensor based control for a hand exoskeleton. In *2007 IEEE International Conference on Robotics and Biomimetics (ROBIO)*. Sanya, China: IEE, pp. 1470–1475.

Westlake, K.P. & Byl, N.N., 2013. Neural plasticity and implications for hand rehabilitation after neurological insult. *Journal of Hand Therapy*, 26(3), pp.87–93. Available at: http://www.ncbi.nlm.nih.gov/pubmed/23391829 [Accessed February 7, 2013].

Winter, B., 2013. Linear models and linear mixed effects models in R with linguistic applications. Available at: http://arxiv.org/pdf/1308.5499.pdf.

Winter, D., 2005. *Biomechanics and motor control of human movement* 3rd ed., Hoboken, New Jersey: John Wiley and Sons.

World Medical Association, 2013. World Medical Association Declaration of Helsinki: ethical principles for medical research involving human subjects. *JAMA : the journal of the American Medical Association*, 310(20), pp.2191–4. Available at: http://www.ncbi.nlm.nih.gov/pubmed/24141714.

# APPENDIX A Additional background data

APPENDIX A provides additional background information regarding the biophysics of EMG signal generation (section A.1); pre-study development of the isometric contraction sequence used in the present study and description of the anatomy of the forearm (section A.2.2); additional sdEMG data not presented in the main body of this dissertation (section A.4); an analysis of the statistical independence of the monopolar EMG signals(section A.5); and a brief investigation into using an alternate ICA algorithm for separating the monopolar EMG data instead of fastICA (section A.6).

## A.1 EMG signal generation biophysics

The description of the biophysics of EMG signal generation presented herein is drawn from the *ABC of EMG* (Konrad 2005) and the *Textbook of Medical Physiology* (Guyton & Hall 2011). Additional sources have been cited where applicable.

Figure A-1 shows the structure of skeletal muscle. Essentially, skeletal muscle tissue is made up of many muscle fibres (C) bundled together into fasciculi (B) which in turn make up the skeletal muscle (A). Each muscle fibre is innervated by a single nerve ending, located near the middle of the muscle fibre, known as the motor end plate. Each muscle fibre is made up of many myofibrils (D) which act together under the direction of the motor nerve linked to each muscle fibre.

Under normal resting conditions (with the muscle at rest and not contracting), ion pumps in the muscle fibre membrane maintain a resting state potential of -80mV between the interior and exterior of the muscle fibre. The arrival of a neuronal action potential (from the central nervous system or from a monosynaptic reflex) at the motor end plate results in the release of the neurotransmitter, acetylcholine, into the synaptic cleft at the motor end plate. Acetylcholine-gated ion channels open in the muscle fibre membrane in response to this neurotransmitter and (positively charged) sodium ions flow to the interior of the muscle membrane. The influx of ions creates a local depolarization zone in the muscle membrane and initiates an action potential. After a certain threshold depolarisation level is achieved (shown in Figure A-2), an action potential is elicited in the muscle fibre (characterised by a rapid monopolar electrical burst up from -30mV to +30mV). This depolarization is immediately restored by the reverse exchange of sodium ions by the ion pumps (Repolarization). This is followed by a post-hyperpolarization period as the ion pumps work to restore the resting state potential.

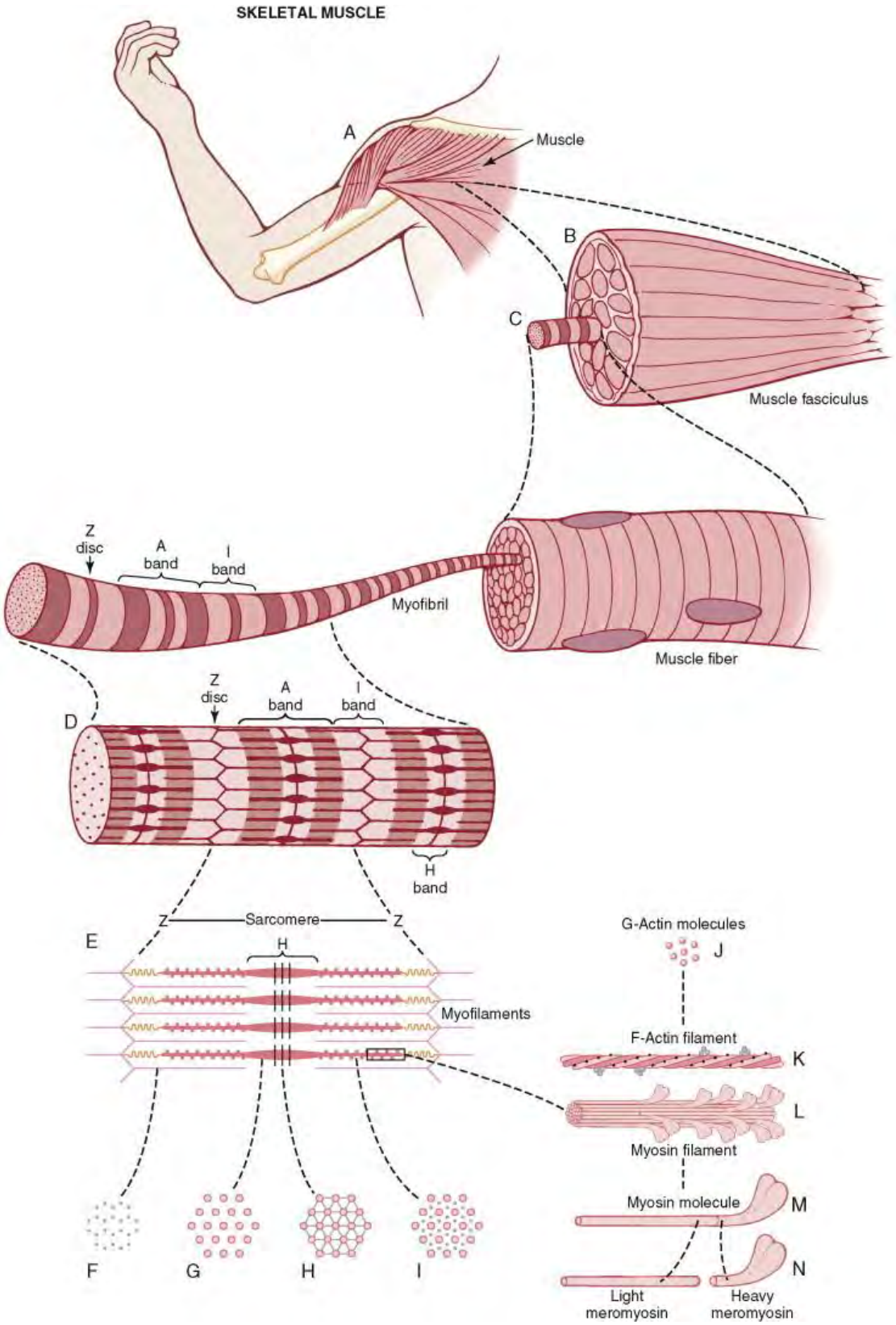


**Figure A-1**: Structure of a single myofibril (D), the smallest subunit of a muscle fibre (C). Muscle fibres are bundled together to form fasciculi (B) within the larger context of all skeletal muscles (A). Myofibrils contain filaments known as actin (K) and myosin (L), which are the primary contractile elements with the myofibril. Image from (Guyton & Hall 2006).

The muscle fibre action potential propagates axially in both directions, away from the motor end plate, toward the tendons. The travelling action potential causes the sarcoplasmic reticulum (shown in Figure A-3) to generously release calcium ions into the intra-cellular space. The calcium ions induce the attractive forces of actin and myosin filaments (the contractile components within the muscle fibre, shown in Figure A-1), causing the muscle fibre to contract. The calcium ions are pumped back into the sarcoplasmic reticulum immediately afterwards and the contraction ceases until the arrival of the next neuronal action potential at the motor end plate.

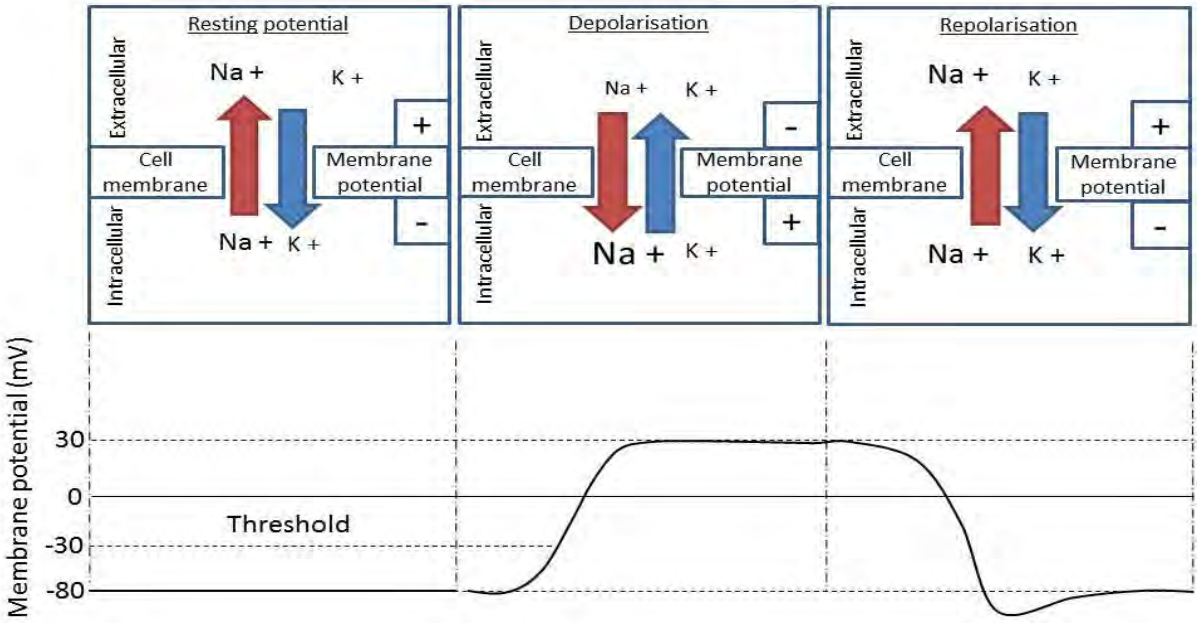


**Figure A-2:** Schematic of the depolarization/ repolarization cycle of the muscle fibre membrane (top) and of the cell potential during cycle (bottom). Adapted and modified from (Konrad 2005)

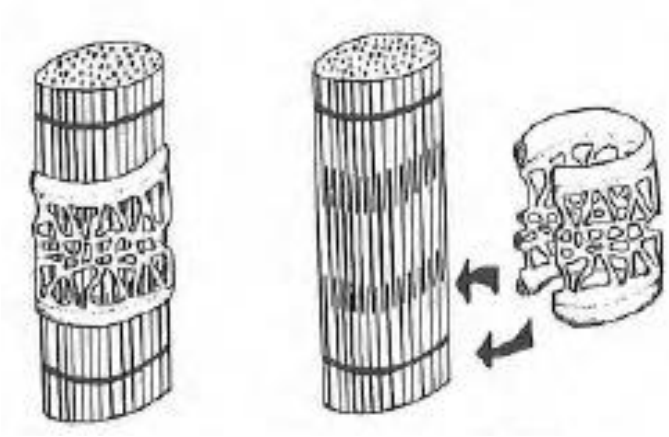

**Figure A-3:** The sarcoplasmic reticulum lies between and envelopes each myofibril within a muscle fibre

EMG activity measured by intramuscular or surface electrodes thus represents the repolarization and depolarization cycles of the muscle fibres.

## A.2 Isometric contraction sequence development

The isometric contractions used in the present study were chosen after conducting a preliminary 'peep over the hedge test' to determine whether sdEMG could be applied to the forearm (whether the technique would even work). The applicability of sdEMG for identification of forearm deep muscle activity in the present study was in doubt since the forearm contains many more muscles than the prior sdEMG investigations of Moroaswi & John (2010) and Sayed et al. (2014).

The general anatomy of the forearm had to be investigated to identify the deep forearm muscles and their corresponding movements in which the deep muscles might be selectively activated (described in section A.2.1). The preliminary 'peep over the hedge' test is then described in section A.2.2

### A.2.1 Anatomy of the forearm

The forearm contains a total of 19 muscles, in an anterior compartment and a posterior compartment. The anterior compartment contains most of the flexors (muscles responsible for flexion of the wrist and fingers) and the posterior compartment contains most of the extensors (muscles responsible for extension of the wrist and fingers). Within both the anterior and posterior compartments, the muscles may be further subdivided into superficial and deep muscles (Gilroy et al. 2008), shown in Figure A-4 and Figure A-5 respectively.

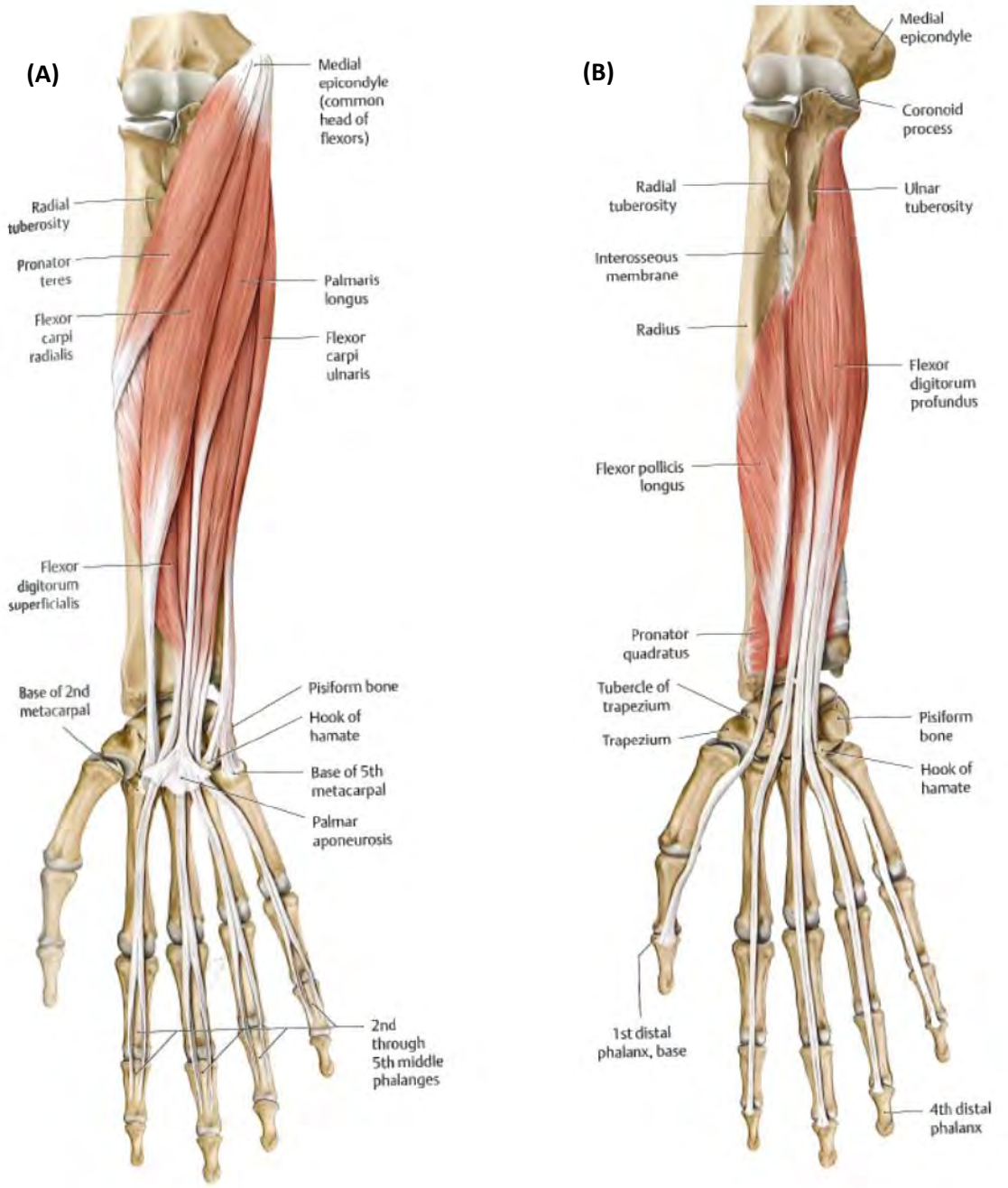


**Figure A-4**: Superficial (A) and deep (B) muscles of the anterior compartment of the forearm. Image from (Gilroy et al. 2008)

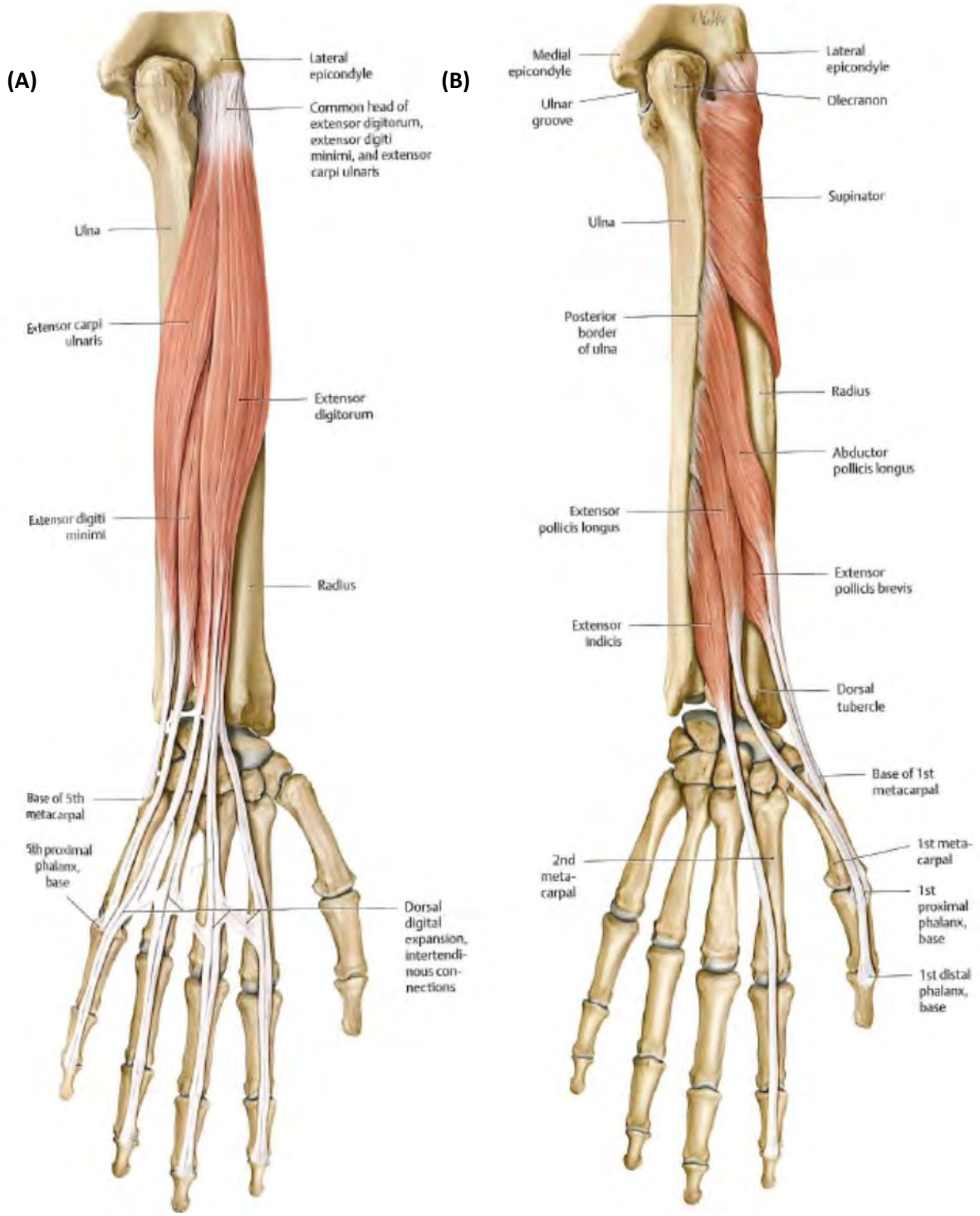


**Figure A-5**: Superficial (A) and deep (B) muscles of the posterior compartment of the forearm. Image from (Gilroy et al. 2008).

As a result of the large number of muscles in the forearm, many different movements of the wrist and hand are possible. A summary of the different natural hand and wrist movements and the corresponding forearm muscles active during each of the muscles is shown in Table A-1.

**Table A-1**: Muscles active during natural movements of the hand and wrist based on clinical muscle weakness tests (Hislop & Montgomery 2007). MP = metacarpophalangeal joint, IP = interphalangeal joint, DIP = distal interphalangeal joint, PIP = proximal interphalangeal joint. The deep forearm muscles are highlighted in yellow. The ++ symbol represents the primary function of the muscle, + represents the secondary function.

| | | **Movement** | | | | | | | | | | |
|---|---|---|---|---|---|---|---|---|---|---|---|---|
| | | Forearm supination | Forearm pronation | Wrist flexion | Wrist extension | Finger PIP flexion | Finger DIP flexion | Index finger extension | Thumb IP flexion | Thumb MP extension | Thumb IP extension | Thumb abduction |
| **Anterior compartment** | Pronator teres | | ++ | | | | | | | | | |
| | Flexor carpi radialis | | + | ++ | | | | | | | | |
| | Palmaris longus | | | + | | | | | | | | + |
| | Flexor carpi ulnaris | | | ++ | | | | | | | | |
| | Flexor digitorum superficialis | | | + | | ++ | | | | | | |
| | **Flexor digitorum profundus** | | | + | | ++ | ++ | | | | | |
| | **Flexor pollicis longus** | | | + | | | | | ++ | | | |
| | **Pronator quadratus** | | ++ | | | | | | | | | |
| **Posterior compartment** | Brachioradialis | + | | | | | | | | | | |
| | Extensor carpi radialis longus | | | | ++ | | | | | | | |
| | Extensor carpi radialis brevis | | | | ++ | | | | | | | |
| | Extensor digitorum | | | | + | | | ++ | | | | |
| | Extensor digiti minimi | | | | + | | | | | | | |
| | Extensor carpi ulnaris | | | | ++ | | | | | | | |
| | **Supinator** | ++ | | | | | | | | | | |
| | **Abductor pollicis longus** | | | **+** | | | | | | | | **++** |
| | **Extensor pollicis brevis** | | | | | | | | | ++ | | + |
| | **Extensor pollicis longus** | | | | | | | | | | ++ | |
| | **Extensor indicis** | | | | **+** | | | **++** | | | | |

### A.2.2 Pre-experimental testing

The literature investigation into the anatomy of the forearm indicated that sdEMG might be able to detect activity from the deep thumb muscles (Flexor Pollicis Longus, Abductor Pollicis Longus, Extensor Pollicis Longus and Extensor Pollicis Brevis) because, from Table A-1, it seemed that these muscles could be selectively activated during relatively easily (since there did not seem to be many other muscles involved during those movements).

Thus the 'peep over the hedge' test targeted the deep forearm muscles involved in various thumb movements. The test was conducted using a reduced set of 20 electrodes and a fixed dynamic movement sequence of Thumb Extension, Thumb Abduction, combination Thumb Extension/Thumb Abduction shown in Table A-2. Each movement was sustained for 3 seconds. The electrodes were placed in two bands of 10 electrodes each on the proximal and distal thirds of the forearm.

**Table A-2:** Movements used in the preliminary test. Images from Theanatomist (2008)

| **Movement** | |
|---|---|
| Thumb Extension | 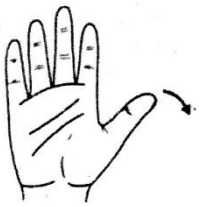 |
| Thumb Abduction | 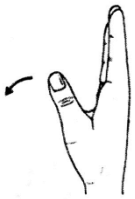 |
| Thumb Extension/Abduction | 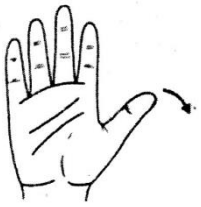 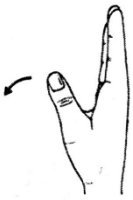 |
| Finger Flexion |  |
| Finger Extension | 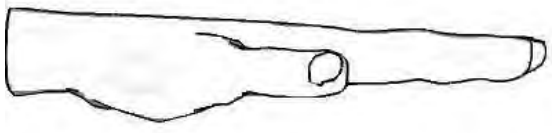 |

Qualitative examination of the ICs derived from the monopolar EMG recordings showed that activity was found during thumb extension and not during thumb abduction (highlighted by red and green ellipses in Figure A-6).

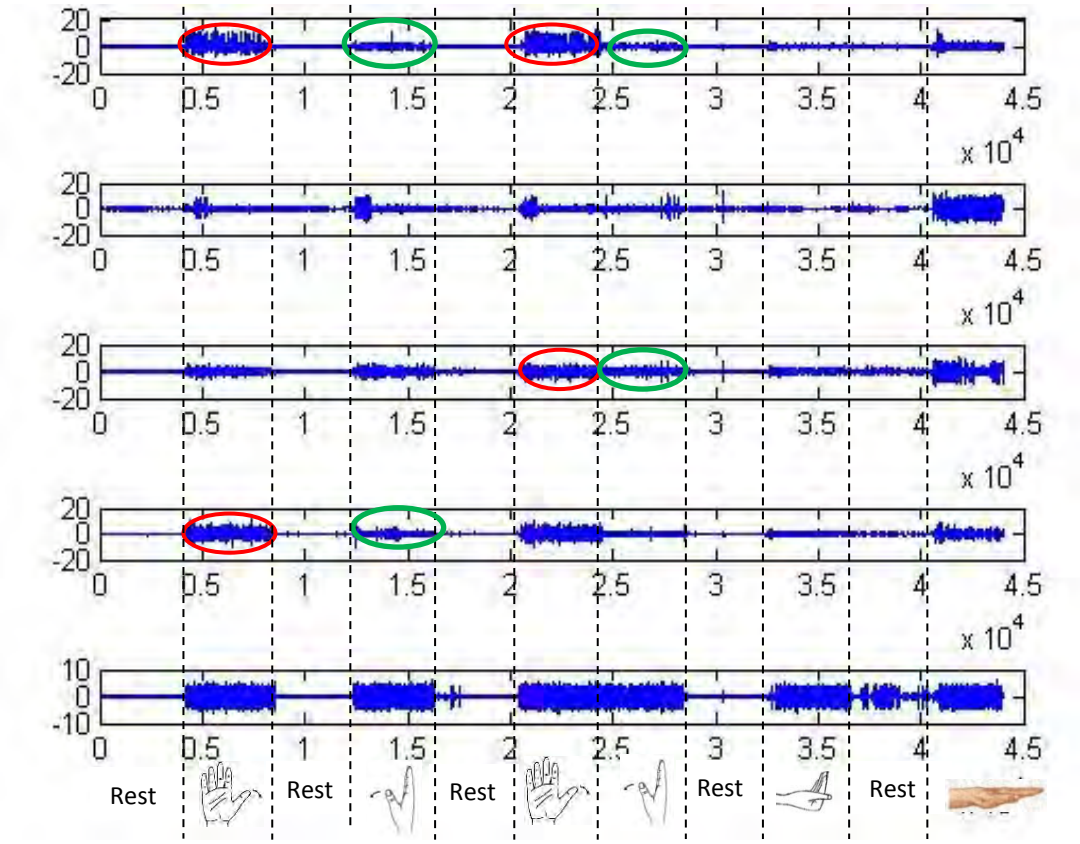


**Figure A-6**: Selected IC waveforms from preliminary 'peep over the hedge' test. Hand movement images from (Theanatomist 2008)

## A.3 Anatomy of the thumb

On the basis of the preliminary 'peep over the hedge' test (described in section A.2.2), the decision was made to target the deep forearm muscles involved in thumb movements for the application of sdEMG to the forearm in the present study. A cross sectional view of the forearm with the muscles under investigation highlighted is shown in Figure A-7.

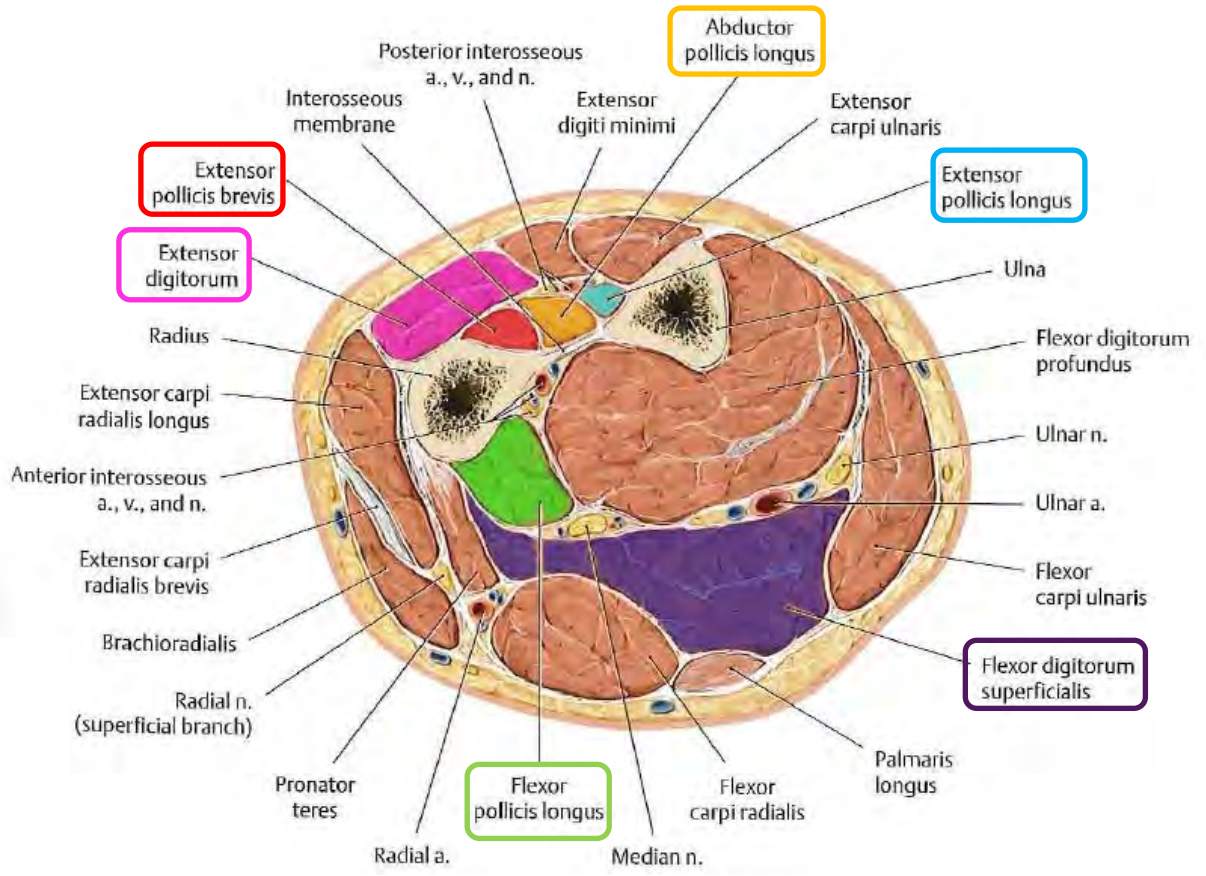


**Figure A-7:** Cross-sectional view of the forearm with muscles under investigation highlighted according to the labelling convention used in Figure A-8 and Figure A-12. Image adapted from Gilroy et al. (2008)

### A.3.1 Deep thumb muscles

The human thumb is an exceptionally mobile structure and a crucial component of many different hand gestures, such as a power grip, key pinch and lateral pinch grip (Lin et al. 2011). The musculature of the thumb may be broadly separated into extrinsic and intrinsic groups (Gilroy et al. 2008). The extrinsic group refers to muscles located in the forearm (shown in Figure A-8), whereas intrinsic group (shown in Figure A-9) refers to the muscles located in the hand. Since the extrinsic thumb muscles Flexor Pollicis Longus (FPL), Extensor Pollicis Longus (EPL), Extensor Pollicis Brevis (EPB) and Abductor Pollicis Longus (APL) were of interest for the present study, their anatomical positions are shown and highlighted in Figure A-8.

.

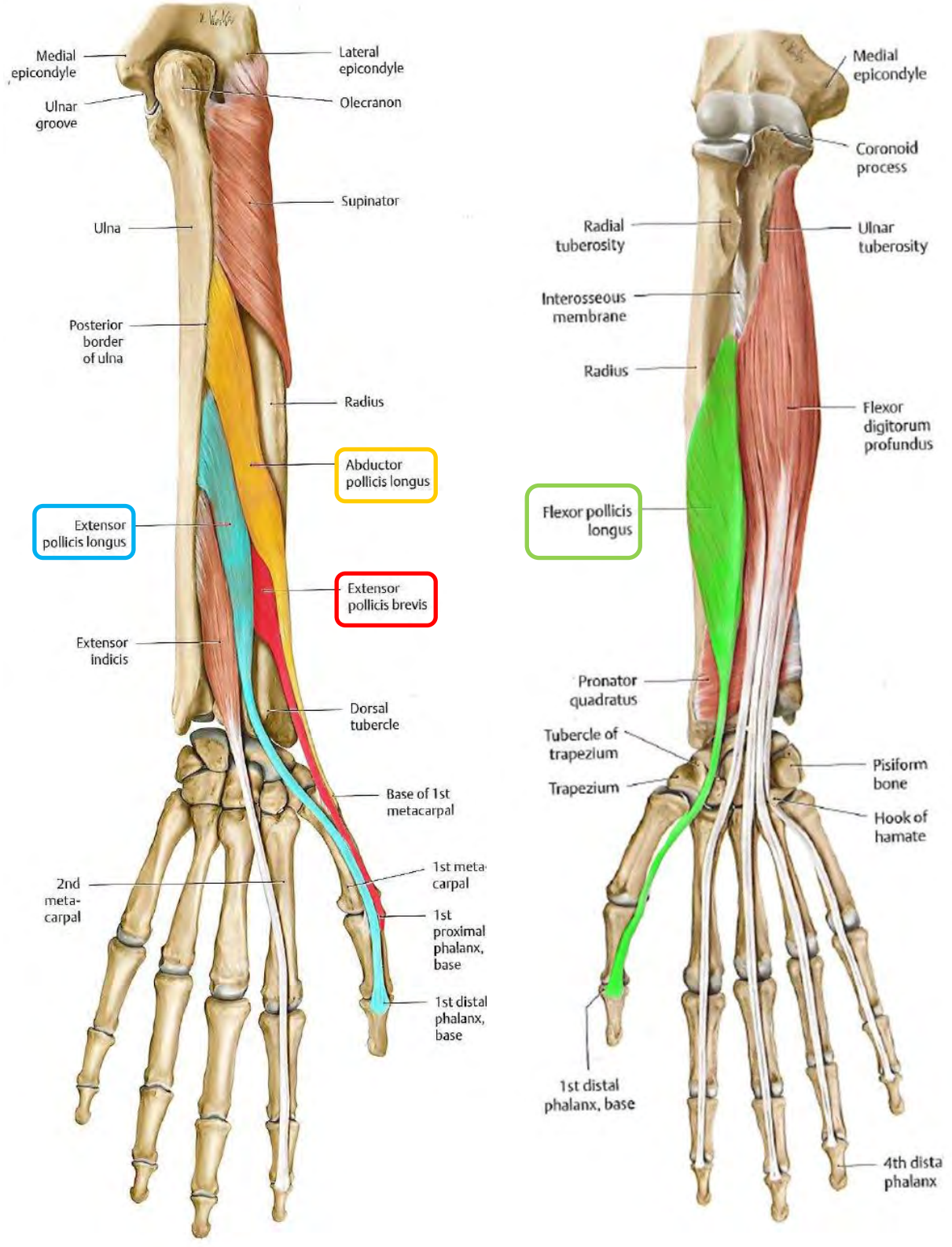


**Figure A-8**: Anatomic positions of the deep (D) muscles Flexor Pollicis Longus (FPL, green), Extensor Pollicis Longus (EPL, turquoise), Extensor Pollicis Brevis (EPB, red) and Abductor Pollicis Longus (APL, yellow). Images adapted from (Gilroy et al. 2008)

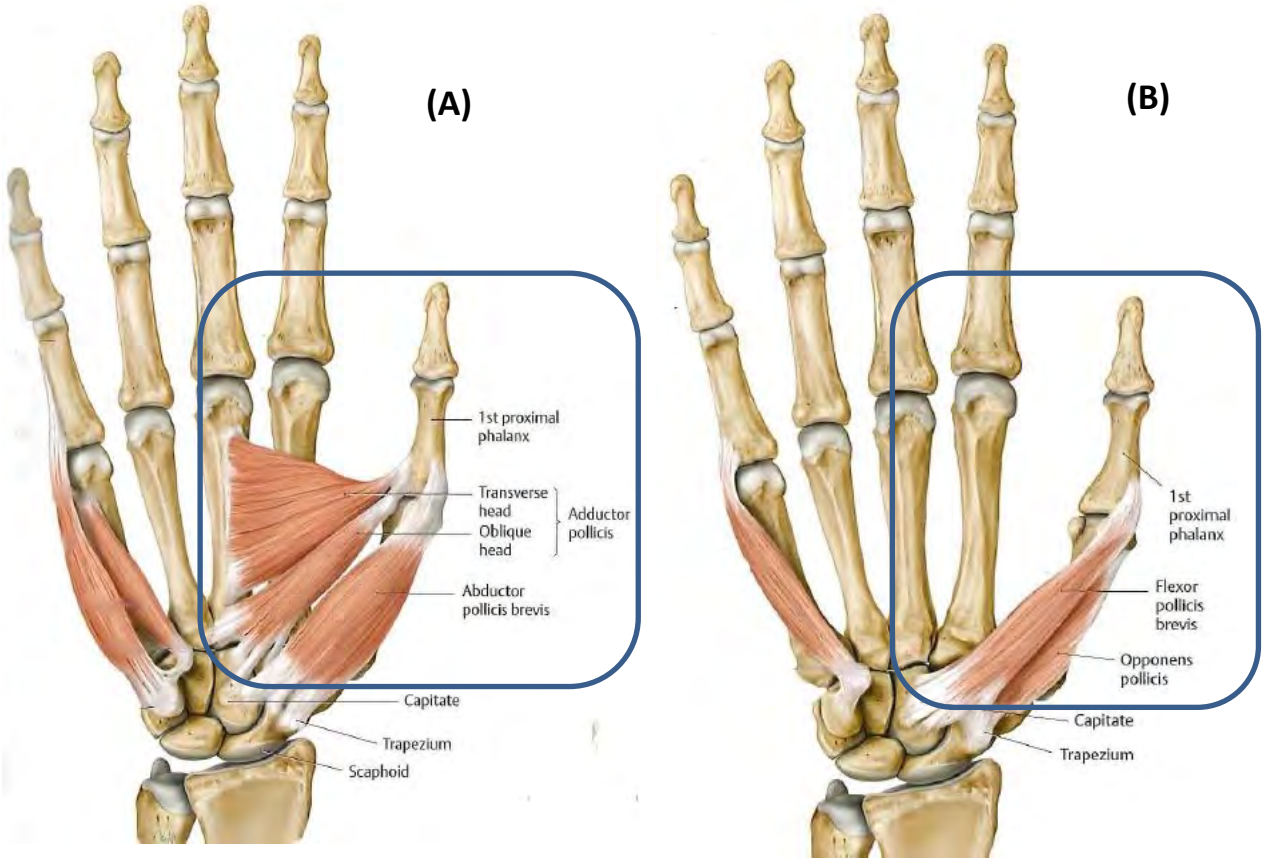


**Figure A-9**: Intrinsic muscles of the thumb (within the blue box). Image (A) shows Abductor Pollicis Brevis and the two heads of Adductor Pollicis with Flexor Pollicis Brevis and Opponens Pollicis removed. Image (B) is the inverse of A, in that Flexor Pollicis Brevis and Opponens Pollicis are shown, with Abductor Pollicis Brevis and Adductor Pollicis removed. Images from (Gilroy et al. 2008)

The thumb consists of three main articulating joints (shown in Figure A-10):

1. The carpometacarpal (CMC) joint between the trapezium in the carpus and the first metacarpal.
2. The metacarpophalangeal (MCP) joint between the first metacarpal and the proximal phalange
3. One interphalangeal (IP) joint between the proximal and distal phalanges.

The articular surfaces of the thumb's CMC and MCP joints allow the thumb to move in complicated combinations of flexion/extension, abduction/ adduction, and pronation/ supination (Cooney et al. 1981). A good representation of the complicated nature of these movements was made by Hollister & Giurintano (1995) by considering the movement axes of these joints as offset hinges (shown in Figure A-11). As a result of the complex musculature and unique articular surfaces of the CMC and MCP joints, the individual roles of each of the deep extrinsic thumb muscles are not clear cut during the different isometric contractions. In reality there is a large degree of synergy between the different muscles, making role identifications for each muscle particularly difficult. A summary of the origin, insertion points and principal actions in which the four deep extrinsic muscles are most widely recognised to be active are presented in Table A-3.

Table A-3: Origin, insertion and actions of the deep extrinsic muscles FPL, EPL, EPB and APL. MCP = metacarpophalangeal, IP = interphalangeal, CMC = carpometacarpal. Table adapted from (Gilroy et al. 2008).

| Muscle | Origin | Insertion | Action |
|---|---|---|---|
| Flexor Pollicis Longus (FPL) | Mid-anterior surface of Radius and adjacent interosseous membrane | Palmar surface of distal phalanx of thumb | Flexion of the thumb's MCP and IP joints |
| Abductor Pollicis Longus (APL) | Dorsal surfaces of radius and ulna | Base of 1st metacarpal | Abduction of the thumb's CMC joint |
| Extensor Pollicis Longus (EPL) | Posterior surface of ulna and interosseous membrane | Base of distal phalanx of thumb | Adduction of the thumb's CMC joint. Extension of the thumb's MCP and IP joint |
| Extensor Pollicis Brevis (EPB) | Posterior surface of radius and interosseous membrane | Base of proximal phalanx of thumb | Extension of the CMC and MCP joint |

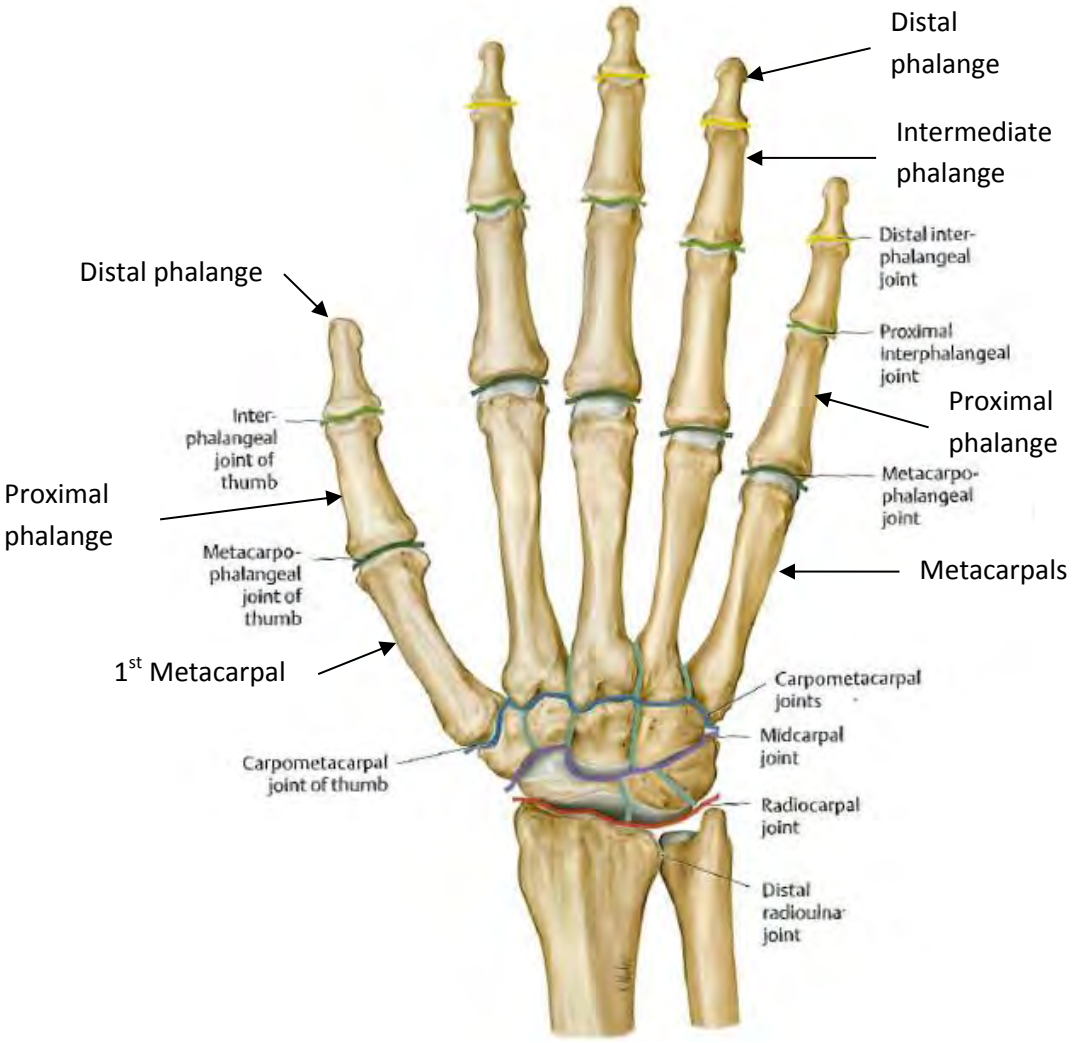


**Figure A-10:** Carpometacarpal (CMC), metacarpophalangeal (MCP) and Interphalangeal (IP) joints of the thumb. The proximal and distal phalanges and 1st metacarpal are also labelled. Image from (Gilroy et al. 2008)

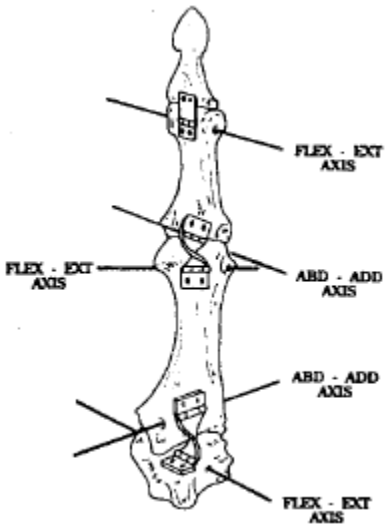


**Figure A-11**: Axes of rotation of the CMC, MCP and IP joints of the thumb. Image from (Hollister & Giurintano 1995)

### A.3.2 Superficial muscles

As mentioned in section 1.4.4, the application of sdEMG to detect the activity from the superficial muscles FD and ED were considered as methodological objectives to test sdEMG's ability to detect superficial muscle activity. The anatomical positions of FD[23] (S) and ED (S) are shown in Figure A-12. The primary function of FD (S) is for flexion of the MCP, PIP and DIP joints (shown in Figure A-10) of the four fingers, while ED (S) is responsible for extension of the same joints. A summary of the origin, insertion and action of FD (S) and ED (S) are shown in Table A-4.

**Table A-4**: Origin, insertion and action of the superficial muscle FD ad ED. MCP = metacarpophalangeal, PIP = proximal interphalangeal, DIP = distal interphalangeal.

| Muscle | Origin | Insertion | Action |
|---|---|---|---|
| Flexor Digitorum (FD) | Medial epicondyle and coronoid process of humerus | Sides of intermediate phalanges of the four fingers | Flexion of the MCP,PIP and DIP joints of the fingers[24] |
| Extensor Digitorum (ED) | Lateral epicondyle of humerus | Base of distal phalanges of the four fingers | Extension of MCP, PIP and DIP joints of the four fingers |

[24] Technically, flexion of the MCP and PIP joints of the four fingers is performed by Flexor Digitorum Superficialis and flexion of the MCP, PIP and DIP joints of the four fingers is performed by Flexor Digitorum Profundus (Gilroy et al. 2008). However, in the present study it was assumed that Flexor Digitorum Superficialis and Profundus acted together since the finger load cell was designed for isometric index finger flexion around the PIP joint, which is under the action of both these muscles.

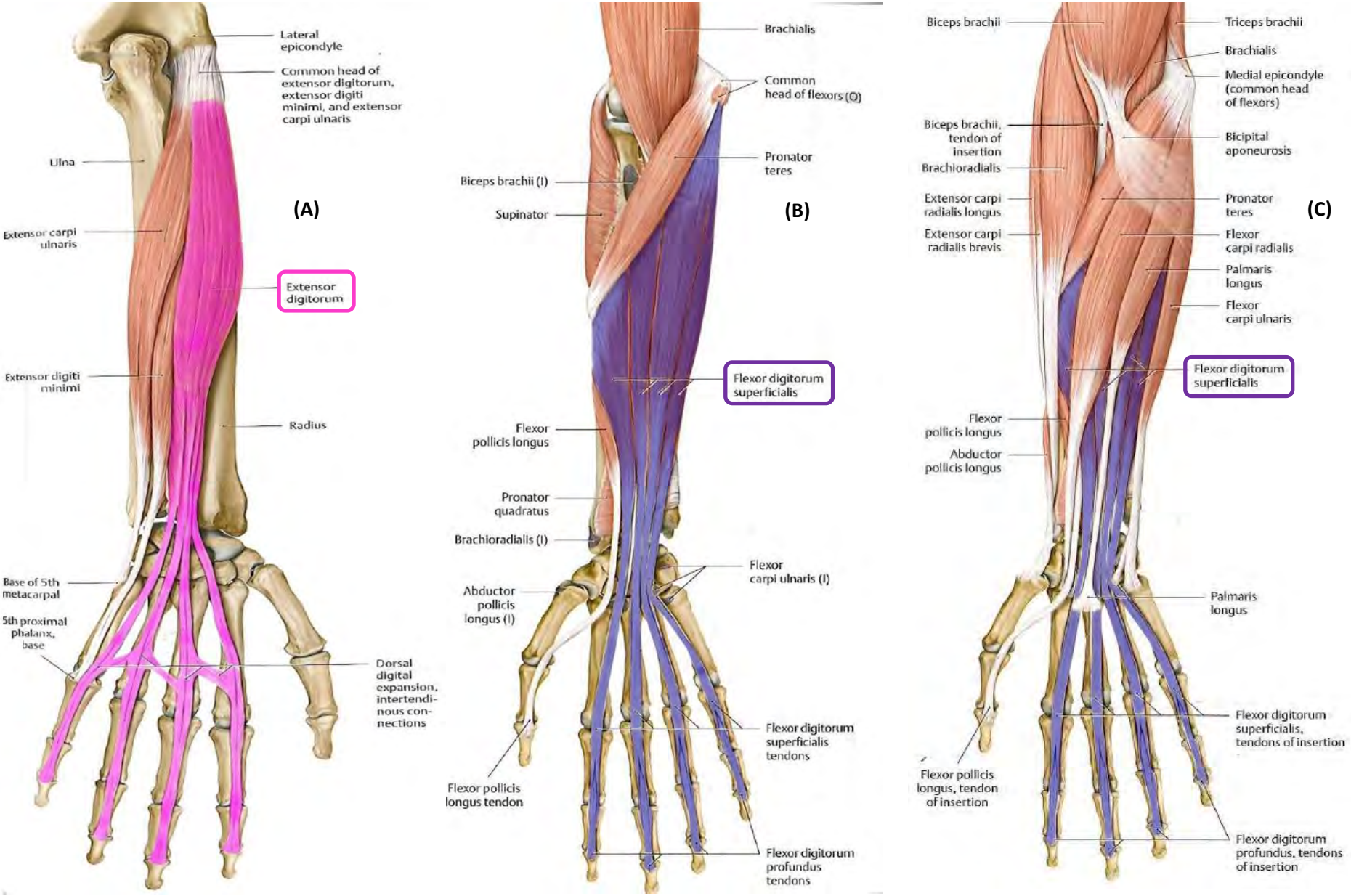


**Figure A-12**: Anatomical locations of the superficial muscles ED (Image A) and FD[23] (images B and C). Images adapted from (Gilroy et al. 2008)

## A.4 Best and worst top r ranked ICs

Due to space limitations in the main body of the dissertation, only a few examples of ICs most likely to represent the activity of the muscles under investigation (top r ranked ICs) were shown. Therefore examples of the best and worst top r ranked ICs for each of the muscles under investigation are presented in sections A.4.1 to A.4.6.

### A.4.1 FPL (D)

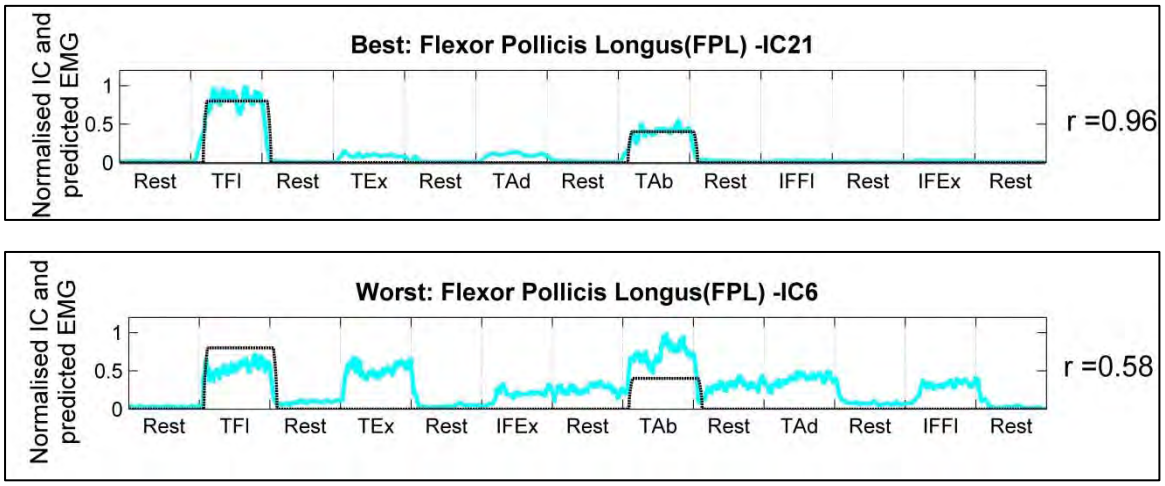


**Figure A-13**: Best and worst top r ranked ICs over all experimental runs for FPL (D). The vertical dotted lines represent the strain gauge derived timing intervals for the respective isometric contractions. The waveforms shown here are divided into segments, each 5s long, according to the isometric contraction performed during that segment.

### A.4.2 EPL (D)

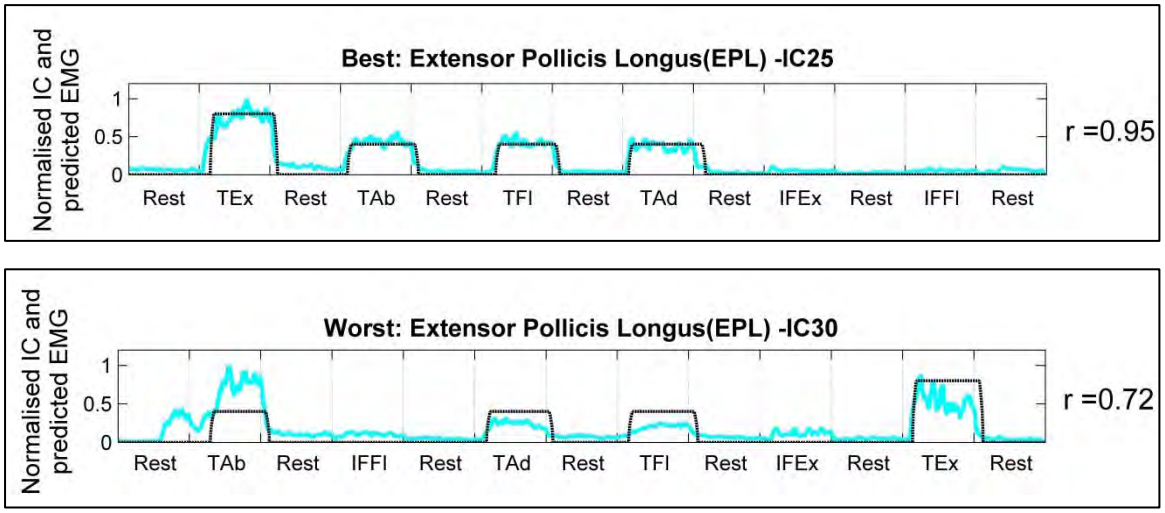


**Figure A-14**: Best and worst top r ranked ICs over all experimental runs for EPL (D). The vertical dotted lines represent the strain gauge derived timing intervals for the respective isometric contractions. The waveforms shown here are divided into segments, each 5s long, according to the isometric contraction performed during that segment.

### A.4.3 EPB (D)

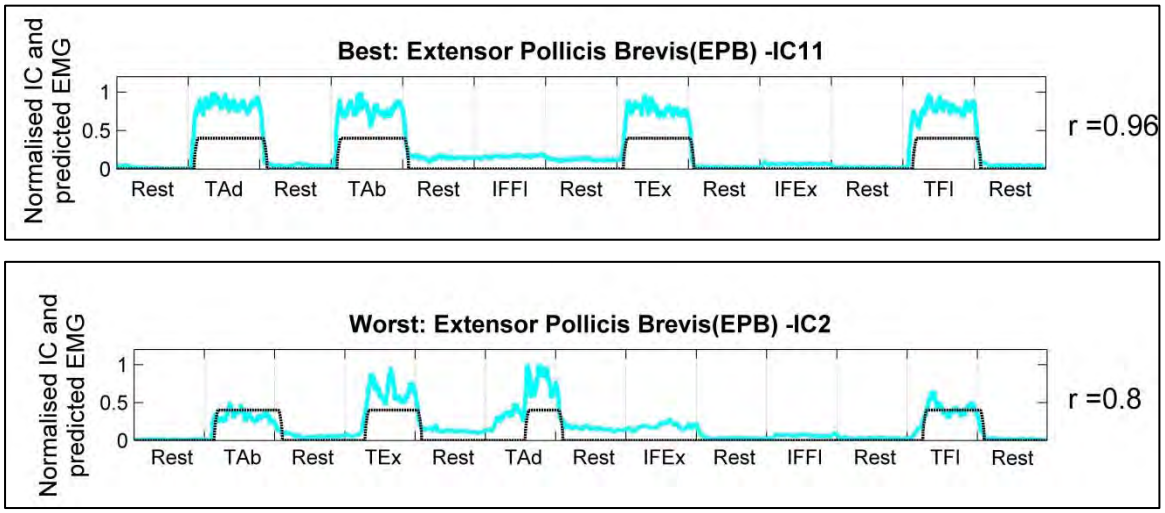


**Figure A-15**: Best and worst top r ranked ICs over all experimental runs for EPB (D). The vertical dotted lines represent the strain gauge derived timing intervals for the respective isometric contractions. The waveforms shown here are divided into segments, each 5s long, according to the isometric contraction performed during that segment.

### A.4.4 APL (D)

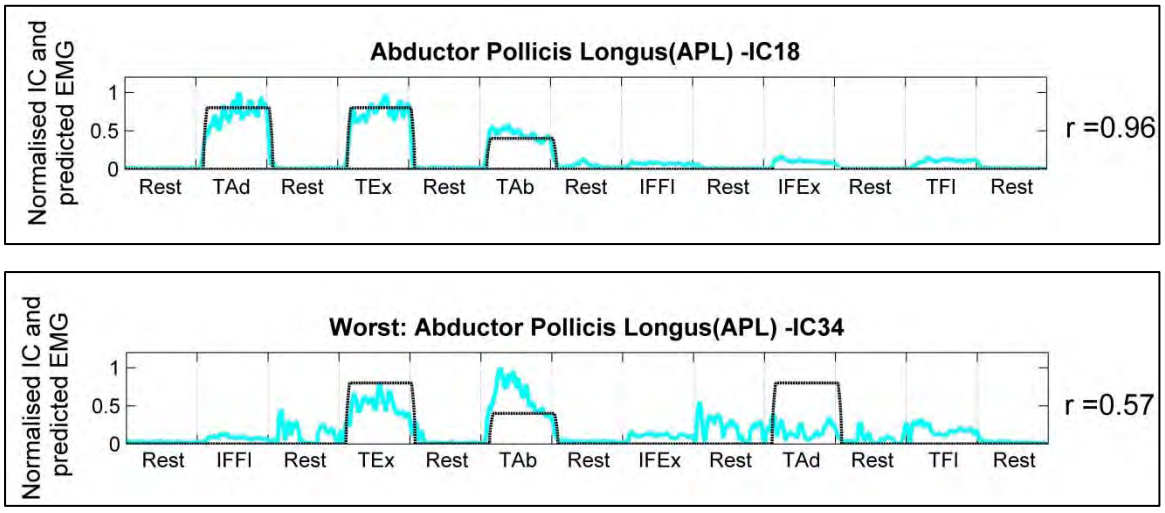


**Figure A-16**: Best and worst top r ranked ICs over all experimental runs for APL (D). The vertical dotted lines represent the strain gauge derived timing intervals for the respective isometric contractions. The waveforms shown here are divided into segments, each 5s long, according to the isometric contraction performed during that segment.

### A.4.5 FD (S)

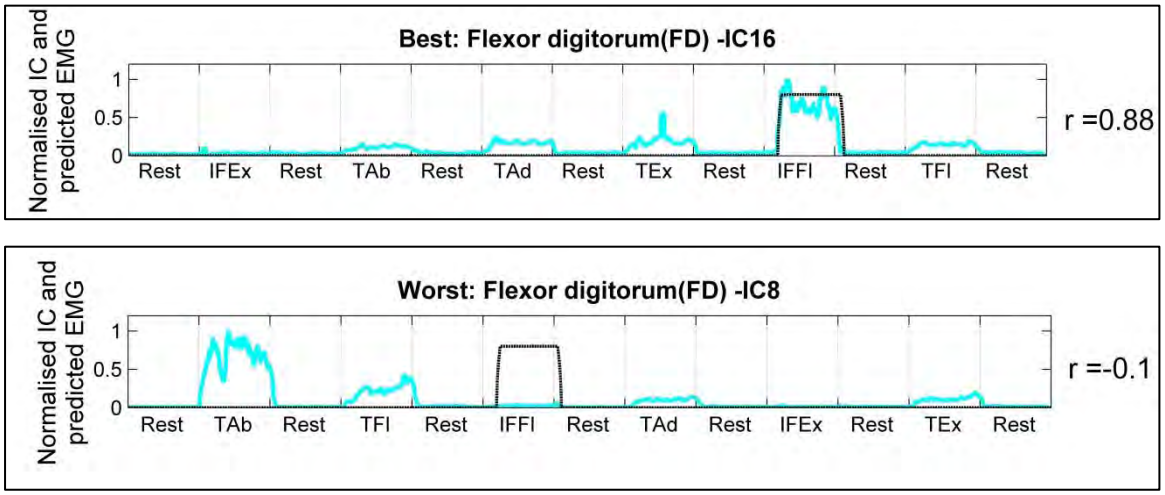


**Figure A-17**: Best and worst top r ranked ICs over all experimental runs for FD (S). The vertical dotted lines represent the strain gauge derived timing intervals for the respective isometric contractions. The waveforms shown here are divided into segments, each 5s long, according to the isometric contraction performed during that segment.

### A.4.6 ED (S)

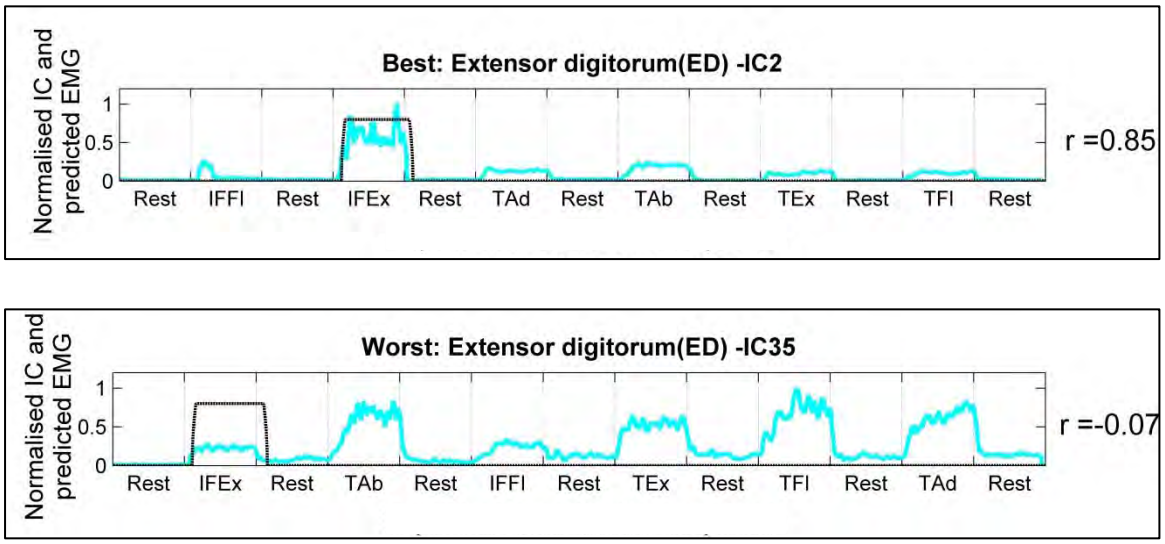


**Figure A-18**: Best and worst top r ranked ICs over all experimental runs for ED (S). The vertical dotted lines represent the strain gauge derived timing intervals for the respective isometric contractions. The waveforms shown here are divided into segments, each 5s long, according to the isometric contraction performed during that segment.

## A.5 Statistical independence of monopolar EMG signals

As mentioned in section 6.1.2, the statistical independence of the experimental signals (and thus the suitability of fastICA to separate the monopolar measurements, see section 1.3.3) was tested by calculating the probability density function (PDF) of a typical monopolar EMG recording, shown in Figure A-19. Its highly peaked appearance is similar to the PDFs of Nazarpour et al. (2013), which were said to be super-Gaussian. By inference, the monopolar signals from the present study appear to be super-Gaussian. Super-Gaussian signals have a positive kurtosis value (a measure of non-Gaussianity) (Hyvärinen & Oja 2000; Hyvärinen & Oja 1997), which means that the monopolar EMG signals were suitable for statistical separation by fastICA, since fastICA separates signals by maximising their kurtosis (James & Hesse 2005).

The double spiked appearance of the PDF in Figure A-19 is due to the common mode signals (noise) present in the monopolar recording configuration. The PDF of a bipolar equivalent waveform (shown in Figure A-20) from the same experimental run is also very peaked and does not contain the double spike because of the bipolar cancellation of the common mode.

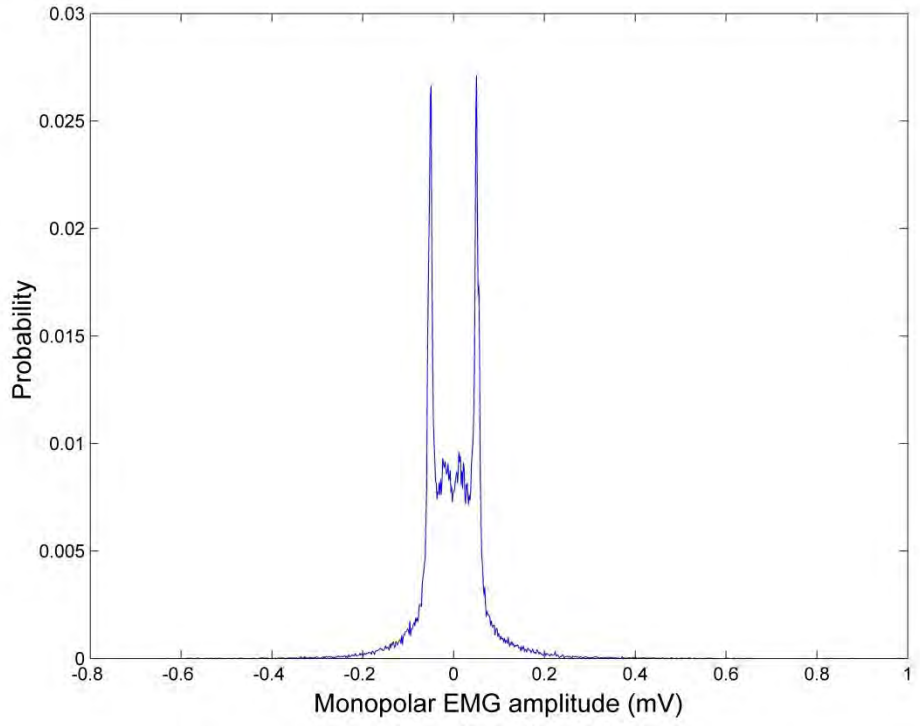


**Figure A-19:** Probability density function (PDF) of a typical monopolar EMG signal, as mentioned in section 6.1.2. The PDF is clearly very peaked and not like a Gaussian distribution. The double spiked appearance of the PDF is due to the monopolar recording configuration.

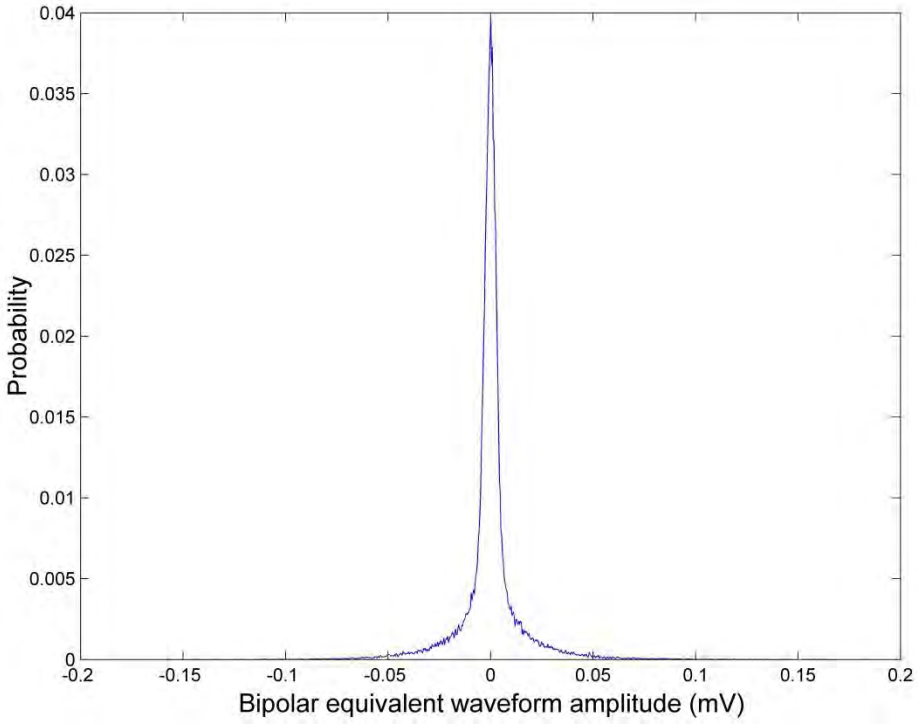


**Figure A-20:** PDF of a bipolar equivalent EMG waveform, derived from the same experimental run from which the PDF in Figure A-19 was calculated. The bipolar equivalent waveform's PDF shows that the double spiked appearance of the PDF in Figure A-19 was due to the monopolar recording configuration.

## A.6 Alternate ICA algorithm for statistical separation

As mentioned in section 5.1.1, The ICA algorithm, Weights-Adjusted Second Order Blind source Identification (WASOBI), was applied to the same monopolar EMG data from Figure 4-5 to determine whether better results could have been achieved had an alternate ICA algorithm (other than fastICA) been used to separate the source activity.

The red ellipse in Figure A-21 highlights the reduced level of activity detected for FPL during IFEx (highlighted by the black box in Figure A-21). There is, however, still a small amount of activity present during IFEx which may be due to co-activity, or that WASOBI is not ideally suited to separating monopolar EMG activity from the forearm either.

WASOBI took 525 seconds (≈9 minutes) to separate the monopolar EMG activity, whereas the average time taken for FastICA to perform the same function was around 30secs. Thus FastICA was almost 20 times faster than WASOBI.

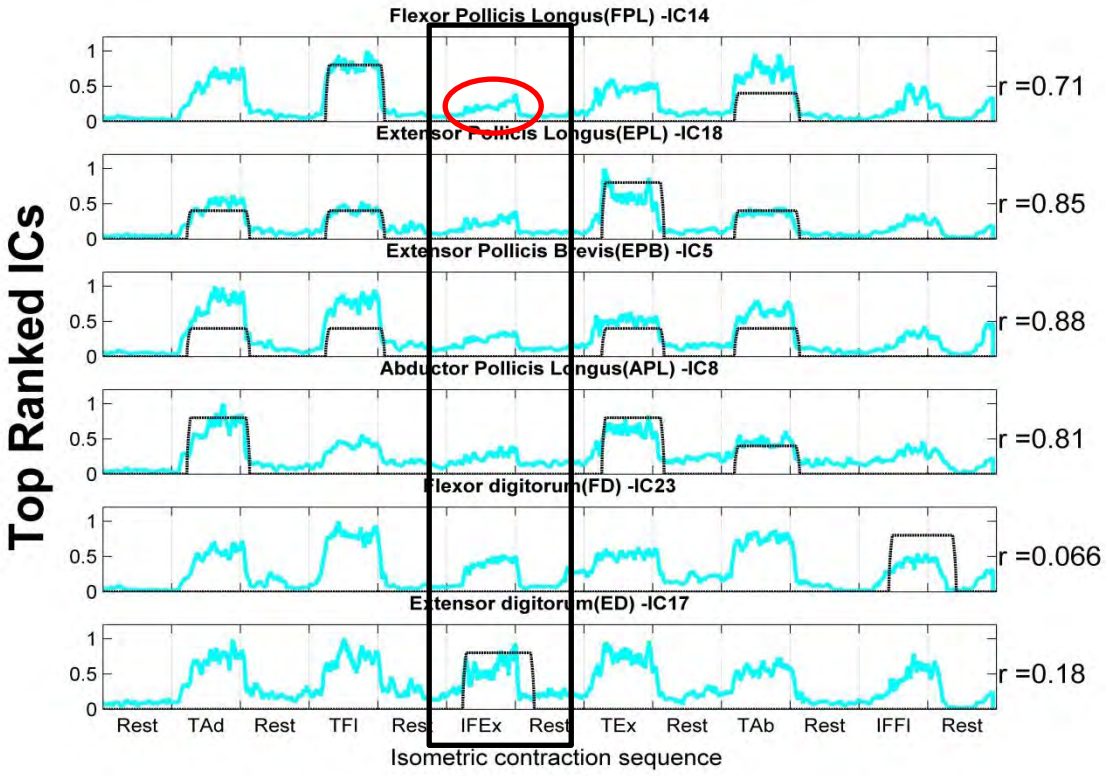


**Figure A-21**: Top r ranked ICs derived from the monopolar EMG data in Figure4-5 by the ICA algorithm, Weights-Adjusted Second Order Blind source Identification (WASOBI). The red ellipse highlights the reduced level of activity detected for FPL during IFEX (highlighted by the black rectangle). There is, however, still a small amount of activity present during IFEx which may be due to a small amount of co-activity, or that WASOBI is not ideally suited either. The elapsed time for the statistical separation of the source activity by WASOBI was ≈20 times longer than FastICA. The vertical dotted lines represent the strain gauge derived timing intervals for the respective isometric contractions. The waveforms shown here are divided into segments, each 5s long, according to the isometric contraction performed during that segment.

It must also be noted that the top r ranked ICs in Figure A-21 look considerably different to the ICs in Figure 4-5 due to the stochastic nature of ICA in general, so direct comparisons of the source separation ability of different ICA algorithms are difficult to make.

# APPENDIX B Force measurement device design and calibration

APPENDIX B provides technical details of the design decisions involved in the development of the thumb dynamometer (section B.1) as well as describing the force measurement device calibration procedure (sections B.2 and B.3 respectively)

## B.1 Dynamometer design

### B.1.1 Flexural strength differences between a tube and a solid rod cantilever beam

As mentioned in section 5.1.2, it was suspected that the dynamometer developed in the present study may have had reduced sensitivity due to modification of Bourbonnais & Duval (1991)'s design. The difference between the designs essentially relates to whether using a solid circular rod (upon which the strain gauges were mounted in Bourbonnais & Duval (1991)'s design) is more or less stiff than a tube structure used for the dynamometer in the present study. The differences in flexural strength of the two beams are related to their area moments of inertia (I) equations in Table B-1:

**Table B-1**: Area moments of inertia equations for a solid round beam and a hollow round beam.

| **Solid round beam** | **Hollow round beam** |
|---|---|
| $I_s = \frac{\pi d^4}{64}$ **Equation B-1** | $I_h = \frac{\pi(D^4 - d^4)}{64}$ **Equation B-2** |

Where D is the outer diameter and d is the inner diameter.

#### Same cross-sectional area

A hollow cylinder is more resistant to bending than a solid round beam with the same cross-sectional area: for instance, take a solid round beam (d = 10mm) and a hollow beam (D = 14.14mm and d = 10mm). The two beams have the same cross-sectional area, but the area moment of inertia is 3 times greater than a solid beam's area moment area, shown in Table B-2. If the two beams are of equal length and subjected to the same force, the hollow beam will be approximately 3 times more resistant to bending than a solid rod.

**Table B-2**: Area moment of inertia comparison between a solid round beam and a hollow cylindrical beam

| **Solid round beam** | | **Hollow cylinder beam** | |
|---|---|---|---|
| Area | $A = \pi\frac{d^2}{4} = \pi\frac{10^2}{4} = 78.5mm^2$ | Area | $A = \pi\frac{D^4 - d^4}{4} = \pi\frac{14.14^2 - 10^2}{4} = 78.5mm^2$ |
| $I_s$ | $I_s = \pi\frac{d^4}{64} = \pi\frac{10^4}{64} = 490.9mm^4$ | $I_h$ | $I_h = \pi\frac{(D^4 - d^4)}{64} = \pi\frac{(14.14^4 - 10^4)}{64} = 1471.4\,mm^4$ |

$$\frac{I_h}{I_s} = \frac{1471.4}{490.9} \approx 3$$

### Same outer diameter

However, due to larger amount of material to bear the load (shown by the reduced area comparison in Table B-3), a solid round beam is more resistant to bending than a hollow cylinder with the same outer diameter: for instance, take a solid round rod (d = 10mm) and a hollow cylinder (D=10mm, d=7.5mm). If the two beams are of equal length and subject to the same force, Table B-3 shows that for a greater than 57% reduction in area (and thus weight if the two beams are of the same material), the hollow cylinder beam is 32% weaker than the solid round rod.

**Table B-3**: Area moment of inertia comparison between a solid round rod and hollow cylindrical tube

| **Solid round beam** | | **Hollow cylinder beam** | |
|---|---|---|---|
| Area | $A_s = \pi\frac{d^2}{4} = \pi\frac{10^2}{4} = 78.5mm^2$ | Area | $A_h = \pi\frac{D^4 - d^4}{4} = \pi\frac{10^2 - 7.5^2}{4} = 34.4mm^2$ |
| $I_s$ | $I_s = \pi\frac{d^4}{64} = \pi\frac{10^4}{64} = 490.9mm^4$ | $I_h$ | $I_h = \pi\frac{(D^4 - d^4)}{64} = \pi\frac{(10^4 - 7.5^4)}{64} = 335.6\,mm^4$ |

Area moment of inertia comparison $\frac{I_h}{I_s} = \frac{335.6}{490.9} \approx 0.68$

Area comparison $\frac{A_h}{A_s} = \frac{34.4}{78.5} \approx 0.43$

Ultimately, it is impossible to determine which of the two dynamometer designs is more sensitive without the full dimensions of Bourbonnais & Duval (1991)'s design. It was assumed that the cross-sectional area of the dynamometer tube developed in the current study is considerably less than the cross-sectional area of Bourbonnais & Duval (1991)'s design, in which case the effects from using a tube instead of a solid round beam would be negligible.

### B.1.2 Dynamometer tube wall thickness calculation and theoretical strain gauge output voltage

As the principle load bearing member, the wall thickness at the fixed end of the thumb dynamometer tube was an important parameter for the sensitivity and longevity of the dynamometer: a tube too thick would have reduced sensitivity; a tube too thin would be at risk of plastic deformation (permanent bending) and unusable thereafter. Thus an analytical calculation of the stress in the tube was conducted.

The tube was modelled as a hollow cylindrical cantilever beam (top diagram in Figure B-1). The symmetry available from the walls of a cylindrical tube allows for bending in multiple directions and was chosen for this reason. The tube was designed with a thicker section (labelled the fixed end in Figure B-1) and a thinner section (labelled the load bearing section in in Figure B-1). The thinner section was considered the principal load bearing structure because very little bending was expected in the thicker section due to the larger amount of material. As a result, the mechanical stresses in the load bearing tube were expected to be concentrated at the junction between the thinner and thicker sections (point A in Figure B-1).

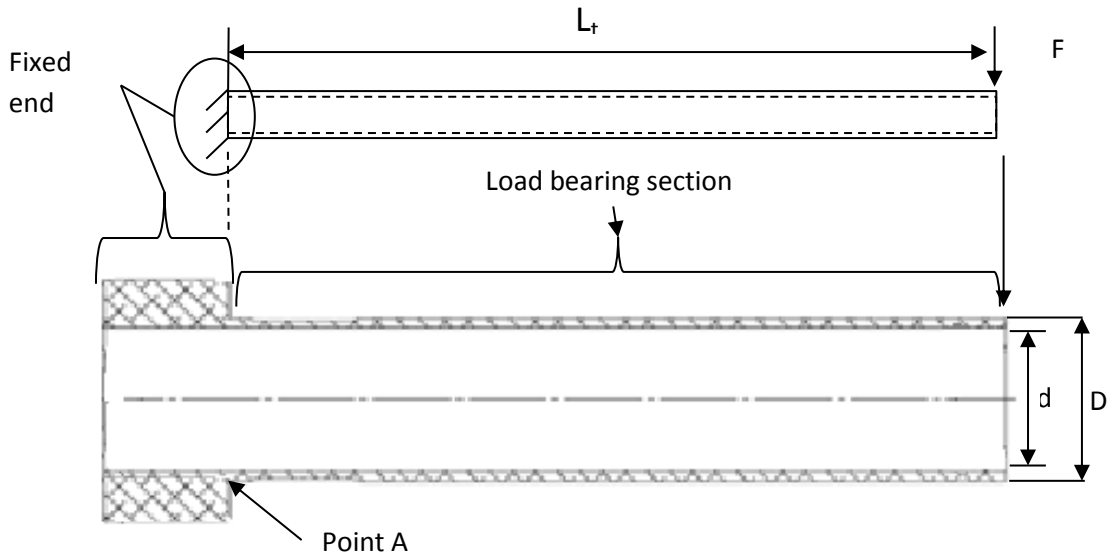


**Figure B-1**: Modelled dynamometer (top) and cross section of actual dynamometer (bottom).

The appropriate tube wall thickness was determined by analytically calculating the strain at point A as a result of applying a force in a similar range to that which the study participants would apply. This was to ensure the expected strain values were within the operating limits of the strain gauges (2-4% max). For a 5mm gauge length strain gauge (such as those used for the thumb dynamometer) these 2-4% strain limits equate to maximum values of approximately 20 000 - 40 000 µstrain (microstrain). The analysis was thus centred on whether the strain as a result of the applied force at point A would be greater than the maximum values. All equations used in the mechanical analysis described herein are derived from Hearn (2005).

Strain (ε) of a bending cantilever beam is calculated as a ratio of the changing beam length ($\Delta L_t$) to original length ($L_t$) according to the equation:

$$\boldsymbol{\varepsilon = \frac{\Delta L_t}{L_t}} \qquad \textbf{Equation B-3}$$

$\Delta L_t$, and thus ε, of a bending beam is often very small and difficult to measure (in the order of $10^{-6}$ m). However, ε is related to the mechanical stress (σ) experienced by the beam according to Young's Modulus (E), a material constant, by the equation:

$$E = \frac{\sigma}{\varepsilon} \qquad \textbf{Equation B-4}$$

The mechanical stress (σ) in the cylindrical cantilever beam as a result of a bending moment (M) is calculated by the equation:

$$\sigma = \frac{My}{I} \qquad \textbf{Equation B-5}$$

Where y is the distance from the outer surface of the tube (the point of maximum stress) to the neutral bending axis (point of zero bending stress). For a cylindrical tube, the y value is equal to half of the outer tube diameter (D/2). The peak bending moment (M) at point A as a result of the applied force (F in Figure B-1) applied at a distance ($L_t$ in Figure B-1) from the fixed end to the strain gauges was given by the equation:

$$M = FL_t \qquad \textbf{Equation B-6}$$

I is the second moment of area for the tube, a number used to account for the shape of the dynamometer tube for calculating the stress in the tube and deflection of the free end. For a cylindrical tube, I is given by:

$$I = \frac{(D^4 - d^4)}{64} \qquad \textbf{Equation B-7}$$

By substituting Equation B-3, Equation B-5, Equation B-7 and Equation B-7 into Equation B-4, the strain experienced by the dynamometer tube may be expressed as:

$$\varepsilon = \frac{32FL_tD}{E(D^4 - d^4)} \qquad \textbf{Equation B-8}$$

The strain at point A was calculated for different values of $L_t$ ranging from 5-150mm using Equation B-8, to determine whether the strain at the fixed end would exceed the operating limits of the strain gauges over a range of different values of $L_t$. D was varied independently of $L_t$ to determine its effect on ε. The material chosen for the dynamometer was Aluminium, which has a Young's Modulus of 70 GPa. Aluminium was more suitable for the dynamometer as it is not as stiff as steel (E = 210 GPa) and would thus produce larger strains when smaller forces are applied. The inner diameter (d in Figure B-1 was fixed at 30mm to allow enough space for the participants' thumb to fit inside the tube. The results of this analysis are shown in the first 4 columns of Table B-4.

In combination with the first 4 columns of Table B-4, theoretical strain gauge output voltages were calculated to determine an appropriate value for $L_t$ that would provide a measurable signal from the strain gauge bridges. The mechanical strain (ε) acting upon the strain gauges at the fixed end causes a proportional change in the resistance (R) of the strain gauge according to the equation:

$$\frac{\Delta R}{R} = G_f \frac{\Delta L}{L} \qquad \textbf{Equation B-9}$$

Where $G_f$ is the gauge factor of the strain gauges. A full Wheatstone bridge configuration was used for both vertical and horizontal strain gauges measurement systems. A theoretical output voltage ($V_o$) was calculated for each analytical ε in Table B-4 using the equation:

$$V_o = B_s G_f G_a \varepsilon \qquad \textbf{Equation B-10}$$

Where Bs is the bridge supply, Ga is the amplifier gain and ε is the calculated strain. Bs for both the horizontal and vertical strain gauge bridges was set to 3.0V and Ga was set to 1001 on the amplifier circuit board.

The strain gauges used in the current study had a gauge factor of 2.0 and a nominal resistance of 120Ω each. Analytical ΔR and % ΔR/R measures and theoretical output voltages were calculated using Equation B-9 and Equation B-10 for each value of $L_t$ are shown in the last 3 columns of Table B-4.

**Table B-4**: Analytical bending moment (M), stress (σ) strain values at point A (labelled in Figure B-1) for various values of the dynamometer tube length ($L_t$) for D = 34mm.

| Tube Length ($L_t$) | M | σ | Strain | ΔR | ΔR/R | $V_o$ |
|---|---|---|---|---|---|---|
| mm | Nm | MPa | | Ω | % | V |
| 5 | 0.60 | 0.39 | 5.64E-06 | 1.4E-03 | 0.11 | 6.77E-02 |
| 10 | 1.20 | 0.79 | 1.13E-05 | 2.7E-03 | 0.23 | 1.35E-01 |
| 15 | 1.80 | 1.18 | 1.69E-05 | 4.1E-03 | 0.34 | 2.03E-01 |
| 20 | 2.40 | 1.58 | 2.26E-05 | 5.4E-03 | 0.45 | 2.71E-01 |
| 25 | 3.00 | 1.97 | 2.82E-05 | 6.8E-03 | 0.56 | 3.38E-01 |
| 30 | 3.60 | 2.37 | 3.38E-05 | 8.1E-03 | 0.68 | 4.06E-01 |
| 35 | 4.20 | 2.76 | 3.95E-05 | 9.5E-03 | 0.79 | 4.74E-01 |
| 40 | 4.80 | 3.16 | 4.51E-05 | 1.1E-02 | 0.90 | 5.41E-01 |
| 45 | 5.40 | 3.55 | 5.08E-05 | 1.2E-02 | 1.02 | 6.09E-01 |
| 50 | 6.00 | 3.95 | 5.64E-05 | 1.4E-02 | 1.13 | 6.77E-01 |
| 55 | 6.60 | 4.34 | 6.20E-05 | 1.5E-02 | 1.24 | 7.44E-01 |
| 60 | 7.20 | 4.74 | 6.77E-05 | 1.6E-02 | 1.35 | 8.12E-01 |
| 65 | 7.80 | 5.13 | 7.33E-05 | 1.8E-02 | 1.47 | 8.80E-01 |
| 70 | 8.40 | 5.53 | 7.90E-05 | 1.9E-02 | 1.58 | 9.47E-01 |
| 75 | 9.00 | 5.92 | 8.46E-05 | 2.0E-02 | 1.69 | 1.02E+00 |
| 80 | 9.60 | 6.32 | 9.02E-05 | 2.2E-02 | 1.80 | 1.08E+00 |
| 85 | 10.20 | 6.71 | 9.59E-05 | 2.3E-02 | 1.92 | 1.15E+00 |
| 90 | 10.80 | 7.11 | 1.02E-04 | 2.4E-02 | 2.03 | 1.22E+00 |
| 95 | 11.40 | 7.50 | 1.07E-04 | 2.6E-02 | 2.14 | 1.29E+00 |
| 100 | 12.00 | 7.90 | 1.13E-04 | 2.7E-02 | 2.26 | 1.35E+00 |
| 105 | 12.60 | 8.29 | 1.18E-04 | 2.8E-02 | 2.37 | 1.42E+00 |
| 110 | 13.20 | 8.69 | 1.24E-04 | 3.0E-02 | 2.48 | 1.49E+00 |
| 115 | 13.80 | 9.08 | 1.30E-04 | 3.1E-02 | 2.59 | 1.56E+00 |
| 120 | 14.40 | 9.47 | 1.35E-04 | 3.2E-02 | 2.71 | 1.62E+00 |
| 125 | 15.00 | 9.87 | 1.41E-04 | 3.4E-02 | 2.82 | 1.69E+00 |
| 130 | 15.60 | 10.26 | 1.47E-04 | 3.5E-02 | 2.93 | 1.76E+00 |
| 135 | 16.20 | 10.66 | 1.52E-04 | 3.7E-02 | 3.05 | 1.83E+00 |
| 140 | 16.80 | 11.05 | 1.58E-04 | 3.8E-02 | 3.16 | 1.89E+00 |
| 145 | 17.40 | 11.45 | 1.64E-04 | 3.9E-02 | 3.27 | 1.96E+00 |
| 150 | 18.00 | 11.84 | 1.69E-04 | 4.1E-02 | 3.38 | 2.03E+00 |

Using Table B-4, final values chosen for D and $L_t$ were 34mm and 150mm respectively. With these values for D and $L_t$, a peak strain value of 169 μstrain and theoretical output voltage of 2.03 V was calculated.

### B.1.3 Dynamometer tube gauge section

During the CAD modelling phase, the analytical ε calculations described in B.1.2 were verified with a simple Finite Element Analysis (FEA) simulation in SolidWorks. The mechanical stress in the dynamometer tube was further concentrated into a specific gauge section on the load bearing

section by cutting a 0.5mm deep x 10mm wide channel into the dynamometer tube at point A. The primary reason for doing so was to create an area with an even strain field in which the strain gauges may be placed and was as not considered in the analytical calculations in section B.1.2. The rear surface of the dynamometer tube was held fixed (zero displacement in any direction) and a 120N downward force was applied to the end of the tube (labelled in Figure B-2)

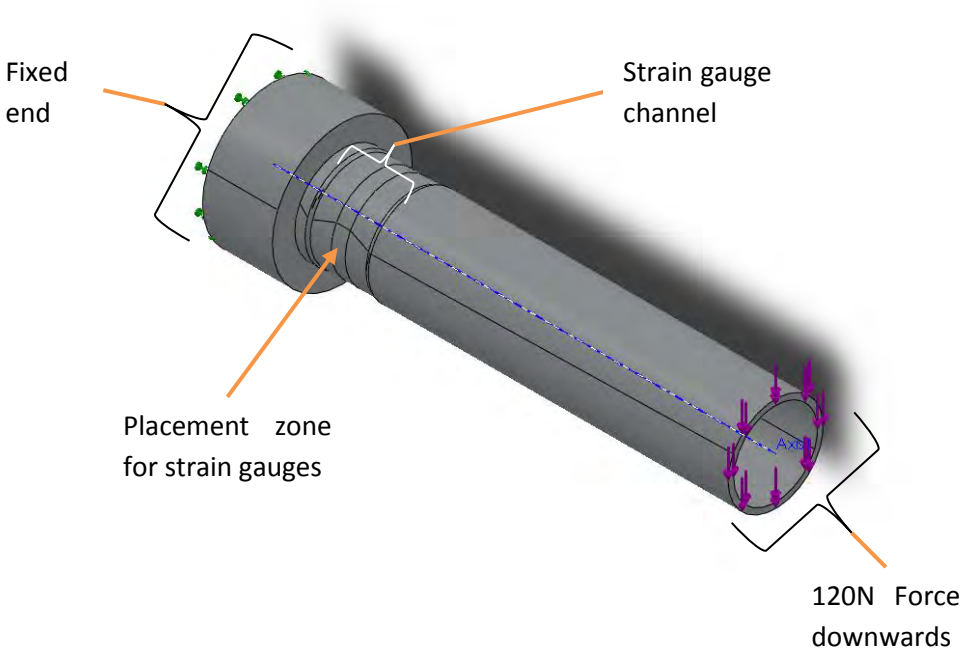


**Figure B-2**: Model set up for FEA simulation in SolidWorks. The rear face of the dynamometer tube was fixed (zero displacement in any direction) and a 120N downward force was applied to the end of the tube.

A solid mesh was applied to the CAD model using 11875 elements (size = 3.8mm) and 21798 nodes (see Figure B-3). The expected von Mises stress distribution on the dynamometer CAD model surface is shown in Figure B-4. The colour scale legend indicates stress in Pa ($Nm^{-2}$), with a peak value of 16.7 MPa. The yield strength of Aluminium 1060 is 76 MPa (eFunda 2015). The peak stress is clearly below that of the yield strength, indicating the wall thickness of the tube in the gauge section was not at risk of plastic deformation.

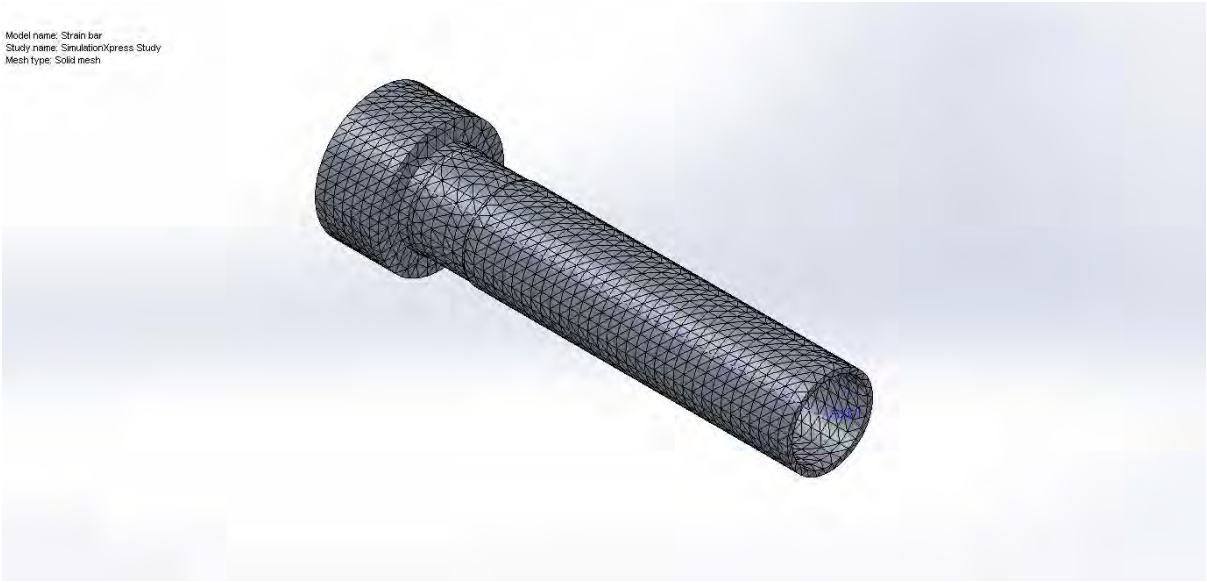


**Figure B-3**: FEA mesh created for the dynamometer CAD model in SolidWorks

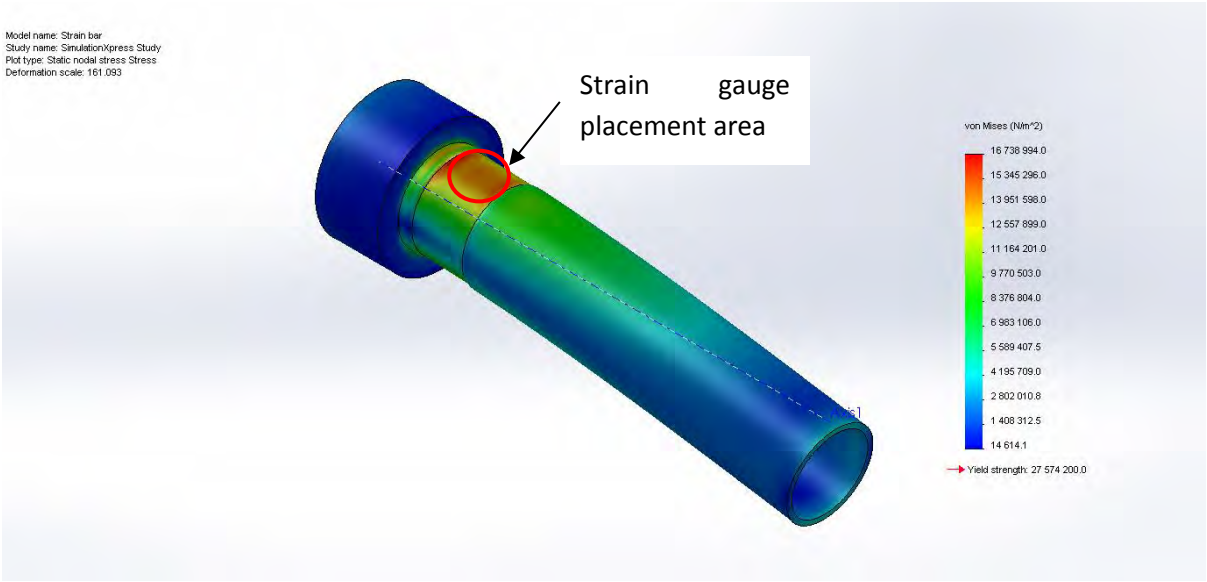


**Figure B-4**: Results of FEA simulation showing the expected von Mises stress distribution in the dynamometer CAD model as a result of the applied force at the tube end. The colour scale legend indicates stress in $Nm^{-2}$ (Pa), with a peak value of 16.7 MPa.

The FEA simulation also helped visualize the expected stress in the gauge section where the strain gauges were to be placed (highlighted in Figure B-4). The consistent colour of the highlighted area indicated the stress in the gauge section was very even and that the peak stress was concentrated into that region.

As mentioned above in section B.1.2, mechanical stress (σ) is related to mechanical strain (ε) according to Equation B-4. Since E is a constant, an area of even σ is then also an area of even ε. An even strain field means that the mechanical strain causes an even ΔR of the strain gauges over the full gauge length according to Equation B-9.

## B.2 Thumb dynamometer calibration

The voltage output of the thumb dynamometer strain gauges was calibrated in each of the four measurement directions separately.

### B.2.1 Vertical (Thumb flexion/extension) calibration

The vertical dynamometer strain gauge bridge was calibrated by applying known masses from 0-11kg (0-107.9 N) in 1 kg (9.81 N) increments to the end of the tube in the manner shown in Figure B-5. For calibration in the upward vertical direction, the dynamometer was rotated through 180° and the same calibration procedure as the downwards vertical direction was applied.

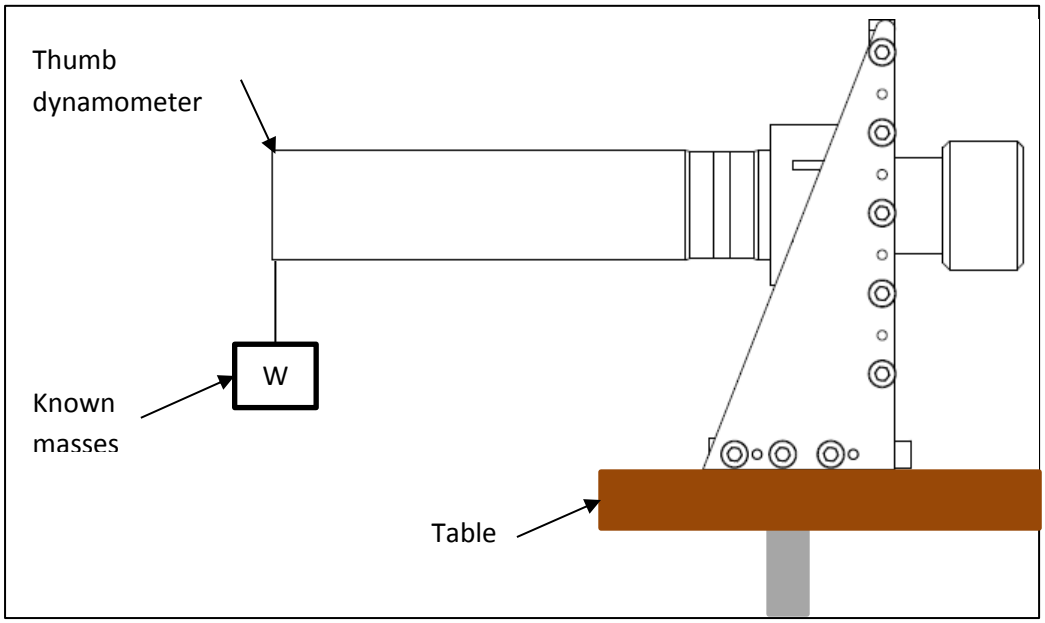


**Figure B-5**: Set up for calibration of the dynamometer in the vertical direction.

The voltage outputs from the vertical and horizontal strain gauge bridge were recorded simultaneously with each force application. Table B-5 shows the calibration data for each mass applied vertically up (positive) and vertically down (negative) and from which the graph in Figure 2-6 was derived.

**Table B-5**: Calibration data for masses applied vertically upwards (positive) and vertically downwards (negative) to the dynamometer.

| Test_1 | | | | Test_2 | | | | Test_3 | | | | Average | | | |
|---|---|---|---|---|---|---|---|---|---|---|---|---|---|---|---|
| Mass | Force | Fv | Fh | Mass | Force | Fv | Fh | Mass | Force | Fv | Fh | Mass | Force | Fv | Fh |
| kg | N | V | V | kg | N | V | V | kg | N | V | V | kg | N | V | V |
| 11.10 | 108.89 | 2.09 | 0.01 | 11.10 | 108.89 | 1.92 | 0.03 | 11.10 | 108.89 | 1.87 | 0.04 | 11.10 | 108.89 | 1.96 | 0.02 |
| 10.10 | 99.08 | 1.91 | -0.03 | 10.10 | 99.08 | 1.75 | 0.02 | 10.10 | 99.08 | 1.71 | 0.02 | 10.10 | 99.08 | 1.79 | 0.01 |
| 9.10 | 89.27 | 1.74 | -0.03 | 9.10 | 89.27 | 1.58 | 0.01 | 9.10 | 89.27 | 1.54 | 0.03 | 9.10 | 89.27 | 1.62 | 0.00 |
| 8.10 | 79.46 | 1.55 | -0.04 | 8.00 | 78.48 | 1.37 | 0.01 | 8.10 | 79.46 | 1.36 | -0.02 | 8.07 | 79.13 | 1.43 | -0.01 |
| 7.10 | 69.65 | 1.36 | -0.03 | 7.00 | 68.67 | 1.19 | 0.01 | 7.00 | 68.67 | 1.17 | -0.01 | 7.03 | 69.00 | 1.24 | -0.01 |
| 6.10 | 59.84 | 1.17 | 0.00 | 6.00 | 58.86 | 1.02 | 0.02 | 6.10 | 59.84 | 0.98 | 0.00 | 6.07 | 59.51 | 1.06 | 0.00 |
| 5.10 | 50.03 | 0.99 | 0.00 | 5.00 | 49.05 | 0.83 | 0.02 | 5.10 | 50.03 | 0.80 | 0.01 | 5.07 | 49.70 | 0.87 | 0.01 |
| 4.00 | 39.24 | 0.78 | 0.01 | 4.00 | 39.24 | 0.66 | 0.02 | 4.10 | 40.22 | 0.56 | 0.02 | 4.03 | 39.57 | 0.67 | 0.01 |
| 2.90 | 28.45 | 0.57 | 0.01 | 3.10 | 30.41 | 0.50 | 0.02 | 3.00 | 29.43 | 0.54 | 0.00 | 3.00 | 29.43 | 0.54 | 0.01 |
| 2.10 | 20.60 | 0.42 | 0.01 | 2.10 | 20.60 | 0.31 | 0.02 | 2.10 | 20.60 | 0.40 | 0.01 | 2.10 | 20.60 | 0.38 | 0.01 |
| 1.10 | 10.79 | 0.25 | 0.01 | 1.10 | 10.79 | 0.14 | 0.03 | 1.10 | 10.79 | 0.24 | 0.02 | 1.10 | 10.79 | 0.21 | 0.02 |
| 0.00 | 0.00 | 0.04 | 0.01 | 0.00 | 0.00 | -0.07 | 0.03 | 0.00 | 0.00 | 0.03 | 0.02 | 0.00 | 0.00 | 0.00 | 0.02 |
| -1.10 | -10.79 | -0.23 | 0.07 | -1.10 | -10.79 | -0.22 | 0.07 | -1.10 | -10.79 | -0.20 | -0.02 | -1.10 | -10.79 | -0.22 | 0.04 |
| -2.10 | -20.60 | -0.39 | 0.08 | -2.00 | -19.62 | -0.35 | 0.07 | -2.10 | -20.60 | -0.32 | 0.07 | -2.07 | -20.27 | -0.35 | 0.07 |
| -3.00 | -29.43 | -0.56 | 0.08 | -3.10 | -30.41 | -0.55 | 0.07 | -2.90 | -28.45 | -0.48 | 0.07 | -3.00 | -29.43 | -0.53 | 0.07 |
| -4.00 | -39.24 | -0.75 | 0.09 | -4.00 | -39.24 | -0.73 | 0.07 | -4.00 | -39.24 | -0.70 | 0.06 | -4.00 | -39.24 | -0.73 | 0.07 |
| -5.00 | -49.05 | -0.93 | 0.09 | -4.90 | -48.07 | -0.87 | 0.07 | -5.10 | -50.03 | -0.87 | 0.06 | -5.00 | -49.05 | -0.89 | 0.07 |
| -5.90 | -57.88 | -1.10 | 0.10 | -6.10 | -59.84 | -1.10 | 0.07 | -5.90 | -57.88 | -1.03 | 0.03 | -5.97 | -58.53 | -1.07 | 0.07 |
| -7.10 | -69.65 | -1.32 | 0.09 | -6.90 | -67.69 | -1.25 | 0.07 | -7.00 | -68.67 | -1.23 | 0.03 | -7.00 | -68.67 | -1.27 | 0.06 |
| -8.00 | -78.48 | -1.48 | 0.09 | -8.00 | -78.48 | -1.45 | 0.07 | -8.10 | -79.46 | -1.42 | 0.02 | -8.03 | -78.81 | -1.45 | 0.06 |
| -9.00 | -88.28 | -1.68 | 0.09 | -9.10 | -89.26 | -1.65 | 0.07 | -9.00 | -88.28 | -1.59 | 0.05 | -9.03 | -88.61 | -1.64 | 0.07 |
| -10.10 | -99.08 | -1.88 | 0.08 | -9.90 | -97.12 | -1.79 | 0.07 | -10.10 | -99.08 | -1.79 | -0.02 | -10.03 | -98.43 | -1.82 | 0.05 |
| -11.10 | -108.89 | -2.05 | 0.13 | -11.10 | -108.89 | -1.98 | 0.07 | -11.10 | -108.89 | -1.96 | 0.01 | -11.10 | -108.89 | -2.00 | 0.07 |

### B.2.2 Horizontal (thumb adduction/ abduction) calibration

Hanging masses from 0-11kg in 1kg increments were attached to the end of the tube using a rope and pulley system in the manner shown in Figure B-6. Table B-6 shows the calibration data for each mass applied horizontally right (positive) and left (negative) to the dynamometer and from which the calibration graph in Figure 2-7 was derived.

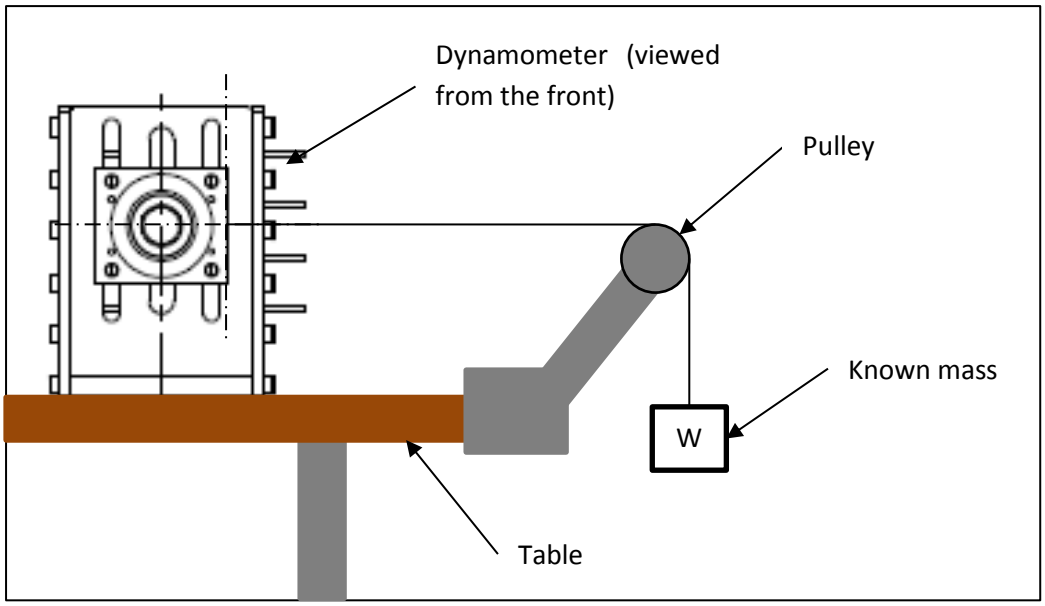


**Figure B-6**: Set up for calibration of the dynamometer, as viewed from the front, in the horizontal direction. The dynamometer was secured to a table and hanging weights were applied to the end of the tube using a pulley system.

**Table B-6**: Calibration data for masses applied horizontally right (positive) and left (negative) to the dynamometer.

| Test_1 | | | | Test_2 | | | | Test_3 | | | | Average | | | |
|---|---|---|---|---|---|---|---|---|---|---|---|---|---|---|---|
| Mass | Force | Fv | Fh | Mass | Force | Fv | Fh | Mass | Force | Fv | Fh | Mass | Force | Fv | Fh |
| kg | N | V | V | kg | N | V | V | kg | N | V | V | kg | N | V | V |
| 11.00 | 107.91 | 0.02 | 1.93 | 11.10 | 108.89 | 0.01 | 1.89 | 11.10 | 108.89 | -0.01 | 1.92 | 11.07 | 108.56 | 0.01 | 1.91 |
| 10.10 | 99.08 | 0.02 | 1.78 | 10.10 | 99.08 | 0.00 | 1.75 | 10.10 | 99.08 | -0.02 | 1.83 | 10.10 | 99.08 | 0.00 | 1.79 |
| 8.90 | 87.31 | 0.01 | 1.58 | 9.00 | 88.29 | 0.00 | 1.58 | 9.00 | 88.29 | -0.01 | 1.67 | 8.97 | 87.96 | 0.00 | 1.61 |
| 8.00 | 78.48 | 0.01 | 1.44 | 8.10 | 79.46 | 0.00 | 1.44 | 8.10 | 79.46 | -0.01 | 1.51 | 8.07 | 79.13 | 0.00 | 1.47 |
| 7.10 | 69.65 | 0.01 | 1.27 | 7.00 | 68.67 | 0.01 | 1.23 | 7.00 | 68.67 | -0.01 | 1.31 | 7.03 | 69.00 | 0.00 | 1.27 |
| 6.10 | 59.83 | 0.00 | 1.07 | 6.00 | 58.85 | 0.00 | 1.06 | 6.10 | 59.83 | -0.01 | 1.16 | 6.07 | 59.50 | 0.00 | 1.10 |
| 5.10 | 50.03 | 0.00 | 0.91 | 5.10 | 50.03 | 0.01 | 0.88 | 5.10 | 50.03 | -0.01 | 0.97 | 5.10 | 50.03 | 0.00 | 0.92 |
| 4.00 | 39.24 | -0.01 | 0.70 | 4.00 | 39.24 | -0.01 | 0.70 | 4.10 | 40.22 | -0.01 | 0.79 | 4.03 | 39.57 | -0.01 | 0.73 |
| 3.10 | 30.42 | -0.01 | 0.55 | 3.00 | 29.44 | 0.00 | 0.53 | 3.00 | 29.44 | 0.00 | 0.59 | 3.03 | 29.77 | 0.00 | 0.56 |
| 2.00 | 19.62 | -0.01 | 0.36 | 2.00 | 19.62 | -0.01 | 0.36 | 2.00 | 19.62 | 0.00 | 0.38 | 2.00 | 19.62 | -0.01 | 0.37 |
| 1.10 | 10.79 | -0.02 | 0.19 | 1.10 | 10.79 | -0.01 | 0.20 | 1.10 | 10.79 | 0.00 | 0.22 | 1.10 | 10.79 | -0.01 | 0.20 |
| 0.00 | 0.00 | -0.02 | -0.01 | 0.00 | 0.00 | -0.01 | -0.01 | 0.00 | 0.00 | 0.00 | 0.02 | 0.00 | 0.00 | -0.01 | 0.00 |
| -1.10 | -10.79 | 0.00 | -0.15 | -1.10 | -10.79 | 0.00 | -0.12 | -1.10 | -10.79 | 0.00 | -0.13 | -10.79 | -10.79 | 0.00 | -0.13 |
| -2.10 | -20.60 | 0.00 | -0.32 | -2.10 | -20.60 | 0.00 | -0.34 | -2.10 | -20.60 | 0.00 | -0.33 | -2.10 | -20.60 | 0.00 | -0.33 |
| -3.00 | -29.43 | 0.00 | -0.46 | -3.00 | -29.43 | 0.00 | -0.50 | -3.10 | -30.41 | 0.00 | -0.49 | -3.03 | -29.76 | 0.00 | -0.48 |
| -4.10 | -40.22 | 0.00 | -0.70 | -4.00 | -39.24 | -0.01 | -0.67 | -4.10 | -40.22 | 0.00 | -0.71 | -4.07 | -39.89 | 0.00 | -0.69 |
| -5.10 | -50.03 | 0.00 | -0.83 | -5.00 | -49.05 | 0.00 | -0.84 | -5.10 | -50.03 | -0.01 | -0.87 | -5.07 | -49.70 | 0.00 | -0.85 |
| -6.00 | -58.86 | 0.00 | -1.01 | -6.10 | -59.84 | -0.01 | -1.10 | -6.00 | -58.86 | -0.01 | -1.03 | -6.03 | -59.19 | -0.01 | -1.05 |
| -7.00 | -68.67 | 0.00 | -1.22 | -7.10 | -69.65 | -0.01 | -1.27 | -7.00 | -68.67 | -0.01 | -1.22 | -7.03 | -69.00 | -0.01 | -1.24 |
| -8.00 | -78.48 | 0.00 | -1.45 | -8.00 | -78.48 | -0.02 | -1.41 | -8.00 | -78.48 | -0.01 | -1.57 | -8.00 | -78.48 | -0.01 | -1.47 |
| -9.00 | -88.29 | 0.00 | -1.62 | -9.10 | -89.27 | -0.02 | -1.58 | -9.10 | -89.27 | 0.00 | -1.66 | -9.07 | -88.94 | -0.01 | -1.62 |
| -10.10 | -99.08 | 0.01 | -1.72 | -10.10 | -99.08 | -0.03 | -1.74 | -10.00 | -98.10 | 0.00 | -1.75 | -10.07 | -98.75 | -0.01 | -1.74 |
| -11.10 | -108.89 | 0.00 | -1.82 | -11.10 | -108.89 | -0.03 | -1.77 | -11.10 | -108.89 | -0.01 | -1.86 | -11.10 | -108.89 | -0.01 | -1.82 |

## B.3 Finger load cell calibration

The finger load cell was calibrated using a spring gauge and 3d printed wedge placed in a vice. The wedge was designed to ensure the calibration force could be applied horizontally as shown in Figure B-7. Table B-7 shows the calibration data for each mass applied horizontally right (positive) and left (negative) to the dynamometer and from which the graph in Figure 2-11 is derived.

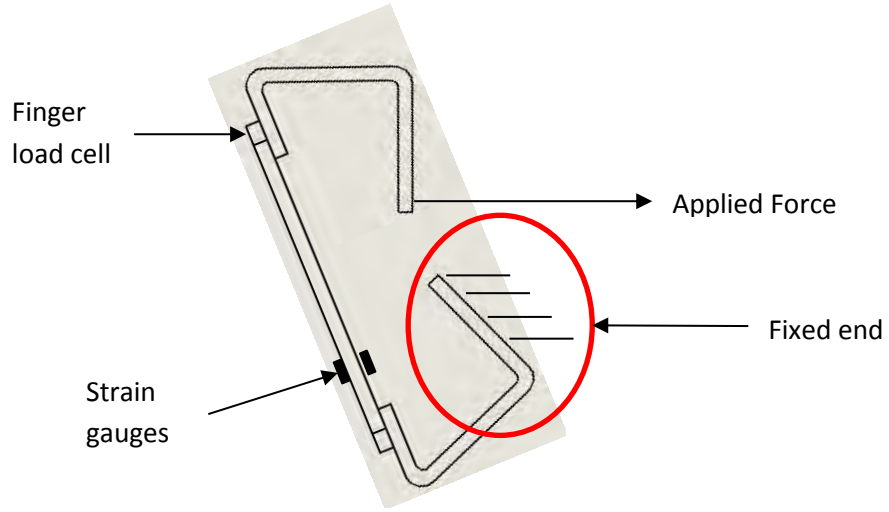


**Figure B-7**: Finger load cell calibration set up. The finger holder closest to the strain gauges was held in a fixed position (highlighted by a red ellipse) by a 3D printed wedge in a vice and a force was applied horizontally in 1N increments to the other finger holder using a spring force gauge.

**Table B-7**: Calibration data of the masses applied in flexion (negative) and extension (positive) directions to the finger load cell

| Test_1 | | | Test_2 | | | Average | | |
|---|---|---|---|---|---|---|---|---|
| Mass | Force | F_finger | Mass | Force | F_finger | Mass | Force | F_finger |
| kg | N | Volts | kg | N | Volts | kg | N | Volts |
| 1.00 | -9.81 | -1.08 | 1.00 | -9.81 | -1.13 | 1.00 | -9.81 | -1.10 |
| 0.80 | -7.85 | -0.79 | 0.80 | -7.85 | -0.89 | 0.80 | -7.85 | -0.84 |
| 0.60 | -5.89 | -0.61 | 0.60 | -5.89 | -0.70 | 0.60 | -5.89 | -0.65 |
| 0.20 | -1.96 | -0.18 | 0.20 | -1.96 | -0.31 | 0.20 | -1.96 | -0.24 |
| 0.00 | 0.00 | 0.01 | 0.00 | 0.00 | -0.11 | 0.00 | 0.00 | -0.05 |
| 0.20 | 1.96 | 0.40 | 0.28 | 2.73 | 0.44 | 0.2 | 2.3 | 0.4 |
| 0.40 | 3.92 | 0.80 | 0.48 | 4.69 | 0.83 | 0.4 | 4.3 | 0.8 |
| 0.60 | 5.89 | 1.18 | 0.68 | 6.65 | 1.22 | 0.6 | 6.3 | 1.2 |
| 0.80 | 7.85 | 1.55 | 0.88 | 8.61 | 1.58 | 0.8 | 8.2 | 1.6 |
| 1.00 | 9.81 | 1.91 | 1.00 | 9.81 | 1.80 | 1.0 | 9.8 | 1.9 |

# APPENDIX C EMG AMPLIFIER SYSTEM

## C.1 EMG amplifier system

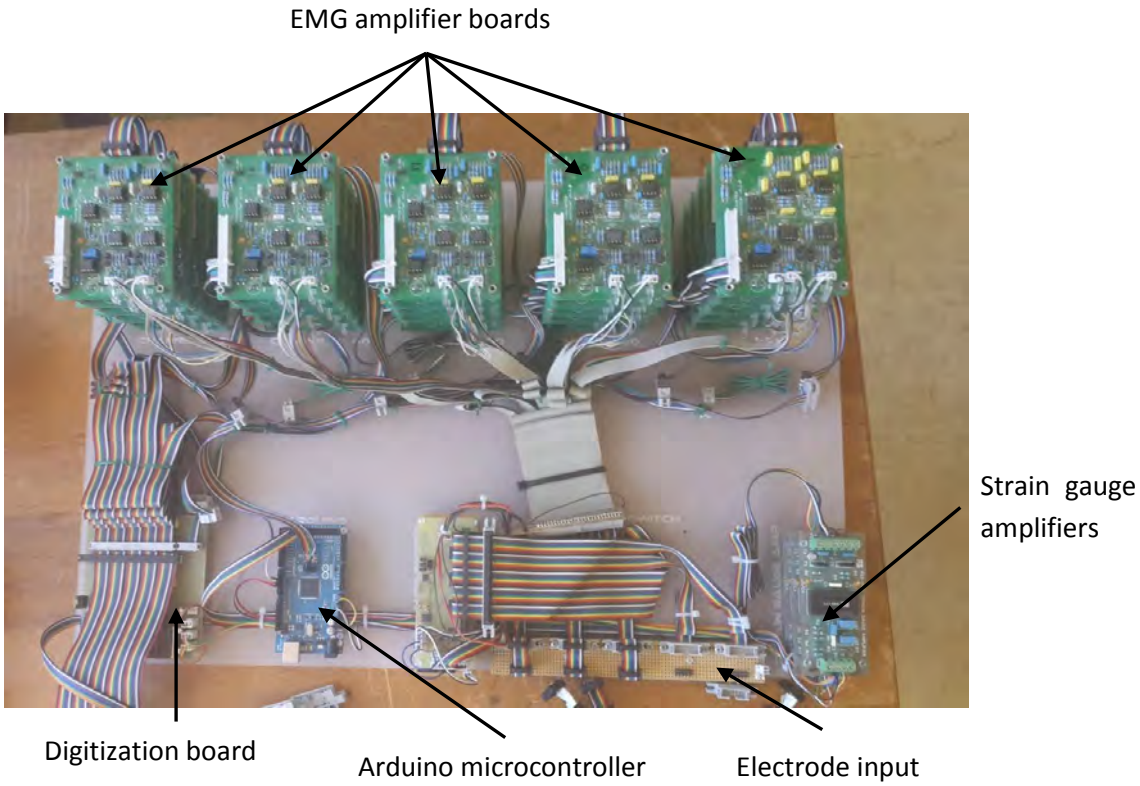


**Figure C-1:** Photo of EMG amplifier system used in the present study

### C.1.1 EMG Amplifier Diagrams

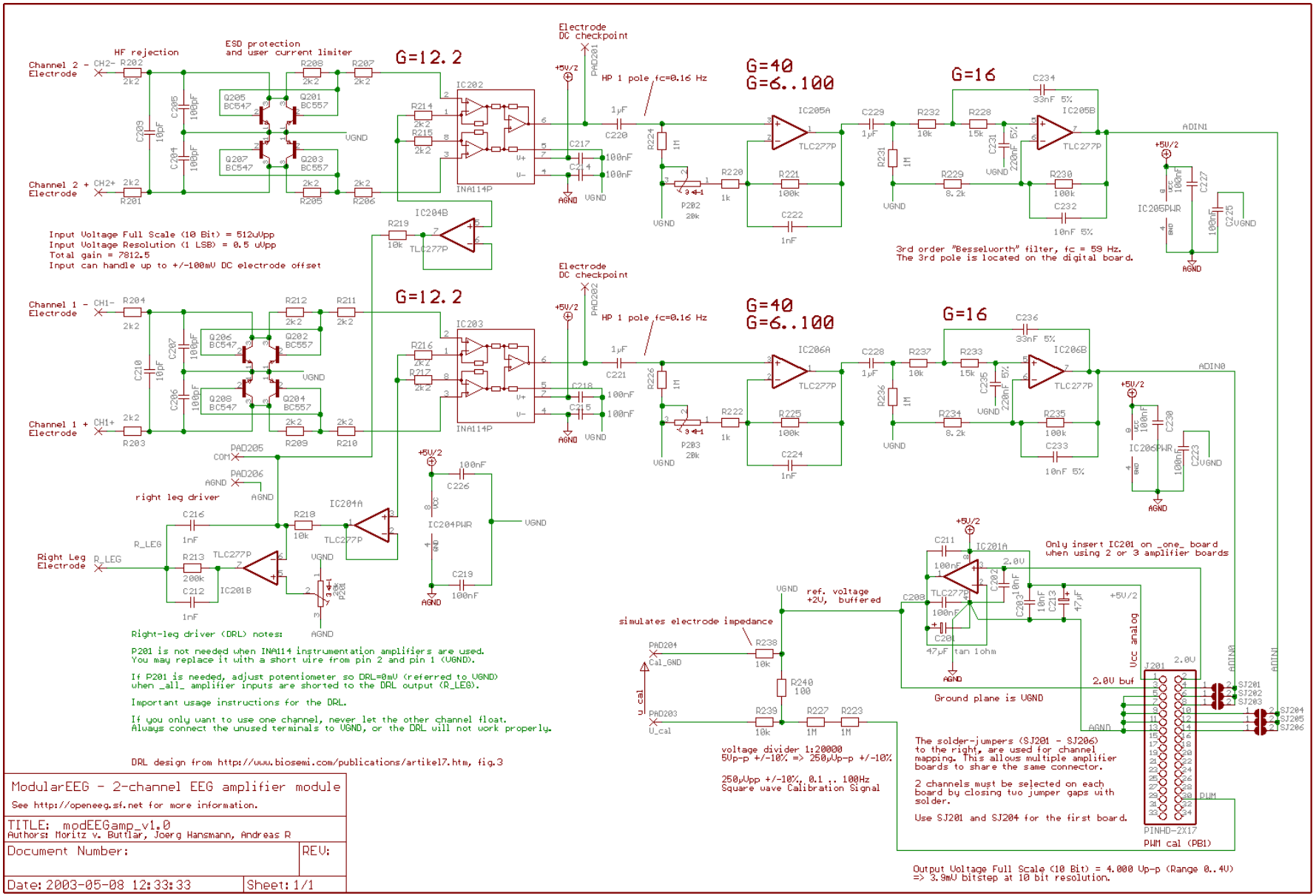


**Figure C-2**: OpenEEG amplifier board schematic diagram by Griffiths et al. (2002). Each board amplifies two EMG channels

### C.1.2 Digitization board diagrams

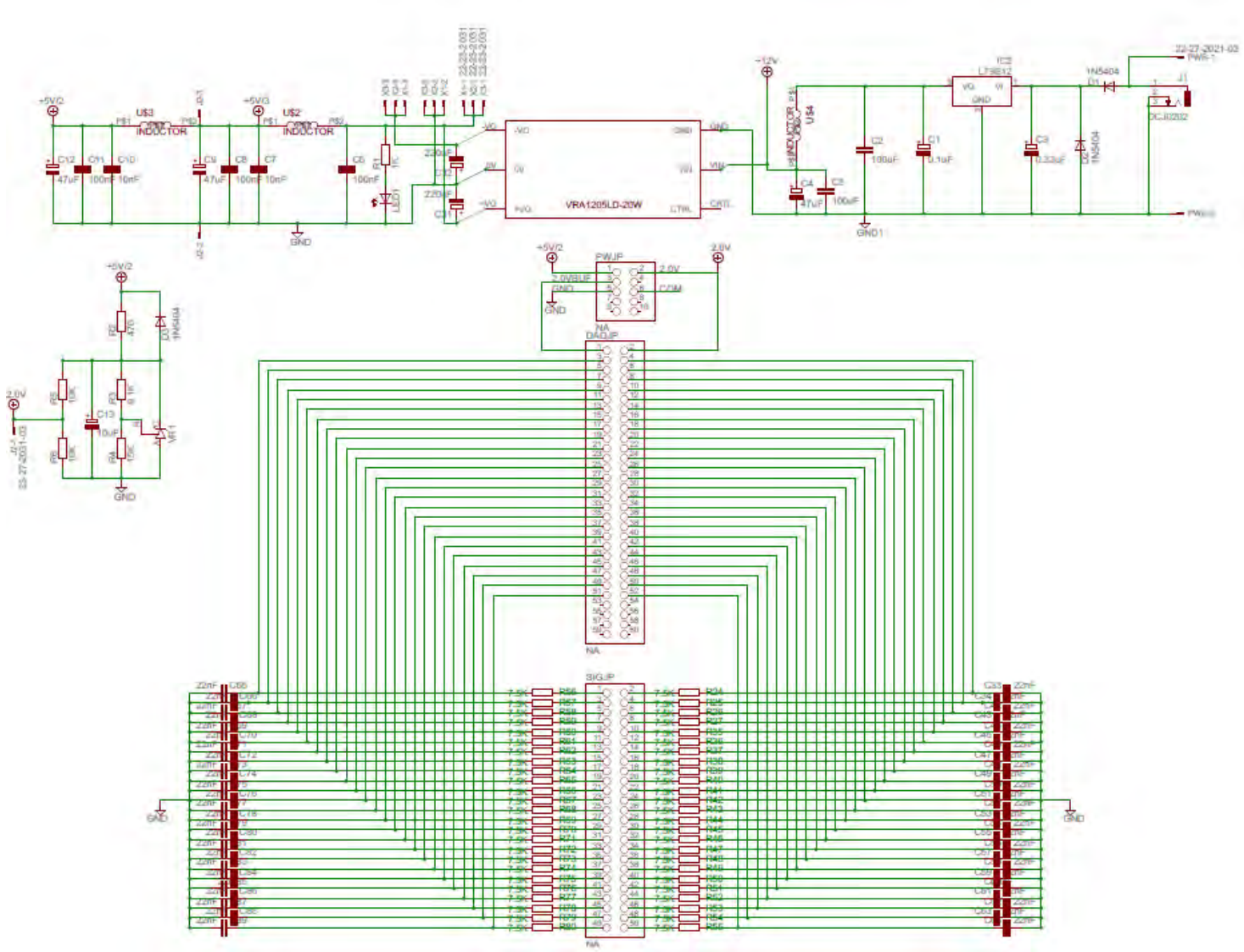


**Figure C-3**: Schematic of digitization circuit board (designed by R. Smith)

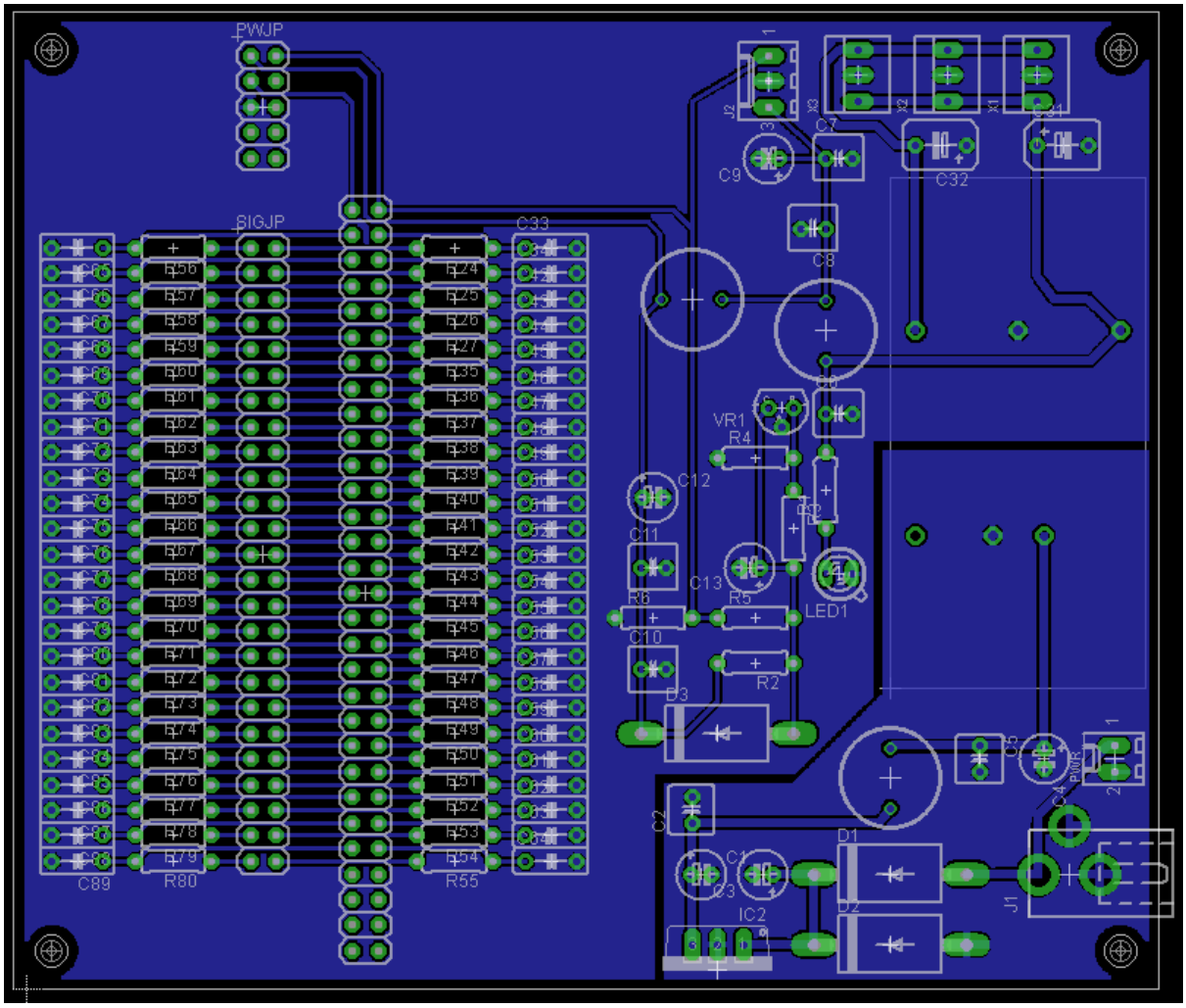


**Figure C-4**: Layout diagram of digitization circuit diagram (designed by R. Smith)

## C.2 Digital gain daughter boards

### C.2.1 Circuit diagrams

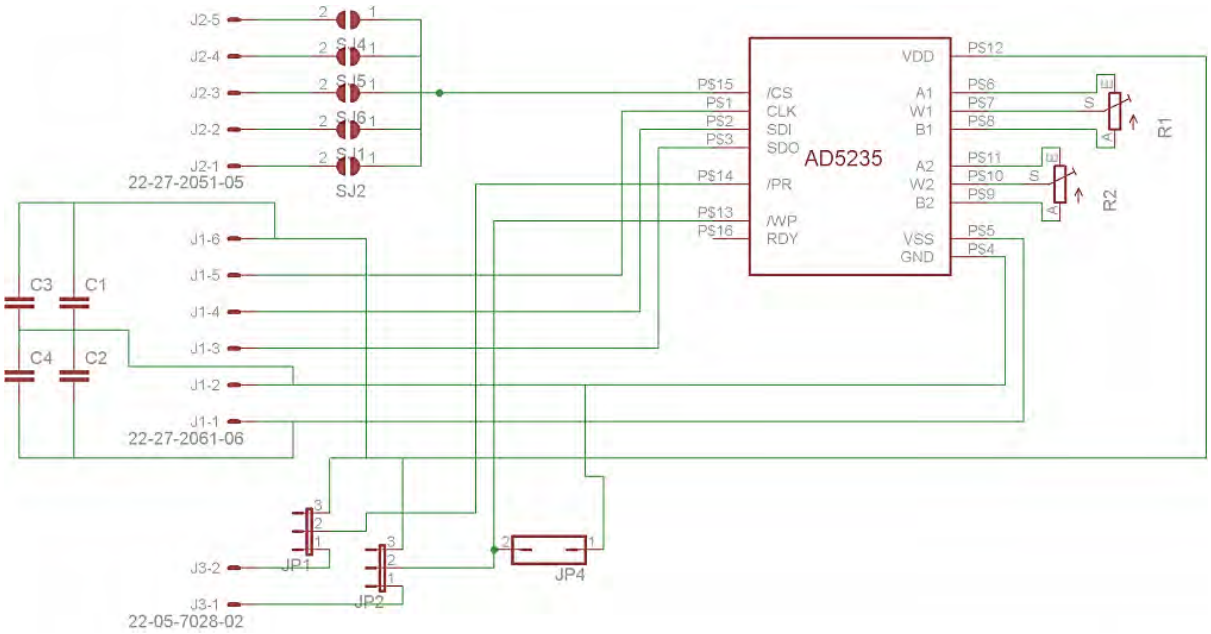


**Figure C-5**: Digital gain daughter board schematic (designed by S Stoeckigt, N Divekar, and LR John)

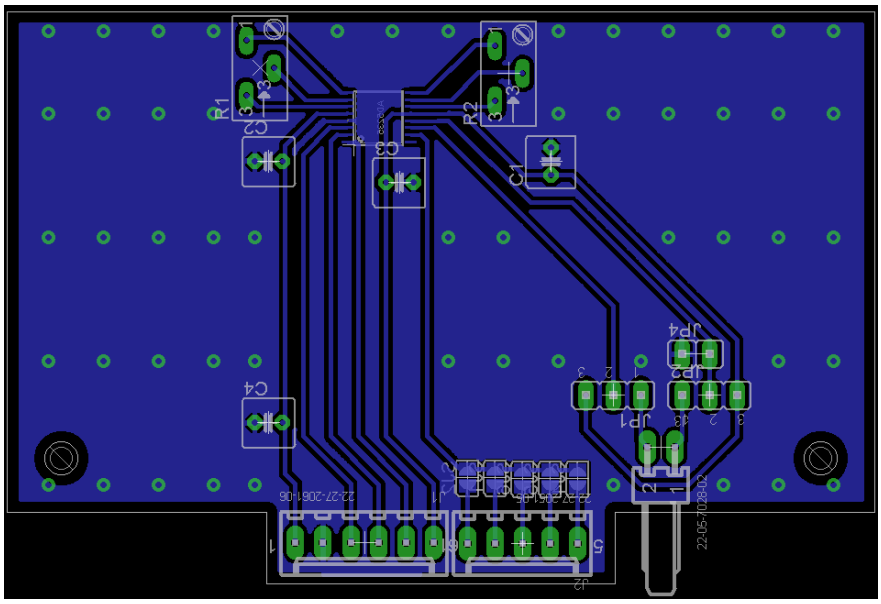


**Figure C-6**: PCB layout of gain daughter board (designed by S Stoeckigt, N Divekar, and LR John)

## C.3 Experimental acquisition programme LabVIEW® code

The LabVIEW® code written to record the monopolar EMG activity and provide visual feedback for the participant during the experiment consisted of sections performing different roles. The code was developed as a collaborative effort as a collaborative effort by the author and C Swanepoel, with contributions from R Smith. Due to its size, it is not possible to present the programme as a whole, so important sub-components of the programme are shown in sections C.3.1 to C.3.7.

### C.3.1 Data acquisition while loop

The data acquisition while loop sampled the monopolar EMG and strain gauge channels with each iteration and appended the samples into a software buffer. A screen shot of the block diagram code fulfilling this function is shown in Figure C-7.

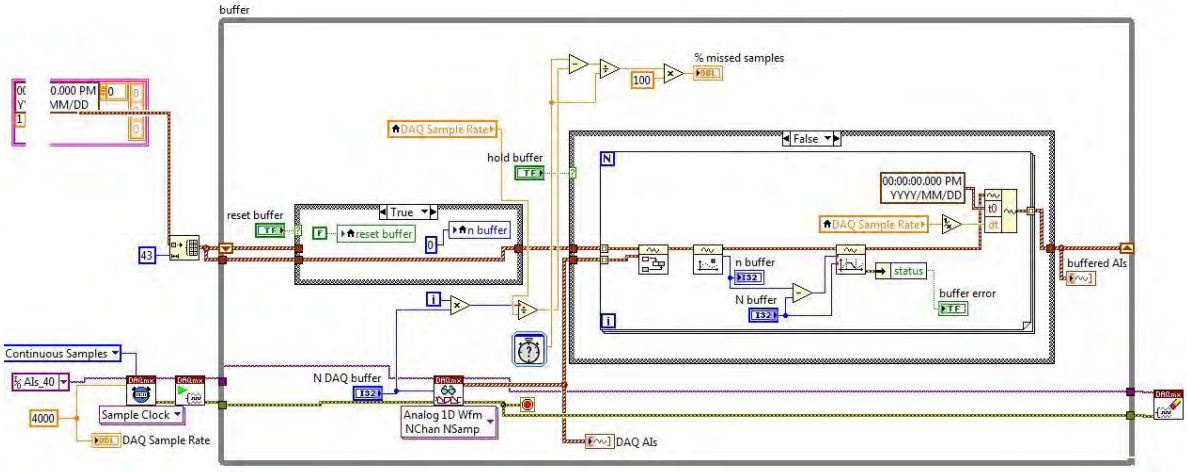


**Figure C-7**: Data acquisition loop

### C.3.2 EMG signal display

The monopolar EMG signals from all the electrodes could be displayed to verify whether the channels were flooded with noise. Screen shots of the Front Panel and Block Diagram code performing this function are shown in Figure C-8 and Figure C-9.

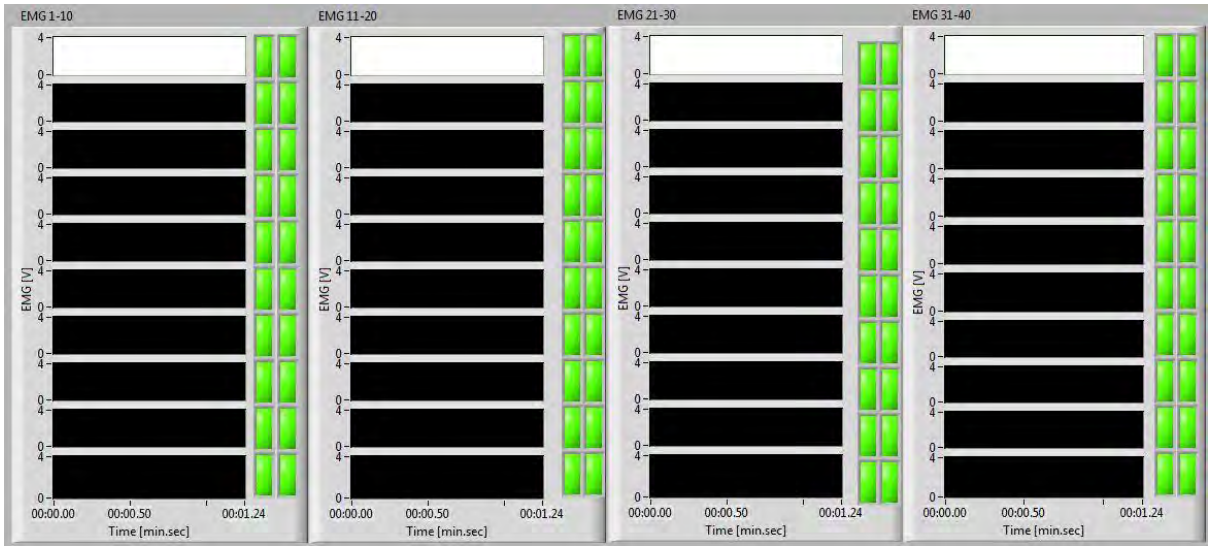


**Figure C-8**: EMG display on Front Panel

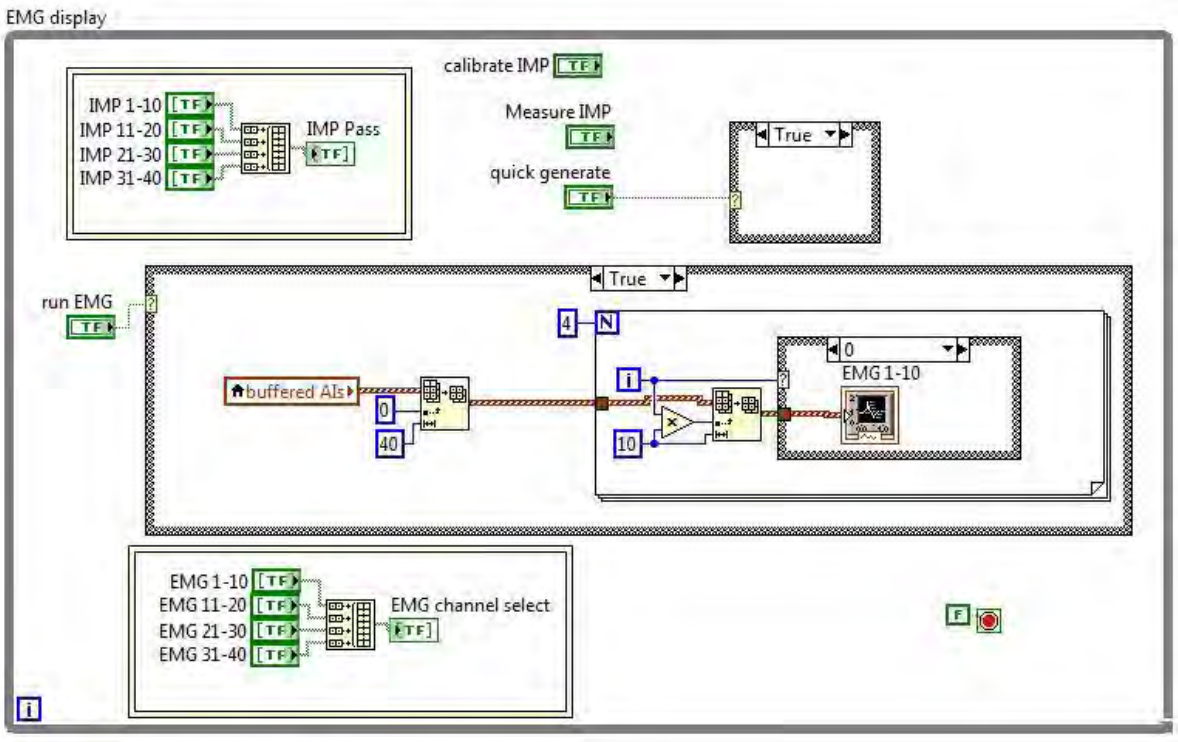


**Figure C-9:** Block Diagram of EMG display function

### C.3.3 MVC measurement

As mentioned in section 3.2.2, the force gauges for providing feedback of the participant effort levels were scaled according to the force generated during MVC measurements for each isometric contraction. Each MVC button (shown in Figure C-10) executed a specific operation to record the peak strain gauge value for each isometric contraction (according to the strain gauge polarity descriptions in Table 2-1 and Table 2-2) in the Block Diagram (shown in Figure C-11)


**Figure C-10**: MVC measurement buttons on the Front Panel

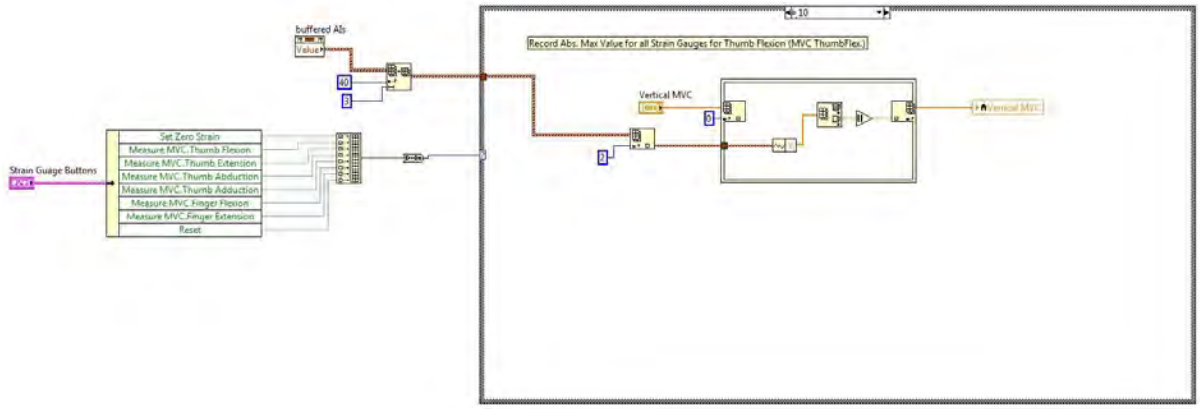


**Figure C-11**: MVC button selector case statement in the Block Diagram

### C.3.4 Visual force feedback

The effort level feedback gauges and images depicting the required movement shown in Table 2-3 were presented to the participant as a combination and modified for each isometric contraction. The output from each of the gauges was scaled for the corresponding isometric contraction using the Block Diagram code shown in Figure C-12.

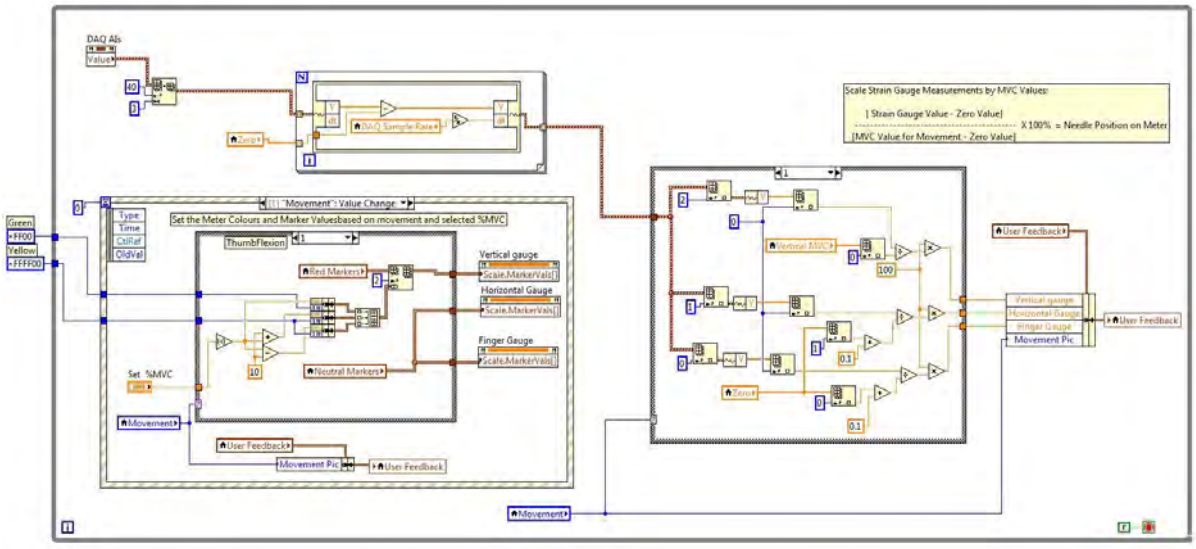


**Figure C-12**: Block diagram of effort level scaling and required isometric contraction visual feedback combinations.

### C.3.5 Visual feedback randomization

The visual feedback randomization procedure for each isometric contraction was performed by the LabVIEW® acquisition programme using the Block Diagram in Figure C-13 to display the visual feedback combinations shown in Table 2-3.

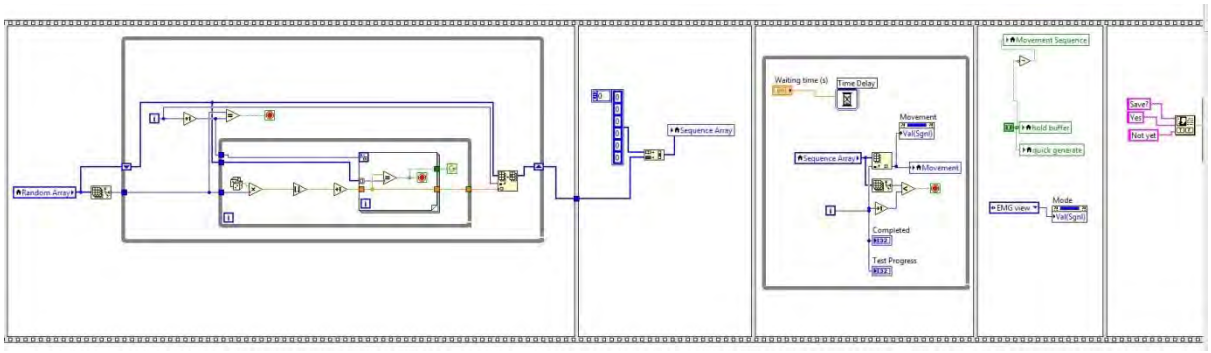


**Figure C-13**: Participant visual feedback randomization procedure Block Diagram code

### C.3.6 Digital gain control

The gain of the EMG amplifiers was set in the LabVIEW® acquisition programme by:

1. selecting the serial port to communicate with the Arduino microcontroller (highlighted by the red rectangle in Figure C-14)
2. selecting a Gain value on the slider or typing a value in the input box (highlighted by the violet rectangle in Figure C-14)
3. pressing the 'Set Gain' button (highlighted by a blue rectangle in Figure C-14)

The LabVIEW® acquisition programme then sends a serial command to the Arduino, a copy of which is shown in the 'arduino in' dialogue box (highlighted by a green box in Figure C-14). The digital potentiometers are set when a return message is seen in the 'arduino out' dialogue box (highlighted by a yellow rectangle in Figure C-14). The Block Diagram code responsible for this function is shown in Figure C-15.

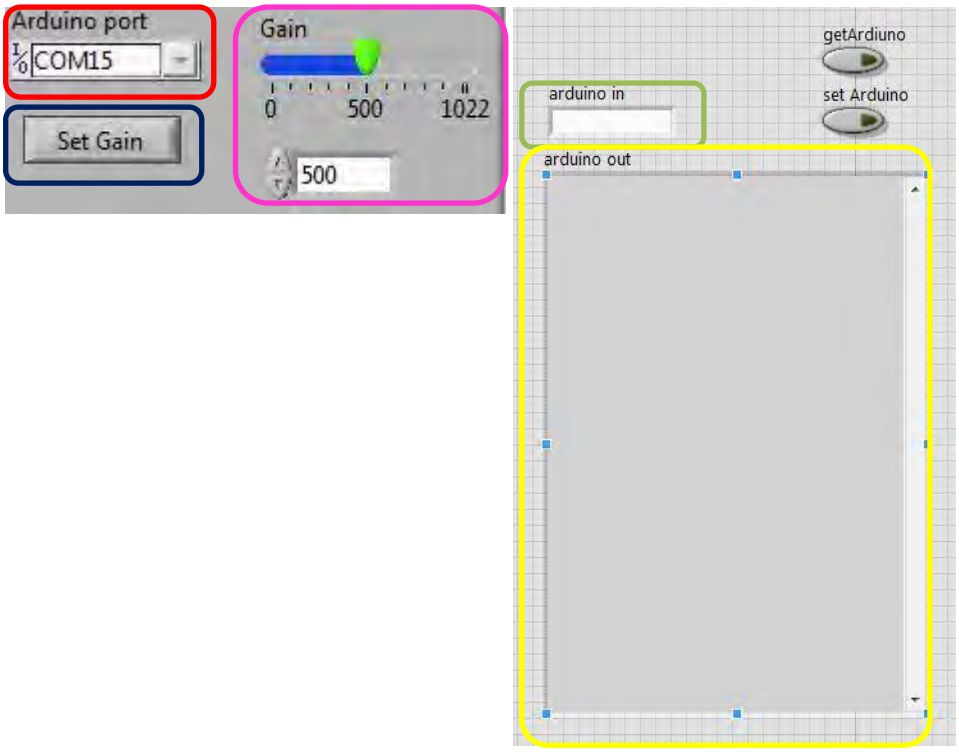


**Figure C-14**: Setting the gain of the amplifier boards by selecting the serial port to communicate with the Arduino microcontroller (highlighted by the red rectangle); selecting a Gain value on the slider or typing a value in the input box (highlighted by the violet rectangle); pressing the 'Set Gain' button (highlighted by a blue rectangle). The LabVIEW® acquisition programme then sends a serial command to the Arduino, a copy of which is shown in the 'arduino in' dialogue box (highlighted by a green rectangle). The digital potentiometers are set when a return message is seen in the 'arduino out' dialogue box (highlighted by a yellow rectangle).

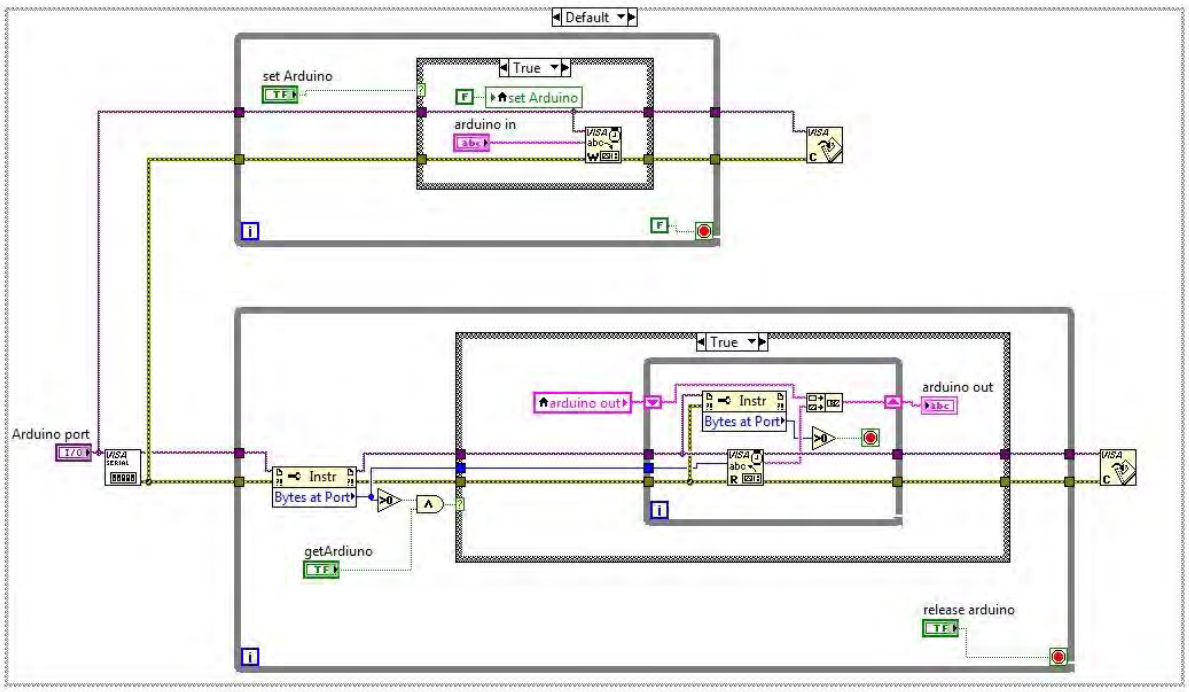


**Figure C-15**: Block Diagram code for setting the gain of the digital potentiometers with the Arduino microcontroller

### C.3.7 Saving the experimental data

After completing an experimental recording, the programme refers back to the EMG display tab and a dialogue box asks whether the examiner wants to save the test (shown in Figure C-16).

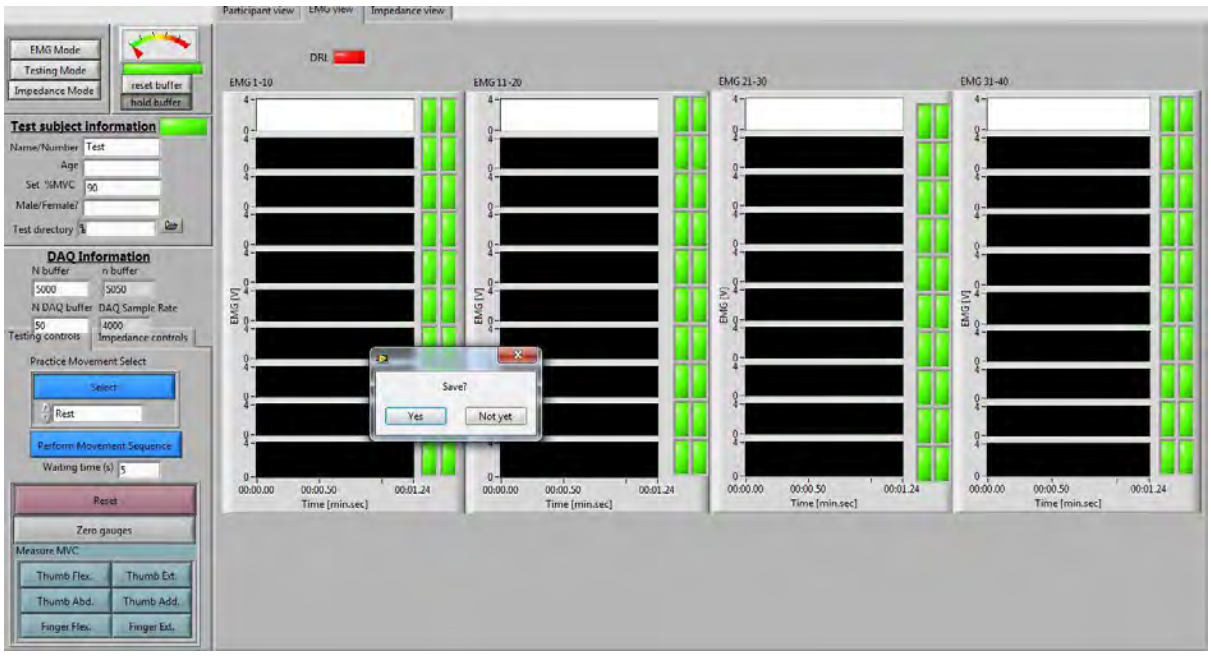


**Figure C-16:** Front Panel display after the completion of an experimental recording

If the examiner is satisfied with the recording and selects the 'Yes' button, the data is saved into a specific format using the Block Diagram code shown in the Figure C-17:

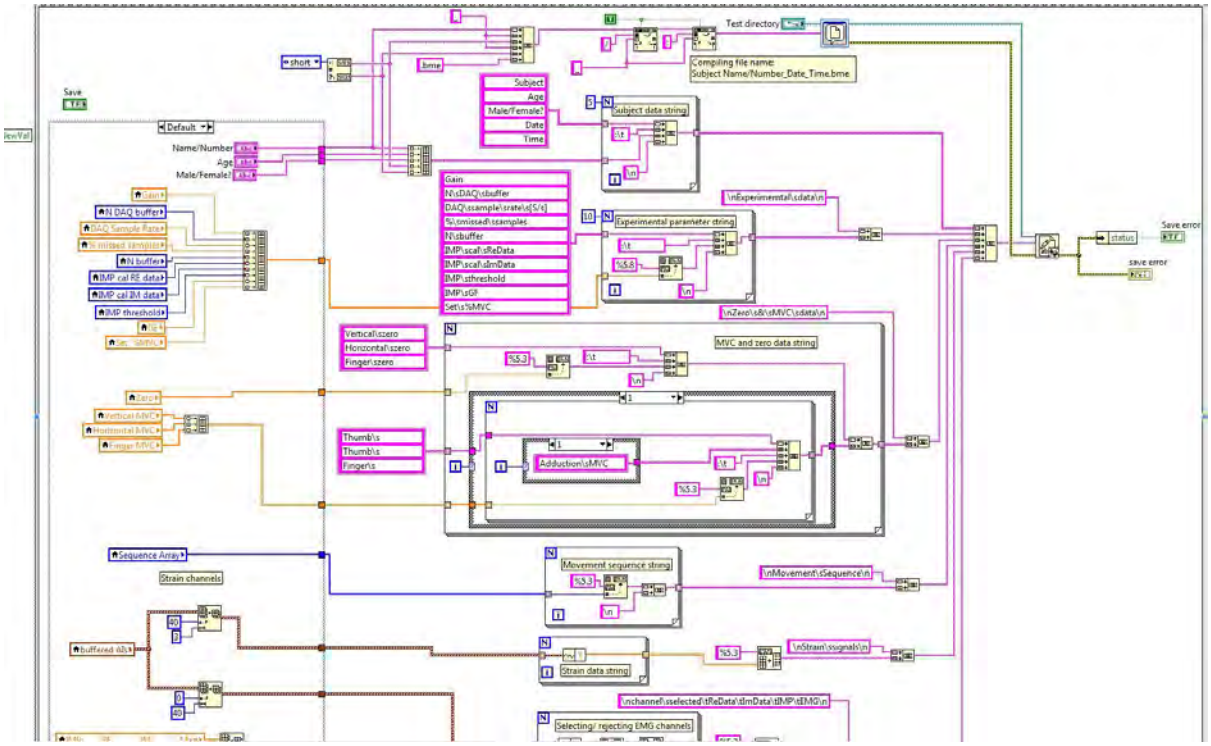


**Figure C-17:** Experimental data save function Block Diagram code

## C.4 Attenuator module

### C.4.1 Attenuator module photos

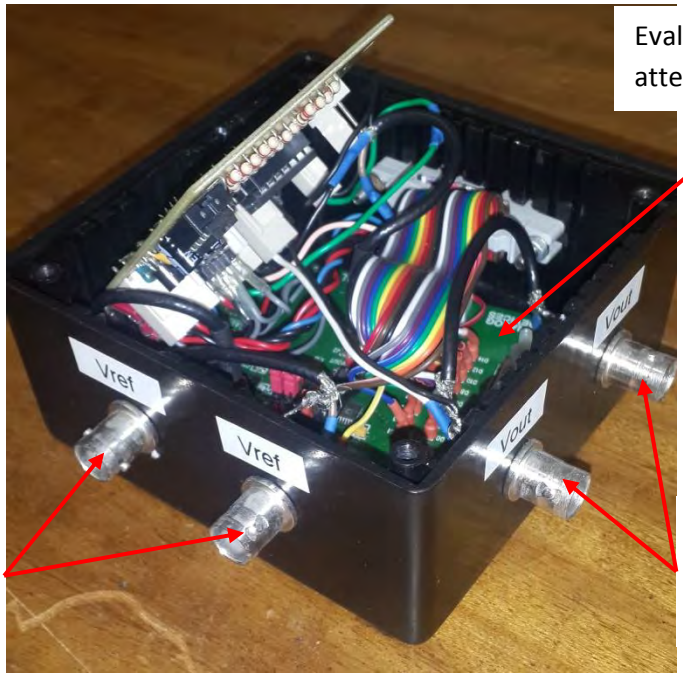


**Figure C-18:** Photo of attenuator module

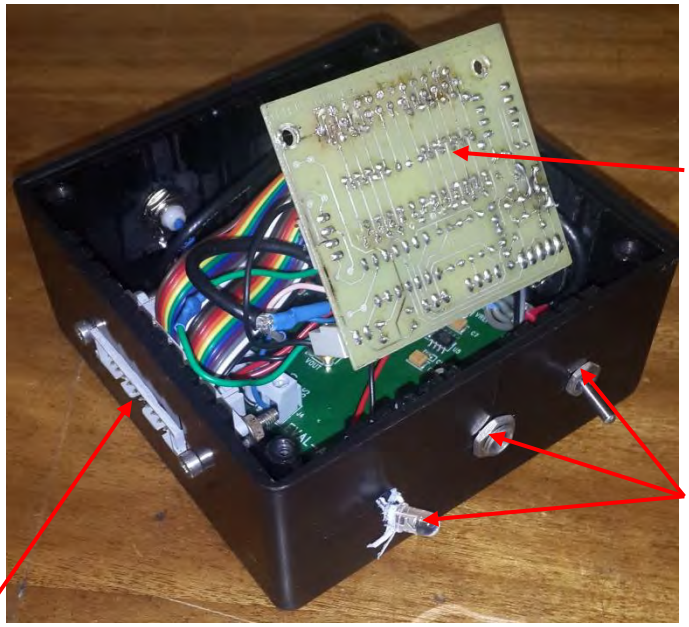

Attenuator power supply circuit board

1. 12V power supply input jack and
2. ON switch
3. ON light

Socket for digital control of EVAL-AD5546SDZ via National Instruments DAQ

**Figure C-19:** Photo of attenuator module

### C.4.2 Circuit diagrams and board layouts

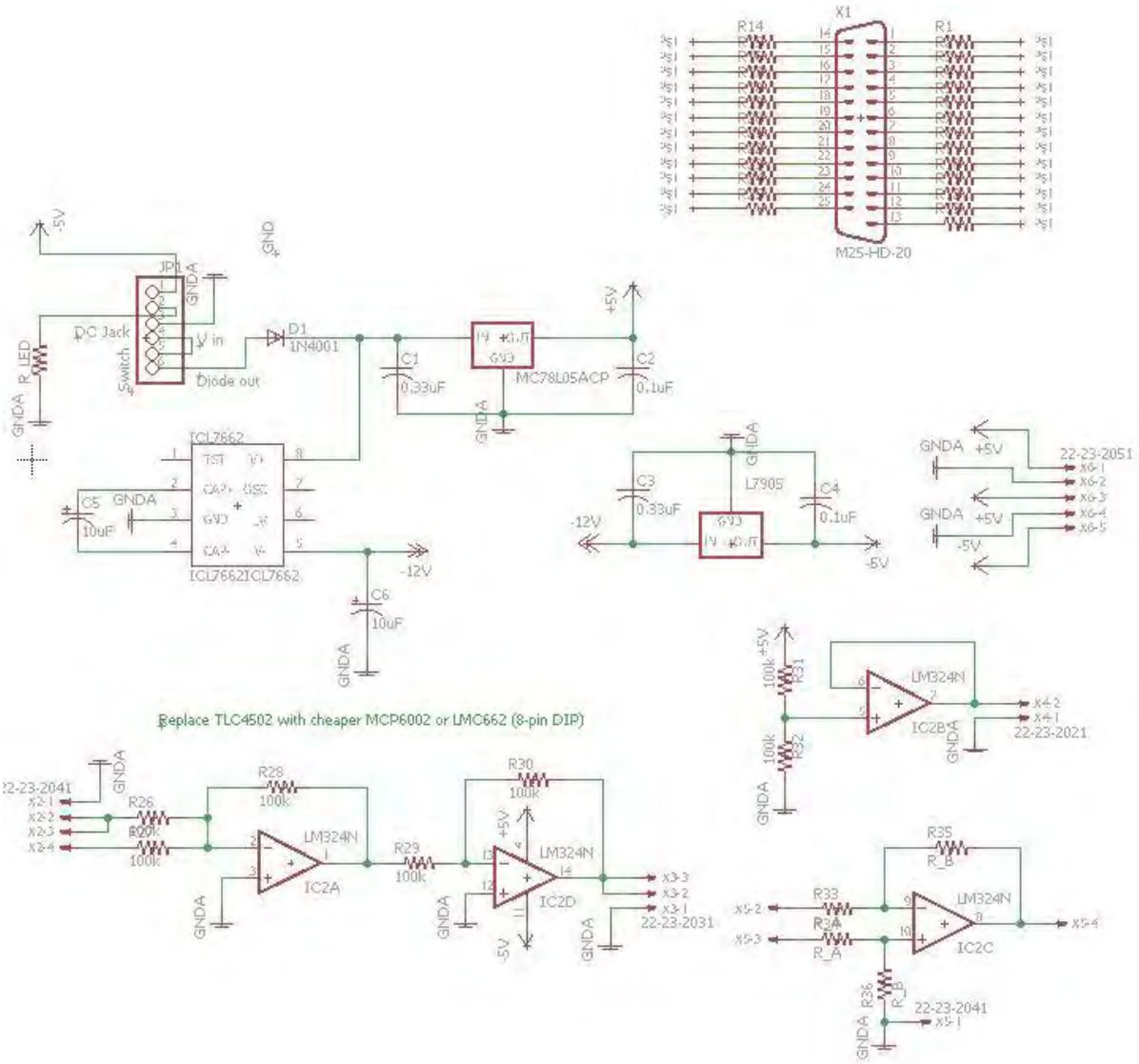


**Figure C-20:** Attenuator power board schematic

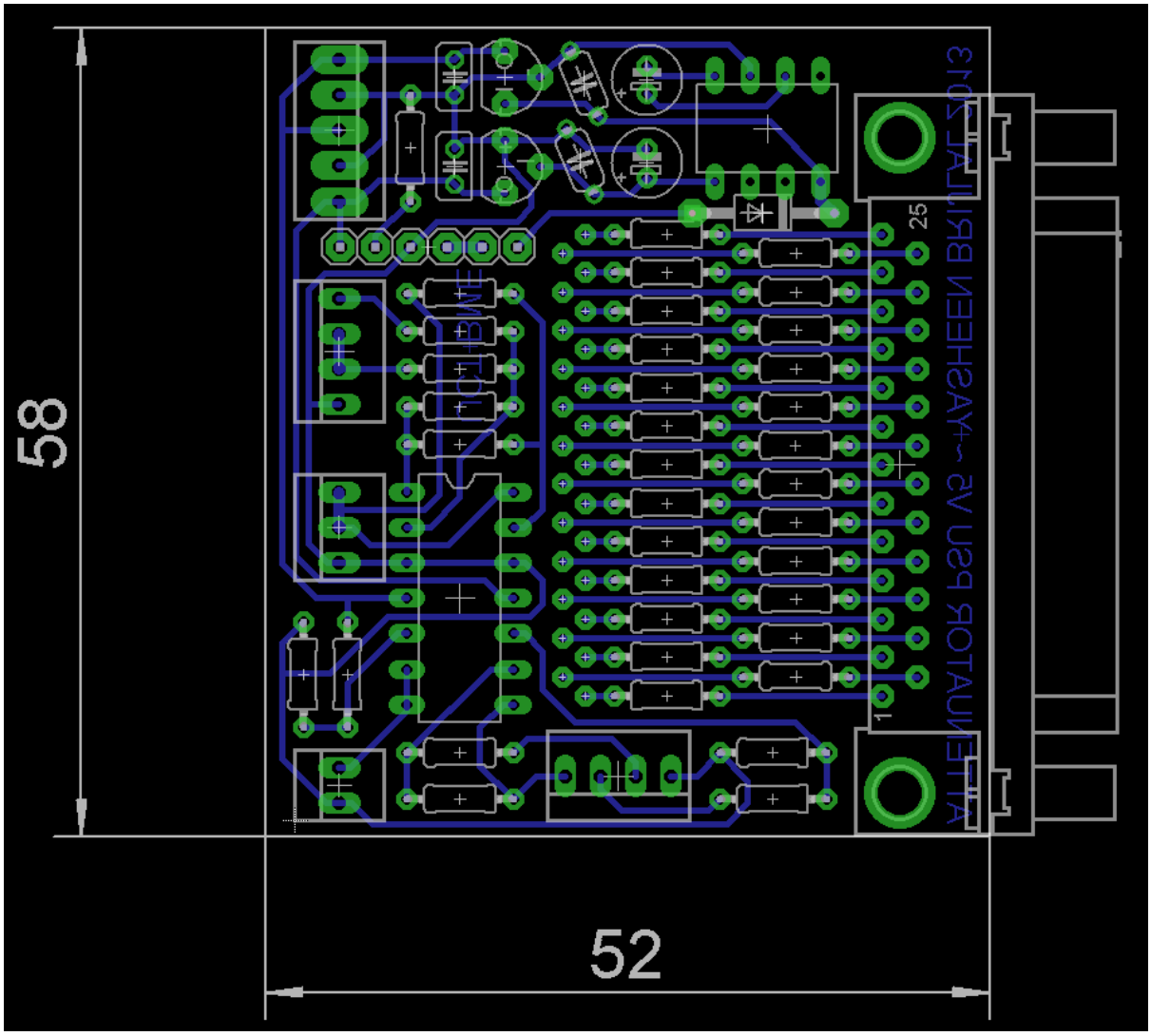


**Figure C-21:** Attenuator power board layout diagram (board layout by Yasheen Brijlal)

### C.4.3 Attenuator module LabVIEW® code

The LabVIEW® code for the Attenuator module set the attenuation coefficient on the EVAL_AD55446SDZ circuit board using a specific digital communication protocol. The attenuation value was selected by clicking the appropriate push button (see Figure C-22).

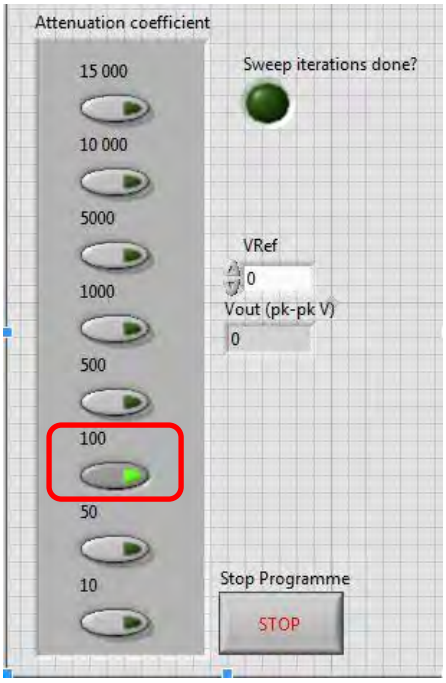


**Figure C-22:** Attenuation push buttons (highlighted by the red rectangle)

The push button then executes the communication protocol in the Block Diagram and sets the appropriate attenuation coefficient (shown in Figure C-23)

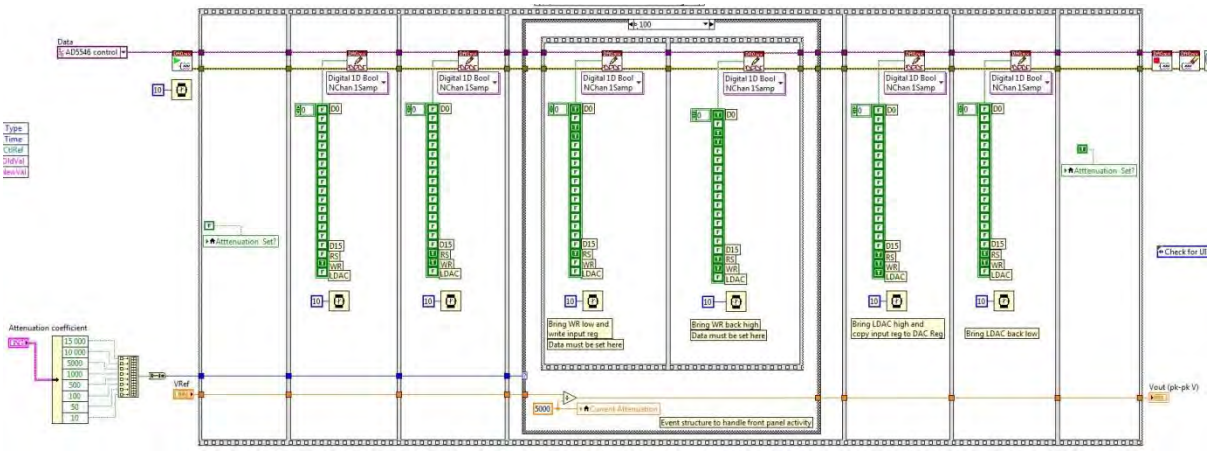

**Figure C-23:** Attenuation coefficient communication Block Diagram code

# APPENDIX D Statistics data

## D.1 R statistical programming code

The R code used in the present study for the statistical analysis was written by Ushma Galal of the Statistical Consultancy Service at the University of Cape Town. Separate R code files were used to calculate the overall accuracy and sensitivity and specificity for each muscle; however the code used was replicated almost identically for each measure. The only differences (highlighted in section D.1.1 below) were:

1. The working directory,
2. The comma separated variable (.csv) file being read
3. Parameter being modelled.

### D.1.1 R code

```
library(gdata)

setwd("c:\\users\\jem\\dropbox\\2014\\r stats work\\final stats
analysis - 19 may 2015\\fpl")

JPdata <- read.csv("FPL_cleaned.csv")

# I am saving the data so you don't need to read it in again.
Just attach it when you want to use it

fix(JPdata)
names(JPdata)
str(JPdata)

library(nlme)

attach(JPdata)


# MODEL - Accuracy
Acc.lme<-lme(Accuracy~Threshold,random=~
1|SID,na.action=na.exclude)
anova(Acc.lme) # this will tell you immediately which variables
are significant
summary(Acc.lme) # this gives significance for each level of the
categorical variables
# don't worry about the correlation matrix in the output
intervals(Acc.lme) # confidence intervals of estimates
```

## D.2 Base Data Assumptions

Table D-1 is a summary of the mean and standard deviation (std dev) values, as well as the spread of the base data (represented by the minimum, maximum, median, 25$^{th}$ and 75$^{th}$ percentile values) used for each muscle's mixed effects model. The median and mean values in Table D-1 show that

the base data for FPL (D), APL (D) were close to normally distributed (since the difference between the two numbers is not very big). However, there is a considerable difference between the median and mean sensitivity values for EPL (D) and EPB (D) the median and mean accuracy values for FD (S) and ED (S) (highlighted in yellow in Table D-1). These differences indicating that the accuracy base data for these muscles might be skewed.

**Table D-1**: Summary table of base data for the deep (D) and superficial (S) muscles. The values highlighted in yellow show a large difference between the mean and median values, indicating that the base data might be skewed.

| Muscles | | Minimum | 25th percentile | Median | Mean | 75th percentile | Maximum | std dev |
|---|---|---|---|---|---|---|---|---|
| **FPL (D)** | Accuracy | 0.00 | 0.31 | 0.47 | 0.49 | 0.69 | 1.00 | 0.28 |
| | Sensitivity | 0.00 | 0.55 | 0.72 | 0.69 | 0.82 | 1.00 | 0.22 |
| | Specificity | 0.05 | 0.51 | 0.63 | 0.62 | 0.73 | 0.98 | 0.16 |
| **EPL (D)** | Accuracy | 0.00 | 0.27 | 0.57 | 0.52 | 0.73 | 1.00 | 0.27 |
| | Sensitivity | 0.00 | 0.86 | 1.00 | 0.85 | 1.00 | 1.00 | 0.29 |
| | Specificity | 0.15 | 0.49 | 0.63 | 0.63 | 0.78 | 0.99 | 0.17 |
| **EPB (D)** | Accuracy | 0.19 | 0.81 | 0.91 | 0.85 | 0.94 | 1.00 | 0.15 |
| | Sensitivity | 0.00 | 0.98 | 1.00 | 0.89 | 1.00 | 1.00 | 0.25 |
| | Specificity | 0.47 | 0.80 | 0.91 | 0.86 | 0.95 | 1.00 | 0.12 |
| **APL (D)** | Accuracy | 0.00 | 0.17 | 0.32 | 0.36 | 0.52 | 1.00 | 0.26 |
| | Sensitivity | 0.00 | 0.58 | 0.70 | 0.67 | 0.90 | 1.00 | 0.29 |
| | Specificity | 0.00 | 0.43 | 0.52 | 0.52 | 0.62 | 0.99 | 0.17 |
| **FD (S)** | Accuracy | 0.00 | 0.00 | 0.03 | 0.18 | 0.22 | 1.00 | 0.28 |
| | Sensitivity | 0.00 | 0.20 | 0.38 | 0.43 | 0.64 | 1.00 | 0.29 |
| | Specificity | 0.00 | 0.19 | 0.35 | 0.39 | 0.58 | 0.98 | 0.24 |
| **ED (S)** | Accuracy | 0.00 | 0.00 | 0.02 | 0.19 | 0.29 | 1.00 | 0.29 |
| | Sensitivity | 0.00 | 0.09 | 0.29 | 0.38 | 0.63 | 1.00 | 0.30 |
| | Specificity | 0.00 | 0.14 | 0.29 | 0.35 | 0.56 | 0.95 | 0.25 |

**Table D-2** shows the results from the random effect variance analysis conducted by the R statistical code. The values indicate that there is more variation between experimental repetitions performed by the same participant than between participants. This result validates the decision to randomize the order in which the isometric contractions were performed in, since it is clear that there is very little learning effect present. I.e. the results were not skewed due to a participant getting better and better with increased practice of an isometric contraction sequence as the experiment progressed.

**Table D-2**: Random effect variance analysis for all the muscles under investigation

| Muscles | Random effect variance analysis | |
|---|---|---|
| | Intra-participant standard error (95% CI) | Inter-participant standard error (95% CI) |
| **FPL (D)** | 0.12 (0.11, 0.12) | 0.12 (0.07, 0.15) |
| **EPL (D)** | 0.13 (0.13, 0.13) | 0.08 (0.05, 0.11) |
| **EPB (D)** | 0.09 (0.09, 0.09) | 0.06 (0.04, 0.08) |
| **APL (D)** | 0.11 (0.11, 0.11) | 0.07 (0.05, 0.10) |
| **FD (S)** | 0.20 (0.19, 0.20) | 0.14 (0.10, 0.21) |
| **ED (S)** | 0.21 (0.21, 0.22) | 0.13 (0.09, 0.19) |

## D.3 'Accuracy' model residual variance

The variances of the residuals from the 'Accuracy' model for each muscle under investigation are presented in the form of scatter plots in sections D.3.1 to D.3.6. The plots serve to indicate whether all the variables had been taken into account and whether there was an even variance for each muscle. For each of the muscles under investigation, the figures indicate a fairly even spread of the standardized residuals with no groupings of data. The tailing off of the values for the higher 'Fitted values' is a result of the exclusionary criteria described in section 3.5.2. Thus the data was adequately modelled and the model results could be considered valid.

### D.3.1 FPL (D)

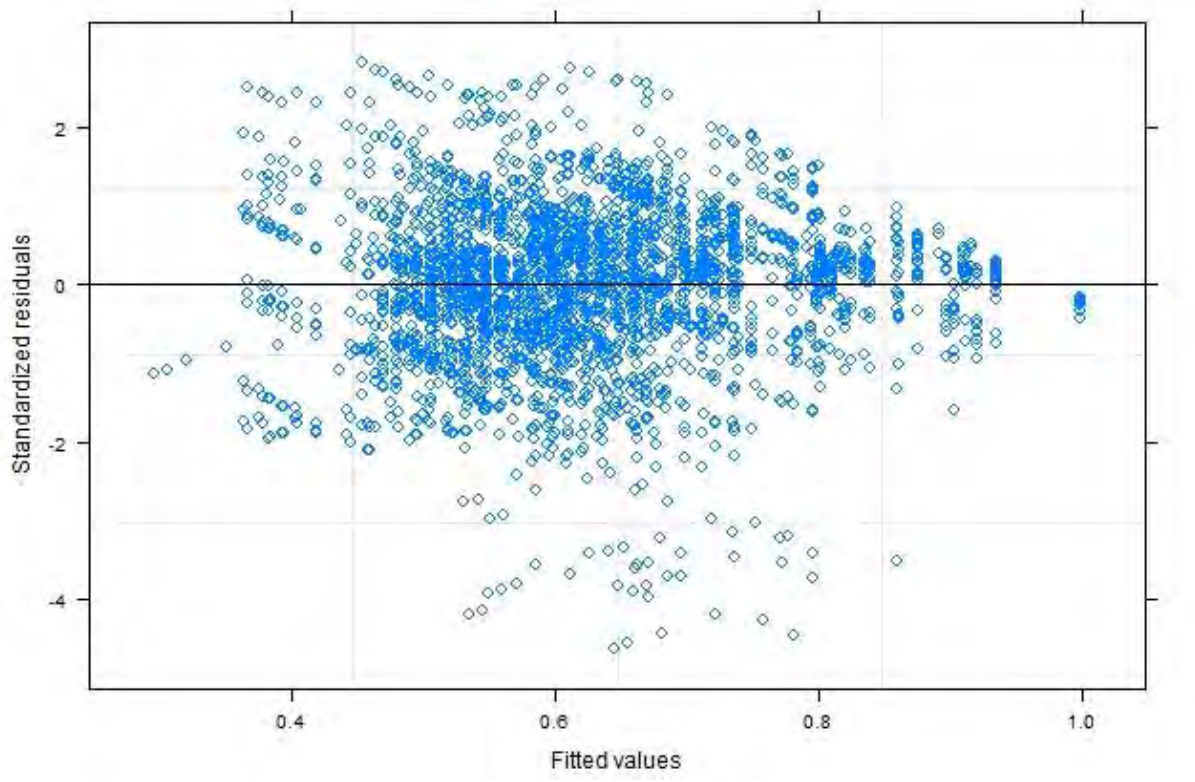


**Figure D-1**: Scatter plot of residuals (random effect error function) from FPL's Accuracy model to verify that the residuals show equal variance across all the independent variables (ThCs). The

horizontal axis ('Fitted values') refers to the observed values to which the model is fitted once the independent variables are accounted for. The vertical axis ('Standardized residuals') refers to the residual error between the model and original values divided by the standard deviation of the residual. The slope present in the residuals towards the higher end of the 'Fitted values' is due to bounding from the experimental exclusion procedure described in section 3.5.2

### D.3.2 EPL (D)

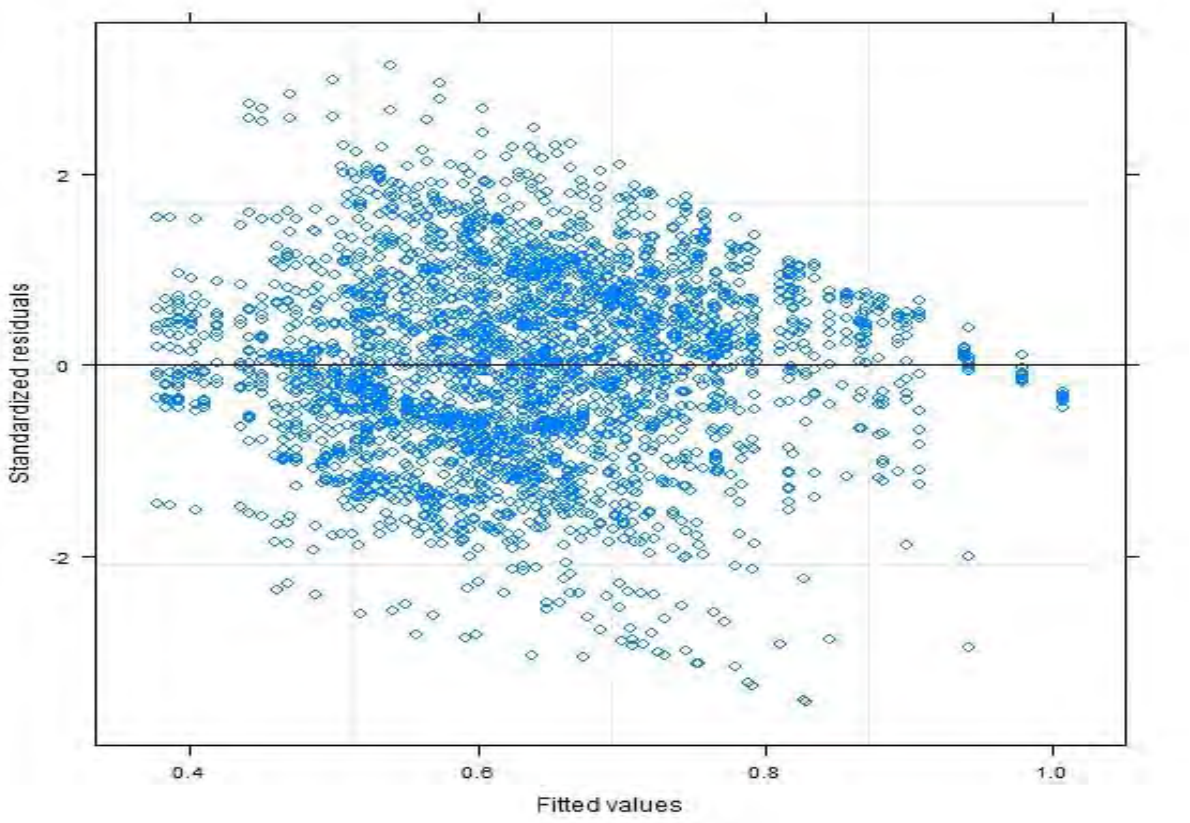


**Figure D-2:** Scatter plot of residuals (random effect error function) from EPL's Accuracy model to verify that the residuals show equal variance across all the independent variables (ThCs). The horizontal axis ('Fitted values') refers to the observed values to which the model is fitted once the independent variables are accounted for. The vertical axis ('Standardized residuals') refers to the residual error between the model and original values divided by its standard deviation. The slope present in the residuals towards the higher end of the 'Fitted values' is due to bounding from the experimental exclusion procedure described in section 3.5.2

### D.3.3 EPB (D)

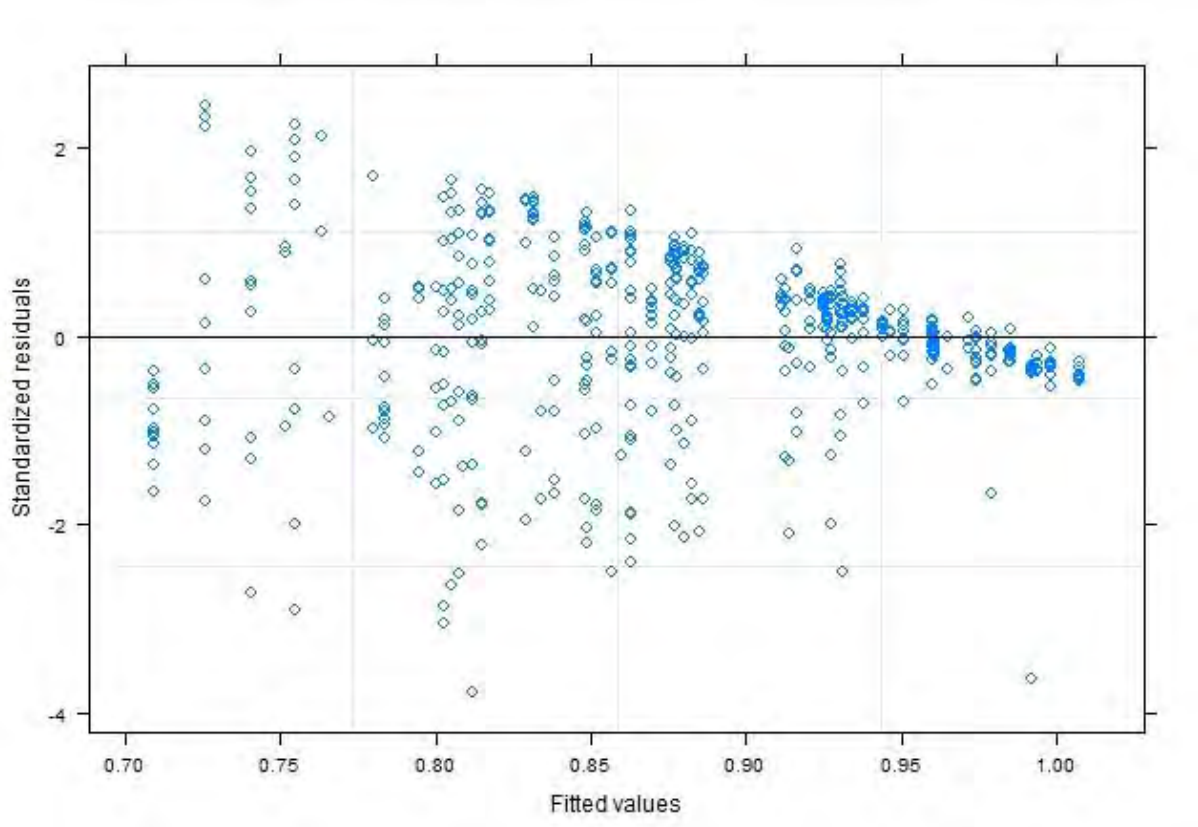


**Figure D-3:** Scatter plot of residuals (random effect error function) from EPB's Accuracy model to verify that the residuals show equal variance across all the independent variables (ThCs). The horizontal axis ('Fitted values') refers to the observed values to which the model is fitted once the independent variables are accounted for. The vertical axis ('Standardized residuals') refers to the residual error between the model and original values divided by the standard deviation of the residual. The slope present in the residuals towards the higher end of the 'Fitted values' is due to bounding from the experimental exclusion procedure described in section 3.5.2

### D.3.4 APL (D)

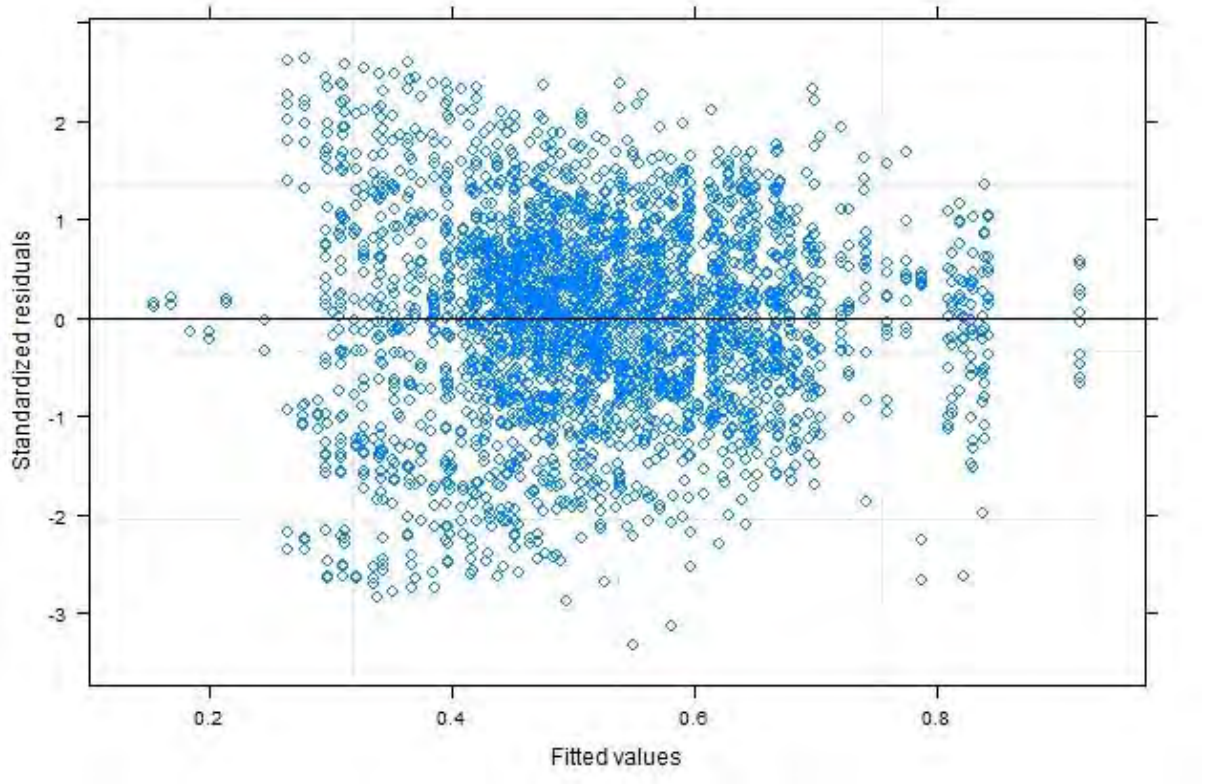


**Figure D-4:** Scatter plot of residuals (random effect error function) from APL's Accuracy model to verify that the residuals show equal variance across all the independent variables (ThCs). The horizontal axis ('Fitted values') refers to the observed values to which the model is fitted once the independent variables are accounted for. The slope present in the residuals towards the higher end of the 'Fitted values' is due to bounding from the experimental exclusion procedure described in section 3.5.2

### D.3.5 FD (S)

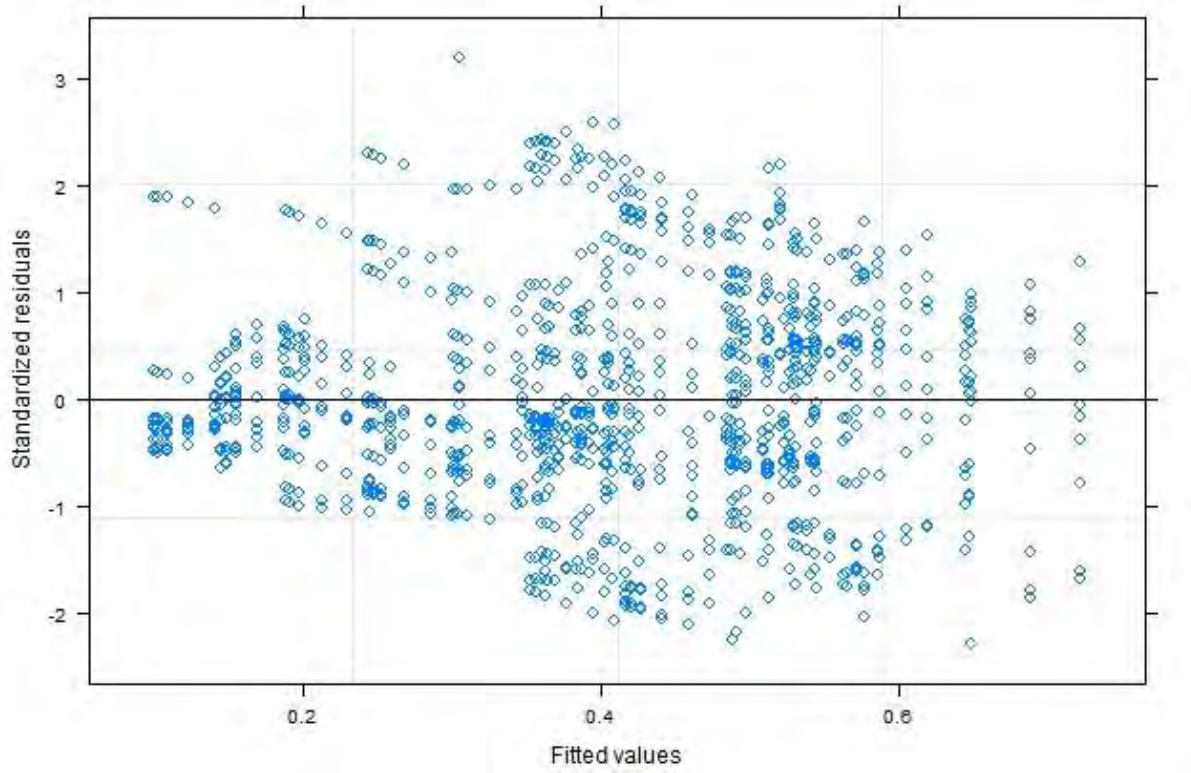


**Figure D-5:** Scatter plot of residuals (random effect error function) from FD's Accuracy model to verify that the residuals show equal variance across all the independent variables (ThCs). The horizontal axis ('Fitted values') refers to the observed values to which the model is fitted once the independent variables are accounted for. The vertical axis ('Standardized residuals') refers to the residual error between the model and original values divided by the standard deviation of the residual. The slope present in the residuals (highlighted by the red lines) is due to bounding from the experimental exclusion procedure. The banding of the 'Standardized residuals' in the vertical axis is indicative of the variation in *pa* for fixed *fa* values.

### D.3.6 ED (S)

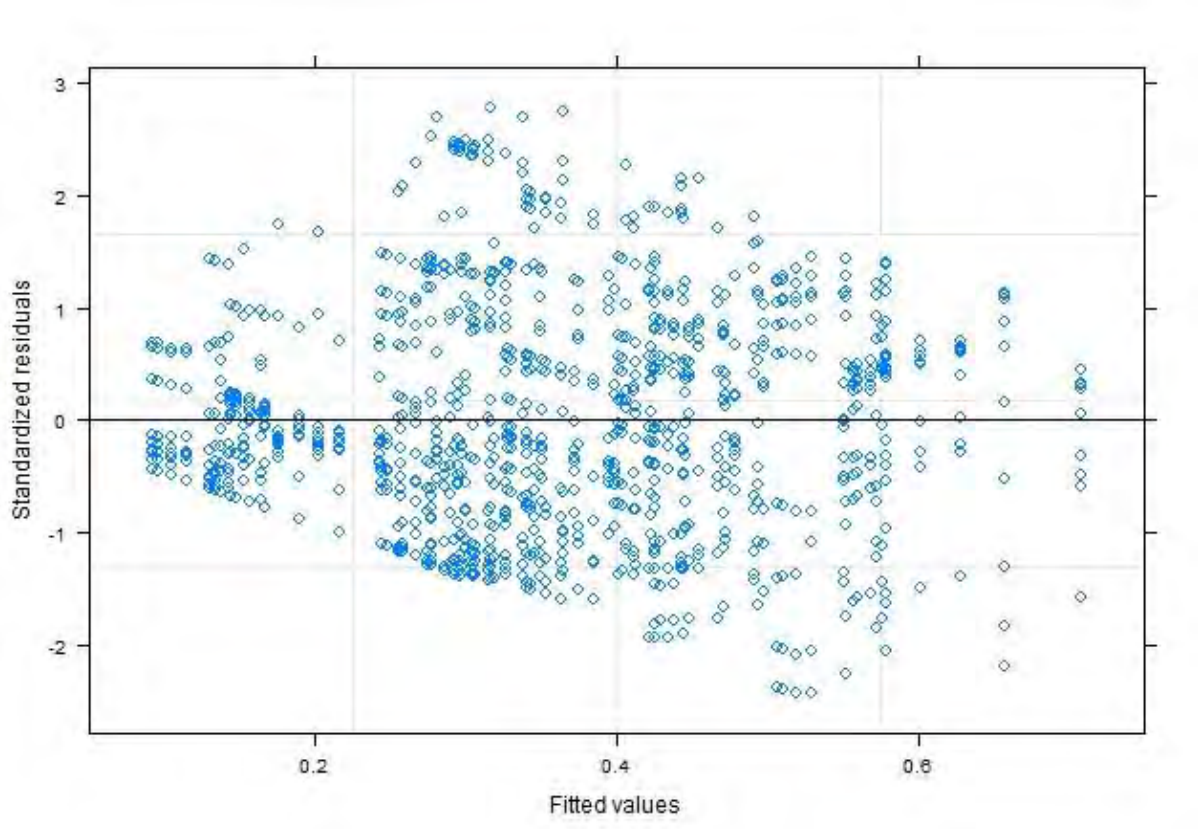


**Figure D-6:** Scatter plot of residuals (random effect error function) from ED's Accuracy model to verify that the residuals show equal variance across all the independent variables (ThCs). The horizontal axis ('Fitted values') refers to the observed values to which the model is fitted once the independent variables are accounted for. The vertical axis ('Standardized residuals') refers to the residual error between the model and original values divided by the standard deviation of the residual. The slope present in the residuals towards the lower end of the 'Fitted values' is due to bounding from the experimental exclusion procedure described in section 3.5.2.

## D.4 'Accuracy' model residual histograms

Histograms of the residuals for the 'Accuracy' models were plotted to ensure the errors (residuals) from each model were normally distributed. The histograms for each muscle under investigation are shown in sections D.4.1 - D.4.6. All the histograms show a roughly normal distribution, thus the assumption for normality of the modelled was upheld and the model was valid.

### D.4.1 FPL (D)

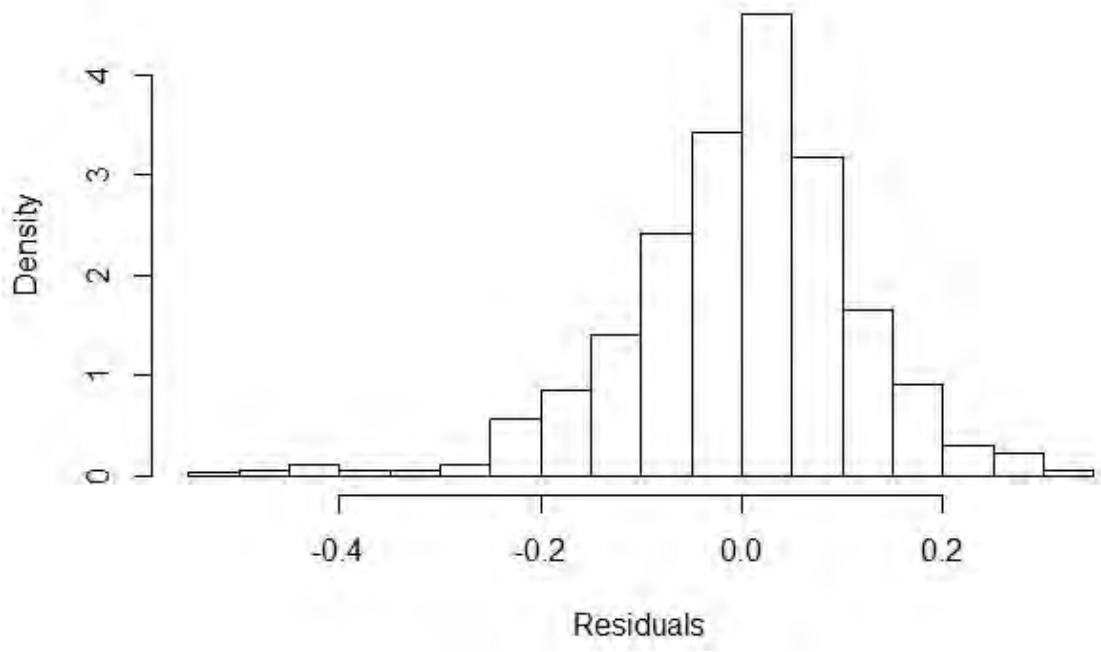


**Figure D-7**: Histogram of residuals from FPL Accuracy model show the residuals are normally distributed, thus the assumption of normality by the mixed effects model holds

### D.4.2 EPL (D)

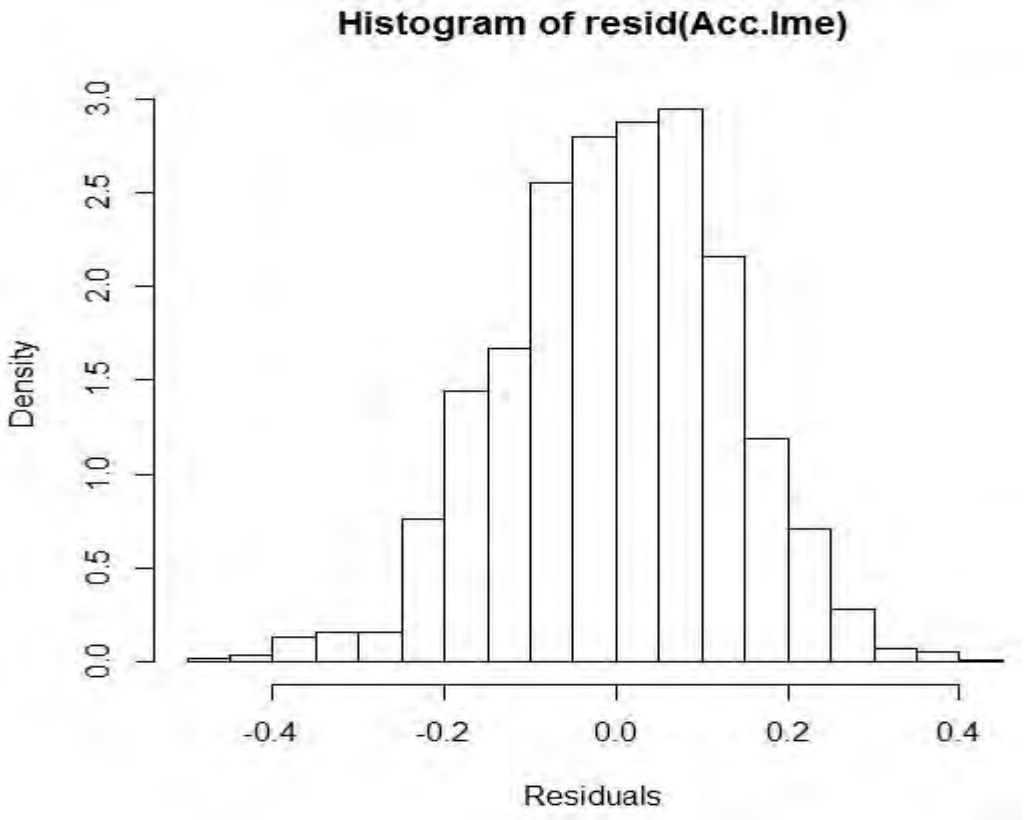


**Figure D-8:** Histogram of residuals from EPL's Accuracy model show the residuals are slightly skewed, but still normally distributed, thus the assumption of normality by the mixed effects model holds

### D.4.3 EPB (D)

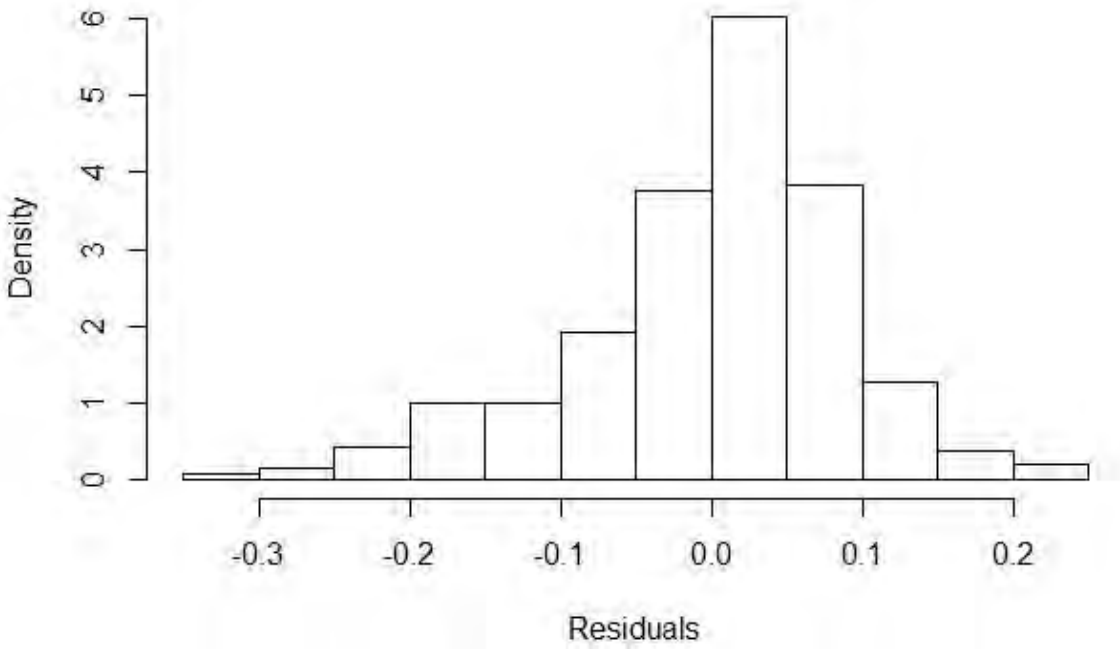


**Figure D-9**: Histogram of residuals from EPB's Accuracy model show the residuals are normally distributed, thus the assumption of normality by the mixed effects model holds

### D.4.4 APL (D)

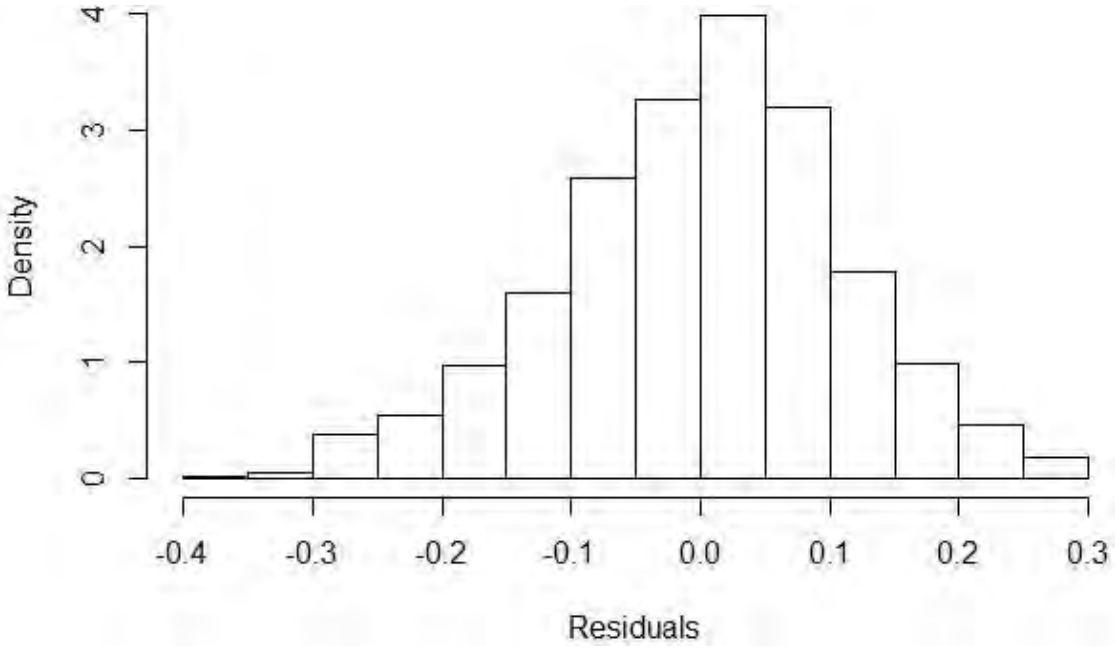


**Figure D-10:** Histogram of residuals from APL's Accuracy model show the residuals are normally distributed, thus the assumption of normality by the mixed effects model holds

### D.4.5 FD (S)

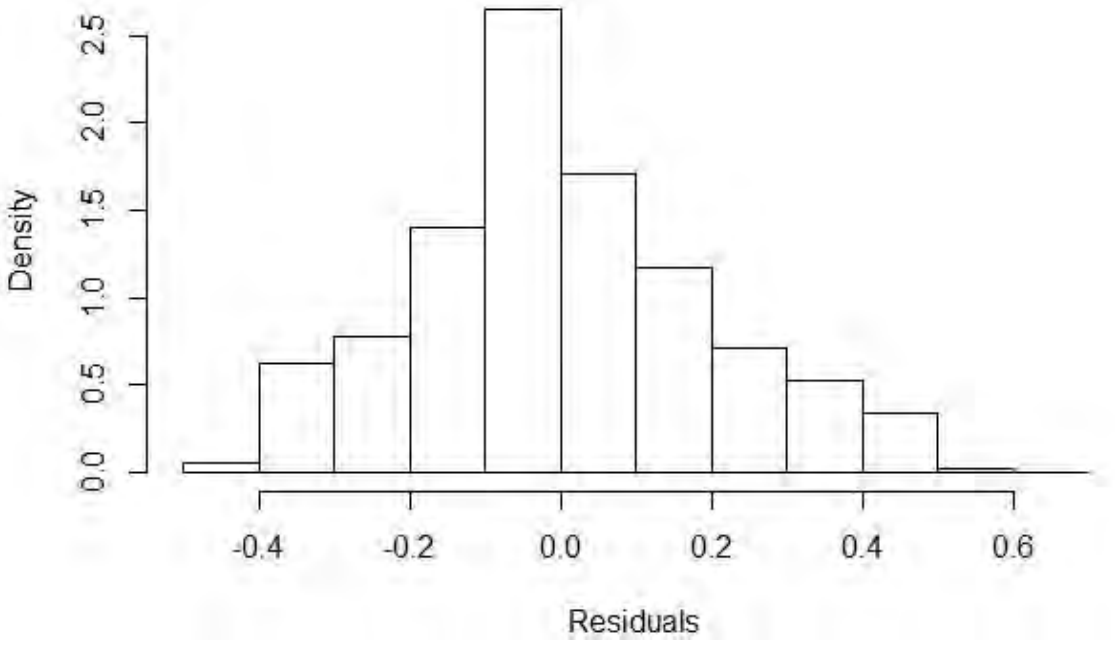


**Figure D-11:** Histogram of residuals from FD's Accuracy model show the residuals are normally distributed, thus the assumption of normality by the mixed effects model holds

### D.4.6 ED (S)

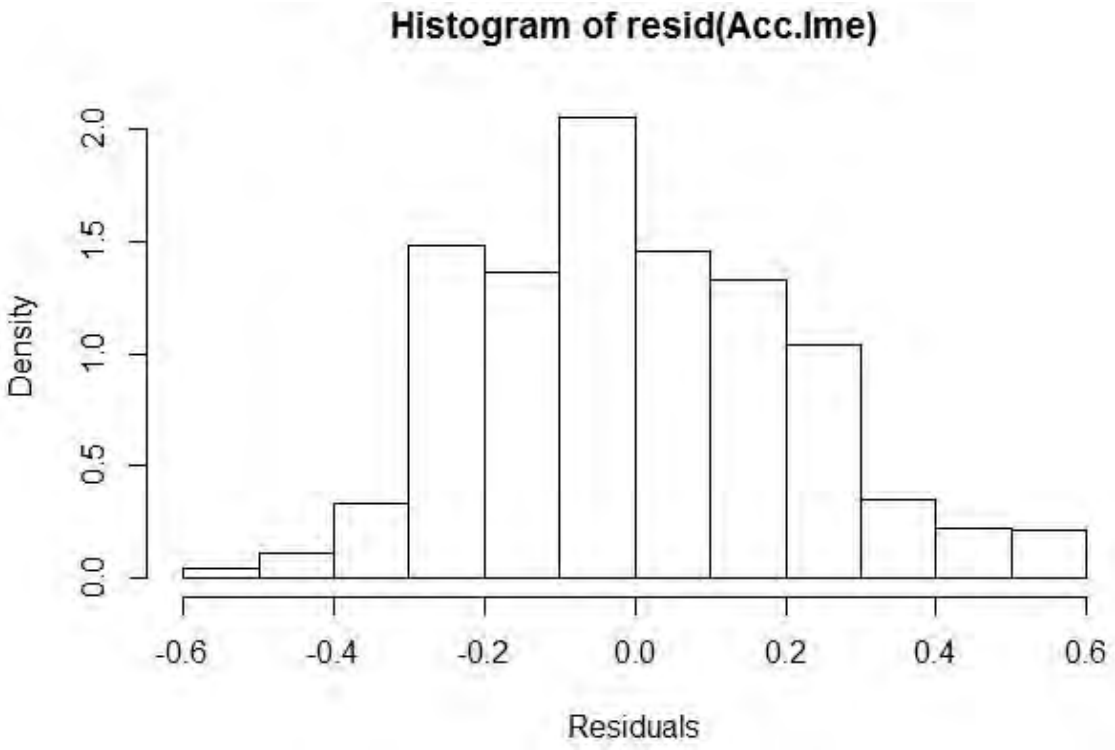


**Figure D-12:** Histogram of residuals from ED's Accuracy model show the residuals are normally distributed, thus the assumption of normality by the mixed effects model holds

## D.5 Fixed effects tables

Full versions of the fixed effects tables described in section 4.4 are presented for each muscle under investigation in sections D.5.1 to D.5.1.

### D.5.1 FPL (D)

**Table D-3:** Full table of variation of the fixed effect 'Accuracy' due to different ThCs for FPL

| Threshold | Accuracy | (95% CI) | Std. Error | DF | t-value | p-value |
|---|---|---|---|---|---|---|
| Ref | 0.76 | (0.70, 0.81) | 0.028 | 2847.000 | 27.059 | <0.001 |
| ThC1 | -0.22 | (-0.24, -0.19) | 0.013 | 2847.000 | -16.148 | <0.001 |
| ThC2 | -0.20 | (-0.23, -0.17) | 0.013 | 2847.000 | -14.923 | <0.001 |
| ThC3 | -0.20 | (-0.23, -0.17) | 0.015 | 2847.000 | -13.754 | <0.001 |
| ThC4 | -0.22 | (-0.26, -0.18) | 0.019 | 2847.000 | -11.699 | <0.001 |
| ThC5 | -0.29 | (-0.45, -0.13) | 0.082 | 2847.000 | -3.497 | 0.001 |
| ThC6 | -0.21 | (-0.23, -0.18) | 0.013 | 2847.000 | -15.378 | <0.001 |
| ThC7 | -0.19 | (-0.22, -0.16) | 0.013 | 2847.000 | -14.156 | <0.001 |
| ThC8 | -0.19 | (-0.22, -0.16) | 0.015 | 2847.000 | -13.052 | <0.001 |
| ThC9 | -0.21 | (-0.24, -0.17) | 0.019 | 2847.000 | -11.061 | <0.001 |
| ThC10 | -0.28 | (-0.44, -0.12) | 0.082 | 2847.000 | -3.371 | 0.001 |
| ThC11 | -0.18 | (-0.21, -0.15) | 0.013 | 2847.000 | -13.413 | <0.001 |
| ThC12 | -0.16 | (-0.19, -0.14) | 0.013 | 2847.000 | -12.202 | <0.001 |
| ThC13 | -0.16 | (-0.19, -0.14) | 0.015 | 2847.000 | -11.288 | <0.001 |

| | | | | | | |
|---|---|---|---|---|---|---|
| ThC14 | -0.18 | (-0.22, -0.14) | 0.019 | 2847.000 | -9.550 | <0.001 |
| ThC15 | -0.26 | (-0.42, -0.1) | 0.082 | 2847.000 | -3.185 | 0.002 |
| ThC16 | -0.14 | (-0.16, -0.11) | 0.013 | 2847.000 | -10.343 | <0.001 |
| ThC17 | -0.12 | (-0.15, -0.10) | 0.013 | 2847.000 | -9.175 | <0.001 |
| ThC18 | -0.12 | (-0.15, -0.10) | 0.015 | 2847.000 | -8.574 | <0.001 |
| ThC19 | -0.14 | (-0.18, -0.10) | 0.019 | 2847.000 | -7.472 | <0.001 |
| ThC20 | -0.23 | (-0.39 , -0.07) | 0.082 | 2847.000 | -2.816 | 0.005 |
| ThC21 | -0.10 | (-0.13 , -0.08) | 0.013 | 2847.000 | -7.635 | <0.001 |
| ThC22 | -0.09 | (-0.11 , -0.06) | 0.013 | 2847.000 | -6.517 | <0.001 |
| ThC23 | -0.09 | (-0.12 , -0.06) | 0.015 | 2847.000 | -6.119 | <0.001 |
| ThC24 | -0.11 | (-0.14 , -0.07) | 0.019 | 2847.000 | -5.722 | <0.001 |
| ThC25 | -0.19 | (-0.35, -0.03) | 0.082 | 2847.000 | -2.348 | 0.019 |
| ThC26 | -0.08 | (-0.10, -0.05) | 0.013 | 2847.000 | -5.897 | <0.001 |
| ThC27 | -0.06 | (-0.09, -0.04) | 0.013 | 2847.000 | -4.778 | <0.001 |
| ThC28 | -0.06 | (-0.09, -0.04) | 0.015 | 2847.000 | -4.459 | <0.001 |
| ThC29 | -0.08 | (-0.12, -0.05) | 0.019 | 2847.000 | -4.443 | <0.001 |
| ThC30 | -0.15 | (-0.31, 0.01) | 0.082 | 2847.000 | -1.788 | 0.074 |

**Table D-4:** Full table of variation of the fixed effect 'Sensitivity' due to different ThCs for FPL

| Threshold | Sensitivity | (95% CI) | Std. Error | DF | t-value | p-value |
|---|---|---|---|---|---|---|
| Ref | 0.88 | (0.8 , 0.96) | 0.041 | 2847.000 | 21.385 | <0.001 |
| ThC1 | -0.65 | (-0.68, -0.61) | 0.018 | 2847.000 | -35.981 | <0.001 |
| ThC2 | -0.59 | (-0.63, -0.56) | 0.018 | 2847.000 | -32.694 | <0.001 |
| ThC3 | -0.55 | (-0.59 , -0.51) | 0.020 | 2847.000 | -28.124 | <0.001 |
| ThC4 | -0.51 | (-0.56 , -0.46) | 0.025 | 2847.000 | -20.177 | <0.001 |
| ThC5 | -0.45 | (-0.67 , -0.23) | 0.111 | 2847.000 | -4.068 | <0.001 |
| ThC6 | -0.62 | (-0.65 , -0.58) | 0.018 | 2847.000 | -34.236 | <0.001 |
| ThC7 | -0.56 | (-0.6 , -0.53) | 0.018 | 2847.000 | -30.956 | <0.001 |
| ThC8 | -0.52 | (-0.56 , -0.48) | 0.020 | 2847.000 | -26.525 | <0.001 |
| ThC9 | -0.47 | (-0.52 , -0.42) | 0.025 | 2847.000 | -18.726 | <0.001 |
| ThC10 | -0.42 | (-0.64 , -0.2) | 0.111 | 2847.000 | -3.780 | <0.001 |
| ThC11 | -0.54 | (-0.57 , -0.5) | 0.018 | 2847.000 | -29.781 | <0.001 |
| ThC12 | -0.48 | (-0.52 , -0.45) | 0.018 | 2847.000 | -26.521 | <0.001 |
| ThC13 | -0.44 | (-0.48 , -0.4) | 0.020 | 2847.000 | -22.515 | <0.001 |
| ThC14 | -0.39 | (-0.44 , -0.34) | 0.025 | 2847.000 | -15.306 | <0.001 |
| ThC15 | -0.37 | (-0.59 , -0.15) | 0.111 | 2847.000 | -3.353 | 0.001 |
| ThC16 | -0.41 | (-0.45 , -0.38) | 0.018 | 2847.000 | -22.817 | <0.001 |
| ThC17 | -0.36 | (-0.39 , -0.32) | 0.018 | 2847.000 | -19.649 | <0.001 |
| ThC18 | -0.32 | (-0.36 , -0.28) | 0.020 | 2847.000 | -16.338 | <0.001 |
| ThC19 | -0.27 | (-0.32 , -0.22) | 0.025 | 2847.000 | -10.603 | <0.001 |
| ThC20 | -0.28 | (-0.50, -0.06) | 0.111 | 2847.000 | -2.504 | 0.012 |
| ThC21 | -0.30 | (-0.34, -0.27) | 0.018 | 2847.000 | -16.677 | <0.001 |

| | | | | | | |
|---|---|---|---|---|---|---|
| ThC22 | -0.25 | (-0.28, -0.21) | 0.018 | 2847.000 | -13.622 | <0.001 |
| ThC23 | -0.21 | (-0.25, -0.17) | 0.020 | 2847.000 | -10.753 | <0.001 |
| ThC24 | -0.17 | (-0.22, -0.12) | 0.025 | 2847.000 | -6.643 | <0.001 |
| ThC25 | -0.16 | (-0.37, 0.06) | 0.111 | 2847.000 | -1.413 | 0.158 |
| ThC26 | -0.23 | (-0.27, -0.19) | 0.018 | 2847.000 | -12.758 | <0.001 |
| ThC27 | -0.18 | (-0.21, -0.14) | 0.018 | 2847.000 | -9.698 | <0.001 |
| ThC28 | -0.14 | (-0.18, -0.1) | 0.020 | 2847.000 | -6.985 | <0.001 |
| ThC29 | -0.09 | (-0.14, -0.05) | 0.025 | 2847.000 | -3.740 | <0.001 |
| ThC30 | -0.01 | (-0.23, 0.21) | 0.111 | 2847.000 | -0.080 | 0.936 |

**Table D-5:** Full table of variation of the fixed effect 'Specificity' due to different ThCs for FPL

| Threshold | Specificity | (95% CI) | Std. Error | DF | t-value | p-value |
|---|---|---|---|---|---|---|
| Ref | 0.70 | (0.63, 0.78) | 0.039 | 2847.000 | 17.819 | <0.001 |
| ThC1 | -0.01 | (-0.04, 0.03) | 0.019 | 2847.000 | -0.310 | 0.756 |
| ThC2 | -0.01 | (-0.05, 0.03) | 0.019 | 2847.000 | -0.559 | 0.576 |
| ThC3 | -0.03 | (-0.07, 0.01) | 0.021 | 2847.000 | -1.462 | 0.144 |
| ThC4 | -0.08 | (-0.13, -0.03) | 0.027 | 2847.000 | -2.941 | 0.003 |
| ThC5 | -0.21 | (-0.44, 0.02) | 0.118 | 2847.000 | -1.769 | 0.077 |
| ThC6 | -0.01 | (-0.04, 0.03) | 0.019 | 2847.000 | -0.310 | 0.756 |
| ThC7 | -0.01 | (-0.05, 0.03) | 0.019 | 2847.000 | -0.559 | 0.576 |
| ThC8 | -0.03 | (-0.07, 0.01) | 0.021 | 2847.000 | -1.462 | 0.144 |
| ThC9 | -0.08 | (-0.13, -0.03) | 0.027 | 2847.000 | -2.941 | 0.003 |
| ThC10 | -0.21 | (-0.44, 0.02) | 0.118 | 2847.000 | -1.769 | 0.077 |
| ThC11 | -0.01 | (-0.04, 0.03) | 0.019 | 2847.000 | -0.310 | 0.756 |
| ThC12 | -0.01 | (-0.05, 0.03) | 0.019 | 2847.000 | -0.559 | 0.576 |
| ThC13 | -0.03 | (-0.07, 0.01) | 0.021 | 2847.000 | -1.462 | 0.144 |
| ThC14 | -0.08 | (-0.13, -0.03) | 0.027 | 2847.000 | -2.941 | 0.003 |
| ThC15 | -0.21 | (-0.44, 0.02) | 0.118 | 2847.000 | -1.769 | 0.077 |
| ThC16 | -0.01 | (-0.04, 0.03) | 0.019 | 2847.000 | -0.310 | 0.757 |
| ThC17 | -0.01 | (-0.05, 0.03) | 0.019 | 2847.000 | -0.559 | 0.577 |
| ThC18 | -0.03 | (-0.07, 0.01) | 0.021 | 2847.000 | -1.462 | 0.144 |
| ThC19 | -0.08 | (-0.13, -0.03) | 0.027 | 2847.000 | -2.941 | 0.003 |
| ThC20 | -0.21 | (-0.44, 0.02) | 0.118 | 2847.000 | -1.769 | 0.077 |
| ThC21 | -0.01 | (-0.04, 0.03) | 0.019 | 2847.000 | -0.310 | 0.757 |
| ThC22 | -0.01 | (-0.05, 0.03) | 0.019 | 2847.000 | -0.558 | 0.577 |
| ThC23 | -0.03 | (-0.07, 0.01) | 0.021 | 2847.000 | -1.461 | 0.144 |
| ThC24 | -0.08 | (-0.13, -0.03) | 0.027 | 2847.000 | -2.941 | 0.003 |
| ThC25 | -0.21 | (-0.44, 0.02) | 0.118 | 2847.000 | -1.769 | 0.077 |
| ThC26 | -0.01 | (-0.04, 0.03) | 0.019 | 2847.000 | -0.309 | 0.757 |
| ThC27 | -0.01 | (-0.05, 0.03) | 0.019 | 2847.000 | -0.558 | 0.577 |
| ThC28 | -0.03 | (-0.07, 0.01) | 0.021 | 2847.000 | -1.461 | 0.144 |
| ThC29 | -0.08 | (-0.13, -0.03) | 0.027 | 2847.000 | -2.940 | 0.003 |

| | | | | | | |
|---|---|---|---|---|---|---|
| ThC30 | -0.21 | (-0.44, 0.02) | 0.118 | 2847.000 | -1.769 | 0.077 |

### D.5.2 EPL (D)

**Table D-6:** Full table of variation of the fixed effect 'Accuracy' due to different ThCs for EPL's

| Threshold | Accuracy | (95% CI) | Std. Error | DF | t-value | p-value |
|---|---|---|---|---|---|---|
| Ref | 0.87 | (0.83 ,0.92) | 0.023 | 2811.000 | 38.271 | <0.001 |
| ThC1 | -0.37 | (-0.40 ,-0.34) | 0.015 | 2811.000 | -24.675 | <0.001 |
| ThC2 | -0.29 | (-0.32 ,-0.26) | 0.015 | 2811.000 | -19.136 | <0.001 |
| ThC3 | -0.24 | (-0.27 ,-0.21) | 0.016 | 2811.000 | -14.746 | <0.001 |
| ThC4 | -0.23 | (-0.28 ,-0.19) | 0.023 | 2811.000 | -9.988 | <0.001 |
| ThC5 | -0.23 | (-0.34 ,-0.12) | 0.055 | 2811.000 | -4.149 | <0.001 |
| ThC6 | -0.37 | (-0.40 ,-0.34) | 0.015 | 2811.000 | -24.110 | <0.001 |
| ThC7 | -0.28 | (-0.31 ,-0.25) | 0.015 | 2811.000 | -18.564 | <0.001 |
| ThC8 | -0.23 | (-0.27 ,-0.20) | 0.016 | 2811.000 | -14.228 | <0.001 |
| ThC9 | -0.23 | (-0.27 ,-0.18) | 0.023 | 2811.000 | -9.651 | <0.001 |
| ThC10 | -0.22 | (-0.33 ,-0.11) | 0.055 | 2811.000 | -3.980 | <0.001 |
| ThC11 | -0.35 | (-0.38 ,-0.32) | 0.015 | 2811.000 | -22.874 | <0.001 |
| ThC12 | -0.27 | (-0.30 ,-0.24) | 0.015 | 2811.000 | -17.336 | <0.001 |
| ThC13 | -0.22 | (-0.25 ,-0.18) | 0.016 | 2811.000 | -13.140 | <0.001 |
| ThC14 | -0.21 | (-0.26 ,-0.17) | 0.023 | 2811.000 | -9.048 | <0.001 |
| ThC15 | -0.20 | (-0.31 ,-0.09) | 0.055 | 2811.000 | -3.674 | <0.001 |
| ThC16 | -0.32 | (-0.35 ,-0.29) | 0.015 | 2811.000 | -20.859 | <0.001 |
| ThC17 | -0.24 | (-0.27 ,-0.21) | 0.015 | 2811.000 | -15.362 | <0.001 |
| ThC18 | -0.19 | (-0.22 ,-0.15) | 0.016 | 2811.000 | -11.412 | <0.001 |
| ThC19 | -0.19 | (-0.23 ,-0.14) | 0.023 | 2811.000 | -8.035 | <0.001 |
| ThC20 | -0.18 | (-0.29 ,-0.07) | 0.055 | 2811.000 | -3.288 | 0.001 |
| ThC21 | -0.28 | (-0.31 ,-0.25) | 0.015 | 2811.000 | -18.267 | <0.001 |
| ThC22 | -0.20 | (-0.23 ,-0.17) | 0.015 | 2811.000 | -12.841 | <0.001 |
| ThC23 | -0.15 | (-0.18 ,-0.12) | 0.016 | 2811.000 | -9.136 | <0.001 |
| ThC24 | -0.15 | (-0.20 ,-0.11) | 0.023 | 2811.000 | -6.541 | <0.001 |
| ThC25 | -0.15 | (-0.26 ,-0.05) | 0.055 | 2811.000 | -2.813 | 0.005 |
| ThC26 | -0.24 | (-0.27 ,-0.21) | 0.015 | 2811.000 | -15.977 | <0.001 |
| ThC27 | -0.16 | (-0.19 ,-0.13) | 0.015 | 2811.000 | -10.562 | <0.001 |
| ThC28 | -0.11 | (-0.15 ,-0.08) | 0.016 | 2811.000 | -6.949 | <0.001 |
| ThC29 | -0.11 | (-0.16 ,-0.07) | 0.023 | 2811.000 | -4.802 | <0.001 |
| ThC30 | -0.11 | (-0.21 ,0.00) | 0.055 | 2811.000 | -1.918 | 0.055 |

**Table D-7:** Full table of variation of the fixed effect 'Sensitivity' due to different ThCs for EPL

| Threshold | Sensitivity | (95% CI) | Std.Error | DF | t-value | p-value |
|---|---|---|---|---|---|---|
| Ref | 0.85 | (0.78, 0.92) | 0.036 | 2811.000 | 24.037 | <0.001 |

| | | | | | | |
|---|---|---|---|---|---|---|
| ThC1 | -0.55 | (-0.60, 0.51) | 0.023 | 2811.000 | -23.897 | <0.001 |
| ThC2 | -0.42 | (-0.47, 0.38) | 0.023 | 2811.000 | -18.171 | <0.001 |
| ThC3 | -0.33 | (-0.38, 0.28) | 0.025 | 2811.000 | -13.244 | <0.001 |
| ThC4 | -0.27 | (-0.34, 0.2) | 0.036 | 2811.000 | -7.619 | <0.001 |
| ThC5 | -0.16 | (-0.32, 0.00) | 0.083 | 2811.000 | -1.920 | 0.055 |
| ThC6 | -0.54 | (-0.58, 0.49) | 0.023 | 2811.000 | -23.332 | <0.001 |
| ThC7 | -0.41 | (-0.46, 0.36) | 0.023 | 2811.000 | -17.600 | <0.001 |
| ThC8 | -0.32 | (-0.37, 0.27) | 0.025 | 2811.000 | -12.726 | <0.001 |
| ThC9 | -0.26 | (-0.33, 0.19) | 0.036 | 2811.000 | -7.285 | <0.001 |
| ThC10 | -0.15 | (-0.31, 0.02) | 0.083 | 2811.000 | -1.755 | 0.079 |
| ThC11 | -0.51 | (-0.56, 0.46) | 0.023 | 2811.000 | -22.095 | <0.001 |
| ThC12 | -0.38 | (-0.43, 0.34) | 0.023 | 2811.000 | -16.370 | <0.001 |
| ThC13 | -0.29 | (-0.34, 0.24) | 0.025 | 2811.000 | -11.638 | <0.001 |
| ThC14 | -0.24 | (-0.31, 0.17) | 0.036 | 2811.000 | -6.684 | <0.001 |
| ThC15 | -0.12 | (-0.28, 0.04) | 0.083 | 2811.000 | -1.451 | 0.147 |
| ThC16 | -0.46 | (-0.51, 0.42) | 0.023 | 2811.000 | -20.081 | <0.001 |
| ThC17 | -0.34 | (-0.38, 0.29) | 0.023 | 2811.000 | -14.396 | <0.001 |
| ThC18 | -0.25 | (-0.30, 0.20) | 0.025 | 2811.000 | -9.909 | <0.001 |
| ThC19 | -0.20 | (-0.27, 0.13) | 0.036 | 2811.000 | -5.679 | <0.001 |
| ThC20 | -0.09 | (-0.25, 0.07) | 0.083 | 2811.000 | -1.069 | 0.285 |
| ThC21 | -0.40 | (-0.45, 0.36) | 0.023 | 2811.000 | -17.497 | <0.001 |
| ThC22 | -0.28 | (-0.32, 0.23) | 0.023 | 2811.000 | -11.885 | <0.001 |
| ThC23 | -0.19 | (-0.24, 0.14) | 0.025 | 2811.000 | -7.635 | <0.001 |
| ThC24 | -0.15 | (-0.22, 0.08) | 0.036 | 2811.000 | -4.196 | <0.001 |
| ThC25 | -0.05 | (-0.21, 0.11) | 0.083 | 2811.000 | -0.602 | 0.547 |
| ThC26 | -0.35 | (-0.40, 0.31) | 0.023 | 2811.000 | -15.225 | <0.001 |
| ThC27 | -0.22 | (-0.27, 0.18) | 0.023 | 2811.000 | -9.625 | <0.001 |
| ThC28 | -0.14 | (-0.19, 0.09) | 0.025 | 2811.000 | -5.461 | <0.001 |
| ThC29 | -0.09 | (-0.16, 0.02) | 0.036 | 2811.000 | -2.473 | 0.014 |
| ThC30 | 0.02 | (-0.14, 0.19) | 0.083 | 2811.000 | 0.274 | 0.784 |

**Table D-8**: Full table of fixed effects for EPL's 'Specificity' model

| Threshold | Specificity | (95% CI) | Std. Error | DF | t-value | p-value |
|---|---|---|---|---|---|---|
| Ref | 0.91 | (0.82, 1.00) | 0.045 | 2811.000 | 20.132 | <0.001 |
| ThC1 | -0.03 | (-0.08, 0.02) | 0.026 | 2811.000 | -1.262 | 0.207 |
| ThC2 | -0.04 | (-0.09, 0.01) | 0.027 | 2811.000 | -1.608 | 0.108 |
| ThC3 | -0.07 | (-0.13, -0.02) | 0.028 | 2811.000 | -2.559 | 0.011 |
| ThC4 | -0.16 | (-0.24, -0.08) | 0.041 | 2811.000 | -3.987 | <0.001 |
| ThC5 | -0.36 | (-0.54, -0.17) | 0.095 | 2811.000 | -3.761 | <0.001 |
| ThC6 | -0.03 | (-0.08, 0.02) | 0.026 | 2811.000 | -1.262 | 0.207 |
| ThC7 | -0.04 | (-0.09, 0.01) | 0.027 | 2811.000 | -1.608 | 0.108 |
| ThC8 | -0.07 | (-0.13, -0.02) | 0.028 | 2811.000 | -2.559 | 0.011 |

| | | | | | | |
|---|---|---|---|---|---|---|
| ThC9 | -0.16 | (-0.24, -0.08) | 0.041 | 2811.000 | -3.987 | <0.001 |
| ThC10 | -0.36 | (-0.54, -0.17) | 0.095 | 2811.000 | -3.761 | <0.001 |
| ThC11 | -0.03 | (-0.08, 0.02) | 0.026 | 2811.000 | -1.263 | 0.207 |
| ThC12 | -0.04 | (-0.09, 0.01) | 0.027 | 2811.000 | -1.608 | 0.108 |
| ThC13 | -0.07 | (-0.13, -0.02) | 0.028 | 2811.000 | -2.559 | 0.011 |
| ThC14 | -0.16 | (-0.24, -0.08) | 0.041 | 2811.000 | -3.987 | <0.001 |
| ThC15 | -0.36 | (-0.54, -0.17) | 0.095 | 2811.000 | -3.761 | <0.001 |
| ThC16 | -0.03 | (-0.08, 0.02) | 0.026 | 2811.000 | -1.263 | 0.207 |
| ThC17 | -0.04 | (-0.09, 0.01) | 0.027 | 2811.000 | -1.608 | 0.108 |
| ThC18 | -0.07 | (-0.13, -0.02) | 0.028 | 2811.000 | -2.559 | 0.011 |
| ThC19 | -0.16 | (-0.24, -0.08) | 0.041 | 2811.000 | -3.987 | <0.001 |
| ThC20 | -0.36 | (-0.54, -0.17) | 0.095 | 2811.000 | -3.761 | <0.001 |
| ThC21 | -0.03 | (-0.08, 0.02) | 0.026 | 2811.000 | -1.263 | 0.207 |
| ThC22 | -0.04 | (-0.09, 0.01) | 0.027 | 2811.000 | -1.608 | 0.108 |
| ThC23 | -0.07 | (-0.13, -0.02) | 0.028 | 2811.000 | -2.559 | 0.011 |
| ThC24 | -0.16 | (-0.24, -0.08) | 0.041 | 2811.000 | -3.987 | <0.001 |
| ThC25 | -0.36 | (-0.54, -0.17) | 0.095 | 2811.000 | -3.761 | <0.001 |
| ThC26 | -0.03 | (-0.08, 0.02) | 0.026 | 2811.000 | -1.263 | 0.207 |
| ThC27 | -0.04 | (-0.09, 0.01) | 0.027 | 2811.000 | -1.608 | 0.108 |
| ThC28 | -0.07 | (-0.13, -0.02) | 0.028 | 2811.000 | -2.559 | 0.011 |
| ThC29 | -0.16 | (-0.24, -0.08) | 0.041 | 2811.000 | -3.987 | <0.001 |
| ThC30 | -0.36 | (-0.54, -0.17) | 0.095 | 2811.000 | -3.761 | <0.001 |

### D.5.3 EPB (D)

**Table D-9:** Full table of variation of the fixed effect 'Accuracy' due to different ThCs for EPB

| Threshold | Accuracy | (95% CI) | Std. Error | DF | t-value | p-value |
|---|---|---|---|---|---|---|
| Ref | 0.94 | (0.90, 0.97) | 0.017 | 2253.000 | 56.048 | <0.001 |
| ThC1 | -0.12 | (-0.14, -0.1) | 0.011 | 2253.000 | -11.620 | <0.001 |
| ThC2 | -0.05 | (-0.07, -0.03) | 0.011 | 2253.000 | -4.412 | <0.001 |
| ThC3 | -0.01 | (-0.04, 0.01) | 0.014 | 2253.000 | -1.013 | 0.311 |
| ThC4 | -0.07 | (-0.12, -0.01) | 0.027 | 2253.000 | -2.483 | 0.013 |
| ThC5 | -0.11 | (-0.20, -0.02) | 0.046 | 2253.000 | -2.398 | 0.017 |
| ThC6 | -0.12 | (-0.14, -0.10) | 0.011 | 2253.000 | -11.620 | <0.001 |
| ThC7 | -0.05 | (-0.07, -0.03) | 0.011 | 2253.000 | -4.412 | <0.001 |
| ThC8 | -0.01 | (-0.04, 0.01) | 0.014 | 2253.000 | -1.013 | 0.311 |
| ThC9 | -0.07 | (-0.12, -0.01) | 0.027 | 2253.000 | -2.483 | 0.013 |
| ThC10 | -0.11 | (-0.20, -0.02) | 0.046 | 2253.000 | -2.398 | 0.017 |
| ThC11 | -0.12 | (-0.14, -0.1) | 0.011 | 2253.000 | -11.620 | <0.001 |
| ThC12 | -0.05 | (-0.07, -0.03) | 0.011 | 2253.000 | -4.412 | <0.001 |
| ThC13 | -0.01 | (-0.04, 0.01) | 0.014 | 2253.000 | -1.013 | 0.311 |
| ThC14 | -0.07 | (-0.12, -0.01) | 0.027 | 2253.000 | -2.483 | 0.013 |
| ThC15 | -0.11 | (-0.20, -0.02) | 0.046 | 2253.000 | -2.398 | 0.017 |

| | | | | | | |
|---|---|---|---|---|---|---|
| ThC16 | -0.12 | (-0.14, -0.1) | 0.011 | 2253.000 | -11.620 | <0.001 |
| ThC17 | -0.05 | (-0.07, -0.03) | 0.011 | 2253.000 | -4.412 | <0.001 |
| ThC18 | -0.01 | (-0.04, 0.01) | 0.014 | 2253.000 | -1.013 | 0.311 |
| ThC19 | -0.07 | (-0.12, -0.01) | 0.027 | 2253.000 | -2.483 | 0.013 |
| ThC20 | -0.11 | (-0.20, -0.02) | 0.046 | 2253.000 | -2.398 | 0.017 |
| ThC21 | -0.12 | (-0.14, -0.10) | 0.011 | 2253.000 | -11.620 | <0.001 |
| ThC22 | -0.05 | (-0.07, -0.03) | 0.011 | 2253.000 | -4.412 | <0.001 |
| ThC23 | -0.01 | (-0.04, 0.01) | 0.014 | 2253.000 | -1.013 | 0.311 |
| ThC24 | -0.07 | (-0.12, -0.01) | 0.027 | 2253.000 | -2.483 | 0.013 |
| ThC25 | -0.11 | (-0.20, -0.02) | 0.046 | 2253.000 | -2.398 | 0.017 |
| ThC26 | -0.12 | (-0.14, -0.1) | 0.011 | 2253.000 | -11.620 | <0.001 |
| ThC27 | -0.05 | (-0.07, -0.03) | 0.011 | 2253.000 | -4.412 | <0.001 |
| ThC28 | -0.01 | (-0.04, 0.01) | 0.014 | 2253.000 | -1.013 | 0.311 |
| ThC29 | -0.07 | (-0.12, -0.01) | 0.027 | 2253.000 | -2.483 | 0.013 |
| ThC30 | -0.11 | (-0.20, -0.02) | 0.046 | 2253.000 | -2.398 | 0.017 |

**Table D-10**: Full table of variation of the fixed effect 'Sensitivity' due to different ThCs for EPB

| Threshold | Sensitivity | (95% CI) | Std. Error | DF | t-value | p-value |
|---|---|---|---|---|---|---|
| Ref | 0.93 | (0.9 ,0.97) | 0.019 | 2253.000 | 47.997 | <0.001 |
| ThC1 | -0.18 | (-0.2 ,-0.15) | 0.012 | 2253.000 | -14.492 | <0.001 |
| ThC2 | -0.06 | (-0.08 ,-0.03) | 0.013 | 2253.000 | -4.345 | <0.001 |
| ThC3 | 0.02 | (-0.01 ,0.05) | 0.016 | 2253.000 | 1.418 | 0.156 |
| ThC4 | 0.07 | (0.01 ,0.13) | 0.032 | 2253.000 | 2.133 | 0.033 |
| ThC5 | 0.04 | (-0.07 ,0.15) | 0.054 | 2253.000 | 0.722 | 0.470 |
| ThC6 | -0.18 | (-0.2 ,-0.15) | 0.012 | 2253.000 | -14.492 | <0.001 |
| ThC7 | -0.06 | (-0.08 ,-0.03) | 0.013 | 2253.000 | -4.345 | <0.001 |
| ThC8 | 0.02 | (-0.01 ,0.05) | 0.016 | 2253.000 | 1.418 | 0.156 |
| ThC9 | 0.07 | (0.01 ,0.13) | 0.032 | 2253.000 | 2.133 | 0.033 |
| ThC10 | 0.04 | (-0.07 ,0.15) | 0.054 | 2253.000 | 0.722 | 0.470 |
| ThC11 | -0.18 | (-0.2 ,-0.15) | 0.012 | 2253.000 | -14.492 | <0.001 |
| ThC12 | -0.06 | (-0.08 ,-0.03) | 0.013 | 2253.000 | -4.345 | <0.001 |
| ThC13 | 0.02 | (-0.01 ,0.05) | 0.016 | 2253.000 | 1.418 | 0.156 |
| ThC14 | 0.07 | (0.01 ,0.13) | 0.032 | 2253.000 | 2.133 | 0.033 |
| ThC15 | 0.04 | (-0.07 ,0.15) | 0.054 | 2253.000 | 0.722 | 0.470 |
| ThC16 | -0.18 | (-0.2 ,-0.15) | 0.012 | 2253.000 | -14.492 | <0.001 |
| ThC17 | -0.06 | (-0.08 ,-0.03) | 0.013 | 2253.000 | -4.345 | <0.001 |
| ThC18 | 0.02 | (-0.01 ,0.05) | 0.016 | 2253.000 | 1.418 | 0.156 |
| ThC19 | 0.07 | (0.01 ,0.13) | 0.032 | 2253.000 | 2.133 | 0.033 |
| ThC20 | 0.04 | (-0.07 ,0.15) | 0.054 | 2253.000 | 0.722 | 0.470 |
| ThC21 | -0.18 | (-0.2 ,-0.15) | 0.012 | 2253.000 | -14.492 | <0.001 |
| ThC22 | -0.06 | (-0.08 ,-0.03) | 0.013 | 2253.000 | -4.345 | <0.001 |
| ThC23 | 0.02 | (-0.01 ,0.05) | 0.016 | 2253.000 | 1.418 | 0.156 |

| | | | | | | |
|---|---|---|---|---|---|---|
| ThC24 | 0.07 | (0.01 ,0.13) | 0.032 | 2253.000 | 2.133 | 0.033 |
| ThC25 | 0.04 | (-0.07 ,0.15) | 0.054 | 2253.000 | 0.722 | 0.470 |
| ThC26 | -0.18 | (-0.2 ,-0.15) | 0.012 | 2253.000 | -14.492 | <0.001 |
| ThC27 | -0.06 | (-0.08 ,-0.03) | 0.013 | 2253.000 | -4.345 | <0.001 |
| ThC28 | 0.02 | (-0.01 ,0.05) | 0.016 | 2253.000 | 1.418 | 0.156 |
| ThC29 | 0.07 | (0.01 ,0.13) | 0.032 | 2253.000 | 2.133 | 0.033 |
| ThC30 | 0.04 | (-0.07 ,0.15) | 0.054 | 2253.000 | 0.722 | 0.470 |

**Table D-11:** Full table of variation of the fixed effect 'Specificity' due to different ThCs for EPB

| Threshold | Specificity | (95% CI) | Std. Error | DF | t-value | p-value |
|---|---|---|---|---|---|---|
| Ref | 0.94 | (0.86, 1.02) | 0.039 | 2253.000 | 23.941 | <0.001 |
| ThC1 | -0.02 | (-0.06, 0.03) | 0.021 | 2253.000 | -0.720 | 0.472 |
| ThC2 | -0.04 | (-0.08, 0.01) | 0.022 | 2253.000 | -1.648 | 0.099 |
| ThC3 | -0.09 | (-0.14, -0.03) | 0.028 | 2253.000 | -3.162 | 0.002 |
| ThC4 | -0.35 | (-0.45, -0.24) | 0.056 | 2253.000 | -6.213 | <0.001 |
| ThC5 | -0.42 | (-0.61, -0.24) | 0.094 | 2253.000 | -4.513 | <0.001 |
| ThC6 | -0.02 | (-0.06, 0.03) | 0.021 | 2253.000 | -0.720 | 0.472 |
| ThC7 | -0.04 | (-0.08, 0.01) | 0.022 | 2253.000 | -1.648 | 0.099 |
| ThC8 | -0.09 | (-0.14, -0.03) | 0.028 | 2253.000 | -3.162 | 0.002 |
| ThC9 | -0.35 | (-0.45, -0.24) | 0.056 | 2253.000 | -6.213 | <0.001 |
| ThC10 | -0.42 | (-0.61, -0.24) | 0.094 | 2253.000 | -4.513 | <0.001 |
| ThC11 | -0.02 | (-0.06, 0.03) | 0.021 | 2253.000 | -0.720 | 0.472 |
| ThC12 | -0.04 | (-0.08, 0.01) | 0.022 | 2253.000 | -1.648 | 0.099 |
| ThC13 | -0.09 | (-0.14, -0.03) | 0.028 | 2253.000 | -3.162 | 0.002 |
| ThC14 | -0.35 | (-0.45, -0.24) | 0.056 | 2253.000 | -6.213 | <0.001 |
| ThC15 | -0.42 | (-0.61, -0.24) | 0.094 | 2253.000 | -4.513 | <0.001 |
| ThC16 | -0.02 | (-0.06, 0.03) | 0.021 | 2253.000 | -0.720 | 0.472 |
| ThC17 | -0.04 | (-0.08, 0.01) | 0.022 | 2253.000 | -1.648 | 0.099 |
| ThC18 | -0.09 | (-0.14, -0.03) | 0.028 | 2253.000 | -3.162 | 0.002 |
| ThC19 | -0.35 | (-0.45, -0.24) | 0.056 | 2253.000 | -6.213 | <0.001 |
| ThC20 | -0.42 | (-0.61, -0.24) | 0.094 | 2253.000 | -4.513 | <0.001 |
| ThC21 | -0.02 | (-0.06, 0.03) | 0.021 | 2253.000 | -0.720 | 0.472 |
| ThC22 | -0.04 | (-0.08, 0.01) | 0.022 | 2253.000 | -1.648 | 0.099 |
| ThC23 | -0.09 | (-0.14, -0.03) | 0.028 | 2253.000 | -3.162 | 0.002 |
| ThC24 | -0.35 | (-0.45, -0.24) | 0.056 | 2253.000 | -6.213 | <0.001 |
| ThC25 | -0.42 | (-0.61, -0.24) | 0.094 | 2253.000 | -4.513 | <0.001 |
| ThC26 | -0.02 | (-0.06, 0.03) | 0.021 | 2253.000 | -0.720 | 0.472 |
| ThC27 | -0.04 | (-0.08, 0.01) | 0.022 | 2253.000 | -1.648 | 0.099 |
| ThC28 | -0.09 | (-0.14, -0.03) | 0.028 | 2253.000 | -3.162 | 0.002 |
| ThC29 | -0.35 | (-0.45, -0.24) | 0.056 | 2253.000 | -6.213 | <0.001 |
| ThC30 | -0.42 | (-0.61, -0.24) | 0.094 | 2253.000 | -4.513 | <0.001 |

### D.5.4 APL (D)

**Table D-12:** Full table of variation of the fixed effect 'Accuracy' due to different ThCs for APL

| Threshold | Accuracy | (95% CI) | Std. Error | DF | t-value | p-value |
|---|---|---|---|---|---|---|
| Ref | 0.80 | (0.76, 0.84) | 0.020 | 2865.000 | 40.298 | <0.001 |
| ThC1 | -0.40 | (-0.43, -0.38) | 0.013 | 2865.000 | -31.106 | <0.001 |
| ThC2 | -0.37 | (-0.40, -0.35) | 0.013 | 2865.000 | -28.506 | <0.001 |
| ThC3 | -0.35 | (-0.37, -0.32) | 0.014 | 2865.000 | -24.961 | <0.001 |
| ThC4 | -0.39 | (-0.43, -0.35) | 0.019 | 2865.000 | -20.497 | <0.001 |
| ThC5 | -0.51 | (-0.63, -0.40) | 0.057 | 2865.000 | -9.034 | <0.001 |
| ThC6 | -0.39 | (-0.41, -0.36) | 0.013 | 2865.000 | -30.094 | <0.001 |
| ThC7 | -0.36 | (-0.38, -0.33) | 0.013 | 2865.000 | -27.496 | <0.001 |
| ThC8 | -0.33 | (-0.36, -0.31) | 0.014 | 2865.000 | -24.028 | <0.001 |
| ThC9 | -0.38 | (-0.42, -0.34) | 0.019 | 2865.000 | -19.801 | <0.001 |
| ThC10 | -0.50 | (-0.61, -0.39) | 0.057 | 2865.000 | -8.768 | <0.001 |
| ThC11 | -0.36 | (-0.38, -0.33) | 0.013 | 2865.000 | -27.473 | <0.001 |
| ThC12 | -0.32 | (-0.35, -0.30) | 0.013 | 2865.000 | -24.876 | <0.001 |
| ThC13 | -0.30 | (-0.33, -0.27) | 0.014 | 2865.000 | -21.701 | <0.001 |
| ThC14 | -0.34 | (-0.38, -0.30) | 0.019 | 2865.000 | -17.895 | <0.001 |
| ThC15 | -0.45 | (-0.57, -0.34) | 0.057 | 2865.000 | -7.972 | <0.001 |
| ThC16 | -0.30 | (-0.33, -0.28) | 0.013 | 2865.000 | -23.425 | <0.001 |
| ThC17 | -0.27 | (-0.30, -0.25) | 0.013 | 2865.000 | -20.842 | <0.001 |
| ThC18 | -0.25 | (-0.28, -0.22) | 0.014 | 2865.000 | -18.168 | <0.001 |
| ThC19 | -0.29 | (-0.32, -0.25) | 0.019 | 2865.000 | -14.944 | <0.001 |
| ThC20 | -0.37 | (-0.48, -0.25) | 0.057 | 2865.000 | -6.430 | <0.001 |
| ThC21 | -0.25 | (-0.27, -0.22) | 0.013 | 2865.000 | -19.117 | <0.001 |
| ThC22 | -0.22 | (-0.24, -0.19) | 0.013 | 2865.000 | -16.561 | <0.001 |
| ThC23 | -0.20 | (-0.22, -0.17) | 0.014 | 2865.000 | -14.223 | <0.001 |
| ThC24 | -0.23 | (-0.26, -0.19) | 0.019 | 2865.000 | -11.871 | <0.001 |
| ThC25 | -0.28 | (-0.39, -0.17) | 0.057 | 2865.000 | -4.968 | <0.001 |
| ThC26 | -0.19 | (-0.22, -0.17) | 0.013 | 2865.000 | -14.796 | <0.001 |
| ThC27 | -0.16 | (-0.19, -0.13) | 0.013 | 2865.000 | -12.289 | <0.001 |
| ThC28 | -0.14 | (-0.17, -0.12) | 0.014 | 2865.000 | -10.443 | <0.001 |
| ThC29 | -0.18 | (-0.22, -0.14) | 0.019 | 2865.000 | -9.378 | <0.001 |
| ThC30 | -0.22 | (-0.33, -0.11) | 0.057 | 2865.000 | -3.853 | <0.001 |

**Table D-13:** Full table of variation of the fixed effect 'Sensitivity' due to different ThCs for APL

| Threshold | Sensitivity | (95% CI) | Std. Error | DF | t-value | p-value |
|---|---|---|---|---|---|---|
| Ref | 0.87 | (0.83, 0.92) | 0.025 | 2865.000 | 35.005 | <0.001 |
| ThC1 | -0.79 | (-0.82, -0.75) | 0.016 | 2865.000 | -48.270 | <0.001 |
| ThC2 | -0.72 | (-0.75, -0.69) | 0.016 | 2865.000 | -43.922 | <0.001 |
| ThC3 | -0.65 | (-0.69, -0.62) | 0.017 | 2865.000 | -37.507 | <0.001 |

| | | | | | | |
|---|---|---|---|---|---|---|
| ThC4 | -0.58 | (-0.63, -0.54) | 0.024 | 2865.000 | -24.355 | <0.001 |
| ThC5 | -0.50 | (-0.64, -0.36) | 0.072 | 2865.000 | -7.033 | <0.001 |
| ThC6 | -0.76 | (-0.79, -0.73) | 0.016 | 2865.000 | -46.656 | <0.001 |
| ThC7 | -0.69 | (-0.72, -0.66) | 0.016 | 2865.000 | -42.309 | <0.001 |
| ThC8 | -0.63 | (-0.66, -0.59) | 0.017 | 2865.000 | -36.017 | <0.001 |
| ThC9 | -0.56 | (-0.60, -0.51) | 0.024 | 2865.000 | -23.238 | <0.001 |
| ThC10 | -0.47 | (-0.61, -0.33) | 0.072 | 2865.000 | -6.614 | <0.001 |
| ThC11 | -0.69 | (-0.72, -0.66) | 0.016 | 2865.000 | -42.475 | <0.001 |
| ThC12 | -0.62 | (-0.66, -0.59) | 0.016 | 2865.000 | -38.127 | <0.001 |
| ThC13 | -0.56 | (-0.60, -0.53) | 0.017 | 2865.000 | -32.305 | <0.001 |
| ThC14 | -0.48 | (-0.53, -0.44) | 0.024 | 2865.000 | -20.184 | <0.001 |
| ThC15 | -0.38 | (-0.52, -0.24) | 0.072 | 2865.000 | -5.368 | <0.001 |
| ThC16 | -0.59 | (-0.62, -0.55) | 0.016 | 2865.000 | -36.016 | <0.001 |
| ThC17 | -0.52 | (-0.55, -0.49) | 0.016 | 2865.000 | -31.683 | <0.001 |
| ThC18 | -0.46 | (-0.50, -0.43) | 0.017 | 2865.000 | -26.672 | <0.001 |
| ThC19 | -0.37 | (-0.42, -0.32) | 0.024 | 2865.000 | -15.467 | <0.001 |
| ThC20 | -0.21 | (-0.35, -0.07) | 0.072 | 2865.000 | -2.969 | <0.001 |
| ThC21 | -0.47 | (-0.51, -0.44) | 0.016 | 2865.000 | -29.129 | <0.001 |
| ThC22 | -0.41 | (-0.44, -0.37) | 0.016 | 2865.000 | -24.834 | <0.001 |
| ThC23 | -0.35 | (-0.39, -0.32) | 0.017 | 2865.000 | -20.355 | <0.001 |
| ThC24 | -0.25 | (-0.30, -0.21) | 0.024 | 2865.000 | -10.524 | <0.001 |
| ThC25 | -0.05 | (-0.19, 0.09) | 0.072 | 2865.000 | -0.683 | <0.001 |
| ThC26 | -0.36 | (-0.39, -0.33) | 0.016 | 2865.000 | -22.223 | <0.001 |
| ThC27 | -0.29 | (-0.33, -0.26) | 0.016 | 2865.000 | -17.998 | <0.001 |
| ThC28 | -0.25 | (-0.28, -0.21) | 0.017 | 2865.000 | -14.297 | <0.001 |
| ThC29 | -0.16 | (-0.20, -0.11) | 0.024 | 2865.000 | -6.512 | <0.001 |
| ThC30 | 0.08 | (-0.06, 0.22) | 0.072 | 2865.000 | 1.062 | <0.001 |

**Table D-14:** Full table of variation of the fixed effect 'Specificity' due to different ThCs for APL

| Threshold | Specificity | (95% CI) | Std. Error | DF | t-value | p-value |
|---|---|---|---|---|---|---|
| Ref | 0.72 | (0.64, 0.8) | 0.041 | 2865.000 | 17.641 | <0.001 |
| ThC1 | -0.03 | (-0.08, 0.03) | 0.028 | 2865.000 | -0.912 | 0.362 |
| ThC2 | -0.03 | (-0.08, 0.03) | 0.028 | 2865.000 | -1.049 | 0.294 |
| ThC3 | -0.04 | (-0.10, 0.02) | 0.030 | 2865.000 | -1.426 | 0.154 |
| ThC4 | -0.20 | (-0.28, -0.12) | 0.041 | 2865.000 | -4.894 | <0.001 |
| ThC5 | -0.53 | (-0.77, -0.29) | 0.123 | 2865.000 | -4.320 | <0.001 |
| ThC6 | -0.03 | (-0.08, 0.03) | 0.028 | 2865.000 | -0.912 | 0.362 |
| ThC7 | -0.03 | (-0.08, 0.03) | 0.028 | 2865.000 | -1.049 | 0.294 |
| ThC8 | -0.04 | (-0.10, 0.02) | 0.030 | 2865.000 | -1.426 | 0.154 |
| ThC9 | -0.20 | (-0.28, -0.12) | 0.041 | 2865.000 | -4.894 | <0.001 |
| ThC10 | -0.53 | (-0.77, -0.29) | 0.123 | 2865.000 | -4.320 | <0.001 |
| ThC11 | -0.03 | (-0.08, 0.03) | 0.028 | 2865.000 | -0.912 | 0.362 |

| | | | | | | |
|---|---|---|---|---|---|---|
| ThC12 | -0.03 | (-0.08, 0.03) | 0.028 | 2865.000 | -1.049 | 0.294 |
| ThC13 | -0.04 | (-0.10, 0.02) | 0.030 | 2865.000 | -1.426 | 0.154 |
| ThC14 | -0.20 | (-0.28, -0.12) | 0.041 | 2865.000 | -4.894 | <0.001 |
| ThC15 | -0.53 | (-0.77, -0.29) | 0.123 | 2865.000 | -4.320 | <0.001 |
| ThC16 | -0.03 | (-0.08, 0.03) | 0.028 | 2865.000 | -0.912 | 0.362 |
| ThC17 | -0.03 | (-0.08, 0.03) | 0.028 | 2865.000 | -1.049 | 0.294 |
| ThC18 | -0.04 | (-0.10, 0.02) | 0.030 | 2865.000 | -1.427 | 0.154 |
| ThC19 | -0.20 | (-0.28, -0.12) | 0.041 | 2865.000 | -4.895 | <0.001 |
| ThC20 | -0.53 | (-0.77, -0.29) | 0.123 | 2865.000 | -4.320 | <0.001 |
| ThC21 | -0.03 | (-0.08, 0.03) | 0.028 | 2865.000 | -0.912 | 0.362 |
| ThC22 | -0.03 | (-0.08, 0.03) | 0.028 | 2865.000 | -1.049 | 0.294 |
| ThC23 | -0.04 | (-0.10, 0.02) | 0.030 | 2865.000 | -1.427 | 0.154 |
| ThC24 | -0.20 | (-0.28, -0.12) | 0.041 | 2865.000 | -4.895 | <0.001 |
| ThC25 | -0.53 | (-0.77, -0.29) | 0.123 | 2865.000 | -4.320 | <0.001 |
| ThC26 | -0.03 | (-0.08, 0.03) | 0.028 | 2865.000 | -0.911 | 0.362 |
| ThC27 | -0.03 | (-0.08, 0.03) | 0.028 | 2865.000 | -1.049 | 0.294 |
| ThC28 | -0.04 | (-0.10, 0.02) | 0.030 | 2865.000 | -1.427 | 0.154 |
| ThC29 | -0.20 | (-0.28, -0.12) | 0.041 | 2865.000 | -4.895 | <0.001 |
| ThC30 | -0.53 | (-0.77, -0.29) | 0.123 | 2865.000 | -4.320 | <0.001 |

### D.5.5 FD (S)

**Table D-15:** Full table of variation of the fixed effect 'Accuracy' due to different ThCs for FD

| Threshold | Accuracy | (95% CI) | Std. Error | DF | t-value | p-value |
|---|---|---|---|---|---|---|
| Ref | 0.52 | (0.44, 0.60) | 0.040 | 4535.000 | 12.971 | <0.001 |
| ThC1 | -0.16 | (-0.20, -0.11) | 0.023 | 4535.000 | -7.006 | <0.001 |
| ThC2 | -0.16 | (-0.20, -0.11) | 0.023 | 4535.000 | -7.006 | <0.001 |
| ThC3 | -0.16 | (-0.20, -0.11) | 0.023 | 4535.000 | -7.006 | <0.001 |
| ThC4 | -0.16 | (-0.20, -0.11) | 0.023 | 4535.000 | -7.006 | <0.001 |
| ThC5 | -0.16 | (-0.20, -0.11) | 0.023 | 4535.000 | -7.006 | <0.001 |
| ThC6 | -0.16 | (-0.20, -0.11) | 0.023 | 4535.000 | -6.879 | <0.001 |
| ThC7 | -0.16 | (-0.20, -0.11) | 0.023 | 4535.000 | -6.879 | <0.001 |
| ThC8 | -0.16 | (-0.20, -0.11) | 0.023 | 4535.000 | -6.879 | <0.001 |
| ThC9 | -0.16 | (-0.20, -0.11) | 0.023 | 4535.000 | -6.879 | <0.001 |
| ThC10 | -0.16 | (-0.20, -0.11) | 0.023 | 4535.000 | -6.879 | <0.001 |
| ThC11 | -0.15 | (-0.19, -0.11) | 0.023 | 4535.000 | -6.593 | <0.001 |
| ThC12 | -0.15 | (-0.19, -0.11) | 0.023 | 4535.000 | -6.593 | <0.001 |
| ThC13 | -0.15 | (-0.19, -0.11) | 0.023 | 4535.000 | -6.593 | <0.001 |
| ThC14 | -0.15 | (-0.19, -0.11) | 0.023 | 4535.000 | -6.593 | <0.001 |
| ThC15 | -0.15 | (-0.19, -0.11) | 0.023 | 4535.000 | -6.593 | <0.001 |
| ThC16 | -0.14 | (-0.18, -0.09) | 0.023 | 4535.000 | -5.925 | <0.001 |
| ThC17 | -0.14 | (-0.18, -0.09) | 0.023 | 4535.000 | -5.925 | <0.001 |
| ThC18 | -0.14 | (-0.18, -0.09) | 0.023 | 4535.000 | -5.925 | <0.001 |

| | | | | | | |
|---|---|---|---|---|---|---|
| ThC19 | -0.14 | (-0.18, -0.09) | 0.023 | 4535.000 | -5.925 | <0.001 |
| ThC20 | -0.14 | (-0.18, -0.09) | 0.023 | 4535.000 | -5.925 | <0.001 |
| ThC21 | -0.12 | (-0.16, -0.07) | 0.023 | 4535.000 | -5.145 | <0.001 |
| ThC22 | -0.12 | (-0.16, -0.07) | 0.023 | 4535.000 | -5.145 | <0.001 |
| ThC23 | -0.12 | (-0.16, -0.07) | 0.023 | 4535.000 | -5.145 | <0.001 |
| ThC24 | -0.12 | (-0.16, -0.07) | 0.023 | 4535.000 | -5.145 | <0.001 |
| ThC25 | -0.12 | (-0.16, -0.07) | 0.023 | 4535.000 | -5.145 | <0.001 |
| ThC26 | -0.10 | (-0.15, -0.06) | 0.023 | 4535.000 | -4.472 | <0.001 |
| ThC27 | -0.10 | (-0.15, -0.06) | 0.023 | 4535.000 | -4.472 | <0.001 |
| ThC28 | -0.10 | (-0.15, -0.06) | 0.023 | 4535.000 | -4.472 | <0.001 |
| ThC29 | -0.10 | (-0.15, -0.06) | 0.023 | 4535.000 | -4.472 | <0.001 |
| ThC30 | -0.10 | (-0.15, -0.06) | 0.023 | 4535.000 | -4.472 | <0.001 |

**Table D-16:** Full table of variation of the fixed effect 'Sensitivity' due to different ThCs for FD

| Threshold | Sensitivity | (95% CI) | Std. Error | DF | t-value | p-value |
|---|---|---|---|---|---|---|
| Ref | 0.73 | (0.66 ,0.79) | 0.034 | 4535.000 | 21.426 | <0.001 |
| ThC1 | -0.72 | (-0.77 ,-0.68) | 0.022 | 4535.000 | -33.032 | <0.001 |
| ThC2 | -0.72 | (-0.77 ,-0.68) | 0.022 | 4535.000 | -33.032 | <0.001 |
| ThC3 | -0.72 | (-0.77 ,-0.68) | 0.022 | 4535.000 | -33.032 | <0.001 |
| ThC4 | -0.72 | (-0.77 ,-0.68) | 0.022 | 4535.000 | -33.032 | <0.001 |
| ThC5 | -0.72 | (-0.77 ,-0.68) | 0.022 | 4535.000 | -33.032 | <0.001 |
| ThC6 | -0.71 | (-0.75 ,-0.66) | 0.022 | 4535.000 | -32.236 | <0.001 |
| ThC7 | -0.71 | (-0.75 ,-0.66) | 0.022 | 4535.000 | -32.236 | <0.001 |
| ThC8 | -0.71 | (-0.75 ,-0.66) | 0.022 | 4535.000 | -32.236 | <0.001 |
| ThC9 | -0.71 | (-0.75 ,-0.66) | 0.022 | 4535.000 | -32.236 | <0.001 |
| ThC10 | -0.71 | (-0.75 ,-0.66) | 0.022 | 4535.000 | -32.236 | <0.001 |
| ThC11 | -0.66 | (-0.7 ,-0.62) | 0.022 | 4535.000 | -29.985 | <0.001 |
| ThC12 | -0.66 | (-0.7 ,-0.62) | 0.022 | 4535.000 | -29.985 | <0.001 |
| ThC13 | -0.66 | (-0.7 ,-0.62) | 0.022 | 4535.000 | -29.985 | <0.001 |
| ThC14 | -0.66 | (-0.7 ,-0.62) | 0.022 | 4535.000 | -29.985 | <0.001 |
| ThC15 | -0.66 | (-0.7 ,-0.62) | 0.022 | 4535.000 | -29.985 | <0.001 |
| ThC16 | -0.56 | (-0.6 ,-0.52) | 0.022 | 4535.000 | -25.391 | <0.001 |
| ThC17 | -0.56 | (-0.6 ,-0.52) | 0.022 | 4535.000 | -25.391 | <0.001 |
| ThC18 | -0.56 | (-0.6 ,-0.52) | 0.022 | 4535.000 | -25.391 | <0.001 |
| ThC19 | -0.56 | (-0.6 ,-0.52) | 0.022 | 4535.000 | -25.391 | <0.001 |
| ThC20 | -0.56 | (-0.6 ,-0.52) | 0.022 | 4535.000 | -25.391 | <0.001 |
| ThC21 | -0.44 | (-0.48 ,-0.39) | 0.022 | 4535.000 | -19.759 | <0.001 |
| ThC22 | -0.44 | (-0.48 ,-0.39) | 0.022 | 4535.000 | -19.759 | <0.001 |
| ThC23 | -0.44 | (-0.48 ,-0.39) | 0.022 | 4535.000 | -19.759 | <0.001 |
| ThC24 | -0.44 | (-0.48 ,-0.39) | 0.022 | 4535.000 | -19.759 | <0.001 |
| ThC25 | -0.44 | (-0.48 ,-0.39) | 0.022 | 4535.000 | -19.759 | <0.001 |
| ThC26 | -0.30 | (-0.35 ,-0.26) | 0.022 | 4535.000 | -13.708 | <0.001 |

| | | | | | | |
|---|---|---|---|---|---|---|
| ThC27 | -0.30 | (-0.35 ,-0.26) | 0.022 | 4535.000 | -13.708 | <0.001 |
| ThC28 | -0.30 | (-0.35 ,-0.26) | 0.022 | 4535.000 | -13.708 | <0.001 |
| ThC29 | -0.30 | (-0.35 ,-0.26) | 0.022 | 4535.000 | -13.708 | <0.001 |
| ThC30 | -0.30 | (-0.35 ,-0.26) | 0.022 | 4535.000 | -13.708 | <0.001 |

**Table D-17:** Full table of variation of the fixed effect 'Specificity' due to different ThCs for FD

| Threshold | Specificity | (95% CI) | Std. Error | DF | t-value | p-value |
|---|---|---|---|---|---|---|
| Ref | 0.48 | (0.38, 0.58) | 0.049 | 4535.000 | 9.850 | <0.001 |
| ThC1 | -0.05 | (-0.10, 0.01) | 0.028 | 4535.000 | -1.746 | 0.081 |
| ThC2 | -0.05 | (-0.10, 0.01) | 0.028 | 4535.000 | -1.746 | 0.081 |
| ThC3 | -0.05 | (-0.10, 0.01) | 0.028 | 4535.000 | -1.746 | 0.081 |
| ThC4 | -0.05 | (-0.10, 0.01) | 0.028 | 4535.000 | -1.746 | 0.081 |
| ThC5 | -0.05 | (-0.10, 0.01) | 0.028 | 4535.000 | -1.746 | 0.081 |
| ThC6 | -0.05 | (-0.10, 0.01) | 0.028 | 4535.000 | -1.746 | 0.081 |
| ThC7 | -0.05 | (-0.10, 0.01) | 0.028 | 4535.000 | -1.746 | 0.081 |
| ThC8 | -0.05 | (-0.10, 0.01) | 0.028 | 4535.000 | -1.746 | 0.081 |
| ThC9 | -0.05 | (-0.10, 0.01) | 0.028 | 4535.000 | -1.746 | 0.081 |
| ThC10 | -0.05 | (-0.10, 0.01) | 0.028 | 4535.000 | -1.746 | 0.081 |
| ThC11 | -0.05 | (-0.10, 0.00) | 0.028 | 4535.000 | -1.826 | 0.068 |
| ThC12 | -0.05 | (-0.10, 0.00) | 0.028 | 4535.000 | -1.826 | 0.068 |
| ThC13 | -0.05 | (-0.10, 0.00) | 0.028 | 4535.000 | -1.826 | 0.068 |
| ThC14 | -0.05 | (-0.10, 0.00) | 0.028 | 4535.000 | -1.826 | 0.068 |
| ThC15 | -0.05 | (-0.10, 0.00) | 0.028 | 4535.000 | -1.826 | 0.068 |
| ThC16 | -0.05 | (-0.11, 0.00) | 0.028 | 4535.000 | -1.908 | 0.057 |
| ThC17 | -0.05 | (-0.11, 0.00) | 0.028 | 4535.000 | -1.908 | 0.057 |
| ThC18 | -0.05 | (-0.11, 0.00) | 0.028 | 4535.000 | -1.908 | 0.057 |
| ThC19 | -0.05 | (-0.11, 0.00) | 0.028 | 4535.000 | -1.908 | 0.057 |
| ThC20 | -0.05 | (-0.11, 0.00) | 0.028 | 4535.000 | -1.908 | 0.057 |
| ThC21 | -0.06 | (-0.11, 0.00) | 0.028 | 4535.000 | -2.032 | 0.042 |
| ThC22 | -0.06 | (-0.11, 0.00) | 0.028 | 4535.000 | -2.032 | 0.042 |
| ThC23 | -0.06 | (-0.11, 0.00) | 0.028 | 4535.000 | -2.032 | 0.042 |
| ThC24 | -0.06 | (-0.11, 0.00) | 0.028 | 4535.000 | -2.032 | 0.042 |
| ThC25 | -0.06 | (-0.11, 0.00) | 0.028 | 4535.000 | -2.032 | 0.042 |
| ThC26 | -0.06 | (-0.12, -0.01) | 0.028 | 4535.000 | -2.311 | 0.021 |
| ThC27 | -0.06 | (-0.12, -0.01) | 0.028 | 4535.000 | -2.311 | 0.021 |
| ThC28 | -0.06 | (-0.12, -0.01) | 0.028 | 4535.000 | -2.311 | 0.021 |
| ThC29 | -0.06 | (-0.12, -0.01) | 0.028 | 4535.000 | -2.311 | 0.021 |
| ThC30 | -0.06 | (-0.12, -0.01) | 0.028 | 4535.000 | -2.311 | 0.021 |

### D.5.1 ED (S)

**Table D-18:** Full table of variation of the fixed effect 'Accuracy' due to different ThCs for ED

| Threshold | Accuracy | (95% CI) | Std. Error | DF | t-value | p-value |
|---|---|---|---|---|---|---|
| Ref | 0.46 | (0.39 ,0.54) | 0.039 | 4529.000 | 11.973 | <0.001 |
| ThC1 | -0.15 | (-0.20 ,-0.10) | 0.025 | 4529.000 | -6.080 | <0.001 |
| ThC2 | -0.15 | (-0.20 ,-0.10) | 0.025 | 4529.000 | -6.080 | <0.001 |
| ThC3 | -0.15 | (-0.20 ,-0.10) | 0.025 | 4529.000 | -6.080 | <0.001 |
| ThC4 | -0.15 | (-0.20 ,-0.10) | 0.025 | 4529.000 | -6.080 | <0.001 |
| ThC5 | -0.15 | (-0.20 ,-0.10) | 0.025 | 4529.000 | -6.080 | <0.001 |
| ThC6 | -0.15 | (-0.20 ,-0.10) | 0.025 | 4529.000 | -5.962 | <0.001 |
| ThC7 | -0.15 | (-0.20 ,-0.10) | 0.025 | 4529.000 | -5.962 | <0.001 |
| ThC8 | -0.15 | (-0.20 ,-0.10) | 0.025 | 4529.000 | -5.962 | <0.001 |
| ThC9 | -0.15 | (-0.20 ,-0.10) | 0.025 | 4529.000 | -5.962 | <0.001 |
| ThC10 | -0.15 | (-0.20 ,-0.10) | 0.025 | 4529.000 | -5.962 | <0.001 |
| ThC11 | -0.14 | (-0.19 ,-0.09) | 0.025 | 4529.000 | -5.585 | <0.001 |
| ThC12 | -0.14 | (-0.19 ,-0.09) | 0.025 | 4529.000 | -5.585 | <0.001 |
| ThC13 | -0.14 | (-0.19 ,-0.09) | 0.025 | 4529.000 | -5.585 | <0.001 |
| ThC14 | -0.14 | (-0.19 ,-0.09) | 0.025 | 4529.000 | -5.585 | <0.001 |
| ThC15 | -0.14 | (-0.19 ,-0.09) | 0.025 | 4529.000 | -5.585 | <0.001 |
| ThC16 | -0.13 | (-0.18 ,-0.08) | 0.025 | 4529.000 | -5.155 | <0.001 |
| ThC17 | -0.13 | (-0.18 ,-0.08) | 0.025 | 4529.000 | -5.155 | <0.001 |
| ThC18 | -0.13 | (-0.18 ,-0.08) | 0.025 | 4529.000 | -5.155 | <0.001 |
| ThC19 | -0.13 | (-0.18 ,-0.08) | 0.025 | 4529.000 | -5.155 | <0.001 |
| ThC20 | -0.13 | (-0.18 ,-0.08) | 0.025 | 4529.000 | -5.155 | <0.001 |
| ThC21 | -0.11 | (-0.15 ,-0.06) | 0.025 | 4529.000 | -4.243 | <0.001 |
| ThC22 | -0.11 | (-0.15 ,-0.06) | 0.025 | 4529.000 | -4.243 | <0.001 |
| ThC23 | -0.11 | (-0.15 ,-0.06) | 0.025 | 4529.000 | -4.243 | <0.001 |
| ThC24 | -0.11 | (-0.15 ,-0.06) | 0.025 | 4529.000 | -4.243 | <0.001 |
| ThC25 | -0.11 | (-0.15 ,-0.06) | 0.025 | 4529.000 | -4.243 | <0.001 |
| ThC26 | -0.08 | (-0.13 ,-0.03) | 0.025 | 4529.000 | -3.178 | 0.002 |
| ThC27 | -0.08 | (-0.13 ,-0.03) | 0.025 | 4529.000 | -3.178 | 0.002 |
| ThC28 | -0.08 | (-0.13 ,-0.03) | 0.025 | 4529.000 | -3.178 | 0.002 |
| ThC29 | -0.08 | (-0.13 ,-0.03) | 0.025 | 4529.000 | -3.178 | 0.002 |
| ThC30 | -0.08 | (-0.13 ,-0.03) | 0.025 | 4529.000 | -3.178 | 0.002 |

**Table D-19:** Full table of variation of the fixed effect 'Sensitivity' due to different ThCs for ED

| Threshold | Sensitivity | (95% CI) | Std. Error | DF | t-value | p-value |
|---|---|---|---|---|---|---|
| Ref | 0.77 | (0.71 ,0.84) | 0.031 | 4529.000 | 24.640 | <0.001 |
| ThC1 | -0.77 | (-0.82 ,-0.73) | 0.022 | 4529.000 | -34.363 | <0.001 |
| ThC2 | -0.77 | (-0.82 ,-0.73) | 0.022 | 4529.000 | -34.363 | <0.001 |
| ThC3 | -0.77 | (-0.82 ,-0.73) | 0.022 | 4529.000 | -34.363 | <0.001 |

| | | | | | | |
|---|---|---|---|---|---|---|
| ThC4 | -0.77 | (-0.82 ,-0.73) | 0.022 | 4529.000 | -34.363 | <0.001 |
| ThC5 | -0.77 | (-0.82 ,-0.73) | 0.022 | 4529.000 | -34.363 | <0.001 |
| ThC6 | -0.75 | (-0.8 ,-0.71) | 0.022 | 4529.000 | -33.610 | <0.001 |
| ThC7 | -0.75 | (-0.8 ,-0.71) | 0.022 | 4529.000 | -33.610 | <0.001 |
| ThC8 | -0.75 | (-0.8 ,-0.71) | 0.022 | 4529.000 | -33.610 | <0.001 |
| ThC9 | -0.75 | (-0.8 ,-0.71) | 0.022 | 4529.000 | -33.610 | <0.001 |
| ThC10 | -0.75 | (-0.8 ,-0.71) | 0.022 | 4529.000 | -33.610 | <0.001 |
| ThC11 | -0.70 | (-0.74 ,-0.66) | 0.022 | 4529.000 | -31.145 | <0.001 |
| ThC12 | -0.70 | (-0.74 ,-0.66) | 0.022 | 4529.000 | -31.145 | <0.001 |
| ThC13 | -0.70 | (-0.74 ,-0.66) | 0.022 | 4529.000 | -31.145 | <0.001 |
| ThC14 | -0.70 | (-0.74 ,-0.66) | 0.022 | 4529.000 | -31.145 | <0.001 |
| ThC15 | -0.70 | (-0.74 ,-0.66) | 0.022 | 4529.000 | -31.145 | <0.001 |
| ThC16 | -0.60 | (-0.65 ,-0.56) | 0.023 | 4529.000 | -26.768 | <0.001 |
| ThC17 | -0.60 | (-0.65 ,-0.56) | 0.023 | 4529.000 | -26.768 | <0.001 |
| ThC18 | -0.60 | (-0.65 ,-0.56) | 0.023 | 4529.000 | -26.768 | <0.001 |
| ThC19 | -0.60 | (-0.65 ,-0.56) | 0.023 | 4529.000 | -26.768 | <0.001 |
| ThC20 | -0.60 | (-0.65 ,-0.56) | 0.023 | 4529.000 | -26.768 | <0.001 |
| ThC21 | -0.46 | (-0.51 ,-0.42) | 0.023 | 4529.000 | -20.481 | <0.001 |
| ThC22 | -0.46 | (-0.51 ,-0.42) | 0.023 | 4529.000 | -20.481 | <0.001 |
| ThC23 | -0.46 | (-0.51 ,-0.42) | 0.023 | 4529.000 | -20.481 | <0.001 |
| ThC24 | -0.46 | (-0.51 ,-0.42) | 0.023 | 4529.000 | -20.481 | <0.001 |
| ThC25 | -0.46 | (-0.51 ,-0.42) | 0.023 | 4529.000 | -20.481 | <0.001 |
| ThC26 | -0.30 | (-0.34 ,-0.25) | 0.023 | 4529.000 | -13.192 | <0.001 |
| ThC27 | -0.30 | (-0.34 ,-0.25) | 0.023 | 4529.000 | -13.192 | <0.001 |
| ThC28 | -0.30 | (-0.34 ,-0.25) | 0.023 | 4529.000 | -13.192 | <0.001 |
| ThC29 | -0.30 | (-0.34 ,-0.25) | 0.023 | 4529.000 | -13.192 | <0.001 |
| ThC30 | -0.30 | (-0.34 ,-0.25) | 0.023 | 4529.000 | -13.192 | <0.001 |

**Table D-20:** Full table of variation of the fixed effect 'Specificity' due to different ThCs for ED

| Threshold | Specificity | (95% CI) | Std. Error | DF | t-value | p-value |
|---|---|---|---|---|---|---|
| Ref | 0.40 | (0.31 ,0.49) | 0.047 | 4529.000 | 8.549 | 0.000 |
| Th1 | -0.02 | (-0.08 ,0.04) | 0.030 | 4529.000 | -0.701 | 0.484 |
| Th2 | -0.02 | (-0.08 ,0.04) | 0.030 | 4529.000 | -0.701 | 0.484 |
| Th3 | -0.02 | (-0.08 ,0.04) | 0.030 | 4529.000 | -0.701 | 0.484 |
| Th4 | -0.02 | (-0.08 ,0.04) | 0.030 | 4529.000 | -0.701 | 0.484 |
| Th5 | -0.02 | (-0.08 ,0.04) | 0.030 | 4529.000 | -0.701 | 0.484 |
| Th6 | -0.02 | (-0.08 ,0.04) | 0.030 | 4529.000 | -0.700 | 0.484 |
| Th7 | -0.02 | (-0.08 ,0.04) | 0.030 | 4529.000 | -0.700 | 0.484 |
| Th8 | -0.02 | (-0.08 ,0.04) | 0.030 | 4529.000 | -0.700 | 0.484 |
| Th9 | -0.02 | (-0.08 ,0.04) | 0.030 | 4529.000 | -0.700 | 0.484 |
| Th10 | -0.02 | (-0.08 ,0.04) | 0.030 | 4529.000 | -0.700 | 0.484 |
| Th11 | -0.02 | (-0.08 ,0.04) | 0.030 | 4529.000 | -0.700 | 0.484 |

| | | | | | | |
|---|---|---|---|---|---|---|
| Th12 | -0.02 | (-0.08 ,0.04) | 0.030 | 4529.000 | -0.700 | 0.484 |
| Th13 | -0.02 | (-0.08 ,0.04) | 0.030 | 4529.000 | -0.700 | 0.484 |
| Th14 | -0.02 | (-0.08 ,0.04) | 0.030 | 4529.000 | -0.700 | 0.484 |
| Th15 | -0.02 | (-0.08 ,0.04) | 0.030 | 4529.000 | -0.700 | 0.484 |
| Th16 | -0.03 | (-0.09 ,0.03) | 0.030 | 4529.000 | -0.945 | 0.345 |
| Th17 | -0.03 | (-0.09 ,0.03) | 0.030 | 4529.000 | -0.945 | 0.345 |
| Th18 | -0.03 | (-0.09 ,0.03) | 0.030 | 4529.000 | -0.945 | 0.345 |
| Th19 | -0.03 | (-0.09 ,0.03) | 0.030 | 4529.000 | -0.945 | 0.345 |
| Th20 | -0.03 | (-0.09 ,0.03) | 0.030 | 4529.000 | -0.945 | 0.345 |
| Th21 | -0.03 | (-0.09 ,0.03) | 0.030 | 4529.000 | -1.016 | 0.310 |
| Th22 | -0.03 | (-0.09 ,0.03) | 0.030 | 4529.000 | -1.016 | 0.310 |
| Th23 | -0.03 | (-0.09 ,0.03) | 0.030 | 4529.000 | -1.016 | 0.310 |
| Th24 | -0.03 | (-0.09 ,0.03) | 0.030 | 4529.000 | -1.016 | 0.310 |
| Th25 | -0.03 | (-0.09 ,0.03) | 0.030 | 4529.000 | -1.016 | 0.310 |
| Th26 | -0.03 | (-0.09 ,0.03) | 0.030 | 4529.000 | -1.096 | 0.273 |
| Th27 | -0.03 | (-0.09 ,0.03) | 0.030 | 4529.000 | -1.096 | 0.273 |
| Th28 | -0.03 | (-0.09 ,0.03) | 0.030 | 4529.000 | -1.096 | 0.273 |
| Th29 | -0.03 | (-0.09 ,0.03) | 0.030 | 4529.000 | -1.096 | 0.273 |
| Th30 | -0.03 | (-0.09 ,0.03) | 0.030 | 4529.000 | -1.096 | 0.273 |

# APPENDIX E MATLAB® Code

The MATLAB® code used to process the EMG and strain gauge data in the present study was developed by the examiner in collaboration with C Swanepoel. Figure E-1 provides an overview of the main functions written for processing the data, along with references to specific MATLAB® m-files which performed important roles. Basic descriptions of each of these files are provided in sections E.1, E.2 and E.3. Full versions of the MATLAB® m-files are available on request

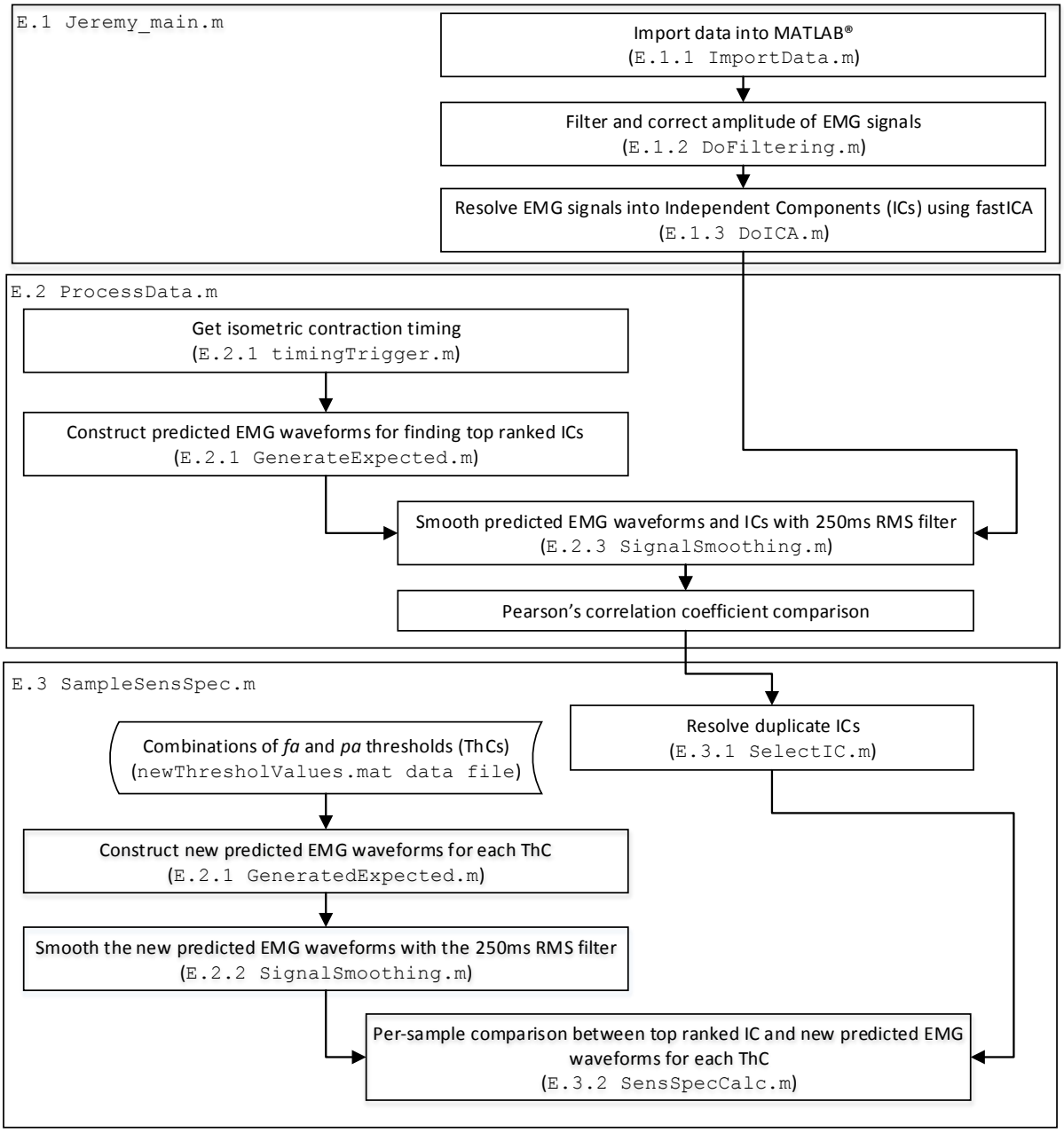


**Figure E-13**: Flow diagram of MATLAB processing steps with reference to important m-files

## E.1 Jeremy_main.m

```
function Jeremy_main()

%=========================================================================

%  Date:     2014/02/23

%  Author:   Cara Swanepoel

%  Adapted by: Jeremy Pitman

%  Email:    jempitman@gmail.com

%

% Jeremy_MAIN:

% 1.Import raw mixed EMG and strain signals obtained with the 50
Channel EMG system, as well as all supporting experimental and
participant information.

% 2.ICA is then performed in order to obtain ICs

% 3.ICs are then correlated to expected data obtained from the
strain signals in order to calculate the correlation coefficients
needed to determine whether or not the targeted muscle activity has
been recorded.

%

% Sub Components:

%     - IMPORTDATA

%     - DOICA

%     - DOFILTERING

%     - FORMATDATA

%     - PROCESSDATA

%         - GETEXPECTED

%         - GETACTUAL

%         - DOCORRELATION

%         - ORDERCC

%
```

### E.1.1 ImportData

```
function [participantName, date, time, MVCData, movementSequence, strainData, channelSelect,impedanceData, mixedEMGData, selectedEMGData] = ImportData2(fileName,saveData)

%==========================================================================

%  Date:     2014/02/24

%  Author:   Cara Swanepoel

%  Adapted by: Jeremy Pitman

%  Email:    jempitman@gmail.com

%

% IMPORTDATA:

% Import the data from the selected file into MATLAB

% Separate the data into the various components

%     - Participant data

%     - Setup data

%     - MVC data

%     - Movement Sequence

%     - Strain data

%     - Channel data

%             - Channel Select

%             - Impedance data

%             - Mixed EMG data

%             - Selected EMG data

%  fileName:      Name of the file to import the data from
```

### E.1.2 DoFiltering.m

```
function [filteredSignals] = DoFiltering(inSignals, sampleFreq, participantName, date, time)

%=========================================================================

%  Date:     2014/02/28

%  Author:   Jeremy Pitman

%  Email:    jempitman@gmail.com

%

% DOFILTERING:

% Perform digital filtering on the raw monopolar EMG waveforms. The signals are zeroed, amplitude corrected, then bandpass filtered using a 4th order Butterworth filter from 5-500Hz.

%

% inSignals:  Input signals to be filtered

% filteredSignals: The filtered signals

%                        (length(inSignals) == length(outSignals))
```

### E.1.3 DoICA

```
function [ICA] = DoICA(mixedEMGData, sampleRate, participantName, date, time)

%=========================================================================

%  Date:     2014/02/28

%  Author:   Cara Swanepoel

%  Adapted by: Jeremy pitman

%  Email:    jempitman@gmail.com

%

% DOICA:

% Perform FASTICA on the signals given as input

%

% ICA:    Estimated independent components

% A:      Mixing matrix

% W:      Estimated separating matrix

%

% mixedEMGData: Mixed EMG Signals

%                   Each     row     represents     one     channel
```

## E.2 ProcessData.m

```
function [muscleCorrelation] = ProcessData2(movementSequence,
muscles,...
    inputSignals, timingArray, window, pattern,...
    participantName, date, time)
%=========================================================================
%  Date:     2014/03/07
%  Author:   Cara Swanepoel
%  Adapted by: Jeremy Pitman
%  Email:    jempitman@gmail.com %
% PROCESSDATA:
%     EXPECTED SIGNALS: Modelled muscle activity derived from needle
EMG studies in previous literature. Timing for modelled
activity derived from strain gauges.
%       ACTUAL SIGNALS:        The actual activation patterns are
determined from the filtered/formatted ICs
%     DO CORRELATION:      Perform correlation between the expected
signals for each muscle and the actual signals
%     RANK CORRRELATION:  Rank the correlations for each muscle to
determine which IC best fits the expected activation pattern
%    SAVE CORR. DATA:    Save the correlation data generated
%
%    Create a structure to hold the data for each muscle:
%        muscleCorrelation: - Muscle Name
%                           - Expected Signal
%                           - Highest 5 correlation coefficients
%                                - IC Name
%                                - IC Signal
%                                - Corr. coeff.
% movementSamples:    Number of sample per movement
% movementSequence:   Sequence that movements were performed in
```

```
% strain:                Signals from the 3 strain gauge bridges (2
thumb, 1 finger)

% inputSignals:         Signals to be processed (filtered/formatted
ICs)

% participantName:     Name of participant (as a string)

% date:                Date (as a string)

%   time:                                  Time   (as   a   string)
```

### E.2.1 timingTrigger.m

```
function [timingArray, newMovementSequence]=
timing_trigger(strainData, MVCData, movementSequence,
movementSamples)

%================================================================

% Date: 11 August 2014

% Author: Jeremy Pitman

% Email: jempitman@gmail.com

%

% timing_trigger: function for determining muscle activation timing
derived from strain gauge information.

%

% strain gauge 1 = vertical movements (thumb flexion and extension)

% strain gauge 2 = horizontal movements (thumb abduction and
adduction)

% strain gauge 3 = finger movements (index finger flexion and
extension)

%

%       tL:             lower threshold limit

%       tH:             upper threshold limit

%       trackL:         array storing position of +ve lower limit

%       trackH:         array storing position of +ve upper limit

%       trackL_neg:     array storing position of -ve lower limit

%        trackH_neg:      array storing position of _ve upper limit
```

### E.2.2 GenerateExpected.m

```
function expectedSigs = GenerateExpected2(movementSequence, muscles,
actualSigSamples, timingArray, pattern, participantName, date, time)

%=========================================================================

%

%  Date:       2014/03/11

%  Author:     Cara Swanepoel

%  Adapted by: Jeremy Pitman

%  Email:      jempitman@gmail.com

% %

% GENERATEEXPECTED:

% Generate the expected activation signals for each muscle based on
the sequence in which the movements were performed.

%    Signal    must    be    normalised    to    the    range    [0,1].
```

### E.2.3 SignalSmoothing.m

```
function [smoothedSignals] = Signal_smoothing(inputSignals, window,
cell)

%=========================================================================
=======

%

%  Date:        2014/09/10

%  Author:      Jeremy Pitman

%  Email:       jempitman@gmail.com

%

% Signal_smoothing:

% Applying an RMS filter to inputSignals.

% Normalise signals to the range [0,1].

%

% smoothedSignals:  RMS performed on input signals

% inputSignals:      Filtered, rectified, normalized IC or expected
signals

% window:           number of samples used for RMS computation

% cell:                identifier if inputSignals are in cell array
form
```

## E.3 SampleSensSpec.m

```
function SampleSensSpec

%=========================================================================

%

%   Date: 2014/09/12

%   Author: Jeremy Pitman

%   Email: jempitman@gmail.com

%

%   SampleSensSpec.m

% Sample based Accuracy, Sensitivity and Specificity analysis of RMS
smoothed IC waveforms and predicted EMG waveforms generated for
different combinations of f and p (ThCs).

%

%   muscleCorrelation:  struct containing highest ranked IC/expected
pair

%   partial:            partial activation threshold

%   full:               full activation threshold
```

### E.3.1 SelectIC.m

```
function topRanked = SelectIC(muscleCorrelation)

%=========================================================================
=======

%

%  Date:     2014/10/25

%  Author:   Cara Swanepoel

%  Email:    cara.swanepoel@gmail.com

%

% SELECTIC:

%

% Select the top correlated IC for each muscle.

% Check for duplicates and decide on selection if there are
duplicates.
```

### E.3.2 SensSpecCalc.m

```
function [TP,TN,FP,FN,Sens,Spec,Acc]= SensSpecCalc(smoothedExpected,
ICs, psSSA, offThresh, meanRest, muscles, tickPosition, xlabels)

%============================================================

%     Date:       2015/02/14

%     Author:     Jeremy Pitman

%     Email:      jempitman@gmail.com

%

%     SensSpecCalc:

%      Calculate sample basis sensitivity, specificity and accurracy
by counting the TN, FN, TP and FP between the predicted and actual
waveforms at different values of partial and full activation
thresholds

%

%     TP: True Positive

%     FN: False Negative

%     TN: True Negative

%     FP: False Positive

%

%       Sens: Sensitivity

%       Spec: Specificity

%       Acc: Accuracy
```

# APPENDIX F Technical documents

APPENDIX F contains the various technical documents relevant to the study such as blank copies of the informed consent forms, datasheets, technical notes and engineering drawings of the various pieces of equipment developed to test the research objectives of the study. A breakdown of the different documents and the pages on which they may be found (following on from page numbering indicated below) is provided in Table F-1:

**Table F-1**: Order of technical documents

| # | Document type | Page(s) |
|---|---|---|
| 1 | Participant Informed Consent Form | 194-196 |
| 2 | Strain gauge amplifier printed circuit board schematic[25] | 197 |
| 3 | Strain gauge amplifier datasheet[26] | 198 |
| 4 | Modifying the OpenEEG Analogue Board for EMG Acquisition Technical Note | 199-206 |
| 5 | Selected pages of the AD5235 digital potentiometer datasheet[27] | 207-210 |
| 6 | Selected pages from the EVAL-AD5546 signal attenuator module user guide[28] | 211-215 |
| 7 | Selected pages from the datasheet for the AD5546 attenuator chip[29] | 216-226 |
| 8 | Engineering drawings of the Thumb Dynamometer | 227-234 |
| 9 | Engineering drawings of the Finger Load Cell | 235-237 |
| 10 | Engineering drawings of the Electrode punch | 238-247 |

[25] Ref: http://za.rs-online.com/web/p/strain-gauge-accessories/0435692/
[26] Ref: http://za.rs-online.com/web/p/strain-gauge-accessories/0846171/
[27] Ref: http://www.analog.com/en/search.html?q=ad5235
[28] Ref: http://www.analog.com/en/search.html?q=ad5546
[29] Ref: http://www.analog.com/en/search.html?q=ad5546

# Subject Consent Form-EMG testing

## *The Development of an EMG-controlled orthotic for stroke rehabilitation of the flaccid hand*

### Definitions

**Electrodes:** Small metal caps placed on the skin or scalp to measure electrical signals.
**Electromyography (EMG):** Electrical biological signals given off by contracting muscles.
**Orthotic device:** Orthopedic assistive device for the support or correction of limb function.

### Informed consent:

Researchers at the MRC/UCT Medical Imaging Research Unit are developing an assistive device for the rehabilitation and regaining of hand function for stroke sufferers, as part of the requirements for a Master's Degree in Biomedical Engineering for the co-principal researcher, Jeremy Pitman. The orthotic device attempts to measure the muscle activity (EMG) in different locations on the forearm with electrodes and then use that activity to control the device to assist you to complete actions, if you are not able. EMG is a safe, non-invasive recording technique that requires the placement of electrodes on your forearm

In this test the EMG signals will be recorded while you perform natural movements of the hand using a movement platform. The movement platform is to ensure that the correct movement is performed with a light to indicate when the action is performed correctly.

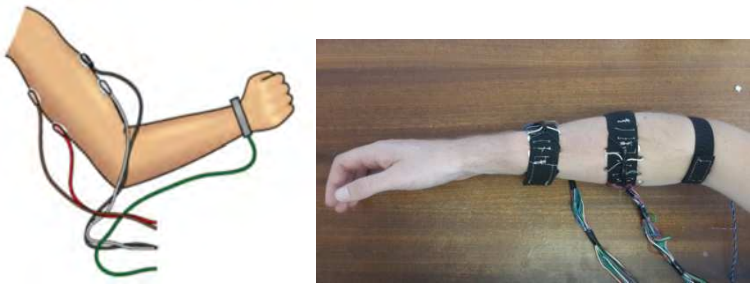

**Figure 1: Left, EMG electrodes applied to the upper limb** (Produceconsumerobot, n.d.)**. Right, electrode bands to be used for testing**

### Testing procedure:

All testing will be carried out at the UCT Faculty of Health Sciences, and has been pre-approved by the Human Ethics Committee (HREC ref: 546/2011). Personal information will be held confidential and you have the right to withdraw from the study at any stage. To ensure good electrical contact, the skin on your forearm will be lightly cleaned with medical alcohol to remove dead skin cells. This should cause very slight discomfort at the most. Two stretchable electrode bands will then be placed over your forearm and the electrodes will be covered with an electrolyte gel, which causes no discomfort. The paste is applied to help the electrode stay in place and provide better signal quality and is easily washed off the skin after the experiment.

A series of instructions will be given to you prior to the start of the testing. You will have to perform the following actions on the movement platform (in random order):

1. Moving the thumb parallel to the palm, towards the little finger.
2. Moving the thumb parallel to the palm, away from the little finger.
3. Moving the thumb towards the palm.
4. Moving the thumb away from the palm.
5. Bending the middle index finger knuckle.
6. Straightening the middle index finger knuckle.
7. Sustain each action for 5 seconds and then return to a rest position.

8. Actions 1-6 above will be repeated 10 times each.

Testing should take approximately 1 hour. You will be paid R50 on successful completion of the recording. There will be no direct benefit to you but the results of the research will add understanding to the application of non-invasive deep muscle EMG to the forearm.

**Possible risks associated with participation:**
EMG recordings are harmless and painless. The recording equipment will be isolated from mains supply by being connected to a battery powered laptop during testing. Temporary mild skin sensitivity may result from the gel used with the electrodes. Only the right arm will be used for testing, thus there is no risk of cardiac arrest. The movement platform has been designed with minimal mechanical impedance and as easy to manipulate as possible. In the unlikely event that you experience discomfort, the investigator should be alerted immediately.

The University of Cape Town (UCT) has insurance cover for the event that research-related injury or harm results from your participation in the trial. The insurer will pay all reasonable medical expenses in accordance with the South African Good Clinical Practice Guidelines (DoH 2006), based on the Association of the British Pharmaceutical Industry Guidelines (ABPI) in the event of an injury or side effect resulting directly from your participation in the trial. You will not be required to prove fault on the part of the University.

The University **will not be liable** for any loss, injuries and/or harm that you may sustain where the loss is caused by

- The use of unauthorised medicine or substances during the study
- Any injury that results from you not following the protocol requirements or the instructions that the study doctor may give you
- Any injury that arises from inadequate action or lack of action to deal adequately with a side effect or reaction to the study medication
- An injury that results from the negligence on your part

"By agreeing to participate in this study, you do not give up your right to claim compensation for injury where you can prove negligence, in separate litigation. In particular, your right to pursue such a claim in a South African court in terms of South African law must be ensured. Note, however, that you will usually be requested to accept that payment made by the University under the SA GCP guideline 4.11 is in full settlement of the claim relating to the medical expenses. "

An injury is considered trial-related if, and to the extent that, it is caused by study activities. You must notify the study doctor immediately of any side effects and/or injuries during the trial, whether they are research-related or other related complications.

UCT reserves the right not to provide compensation if, and to the extent that, your injury came about because you chose not to follow the instructions that you were given while you were taking part in the study. Your right in law to claim compensation for injury where you prove negligence is not affected. Copies of these guidelines are available on request.

**Statement of understanding and consent:**
I confirm that I am over 18 years of age and the exact procedure and techniques and the possible complications of the above tests have been thoroughly explained to me. I am free to withdraw from the study at any time should I choose to do so. I understand that I may not go through with the testing procedure if I suffer from muscular disorders of any kind, and may ask questions at any time during the testing procedure. I know that the personal information required by the researchers and derived from the testing procedure will remain strictly confidential and will only be revealed as a

number in classification analysis. I have carefully read this form and understand the nature, purpose and procedures of this study. I agree to participate in this research project conducted by the MRC/UCT Medical Imaging Research Unit.

**Name of volunteer:**_____
**Signature:**_____
**Name of investigator:**_____
**Signature:**_____
**Date:**_____

**Researchers:**

Co-Principal Investigator: Dr. LR John (Senior lecturer, University of Cape Town)
Co-Principal Investigator: Mr. Jeremy Pitman (MSc(Med): BME student, University of Cape Town)

**Contact details:**


| | |
|---|---|
| Principal Investigator: Lester John, BScEng, PhD<br>Electronic & Biomedical Engineer<br>MRC/UCT Medical Imaging Research Unit<br>Department of Human Biology<br>Faculty of Health Sciences<br>University of Cape Town<br>Observatory 7925<br>South Africa<br>Tel: +27 21 406-6548; Fax: +27 21 448-7226<br>Lester.John@uct.ac.za<br>http://www.uct.ac.za/departments/humanbio | UCT Research Ethics Committee contact:<br>UCT Research Ethics Committee<br>Health Sciences Faculty<br>E53 Room 44.1<br>Old Main Building<br>Groote Schuur Hospital<br>Observatory 7925<br>South Africa<br>Tel: +27 21 406-6338<br>Fax: +27 21 406-6411<br>Sumayah.Ariefdien@uct.ac.za |

## GB — RS Stock No.

435-692

A printed circuit board to accept the RS Strain Gauge Amplifier and associated components to make an amplifier decoder for resistive bridge type sensors.

### Assembly

All components positions are marked on the PCB, shorting links are indicated by solid lines.The components list below includes PCB mounting screw terminals for ease of connection, however these need not be used as wires can be directly soldered to the board. The values of R1 and R2 given below set the gain to 1000. The gain can be set to other values and is defined by the equation.

$$\text{Gain} = 1+\frac{R_1}{R_2}$$

C5, C6 and C7 are for reduction of noise and considerably slow the output response. In some applications these components are best removed.



## D — RS Best-Nr.

435-692

Die Leiterplatte dient zur Aufnahme des RS DMS-Verstärkers und der zugehörigen Bauteile, so daß ein Verstärker/Dekoder für Sensoren mit ohmscher Brücken-Konfiguration erstellt wird.

### Montage

Alle Bauteilpositionen sind auf der Leiterplatte aufgedruckt, Kurzschlußverbindungen sind durch durchgehende Linien gekennzeichnet. Die Liste der Bauteile (siehe unten) umfaßt u.a. eine Schraubklemme zur einfachen Leiterplattenmontage, die Drähte können jedoch auch direkt mit der Platte verlötet werden. Die unten genannten Werte von R1 und R2 ergeben eine Verstärkung von 1000. Eine andere Einstellung de Verstärkung ist anhand der folgenden Formel möglich:

$$\text{Verstärkung} = 1+\frac{R_1}{R_2}$$

C5, C6 und C7 dienen der Rauschverminderung, verlangsamen die Ausgabegeschwindigkeit jedoch erheblich. Bei manchen Anwendungen empfiehlt es sich daher, diese Bauteile wegzulassen.



## E — Código RS.

435-692

Se trata de una tarjeta de circuito impreso que acepta el amplificador RS para galga extensométrica y los componentes correspondientes, lo que le convierte en un decodificador amplificador para sensores del tipo de puente de resistencias.

### Conjunto

En la tarjeta de circuito impreso están marcadas las posiciones de todos los componentes; los puentes de enlace están indicados por trazos continuos. La siguiente lista de componentes incluye los terminales de tornillo para montaje de la tarjeta con el fin de facilitar su conexión, aunque no es necesario utilizarlos, ya que se pueden soldar directamente los holos a la tarjeta.

Los valores de R1 y R2 que se indican a continuación dan una ganancia de 1.000. La ganancia se puede ajustar a otros valores y viene definida por la ecuación.

$$\text{Ganancia} = 1+\frac{R_1}{R_2}$$

Los condensadores C5, C6 y C7 están destinados a reducir el ruido y ralentizar considerablemente la respuesta de salida. En determinadas aplicaciones conviene quitar estos componentes.



## F — Code commande RS.

435-692

Carte de circuits imprimés recevant l'amplificateur de la jauge extensométrique RS et les composants correspondants, pour offrir un décodeur d'amplificateur pour les capteurs de type pont résistif.

### Assemblage

Toutes les positions des composants sont indiquées sur la carte de circuits imprimés, les liaisons de court-circuitage sont indiquées par une ligne continue. La liste des composants ci-dessous comprend les bornes de montage à vis de la carte de circuits imprimés pour faciliter les connexions; cependant, celles-ci ne sont pas nécessaires, car on peut souder directement les fils à la carte.
Les valeurs R1 et R2 ci-dessous établissent le gain à 1 000. On peut régler le gain à un autre chiffre et le définir par l'équation.

$$\text{Gain} = 1+\frac{R_1}{R_2}$$

C5, C6 et C7 sont pour la réduction du bruit et ralentissent considérablement la réponse de sortie. Dans certains cas, il vaut mieux enlever ces composants.



## I — RS Codici.

435-692

Un circuito stampato accoglie l'amplificatore per estensimetri RS ed altri componenti ad esso associati, per realizzare un amplificatore/decodificatore per sensori con configurazione a ponte resistivo.

### Complessivo

La posizione di ogni componente è contrassegnata sulla scheda, ed i collegamenti di corto circuito sono indicati da delle linee solide. I componenti elencati qui di seguito sono compresi dei terminali con vite di montaggio su scheda per un facile collegamento. Non è tuttavia necessario utilizzare tali viti, in quanto è possibile saldare i fili direttamente sulla scheda. I valori R1 ed R2 riportati qui di seguito, impostano il guadagno a 1000. Il guadagno può essere impostato ad altri valori e viene definito in base alla seguente equazione:

$$\text{Guadagno} = 1+\frac{R_1}{R_2}$$

C5, C6 e C7 servono per ridurre il disturbo e rallentare in modo considerevole la risposta di uscita. In alcune applicazioni è meglio eliminare questi componenti.



*Issued / Herausgegeben / Publicado / Publication / Publicatto 06/2003* **1200001386/V7412**

Instruction Leaflet
Bedienungsanleitung
Hojas de instrucciones
Feuille d'instructions
Foglio d'instruzioni

# Strain Gauge Amplifier PCB (GB)

# Leiterplatte für Dehnungsmeßstreifen -Verstärker (D)

# PCB de amplificación para galga extensométrica (E)

# Carte de circuits imprimés de l'amplificateur de jauge extensométrique (F)

# Scheda circuito stampato per amlificatore di estensimetri (I)

## Figures / Figures / Figura

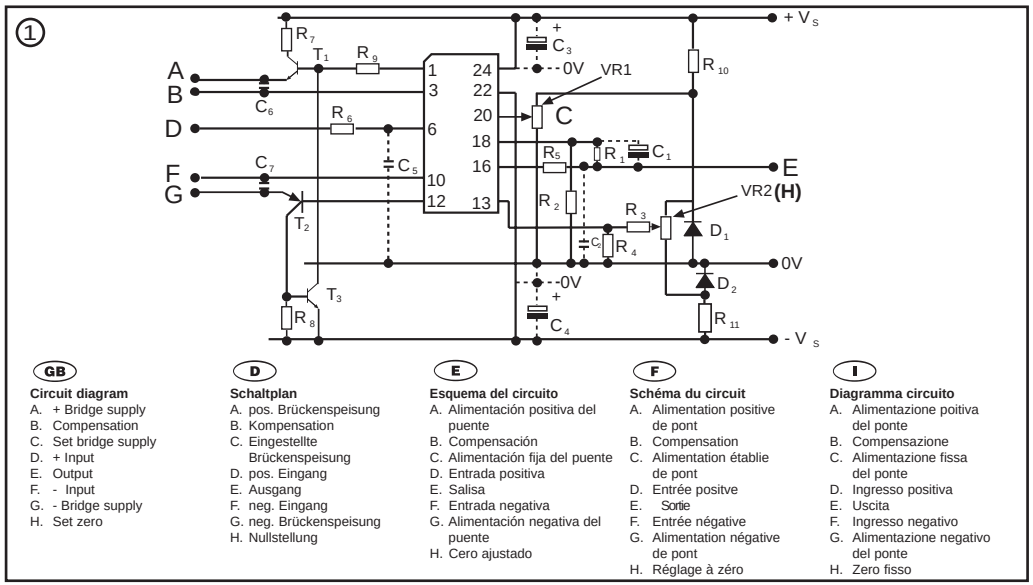


**GB**
**Circuit diagram**
A. + Bridge supply
B. Compensation
C. Set bridge supply
D. + Input
E. Output
F. - Input
G. - Bridge supply
H. Set zero

**D**
**Schaltplan**
A. pos. Brückenspeisung
B. Kompensation
C. Eingestellte Brückenspeisung
D. pos. Eingang
E. Ausgang
F. neg. Eingang
G. neg. Brückenspeisung
H. Nullstellung

**E**
**Esquema del circuito**
A. Alimentación positiva del puente
B. Compensación
C. Alimentación fija del puente
D. Entrada positiva
E. Salisa
F. Entrada negativa
G. Alimentación negativa del puente
H. Cero ajustado

**F**
**Schéma du circuit**
A. Alimentation positive de pont
B. Compensation
C. Alimentation établie de pont
D. Entrée positve
E. Sortie
F. Entrée négative
G. Alimentation négative de pont
H. Réglage à zéro

**I**
**Diagramma circuito**
A. Alimentazione poitiva del ponte
B. Compensazione
C. Alimentazione fissa del ponte
D. Ingresso positiva
E. Uscita
F. Ingresso negativo
G. Alimentazione negativo del ponte
H. Zero fisso

**Components List / Liste der Bauteile / Lista de componentes / Liste des componants / Elenco componeti**

| Component / Bauteile / Componentes / Componsant / Componente | Value / Wert / Valor / Valeur / Valore | RS Stock no. / RS Best.-Nr / Código RS / Code Commande RS / Codice | Quantity Required / Benötigte Anzahl / Cantidad necesaria / Quantité necessaire / Quantità |
|---|---|---|---|
| R1 & R3 | 100 KΩ | 148-972 | 1 |
| R2 & R6 | 100 Ω | 148-269 | 1 |
| R4 | 68Ω | 148-219 | 1 |
| R5 & R8 | 10Ω | 148-017 | 1 |
| R7 | 47Ω | 148-174 | 1 |
| R9 | 1KΩ | 148-506 | 1 |
| R10 & R11 | 680Ω | 148-461 | 1 |
| VR1 & VR2 | 10K | 186-520 | 2 |
| C1, C6 & C7 | 100nF | 312-1469 | 1 |
| C2 & C5 | 10nF | 312-1431 | 1 |
| C3 & C4 | 10µF | 103-957 | 1 |
| T1 | BD135 | 299-323 | 1 |
| T2 | BD136 | 299-339 | 1 |
| T3 | BC108 | 293-533 | 1 |
| 4-Way Connector/ 4poliger Stecker/ Conector de 4 vias/ 4-point Connecteurs/ Connettore a 4 vie | | 425-847 | 1 |
| 3-Way Connector/ 3poliger Stecker/ Conector de 3vias/ 3-point Connecteurs/ Connettore a 3 vie | | 424-686 | 1 |
| Strain Gauge Amp/ Dehnungsmeß-Sensor/ Amplificador para galga extensométrica/ l'amplificateur de la jauge extensométrique/ Amplificatore de estensimetrii | | 846-171 | 1 |
| Diode / Diodo / Diodi D1 & D2 | LM4040DIZ-5.0 | 168-9351 / 299-187 | 2 |

TECHNOLOGY IN TEMPERATURE

# TECHNICAL SPECIFICATION

## RS 846-171 STRAIN GAUGE AMPLIFIER DATA SHEET

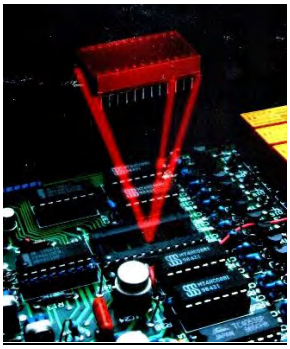

### General

This component enables the signals from Strain Gauges to be amplified. It includes the ability to control a negative supply to a bridge in order to minimise common mode interference, the circuitry ensures the negative supply mirrors the positive supply.

The amplifier is to be housed within a 24 pin dual in line package (32 x 24 x 13.5 mm). The unit is sensitive to electrostatic discharge and therefore static handling procedures must be followed.

### Electrical

All the specifications below are worse case ratings @ 25˚C ±12V supply

Items that are asterixed thus '*' are taken from manufacturers data

| | |
|---|---|
| Supply Voltage | :* ±2 to ±20 V DC |
| Supply current | :* 4mA |
| Input offset voltage | :* 200µV |
| Input offset voltage/temperature drift | :* 0.5µV/□C |
| Input offset voltage/supply voltage | :* 3µV/V |
| Input offset voltage/time | :* 0.3µV/month |
| Input impedance | :* >15MΩ |
| Input noise voltage | :* 0.9µV pk-pk |
| Bandwidth (unity gain) | :* 450 KHz |
| Output current | : 5mA |
| Output voltage span (Rl=10K) | : ±(Vs-2)V |
| Closed loop gain (adjustable) | :* 3 to 60,000 |
| Open loop gain | :* >120 dB |
| Common mode rejection ratio | :* >120 dB |
| Bridge supply voltage/temperature | : 20µV/˚C |
| Maximum bridge supply current | :* 12mA |
| Power dissipation | : 0.5W |
| Warm up time | : 5 minutes |
| Operating temperature range | :* -25˚C to +85˚C |

# Modifying the OpenEEG Analogue Board for EMG Acquisition

Andrew McNaught
MRC/UCT Medical Imaging Research Unit, University of Cape Town
andrew.mcnaught@uct.ac.za

## Contents

# Background theory

## Changing the Cut-off Frequency

In an electronic circuit with inductors and capacitors, the cut-off frequency can be shifted from $f_1$ to $f_2$ by scaling all Inductors (L) and Capacitors (C) by an appropriate factor such that they have the same impedance (X) at $f_2$ as they did have at $f_1$ (Wilkinson, 2009).

$$X = \frac{1}{2\pi f_2 C_{new}} = \frac{1}{2\pi f_1 C_{original}}$$

$$\therefore C_{new} = \frac{f_1}{f_2} C_{original} \qquad (1)$$

Thus if the cut-off frequency of a low pass filter is required to be 10 times higher, then the capacitors must be made 10 times smaller in value. Resistor values do not change (Wilkinson, 2009).

## High Pass Filter

In the 5-20 Hz frequency range, the sEMG spectrum contains information concerning the firing rates of the active motor units, but in many cases (e.g. in movement analysis) this information may not be of great interest (Stegeman D.F.).

In most cases a high pass filter between 10 and 20 Hz will preserve the important frequencies in the sEMG while removing slow variations in the signal caused by the movement artefacts. Note that sudden signal changes due to movements may not be completely attenuated by a 10 – 20 Hz filter (Stegeman D.F.).

## Low Pass Filter

With the exception of a few cases, about 95% of sEMG power is accounted for by harmonics up to 400 Hz and most of the remaining percents by electrode and equipment noise. A low pass filter has to be applied to the signal to further attenuate these unwanted components (Stegeman D.F.). The low pass filter cut-off frequency is usually chosen near to 500 Hz.

## Sampling Frequency and Resolution

The sampling frequency must be 1000 samples/second or higher to satisfy the Nyquist criterion for stability (sampling must be >2 times the highest frequency in the signal).

Modern amplifiers have a noise level of a few mVs. Therefore, a digitisation of about 0.5 mV/bit is sufficiently accurate. A 16 bit A/D convertor has $2^{16-1}$ = 65535 levels, meaning that without gain adaptations the range of measurements with such a convertor is ± 16 mV, which is enough for almost any sEMG application (Stegeman D.F.).

## Filter Modifications

The original OpenEEG filter has the following cut-off frequencies (see Appendix A1):

- high pass (HP) = 280mHz
- low pass (LP) = 58Hz

The desired cut-off frequencies are as follows:

- HP = 5Hz
- LP = 500Hz

Note that further high pass filtering (up to 20Hz) can be implemented digitally to remove undesired movement artefacts.

## Implementing the Changes

### Changing the Capacitors

Each of the following capacitors needs to be de-soldered and replaced with the appropriate E12 value. Using a solder-sucker is recommended to prevent the circuit board tracks from being damaged.

| Filter | Capacitor | Old Value (nF) | New Value (nF) | E12 Value (nF) |
|---|---|---|---|---|
| High Pass | C220 & C221 | 1000 | 56.2 | 57 |
| | C229 & C228 | 1000 | 56.2 | 57 |
| Low Pass | C231 & C235 | 220 | 25.67 | 22 |
| | C232 & C233 | 10 | 1.17 | 1 |
| | C234 & C236 | 33 | 3.85 | 3.3 |
| | C103 – C109 * | 220 | 25.67 | 22 |

*Note that C103 – C109 are on the digital board.

## References

Stegeman D.F., H. H. (n.d.). Standards for surface electromyography: the European project "Surface EMG for non-invasive assessment of muscles (SENIAM)".

Wilkinson, A. (2009). Department of Electrical Engineering. *University of Cape Town* .

# Appendix A1 – original OpenEEG filter

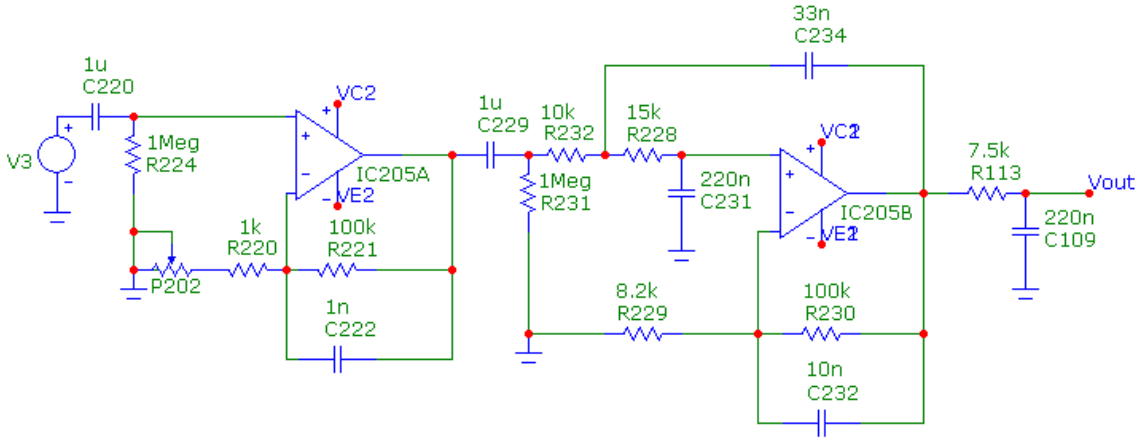


Figure 1 The original OpenEEG filter circuit

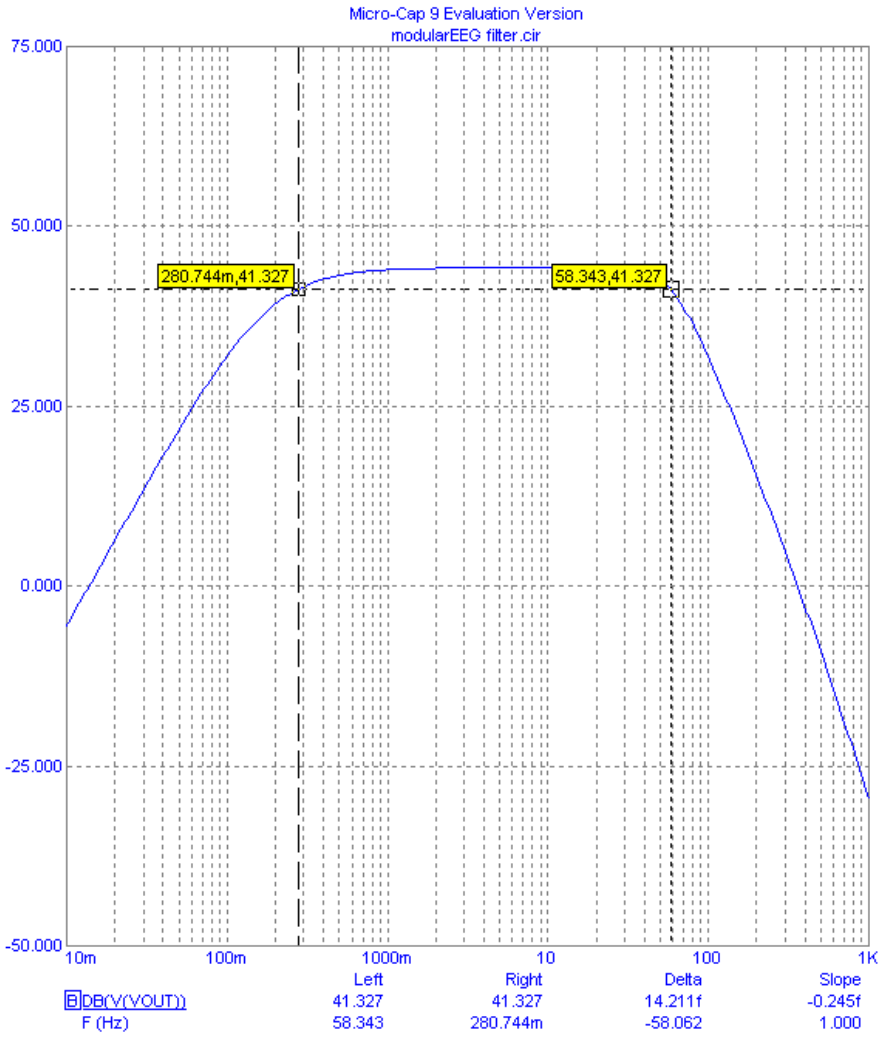


Figure 2 3dB roll-off for the original OpenEEG filter

# Appendix A2 – modified OpenEEG filter

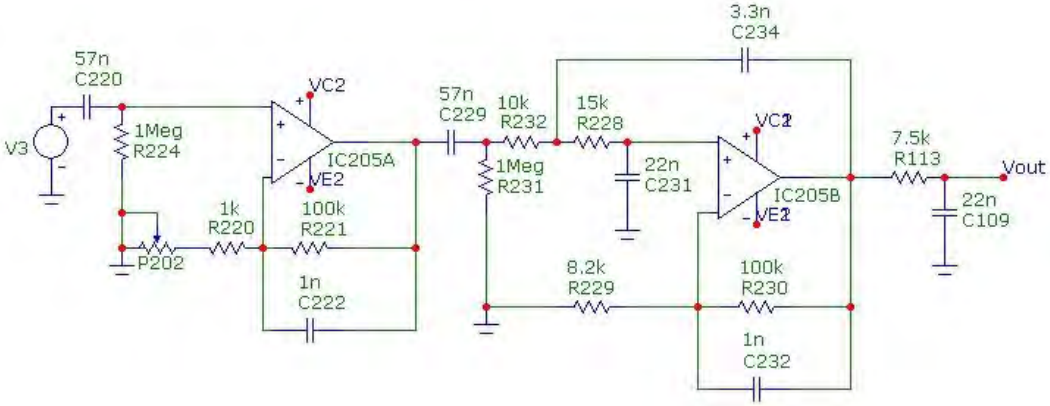


Figure 3 The modified OpenEEG filter circuit

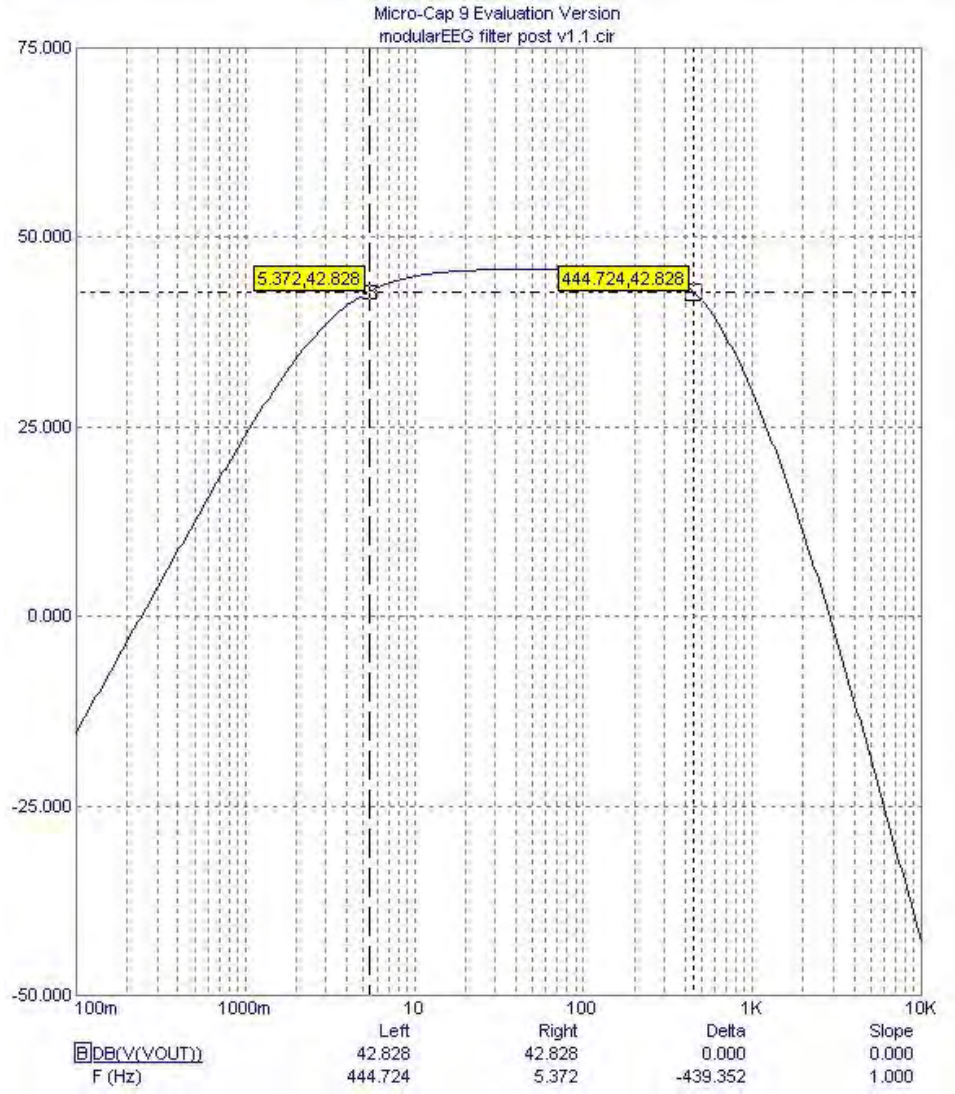


Figure 4 3dB roll-off for the modified OpenEEG filter

# Nonvolatile Memory, Dual 1024-Position Digital Potentiometer

Data Sheet **AD5235**

## FEATURES

**Dual-channel, 1024-position resolution**
**25 kΩ, 250 kΩ nominal resistance**
**Maximum ±8% nominal resistor tolerance error**
**Low temperature coefficient: 35 ppm/°C**
**2.7 V to 5 V single supply or ±2.5 V dual supply**
**SPI-compatible serial interface**
**Nonvolatile memory stores wiper settings**
**Power-on refreshed with EEMEM settings**
**Permanent memory write protection**
**Resistance tolerance stored in EEMEM**
**26 bytes extra nonvolatile memory for user-defined information**
**1M programming cycles**
**100-year typical data retention**

## APPLICATIONS

**DWDM laser diode driver, optical supervisory systems**
**Mechanical potentiometer replacement**
**Instrumentation: gain, offset adjustment**
**Programmable voltage-to-current conversion**
**Programmable filters, delays, time constants**
**Programmable power supply**
**Low resolution DAC replacement**
**Sensor calibration**

## GENERAL DESCRIPTION

The AD5235 is a dual-channel, nonvolatile memory,[1] digitally controlled potentiometer[2] with 1024-step resolution, offering guaranteed maximum low resistor tolerance error of ±8%. The device performs the same electronic adjustment function as a mechanical potentiometer with enhanced resolution, solid state reliability, and superior low temperature coefficient performance. The versatile programming of the AD5235 via an SPI®-compatible serial interface allows 16 modes of operation and adjustment including scratchpad programming, memory storing and restoring, increment/decrement, ±6 dB/step log taper adjustment, wiper setting readback, and extra EEMEM[1] for user-defined information such as memory data for other components, look-up table, or system identification information.

[1] The terms nonvolatile memory and EEMEM are used interchangeably.
[2] The terms digital potentiometer and RDAC are used interchangeably.

## FUNCTIONAL BLOCK DIAGRAM

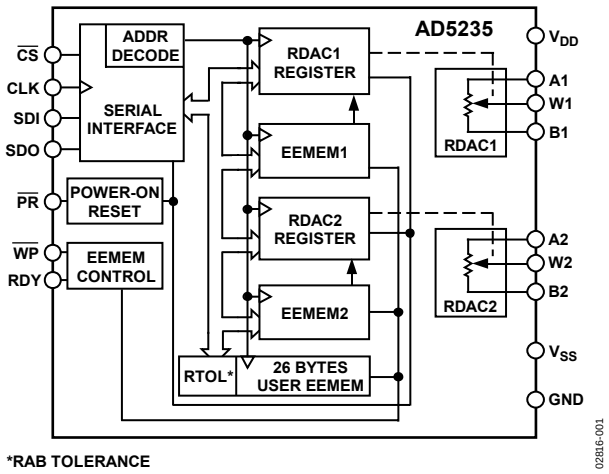


*Figure 1.*

In the scratchpad programming mode, a specific setting can be programmed directly to the RDAC[2] register, which sets the resistance between Terminal W and Terminal A and Terminal W and Terminal B. This setting can be stored into the EEMEM and is restored automatically to the RDAC register during system power-on.

The EEMEM content can be restored dynamically or through external $\overline{PR}$ strobing, and a $\overline{WP}$ function protects EEMEM contents. To simplify the programming, the independent or simultaneous linear-step increment or decrement commands can be used to move the RDAC wiper up or down, one step at a time. For logarithmic ±6 dB changes in the wiper setting, the left or right bit shift command can be used to double or halve the RDAC wiper setting.

The AD5235 patterned resistance tolerance is stored in the EEMEM. The actual end-to-end resistance can, therefore, be known by the host processor in readback mode. The host can execute the appropriate resistance step through a software routine that simplifies open-loop applications as well as precision calibration and tolerance matching applications.

The AD5235 is available in a thin, 16-lead TSSOP package. The part is guaranteed to operate over the extended industrial temperature range of −40°C to +85°C.

**Rev. F**


**One Technology Way, P.O. Box 9106, Norwood, MA 02062-9106, U.S.A.**
**Tel: 781.329.4700** **www.analog.com**
**Fax: 781.461.3113** 

# TABLE OF CONTENTS

## REVISION HISTORY

**6/12—Rev. E to Rev. F**

Changes to Table 1 Conditions ..... 4
Removed Positive Supply Current RDY and/or SDO Floating Parameters and Negative Supply Current RDY and/or SDO Floating Parameters, Table 1 ..... 5
Added Endnote 2 to Ordering Guide ..... 30

**4/11—Rev. D to Rev. E**

Changes to Figure 12 ..... 11

**4/11—Rev. C to Rev. D**

Changes to EEMEM Performance ..... Throughout
Changes to Features and General Descriptions Sections ..... 1
Changes to Specifications Section ..... 4
Changes to Pin 5, Pin 13, Pin 14 Descriptions ..... 9
Changes to Typical Performance Characteristics Section ..... 10
Changes to Table 7 ..... 19
Changes to Table 9 ..... 21
Changes to Rheostat Operation Section, Table 12, Table 13 ..... 22
Changes to Table 16, Table 19, and EVAL-AD5235SDZ Evaluation Kit Section ..... 23
Changes to RDAC Circuit Simulation Model Section ..... 29
Updated Outline Dimensions ..... 30
Changes to Ordering Guide ..... 30

**4/09—Rev. B to Rev. C**

Changes to Figure 1 ..... 1
Changes to Specifications ..... 3
Changes to SDO, Description Column, Table 4 ..... 8
Changes to Figure 18 ..... 11
Changes to Theory of Operation Section ..... 14
Changes to Serial Data Interface Section ..... 15
Changes to Linear Increment and Decrement Instructions Section, Logarithmic Taper Mode Adjustment Section, and Figure 42 ..... 18
Changes to Rheostat Operations Section ..... 20
Changes to Bipolar Programmable Gain Amplifier Section, Figure 49, Table 21, and 10-Bit Bipolar DAC Section ..... 23
Changes to Programmable Oscillator Section and Figure 56 ..... 25
Changes to Ordering Guide ..... 28

**7/04—Rev. A to Rev. B**

Updated Formatting ..... Universal
Edits to Features, General Description, and Block Diagram ..... 1
Changes to Specifications ..... 3
Replaced Timing Diagrams ..... 6
Changes to Absolute Maximum Ratings ..... 7
Changes to Pin Function Descriptions ..... 8
Changes to Typical Performance Characteristics ..... 9
Additional Test Circuit (Figure 36) ..... 9
Edits to Theory of Operation ..... 14
Edits to Applications ..... 23
Updated Outline Dimensions ..... 27

**8/02—Rev. 0 to Rev. A**

Change to Features and General Description ..... 1
Change to Specifications ..... 2
Change to Calculating Actual End-to-End Terminal Resistance Section ..... 14

# SPECIFICATIONS

## ELECTRICAL CHARACTERISTICS—25 kΩ, 250 kΩ VERSIONS

$V_{DD}$ = 2.7 V to 5.5 V, $V_{SS}$ = 0 V; $V_{DD}$ = 2.5 V, $V_{SS}$ = −2.5 V, $V_A = V_{DD}$, $V_B = V_{SS}$, −40°C < $T_A$ < +85°C, unless otherwise noted.

These specifications apply to versions with a date code 1209 or later.

**Table 1.**

| Parameter | Symbol | Conditions | Min | Typ[1] | Max | Unit |
|---|---|---|---|---|---|---|
| DC CHARACTERISTICS—RHEOSTAT MODE (All RDACs) | | | | | | |
| Resistor Differential Nonlinearity[2] | R-DNL | $R_{WB}$ | −1 | | +1 | LSB |
| Resistor Integral Nonlinearity[2] | R-INL | $R_{WB}$ | −2 | | +2 | LSB |
| Nominal Resistor Tolerance | $\Delta R_{AB}/R_{AB}$ | | −8 | | +8 | % |
| Resistance Temperature Coefficient | $(\Delta R_{AB}/R_{AB})/\Delta T \times 10^6$ | | | 35 | | ppm/°C |
| Wiper Resistance | $R_W$ | $I_W$ = 1 V/$R_{WB}$, code = midscale | | | | |
| | | $V_{DD}$ = 5 V | | 30 | 60 | Ω |
| | | $V_{DD}$ = 3 V | | 50 | | Ω |
| Nominal Resistance Match | $R_{AB1}/R_{AB2}$ | | | ±0.1 | | % |
| DC CHARACTERISTICS—POTENTIOMETER DIVIDER MODE (All RDACs) | | | | | | |
| Resolution | N | | | | 10 | Bits |
| Differential Nonlinearity[3] | DNL | | −1 | | +1 | LSB |
| Integral Nonlinearity[3] | INL | | −1 | | +1 | LSB |
| Voltage Divider Temperature Coefficient | $(\Delta V_W/V_W)/\Delta T \times 10^6$ | Code = midscale | | 15 | | ppm/°C |
| Full-Scale Error | $V_{WFSE}$ | Code = full scale | −6 | | 0 | LSB |
| Zero-Scale Error | $V_{WZSE}$ | Code = zero scale | 0 | | 4 | LSB |
| RESISTOR TERMINALS | | | | | | |
| Terminal Voltage Range[4] | $V_A$, $V_B$, $V_W$ | | $V_{SS}$ | | $V_{DD}$ | V |
| Capacitance Ax, Bx[5] | $C_A$, $C_B$ | f = 1 MHz, measured to GND, code = midscale | | 11 | | pF |
| Capacitance Wx[5] | $C_W$ | f = 1 MHz, measured to GND, code = midscale | | 80 | | pF |
| Common-Mode Leakage Current[5, 6] | $I_{CM}$ | $V_W = V_{DD}/2$ | | 0.01 | ±1 | µA |
| DIGITAL INPUTS AND OUTPUTS | | | | | | |
| Input Logic High | $V_{IH}$ | With respect to GND, $V_{DD}$ = 5 V | 2.4 | | | V |
| Input Logic Low | $V_{IL}$ | With respect to GND, $V_{DD}$ = 5 V | | | 0.8 | V |
| Input Logic High | $V_{IH}$ | With respect to GND, $V_{DD}$ = 3 V | 2.1 | | | V |
| Input Logic Low | $V_{IL}$ | With respect to GND, $V_{DD}$ = 3 V | | | 0.6 | V |
| Input Logic High | $V_{IH}$ | With respect to GND, $V_{DD}$ = +2.5 V, $V_{SS}$ = −2.5 V | 2.0 | | | V |
| Input Logic Low | $V_{IL}$ | With respect to GND, $V_{DD}$ = +2.5 V, $V_{SS}$ = −2.5 V | | | 0.5 | V |
| Output Logic High (SDO, RDY) | $V_{OH}$ | $R_{PULL-UP}$ = 2.2 kΩ to 5 V (see Figure 38) | 4.9 | | | V |
| Output Logic Low | $V_{OL}$ | $I_{OL}$ = 1.6 mA, $V_{LOGIC}$ = 5 V (see Figure 38) | | | 0.4 | V |
| Input Current | $I_{IL}$ | $V_{IN}$ = 0 V or $V_{DD}$ | | | ±1 | µA |
| Input Capacitance[5] | $C_{IL}$ | | | 5 | | pF |

| Parameter | Symbol | Conditions | Min | Typ[1] | Max | Unit |
|---|---|---|---|---|---|---|
| POWER SUPPLIES | | | | | | |
| Single-Supply Power Range | $V_{DD}$ | $V_{SS}$ = 0 V | 2.7 | | 5.5 | V |
| Dual-Supply Power Range | $V_{DD}/V_{SS}$ | | ±2.25 | | ±2.75 | V |
| Positive Supply Current | $I_{DD}$ | $V_{IH} = V_{DD}$ or $V_{IL}$ = GND | | 2 | 5 | µA |
| Negative Supply Current | $I_{SS}$ | $V_{DD}$ = +2.5 V, $V_{SS}$ = −2.5 V | | | | |
| | | $V_{IH} = V_{DD}$ or $V_{IL}$ = GND | −4 | −2 | | µA |
| EEMEM Store Mode Current | $I_{DD}$ (store) | $V_{IH} = V_{DD}$ or $V_{IL}$ = GND, $V_{SS}$ = GND, $I_{SS} \approx 0$ | | 2 | | mA |
| | $I_{SS}$ (store) | $V_{DD}$ = +2.5 V, $V_{SS}$ = −2.5 V | | −2 | | mA |
| EEMEM Restore Mode Current[7] | $I_{DD}$ (restore) | $V_{IH} = V_{DD}$ or $V_{IL}$ = GND, $V_{SS}$ = GND, $I_{SS} \approx 0$ | | 320 | | µA |
| | $I_{SS}$ (restore) | $V_{DD}$ = +2.5 V, $V_{SS}$ = −2.5 V | | −320 | | µA |
| Power Dissipation[8] | $P_{DISS}$ | $V_{IH} = V_{DD}$ or $V_{IL}$ = GND | | 10 | 30 | µW |
| Power Supply Sensitivity[5] | $P_{SS}$ | $\Delta V_{DD}$ = 5 V ± 10% | | 0.006 | 0.01 | %/% |
| DYNAMIC CHARACTERISTICS[5, 9] | | | | | | |
| Bandwidth | BW | −3 dB, $R_{AB}$ = 25 kΩ/250 kΩ | | 125/12 | | kHz |
| Total Harmonic Distortion | $THD_W$ | $V_A$ = 1 V rms, $V_B$ = 0 V, f = 1 kHz, code = midscale | | | | |
| | | $R_{AB}$ = 25 kΩ | | 0.009 | | % |
| | | $R_{AB}$ = 250 kΩ | | 0.035 | | % |
| $V_W$ Settling Time | $t_S$ | $V_A = V_{DD}$, $V_B$ = 0 V, $V_W$ = 0.50% error band, from zero scale to midscale | | | | |
| | | $R_{AB}$ = 25 kΩ | | 4 | | µs |
| | | $R_{AB}$ = 250 kΩ | | 36 | | µs |
| Resistor Noise Density | $e_{N\_WB}$ | $R_{AB}$ = 25 kΩ/250 kΩ | | 20/64 | | nV/√Hz |
| Crosstalk ($C_{W1}/C_{W2}$) | $C_T$ | $V_{A1} = V_{DD}$, $V_{B1} = V_{SS}$, measured $V_{W2}$ with $V_{W1}$ making full-scale change, $R_{AB}$ = 25 kΩ/250 kΩ | | 30/60 | | nV-s |
| Analog Crosstalk | $C_{TA}$ | $V_{AB2}$ = 5 V p-p, f = 1 kHz, measured $V_{W1}$, Code 1 = midscale, Code 2 = full scale, $R_{AB}$ = 25 kΩ/250 kΩ | | −110/−100 | | dB |

[1] Typicals represent average readings at 25°C and $V_{DD}$ = 5 V.
[2] Resistor position nonlinearity error (R-INL) is the deviation from an ideal value measured between the maximum resistance and the minimum resistance wiper positions. R-DNL measures the relative step change from ideal between successive tap positions. $I_{WB} = (V_{DD} - 1)/R_{WB}$ (see Figure 27).
[3] INL and DNL are measured at $V_W$ with the RDAC configured as a potentiometer divider similar to a voltage output DAC. $V_A = V_{DD}$ and $V_B = V_{SS}$. DNL specification limits of ±1 LSB maximum are guaranteed monotonic operating conditions (see Figure 28).
[4] Resistor Terminal A, Resistor Terminal B, and Resistor Terminal W have no limitations on polarity with respect to each other. Dual-supply operation enables ground-referenced bipolar signal adjustment.
[5] Guaranteed by design and not subject to production test.
[6] Common-mode leakage current is a measure of the dc leakage from any Terminal A, Terminal B, or Terminal W to a common-mode bias level of $V_{DD}/2$.
[7] EEMEM restore mode current is not continuous. Current is consumed while EEMEM locations are read and transferred to the RDAC register.
[8] $P_{DISS}$ is calculated from $(I_{DD} \times V_{DD}) + (I_{SS} \times V_{SS})$.
[9] All dynamic characteristics use $V_{DD}$ = +2.5 V and $V_{SS}$ = −2.5 V.

## INTERFACE TIMING AND EEMEM RELIABILITY CHARACTERISTICS—25 kΩ, 250 kΩ VERSIONS

Guaranteed by design and not subject to production test. See the Timing Diagrams section for the location of measured values. All input control voltages are specified with $t_R = t_F = 2.5$ ns (10% to 90% of 3 V) and timed from a voltage level of 1.5 V. Switching characteristics are measured using both $V_{DD} = 2.7$ V and $V_{DD} = 5$ V.

**Table 2.**

| Parameter | Symbol | Conditions | Min | Typ[1] | Max | Unit |
|---|---|---|---|---|---|---|
| Clock Cycle Time ($t_{CYC}$) | $t_1$ | | 20 | | | ns |
| $\overline{CS}$ Setup Time | $t_2$ | | 10 | | | ns |
| CLK Shutdown Time to $\overline{CS}$ Rise | $t_3$ | | 1 | | | $t_{CYC}$ |
| Input Clock Pulse Width | $t_4$, $t_5$ | Clock level high or low | 10 | | | ns |
| Data Setup Time | $t_6$ | From positive CLK transition | 5 | | | ns |
| Data Hold Time | $t_7$ | From positive CLK transition | 5 | | | ns |
| $\overline{CS}$ to SDO-SPI Line Acquire | $t_8$ | | | | 40 | ns |
| $\overline{CS}$ to SDO-SPI Line Release | $t_9$ | | | | 50 | ns |
| CLK to SDO Propagation Delay[2] | $t_{10}$ | $R_P = 2.2$ kΩ, $C_L < 20$ pF | | | 50 | ns |
| CLK to SDO Data Hold Time | $t_{11}$ | $R_P = 2.2$ kΩ, $C_L < 20$ pF | 0 | | | ns |
| $\overline{CS}$ High Pulse Width[3] | $t_{12}$ | | 10 | | | ns |
| $\overline{CS}$ High to $\overline{CS}$ High[3] | $t_{13}$ | | 4 | | | $t_{CYC}$ |
| RDY Rise to $\overline{CS}$ Fall | $t_{14}$ | | 0 | | | ns |
| $\overline{CS}$ Rise to RDY Fall Time | $t_{15}$ | | | 0.15 | 0.3 | ms |
| Store EEMEM Time[4, 5] | $t_{16}$ | Applies to Instructions 0x2, 0x3 | | 15 | 50 | ms |
| Read EEMEM Time[4] | $t_{16}$ | Applies to Instructions 0x8, 0x9, 0x10 | | 7 | 30 | µs |
| $\overline{CS}$ Rise to Clock Rise/Fall Setup | $t_{17}$ | | 10 | | | ns |
| Preset Pulse Width (Asynchronous)[6] | $t_{PRW}$ | | 50 | | | ns |
| Preset Response Time to Wiper Setting[6] | $t_{PRESP}$ | $\overline{PR}$ pulsed low to refresh wiper positions | | 30 | | µs |
| Power-On EEMEM Restore Time[6] | $t_{EEMEM}$ | | | 30 | | µs |
| FLASH/EE MEMORY RELIABILITY | | | | | | |
| Endurance[7] | | $T_A = 25°C$ | | 1 | | MCycles |
| | | | 100 | | | kCycles |
| Data Retention[8] | | | | 100 | | Years |

[1] Typicals represent average readings at 25°C and $V_{DD} = 5$ V.
[2] Propagation delay depends on the value of $V_{DD}$, $R_{PULL-UP}$, and $C_L$.
[3] Valid for commands that do not activate the RDY pin.
[4] The RDY pin is low only for Instruction 2, Instruction 3, Instruction 8, Instruction 9, Instruction 10, and the $\overline{PR}$ hardware pulse: CMD_8 ~ 20 µs; CMD_9, CMD_10 ~ 7 µs; CMD_2, CMD_3 ~ 15 ms; $\overline{PR}$ hardware pulse ~ 30 µs.
[5] Store EEMEM time depends on the temperature and EEMEM writes cycles. Higher timing is expected at a lower temperature and higher write cycles.
[6] Not shown in Figure 2 and Figure 3.
[7] Endurance is qualified to 100,000 cycles per JEDEC Standard 22, Method A117 and measured at −40°C, +25°C, and +85°C.
[8] Retention lifetime equivalent at junction temperature ($T_J$) = 85°C per JEDEC Standard 22, Method A117. Retention lifetime based on an activation energy of 1 eV derates with junction temperature in the Flash/EE memory.

### *Timing Diagrams*

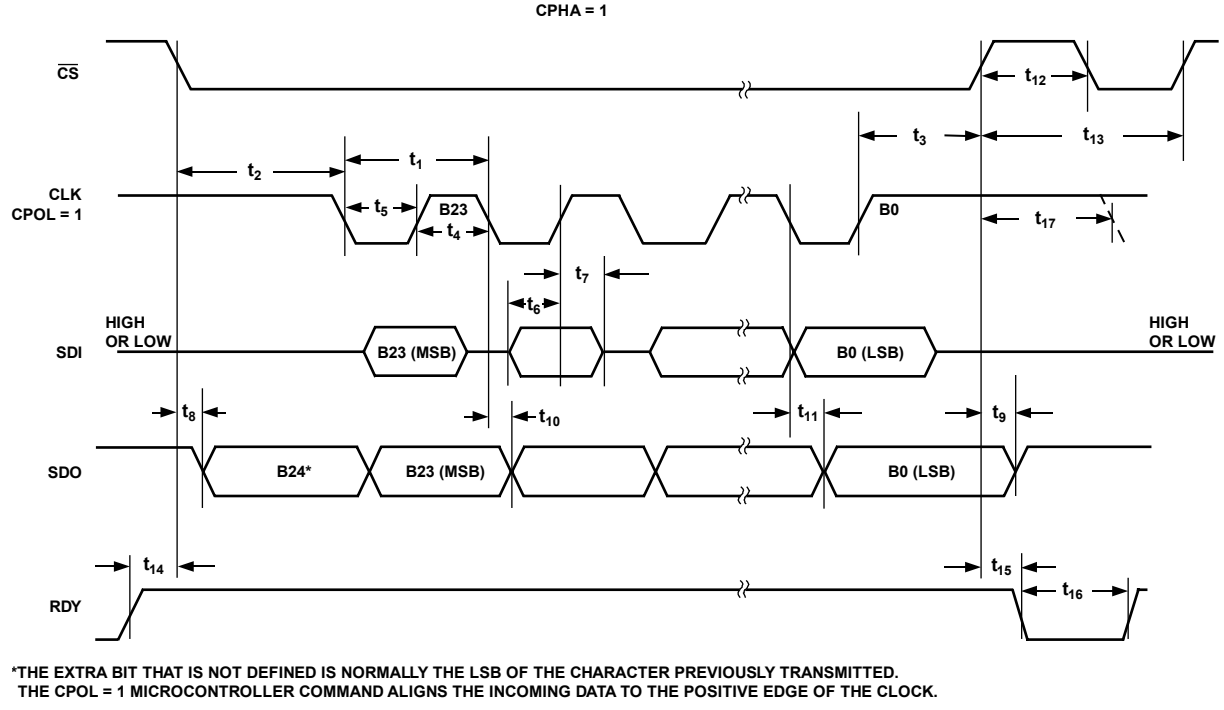


*Figure 2. CPHA = 1 Timing Diagram*

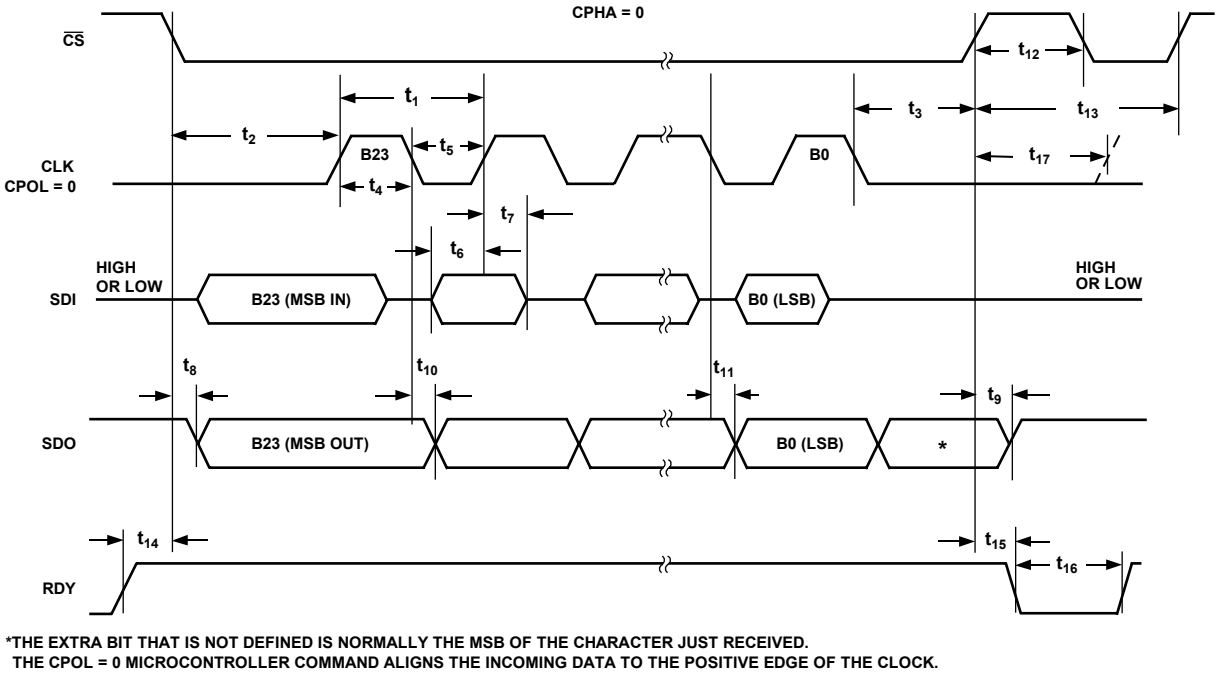


*Figure 3. CPHA = 0 Timing Diagram*

# ABSOLUTE MAXIMUM RATINGS

$T_A$ = 25°C, unless otherwise noted.

**Table 3.**

| Parameter | Rating |
|---|---|
| $V_{DD}$ to GND | −0.3 V to +7 V |
| $V_{SS}$ to GND | +0.3 V to −7 V |
| $V_{DD}$ to $V_{SS}$ | 7 V |
| $V_A$, $V_B$, $V_W$ to GND | $V_{SS}$ − 0.3 V to $V_{DD}$ + 0.3 V |
| $I_A$, $I_B$, $I_W$ | |
| Pulsed[1] | ±20 mA |
| Continuous | ±2 mA |
| Digital Input and Output Voltage to GND | −0.3 V to $V_{DD}$ + 0.3 V |
| Operating Temperature Range[2] | −40°C to +85°C |
| Maximum Junction Temperature ($T_J$ max) | 150°C |
| Storage Temperature Range | −65°C to +150°C |
| Lead Temperature, Soldering | |
| Vapor Phase (60 sec) | 215°C |
| Infrared (15 sec) | 220°C |
| Thermal Resistance | |
| Junction-to-Ambient $\theta_{JA}$,TSSOP-16 | 150°C/W |
| Junction-to-Case $\theta_{JC}$, TSSOP-16 | 28°C/W |
| Package Power Dissipation | ($T_J$ max − $T_A$)/$\theta_{JA}$ |

[1] Maximum terminal current is bounded by the maximum current handling of the switches, maximum power dissipation of the package, and maximum applied voltage across any two of the A, B, and W terminals at a given resistance.

[2] Includes programming of nonvolatile memory.

Stresses above those listed under Absolute Maximum Ratings may cause permanent damage to the device. This is a stress rating only; functional operation of the device at these or any other conditions above those indicated in the operational section of this specification is not implied. Exposure to absolute maximum rating conditions for extended periods may affect device reliability.

## ESD CAUTION

**ESD (electrostatic discharge) sensitive device.** Charged devices and circuit boards can discharge without detection. Although this product features patented or proprietary protection circuitry, damage may occur on devices subjected to high energy ESD. Therefore, proper ESD precautions should be taken to avoid performance degradation or loss of functionality.

# PIN CONFIGURATION AND FUNCTION DESCRIPTIONS

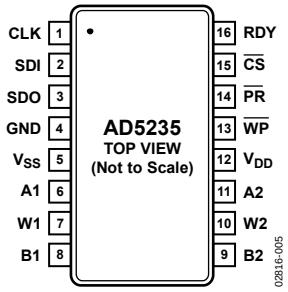


*Figure 4. Pin Configuration*

**Table 4. Pin Function Descriptions**

| Pin No. | Mnemonic | Description |
|---|---|---|
| 1 | CLK | Serial Input Register Clock. Shifts in one bit at a time on positive clock edges. |
| 2 | SDI | Serial Data Input. Shifts in one bit at a time on positive clock CLK edges. MSB loads first. |
| 3 | SDO | Serial Data Output. Serves readback and daisy-chain functions. Command 9 and Command 10 activate the SDO output for the readback function, delayed by 24 or 25 clock pulses, depending on the clock polarity before and after the data-word (see Figure 2 and Figure 3). In other commands, the SDO shifts out the previously loaded SDI bit pattern, delayed by 24 or 25 clock pulses depending on the clock polarity (see Figure 2 and Figure 3). This previously shifted out SDI can be used for daisy-chaining multiple devices. Whenever SDO is used, a pull-up resistor in the range of 1 kΩ to 10 kΩ is needed. |
| 4 | GND | Ground Pin, Logic Ground Reference. |
| 5 | $V_{SS}$ | Negative Supply. Connect to 0 V for single-supply applications. If $V_{SS}$ is used in dual supply, it must be able to sink 2 mA for 15 ms when storing data to EEMEM. |
| 6 | A1 | Terminal A of RDAC1. |
| 7 | W1 | Wiper terminal of RDAC1. ADDR (RDAC1) = 0x0. |
| 8 | B1 | Terminal B of RDAC1. |
| 9 | B2 | Terminal B of RDAC2. |
| 10 | W2 | Wiper terminal of RDAC2. ADDR (RDAC2) = 0x1. |
| 11 | A2 | Terminal A of RDAC2. |
| 12 | $V_{DD}$ | Positive Power Supply. |
| 13 | $\overline{WP}$ | Optional Write Protect. When active low, $\overline{WP}$ prevents any changes to the present contents, except $\overline{PR}$ strobe. CMD_1 and COMD_8 refresh the RDAC register from EEMEM. Tie $\overline{WP}$ to $V_{DD}$, if not used. |
| 14 | $\overline{PR}$ | Optional Hardware Override Preset. Refreshes the scratchpad register with current contents of the EEMEM register. Factory default loads midscale until EEMEM is loaded with a new value by the user. $\overline{PR}$ is activated at the logic high transition. Tie $\overline{PR}$ to $V_{DD}$, if not used. |
| 15 | $\overline{CS}$ | Serial Register Chip Select Active Low. Serial register operation takes place when $\overline{CS}$ returns to logic high. |
| 16 | RDY | Ready. Active high open-drain output. Identifies completion of Instruction 2, Instruction 3, Instruction 8, Instruction 9, Instruction 10, and $\overline{PR}$. |

One Technology Way • P.O. Box 9106 • Norwood, MA 02062-9106, U.S.A. • Tel: 781.329.4700 • Fax: 781.461.3113 • www.analog.com

# Evaluating the AD5546 Current Output/Serial Input DACs

## FEATURES

**Full-featured evaluation board for the AD5546**
**Graphic user interface software for board control and data analysis**
**Connector to EVAL-SDP-CB1Z system demonstration platform board**
**Various power supply options**

## APPLICATIONS

**Automatic test equipment**
**Instrumentation**
**Digitally controlled calibration**
**Digital waveform generation**

## GENERAL DESCRIPTION

The AD5546 is a precision 16-bit, multiplying, low power, current output, parallel input digital-to-analog converter (DAC). It operates from a single 2.7 V to 5.5 V supply with ±10 V multiplying references for four-quadrant outputs. Built-in four-quadrant resistors facilitate the resistance matching and temperature tracking that minimize the number of components needed for multiquadrant applications.

The applied external reference input voltage ($V_{REF}$) determines the full-scale output current. The feedback resistor ($R_{FB}$) simplifies the I-to-V conversion with an external buffer.

The AD5546 is packaged in compact 28-lead TSSOP packages with operating temperatures from −40°C to +125°C.

The EVAL-AD5546SDZ is used in conjunction with the EVAL-SDP-CB1Z system demonstration platform (SDP) board available from Analog Devices, Inc., which is purchased separately from the evaluation board. The USB-to-SPI communication to the DAC is completed using this Blackfin®-based demonstration board.

## FUNCTIONAL BLOCK DIAGRAM

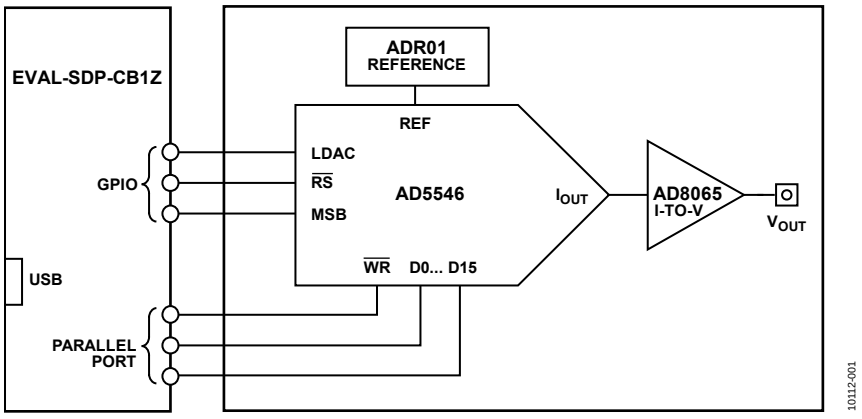


*Figure 1.*

# TABLE OF CONTENTS



## REVISION HISTORY

**3/12—Rev. 0 to Rev. A**

Added New Table 1; Renumbered Sequentially ..... 4
Changes to the Example Section ..... 5
Replaced Evaluation Board Schematics and Artwork Section ... 6

**11/11—Revision 0: Initial Version**

# APPLICATIONS PROVIDED

The EVAL-AD5546SDZ board provides the possibility of configuring the DAC in two different unipolar two-quadrant multiplying modes. Table 1 show how to select the desired voltage reference. Table 2 shows the connections needed to obtain these unipolar modes.

**Table 1. Voltage Reference Selection**

| Link Connections | | |
|---|---|---|
| **Link No.** | **Position** | **Function** |
| LK1 | IN | Internal voltage reference ADR01 connected. |
| | OUT | External voltage reference connected to VREF (J3 SMB connector). |

**Table 2. Applications Provided**

| Link Connections | | |
|---|---|---|
| **Link No.** | **Position** | **Function** |
| LK2 | A | Unipolar two-quadrant multiplying mode, $V_{OUT}$ = 0 V to $-V_{REF}$ |
| LK3 | A | |
| LK4 | In | |
| LK2 | B | Unipolar two-quadrant multiplying mode, $V_{OUT}$ = 0 V to + $V_{REF}$ |
| LK3 | B | |
| LK4 | Out | |

# EVALUATION BOARD SCHEMATICS AND ARTWORK

## SCHEMATICS

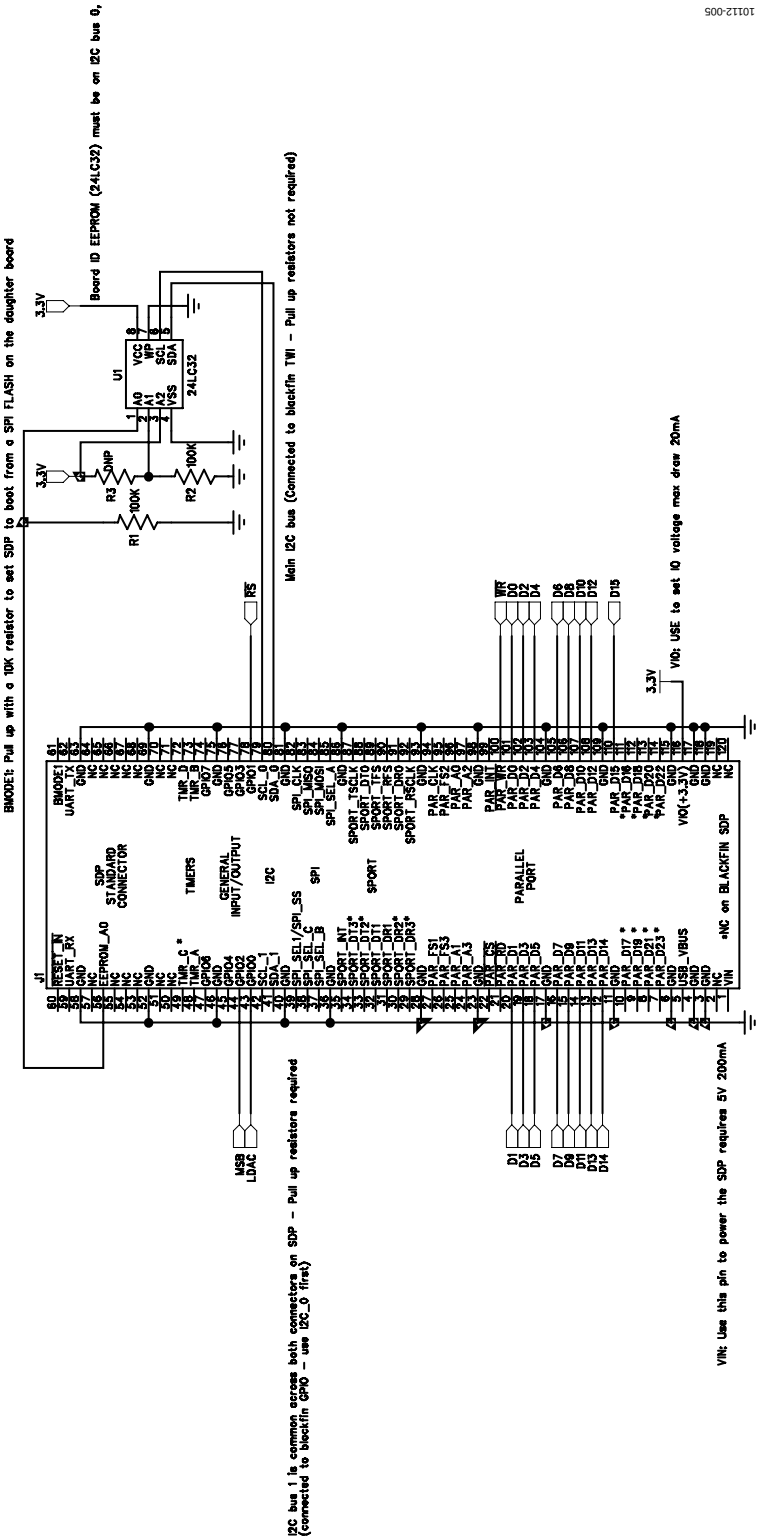


*Figure 5. EVAL-AD5546SDZ Schematic, SDP Connector*

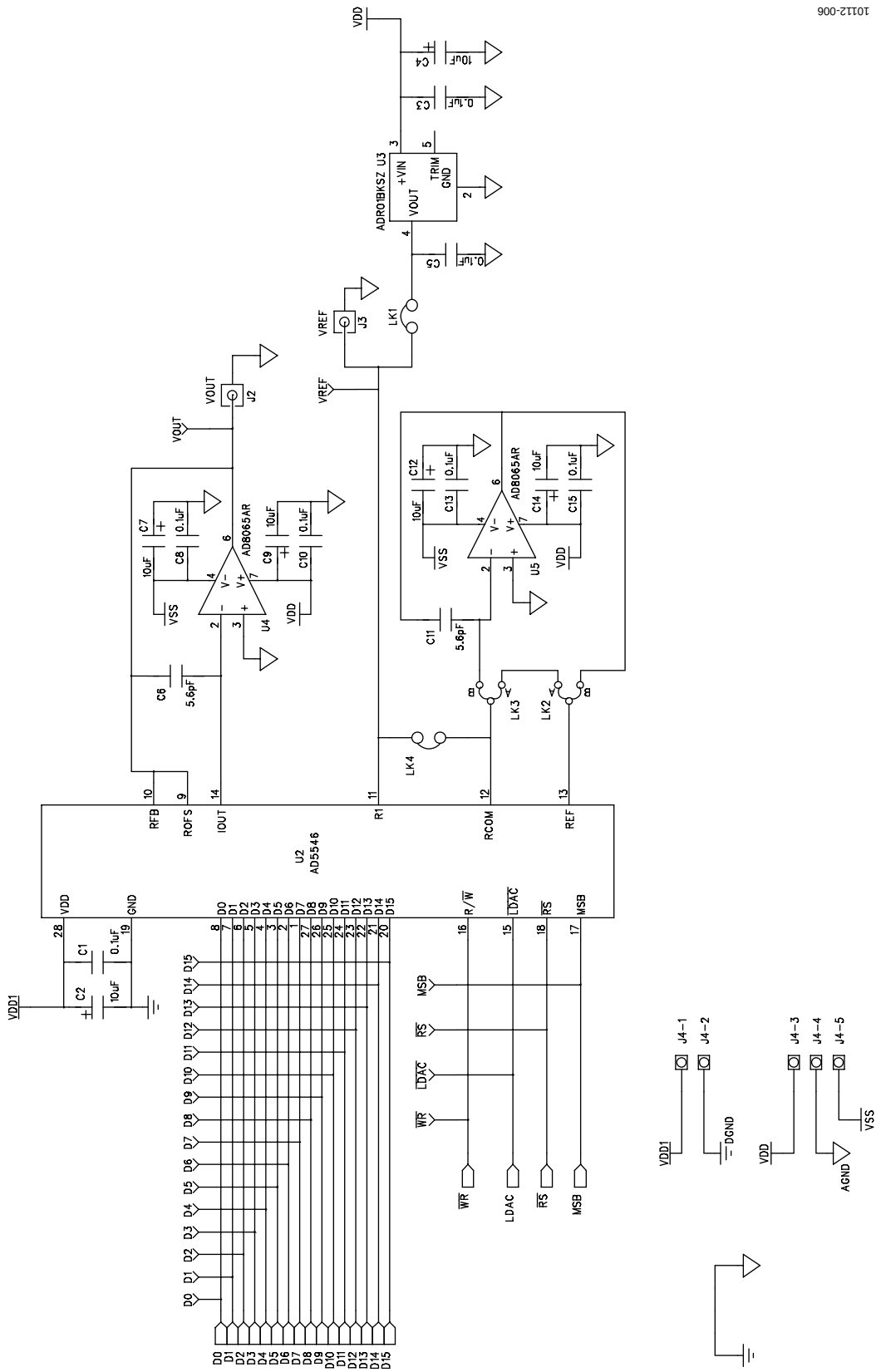


*Figure 6. EVAL-AD5546SDZ Schematic, DAC*

# Current Output, Parallel Input, 16-/14-Bit Multiplying DACs with Four-Quadrant Resistors

Data Sheet

# AD5546/AD5556

## FEATURES

- 16-bit resolution
- 14-bit resolution
- 2- or 4-quadrant multiplying DAC
- ±1 LSB DNL
- ±1 LSB INL
- Operating supply voltage: 2.7 V to 5.5 V
- Low noise: 12 nV/√Hz
- Low power: $I_{DD}$ = 10 µA
- 0.5 µs settling time
- Built-in $R_{FB}$ facilitates current-to-voltage conversion
- Built-in 4-quadrant resistors allow 0 V to −10 V, 0 V to +10 V, or ±10 V outputs
- 2 mA full-scale current ±20%, with $V_{REF}$ = 10 V
- Automotive operating temperature: −40°C to +125°C
- Compact TSSOP-28 package

## APPLICATIONS

- Automatic test equipment
- Instrumentation
- Digitally controlled calibration
- Digital waveform generation

## FUNCTIONAL BLOCK DIAGRAM

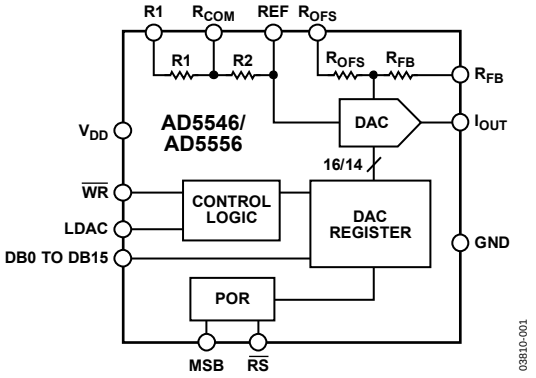


*Figure 1. AD5546/AD5556 Simplified Block Diagram*

## GENERAL DESCRIPTION

The AD5546/AD5556 are precision 16-/14-bit, multiplying, low power, current output, parallel input digital-to-analog converters (DACs). They operate from a single 2.7 V to 5.5 V supply with ±10 V multiplying references for four-quadrant outputs. Built-in four-quadrant resistors facilitate the resistance matching and temperature tracking that minimize the number of components needed for multiquadrant applications. The feedback resistor ($R_{FB}$) simplifies the I-V conversion with an external buffer. The AD5546/AD5556 are packaged in compact TSSOP-28 packages with operating temperatures from −40°C to +125°C.

The EVAL-AD5546SDZ is available for evaluating DAC performance. For more information, see the UG-309 evaluation board user guide.

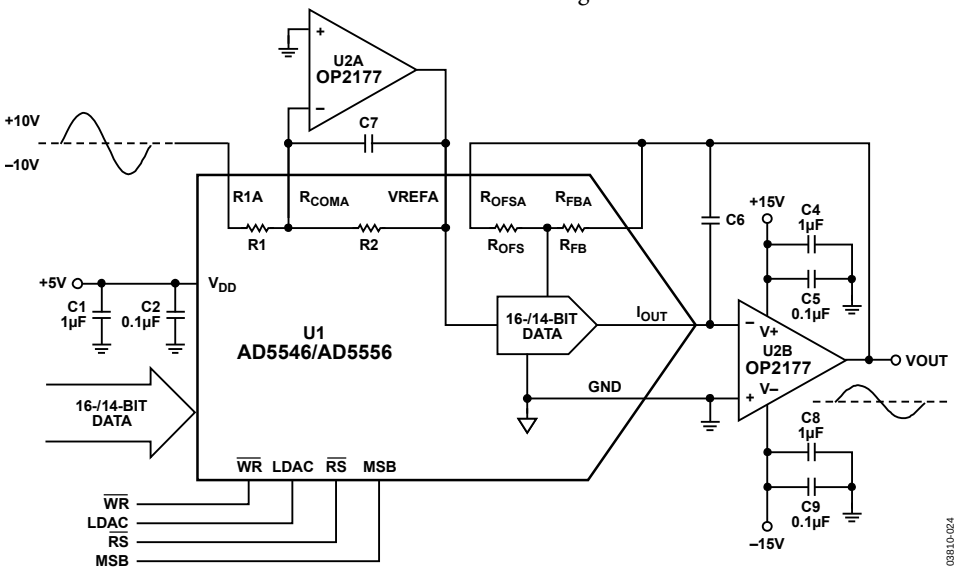


*Figure 2. 16-/14-Bit, Four-Quadrant Multiplying DAC with a Minimum of External Components*


**Rev. D**





One Technology Way, P.O. Box 9106, Norwood, MA 02062-9106, U.S.A.
Tel: 781.329.4700 www.analog.com
Fax: 781.461.3113

# TABLE OF CONTENTS



## REVISION HISTORY

**11/11—Rev. C to Rev. D**

Changes to General Description Section ... 1
Changes to Ordering Guide ... 18

**1/11—Rev. B to Rev. C**

Changes to Figure 2 ... 1
Changes to Figure 21 ... 13

**4/10—Rev. A to Rev. B**

Changes to Table 1 ... 4
Moved Timing Diagram Section and Figure 5 to Specifications Section ... 4
Moved Table 5 Through Table 7 to Digital Section Section ... 7
Replaced Figure 15 and Figure 16 ... 9
Deleted Figure 17 and Figure 18 ... 9
Added Reference Selection Section, Amplifier Selection Section, and Table 11 Through Table 13 ... 15

**9/09—Rev. 0 to Rev. A**

Changes to Features Section ... 1
Changes to Static Performance, Relative Accuracy, Grade: AD5546C Parameter, Table 1 ... 3
Changes to Ordering Guide ... 16

**1/04—Revision 0: Initial Version**

# SPECIFICATIONS

## ELECTRICAL CHARACTERISTICS

$V_{DD}$ = 2.7 V to 5.5 V, $I_{OUT}$ = virtual GND, GND = 0 V, $V_{REF}$ = −10 V to 10 V, $T_A$ = full operating temperature range, unless otherwise noted.

**Table 1.**

| Parameter | Symbol | Conditions | Min | Typ | Max | Unit |
|---|---|---|---|---|---|---|
| STATIC PERFORMANCE[1] | | | | | | |
| Resolution | N | AD5546, 1 LSB = $V_{REF}/2^{16}$ = 153 µV at $V_{REF}$ = 10 V | | 16 | | Bits |
| | | AD5556, 1 LSB = $V_{REF}/2^{14}$ = 610 µV at $V_{REF}$ = 10 V | | 14 | | Bits |
| Relative Accuracy | INL | Grade: AD5556C | | | ±1 | LSB |
| | | Grade: AD5546B | | | ±2 | LSB |
| | | Grade: AD5546C | | | ±1 | LSB |
| Differential Nonlinearity | DNL | Monotonic | | | ±1 | LSB |
| Output Leakage Current | $I_{OUT}$ | Data = zero scale, $T_A$ = 25°C | | | 10 | nA |
| | | Data = zero scale, $T_A$ = $T_A$ maximum | | | 20 | nA |
| Full-Scale Gain Error | $G_{FSE}$ | Data = full scale | | ±1 | ±4 | mV |
| Bipolar Mode Gain Error | $G_E$ | Data = full scale | | ±1 | ±4 | mV |
| Bipolar Mode Zero-Scale Error | $G_{ZSE}$ | Data = full scale | | ±1 | ±2.5 | mV |
| Full-Scale Tempco[2] | $TCV_{FS}$ | | | 1 | | ppm/°C |
| REFERENCE INPUT | | | | | | |
| $V_{REF}$ Range | $V_{REF}$ | | −18 | | +18 | V |
| REF Input Resistance | REF | | 4 | 5 | 6 | kΩ |
| R1 and R2 Resistance | R1 and R2 | | 4 | 5 | 6 | kΩ |
| R1-to-R2 Mismatch | Δ(R1 to R2) | | | ±0.5 | ±1.5 | Ω |
| Feedback and Offset Resistance | $R_{FB}$, $R_{OFS}$ | | 8 | 10 | 12 | kΩ |
| Input Capacitance[2] | $C_{REF}$ | | | 5 | | pF |
| ANALOG OUTPUT | | | | | | |
| Output Current | $I_{OUT}$ | Data = full scale | | 2 | | mA |
| Output Capacitance[2] | $C_{OUT}$ | Code dependent | | 200 | | pF |
| LOGIC INPUT AND OUTPUT | | | | | | |
| Logic Input Low Voltage | $V_{IL}$ | $V_{DD}$ = 5 V | | | 0.8 | V |
| | | $V_{DD}$ = 3 V | | | 0.4 | V |
| Logic Input High Voltage | $V_{IH}$ | $V_{DD}$ = 5 V | 2.4 | | | V |
| | | $V_{DD}$ = 3 V | 2.1 | | | V |
| Input Leakage Current | $I_{IL}$ | | | | 10 | µA |
| Input Capacitance[2] | $C_{IL}$ | | | | 10 | pF |
| INTERFACE TIMING[2, 3] | | | | | | |
| Data to $\overline{WR}$ Setup Time | $t_{DS}$ | $V_{DD}$ = 5 V | 20 | | | ns |
| | | $V_{DD}$ = 3 V | 35 | | | ns |
| Data to $\overline{WR}$ Hold Time | $t_{DH}$ | $V_{DD}$ = 5 V | 0 | | | ns |
| | | $V_{DD}$ = 3 V | 0 | | | ns |
| $\overline{WR}$ Pulse Width | $t_{\overline{WR}}$ | $V_{DD}$ = 5 V | 20 | | | ns |
| | | $V_{DD}$ = 3 V | 35 | | | ns |
| LDAC Pulse Width | $t_{LDAC}$ | $V_{DD}$ = 5 V | 20 | | | ns |
| | | $V_{DD}$ = 3 V | 35 | | | ns |

| Parameter | Symbol | Conditions | Min | Typ | Max | Unit |
|---|---|---|---|---|---|---|
| $\overline{RS}$ Pulse Width | $t_{RS}$ | $V_{DD}$ = 5 V | 20 | | | ns |
| | | $V_{DD}$ = 3 V | 35 | | | ns |
| $\overline{WR}$ to LDAC Delay Time | $t_{LWD}$ | $V_{DD}$ = 5 V | 0 | | | ns |
| | | $V_{DD}$ = 3 V | 0 | | | ns |
| SUPPLY CHARACTERISTICS | | | | | | |
| Power Supply Range | $V_{DD\ RANGE}$ | | 2.7 | | 5.5 | V |
| Positive Supply Current | $I_{DD}$ | Logic inputs = 0 V | | | 10 | μA |
| Power Dissipation | $P_{DISS}$ | Logic inputs = 0 V | | | 0.055 | mW |
| Power Supply Sensitivity | $P_{SS}$ | $\Delta V_{DD}$ = ±5% | | | 0.003 | %/% |
| AC CHARACTERISTICS[4] | | | | | | |
| Output Voltage Settling Time | $t_S$ | To ±0.1% of full scale, data cycles from zero scale to full scale to zero scale | | 0.5 | | μs |
| Reference Multiplying BW | BW | $V_{REF}$ = 100 mV rms, data = full scale, C6 =5.6 pF[5] | | 6.8 | | MHz |
| DAC Glitch Impulse | Q | $V_{REF}$ = 0 V, midscale minus 1 to midscale | | –3 | | nV-s |
| Multiplying Feedthrough Error | $V_{OUT}/V_{REF}$ | $V_{REF}$ = 100 mV rms, f = 10 kHz | | 79 | | dB |
| Digital Feedthrough | $Q_D$ | $\overline{WR}$ = 1, LDAC toggles at 1 MHz | | 7 | | nV-s |
| Total Harmonic Distortion | THD | $V_{REF}$ = 5 V p-p, data = full-scale, f = 1 kHz | | –103 | | dB |
| Output Noise Density | $e_N$ | f = 1 kHz, BW = 1 Hz | | 12 | | nV/rt Hz |

[1] All static performance tests (except $I_{OUT}$) are performed in a closed-loop system, using an external precision OP97 I-V converter amplifier. The AD554x RFB terminal is tied to the amplifier output. The op amp +IN is grounded, and the DAC $I_{OUT}$ is tied to the op amp –IN. Typical values represent average readings measured at 25°C.
[2] These parameters are guaranteed by design and are not subject to production testing.
[3] All input control signals are specified with $t_R = t_F$ = 2.5 ns (10% to 90% of 3 V) and timed from a voltage level of 1.5 V.
[4] All ac characteristic tests are performed in a closed-loop system using an AD8038 I-V converter amplifier except for THD where an AD8065 was used.
[5] C6 is the C6 capacitor shown in Figure 20.

## TIMING DIAGRAM

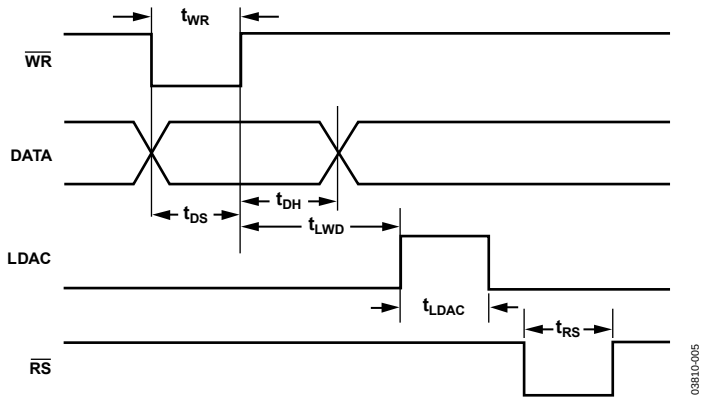


*Figure 3. AD5546/AD5556 Timing Diagram*

# ABSOLUTE MAXIMUM RATINGS

**Table 2.**

| Parameter | Rating |
|---|---|
| $V_{DD}$ to GND | −0.3 V, +8 V |
| $R_{FB}$, $R_{OFS}$, R1, $R_{COM}$, and REF to GND | −18 V, 18 V |
| Logic Inputs to GND | −0.3 V, +8 V |
| V ($I_{OUT}$) to GND | −0.3 V, $V_{DD}$ + 0.3 V |
| Input Current to Any Pin Except Supplies | ±50 mA |
| Thermal Resistance ($\theta_{JA}$) | 128°C |
| Maximum Junction Temperature ($T_{J\,MAX}$) | 150°C |
| Operating Temperature Range | −40°C to +125°C |
| Storage Temperature Range | −65°C to +150°C |
| Lead Temperature: | |
| Vapor Phase, 60 s | 215°C |
| Infrared, 15 s | 220°C |
| Package Power Dissipation | $(T_{J\,MAX} - T_A)/\theta_{JA}$ |

Stresses above those listed under Absolute Maximum Ratings may cause permanent damage to the device. This is a stress rating only; functional operation of the device at these or any other conditions above those listed in the operational sections of this specification is not implied. Exposure to absolute maximum rating conditions for extended periods may affect device reliability.

## ESD CAUTION

**ESD (electrostatic discharge) sensitive device.** Charged devices and circuit boards can discharge without detection. Although this product features patented or proprietary protection circuitry, damage may occur on devices subjected to high energy ESD. Therefore, proper ESD precautions should be taken to avoid performance degradation or loss of functionality.

# PIN CONFIGURATIONS AND FUNCTION DESCRIPTIONS

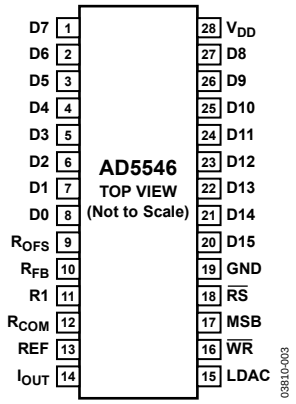


*Figure 4. AD5546 Pin Configuration*

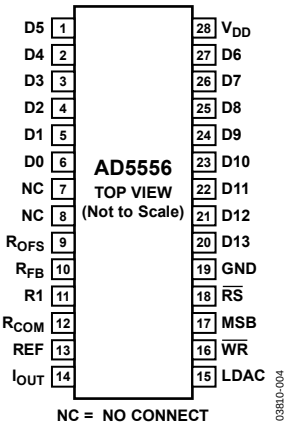


*Figure 5. AD5556 Pin Configuration*

**Table 3. AD5546 Pin Function Descriptions**

| Pin No. | Mnemonic | Description |
|---|---|---|
| 1 to 8 | D7 to D0 | Digital Input Data Bits[D7: D0]. The signal level must be ≤ $V_{DD}$ + 0.3 V. |
| 9 | $R_{OFS}$ | Bipolar Offset Resistor. Accepts up to ±18 V. In two-quadrant mode, ties to $R_{FB}$. In four-quadrant mode, ties to R1 and the external reference. |
| 10 | $R_{FB}$ | Internal Matching Feedback Resistor. Connects to the output of an external op amp for I-V conversion. |
| 11 | R1 | Four-Quadrant Resistor R1. In two-quadrant mode, shorts to the REF pin. In four-quadrant mode, ties to $R_{OFS}$. |
| 12 | $R_{COM}$ | Center Tap Point of Two Four-Quadrant Resistors, R1 and R2. In four-quadrant mode, ties to the inverting node of the reference amplifier. In two-quadrant mode, shorts to the REF pin. |
| 13 | REF | DAC Reference Input in Two-Quadrant Mode and R2 Terminal in Four-Quadrant Mode. In two-quadrant mode, this pin is the reference input with constant input resistance vs. code. In four-quadrant mode, this pin is driven by the external reference amplifier. |
| 14 | $I_{OUT}$ | DAC Current Output. Connects to the inverting node of an external op amp for I-V conversion. |
| 15 | LDAC | Digital Input Load DAC Control. Signal level must be ≤ $V_{DD}$ + 0.3 V. |
| 16 | $\overline{WR}$ | Write Control Digital Input in Active Low. Transfers shift-register data to the DAC register on the rising edge. The signal level must be ≤ $V_{DD}$ + 0.3 V. |
| 17 | MSB | Power-On Reset State. MSB = 0 resets at zero scale; MSB = 1 resets at midscale. The signal level must be ≤ $V_{DD}$ + 0.3 V. |
| 18 | $\overline{RS}$ | Reset in Active Low. Resets to zero scale if MSB = 0, and resets to midscale if MSB = 1. The signal level must be ≤ $V_{DD}$ + 0.3 V. |
| 19 | GND | Analog and Digital Grounds. |
| 20 to 21 | D15 to D14 | Digital Input Data Bits[D15:D14]. The signal level must be ≤ $V_{DD}$ + 0.3 V. |
| 22 to 27 | D13 to D8 | Digital Input Data Bits[D13:D8]. The signal level must be ≤ $V_{DD}$ + 0.3 V. |
| 28 | $V_{DD}$ | Positive Power Supply Input. Specified range of operation: 2.7 V to 5.5 V. |

**Table 4. AD5556 Pin Function Descriptions**

| Pin No. | Mnemonic | Description |
|---|---|---|
| 1 to 6 | D5 to D0 | Digital Input Data Bits[D5:D0]. The signal level must be ≤ $V_{DD}$+0.3 V. |
| 7 to 8 | NC | No Connection. The user should not connect anything other than dummy pads on these terminals. |
| 9 | $R_{OFS}$ | Bipolar Offset Resistor. Accepts up to ±18 V. In two-quadrant mode, ties to RFB. In four-quadrant mode, ties to R1 and the external reference. |
| 10 | $R_{FB}$ | Internal Matching Feedback Resistor. Connects to the output of an external op amp for I-V conversion. |
| 11 | R1 | Four-Quadrant Resistor R1. In two-quadrant mode, shorts to the REF pin. In four-quadrant mode, ties to $R_{OFS}$. |
| 12 | $R_{COM}$ | Center Tap Point of Two Four-Quadrant Resistors, R1 and R2. In four-quadrant mode, ties to the inverting node of the reference amplifier. In two-quadrant mode, shorts to the REF pin. |

| Pin No. | Mnemonic | Description |
|---|---|---|
| 13 | REF | DAC Reference Input in Two-Quadrant Mode and R2 Terminal in Four-Quadrant Mode. In two-quadrant mode, this pin is the reference input with constant input resistance vs. code. In four-quadrant mode, this pin is driven by the external reference amplifier. |
| 14 | $I_{OUT}$ | DAC Current Output. Connects to the inverting node of an external op amp for I-V conversion. |
| 15 | LDAC | Digital Input Load DAC Control. The signal level must be ≤ $V_{DD}$ + 0.3 V. |
| 16 | $\overline{WR}$ | Write Control Digital Input in Active Low. Transfers shift-register data to the DAC register on the rising edge. The signal level must be ≤ $V_{DD}$ + 0.3 V. |
| 17 | MSB | Power On Reset State. MSB = 0 resets at zero scale; MSB = 1 resets at midscale. The signal level must be ≤ $V_{DD}$ + 0.3 V. |
| 18 | $\overline{RS}$ | Reset in Active Low. Resets to zero scale if MSB = 0 and resets to midscale if MSB = 1. The signal level must be ≤ $V_{DD}$ + 0.3 V. |
| 19 | GND | Analog and Digital Grounds. |
| 20 to 27 | D13 to D6 | Digital Input Data Bits[D13:D6]. The signal level must be ≤ $V_{DD}$ + 0.3 V. |
| 28 | $V_{DD}$ | Positive Power Supply Input. Specified range of operation: 2.7 V to 5.5 V. |

## DIGITAL SECTION

The AD5546/AD5556 have 16-/14-bit parallel inputs. The devices are double buffered with 16-/14-bit registers. The double-buffered feature allows the update of several AD5546/AD5556 simultaneously. For the AD5546, the input register is loaded directly from a 16-bit controller bus when the $\overline{WR}$ pin is brought low. The DAC register is updated with data from the input register when LDAC is brought high. Updating the DAC register updates the DAC output with the new data (see Figure 17). To make both registers transparent, tie $\overline{WR}$ low and LDAC high. The asynchronous $\overline{RS}$ pin resets the part to zero scale if the MSB pin = 0 and to midscale if the MSB pin = 1.

**Table 5. AD5546 Parallel Input Data Format**

| | MSB | | | | | | | | | | | | | | | LSB |
|---|---|---|---|---|---|---|---|---|---|---|---|---|---|---|---|---|
| Bit Position | B15 | B14 | B13 | B12 | B11 | B10 | B9 | B8 | B7 | B6 | B5 | B4 | B3 | B2 | B1 | B0 |
| Data Word | D15 | D14 | D13 | D12 | D11 | D10 | D9 | D8 | D7 | D6 | D5 | D4 | D3 | D2 | D1 | D0 |

**Table 6. AD5556 Parallel Input Data Format**

| | MSB | | | | | | | | | | | | | LSB |
|---|---|---|---|---|---|---|---|---|---|---|---|---|---|---|
| Bit Position | B13 | B12 | B11 | B10 | B9 | B8 | B7 | B6 | B5 | B4 | B3 | B2 | B1 | B0 |
| Data Word | D13 | D12 | D11 | D10 | D9 | D8 | D7 | D6 | D5 | D4 | D3 | D2 | D1 | D0 |

**Table 7. Control Inputs**

| $\overline{RS}$ | $\overline{WR}$ | LDAC | Register Operation |
|---|---|---|---|
| 0 | X[1] | X[1] | Reset output to 0, with MSB pin = 0 and to midscale with MSB pin = 1. |
| 1 | 0 | 0 | Load input register with data bits. |
| 1 | 1 | 1 | Load DAC register with the contents of the input register. |
| 1 | 0 | 1 | Input and DAC registers are transparent. |
| 1 | ⊓ | ⊓ | When LDAC and $\overline{WR}$ are tied together and programmed as a pulse, the data bits are loaded into the input register on the falling edge of the pulse and then loaded into the DAC register on the rising edge of the pulse. |
| 1 | 1 | 0 | No register operation. |

[1] X = don't care.

## ESD PROTECTION CIRCUITS

All logic input pins contain back-biased ESD protection Zeners connected to ground (GND) and $V_{DD}$, as shown in Figure 18. As a result, the voltage level of the logic input should not be greater than the supply voltage.

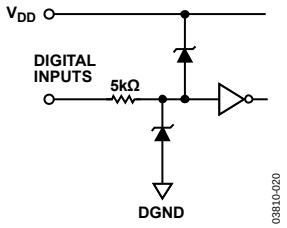


*Figure 18. Equivalent ESD Protection Circuits*

## AMPLIFIER SELECTION

In addition to offset voltage, the bias current is important in op amp selection for precision current output DACs. An input bias current of 30 nA in the op amp contributes to 1 LSB in the AD5546's full-scale error. The OP1177 and AD8628 op amps are good candidates for the I-V conversion.

## REFERENCE SELECTION

The initial accuracy and the rated output of the voltage reference determine the full span adjustment. The initial accuracy is usually a secondary concern in precision because it can be trimmed. Figure 23 shows an example of a trimming circuit. The zero scale error can also be minimized by standard op amp nulling techniques.

The voltage reference temperature coefficient (TC) and long-term drift are primary considerations. For example, a 5 V reference with a TC of 5 ppm/°C means that the output changes by 25 μV per degree Celsius. As a result, the reference that operates at 55°C contributes an additional 750 μV full-scale error.

Similarly, the same 5 V reference with a ±50 ppm long-term drift means that the output may change by ±250 μV over time. Therefore, it is practical to calibrate a system periodically to maintain its optimum precision.

# APPLICATIONS INFORMATION

## UNIPOLAR MODE

### *Two-Quadrant Multiplying Mode, $V_{OUT}$ = 0 V to $-V_{REF}$*

The AD5546/AD5556 DAC architecture uses a current-steering R-2R ladder design that requires an external reference and op amp to convert the unipolar mode of output voltage to

AD5546

$$V_{OUT} = -V_{REF} \times D/65{,}536 \quad (1)$$

AD5556

$$V_{OUT} = -V_{REF} \times D/16{,}384 \quad (2)$$

where $D$ is the decimal equivalent of the input code.

The output voltage polarity is opposite to the $V_{REF}$ polarity in this case (see Figure 19). Table 8 shows the negative output vs. code for the AD5546.

**Table 8. AD5546 Unipolar Mode Negative Output vs. Code**

| D in Binary | $V_{OUT}$ (V) |
|---|---|
| 1111 1111 1111 1111 | $-V_{REF}(65{,}535/65{,}536)$ |
| 1000 0000 0000 0000 | $-V_{REF}/2$ |
| 0000 0000 0000 0001 | $-V_{REF}(1/65{,}536)$ |
| 0000 0000 0000 0000 | 0 |

### *Two-Quadrant Multiplying Mode, $V_{OUT}$ = 0 V to $+V_{REF}$*

The AD5546/AD5556 are designed to operate with either positive or negative reference voltages. As a result, positive output can be achieved with an additional op amp, (see Figure 20), and the output becomes

AD5546

$$V_{OUT} = +V_{REF} \times D/65{,}536 \quad (3)$$

AD5556

$$V_{OUT} = +V_{REF} \times D/16{,}384 \quad (4)$$

Table 9 shows the positive output vs. code for the AD5546.

**Table 9. AD5546 Unipolar Mode Positive Output vs. Code**

| D in Binary | $V_{OUT}$ (V) |
|---|---|
| 1111 1111 1111 1111 | $+V_{REF}(65{,}535/65{,}536)$ |
| 1000 0000 0000 0000 | $+V_{REF}/2$ |
| 0000 0000 0000 0001 | $+V_{REF}(1/65{,}536)$ |
| 0000 0000 0000 0000 | 0 |

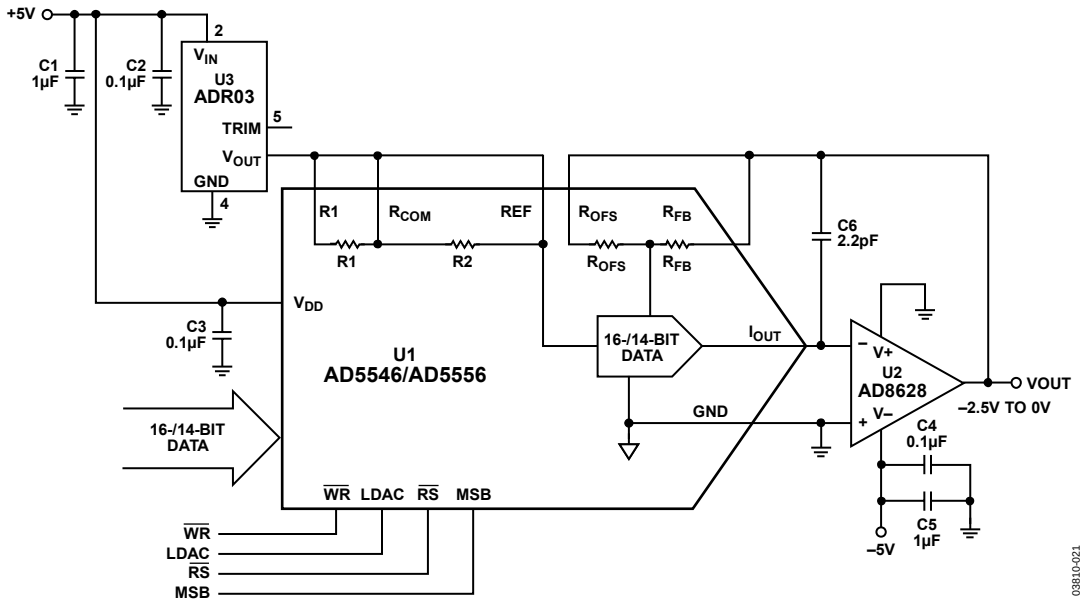


*Figure 19. Unipolar Two-Quadrant Multiplying Mode, $V_{OUT}$ = 0 to $-V_{REF}$*

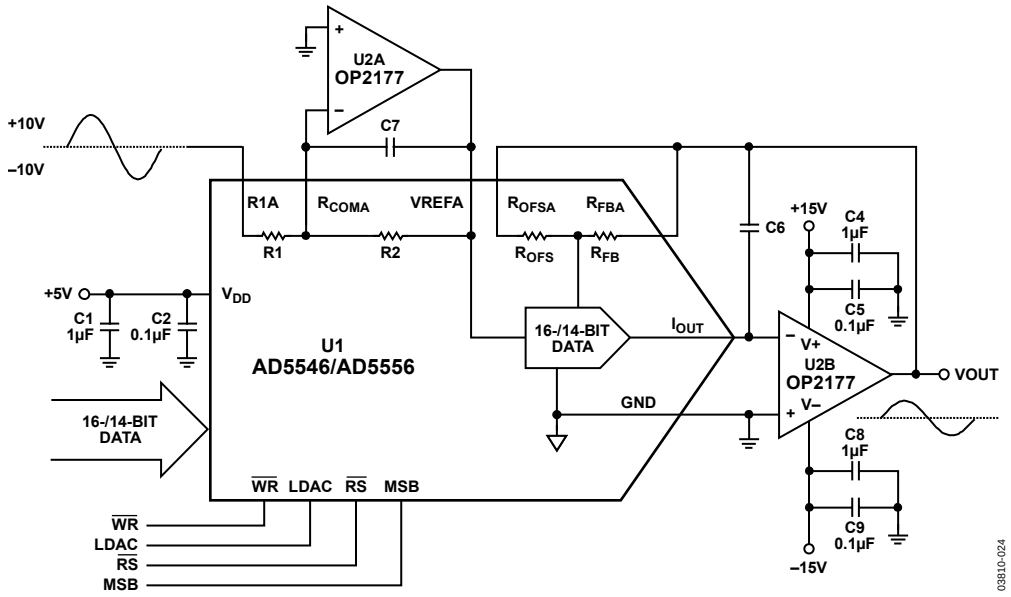


*Figure 20. Unipolar Two-Quadrant Multiplying Mode, $V_{OUT}$ = 0 to +$V_{REF}$*

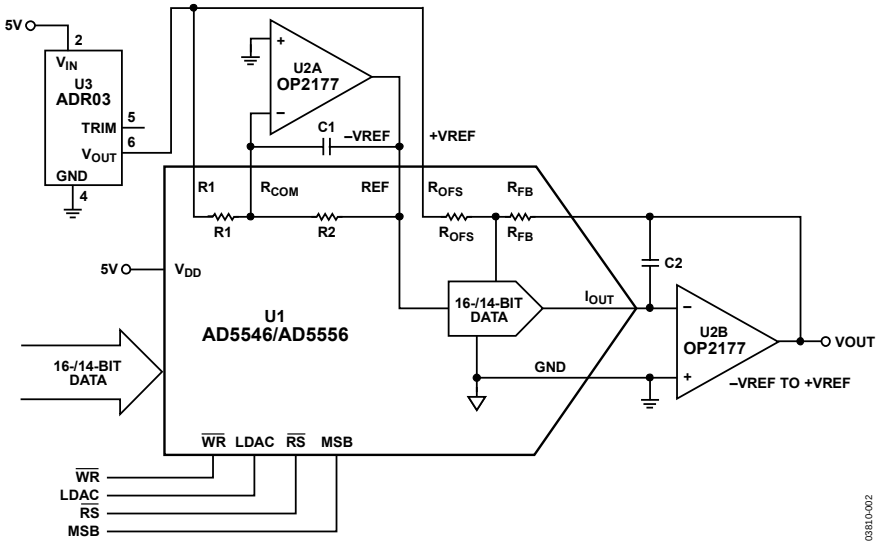


*Figure 21. Four-Quadrant Multiplying Mode, $V_{OUT}$ = –$V_{REF}$ to +$V_{REF}$*

## BIPOLAR MODE

### *Four-Quadrant Multiplying Mode, $V_{OUT}$ = –$V_{REF}$ to +$V_{REF}$*

The AD5546/AD5556 contain on-chip all the four-quadrant resistors necessary for the precision bipolar multiplying operation. Such a feature minimizes the number of exponent components to only a voltage reference, dual op amp, and compensation capacitor (see Figure 21). For example, with a 10 V reference, the circuit yields a precision, bipolar –10 V to +10 V output.

AD5546

$$V_{OUT} = (D/32768 - 1) \times V_{REF} \quad (5)$$

AD5556

$$V_{OUT} = (D/16384 - 1) \times V_{REF} \quad (6)$$

Table 10 shows some of the results for the 16-bit AD5546.

**Table 10. AD5546 Output vs. Code**

| D in Binary | $V_{OUT}$ |
|---|---|
| 1111 1111 1111 1111 | $+V_{REF}(32,767/32,768)$ |
| 1000 0000 0000 0001 | $+V_{REF}(1/32,768)$ |
| 1000 0000 0000 0000 | 0 |
| 0111 1111 1111 1111 | $-V_{REF}(1/32,768)$ |
| 0000 0000 0000 0000 | $-V_{REF}$ |

## AC REFERENCE SIGNAL ATTENUATOR

Besides handling digital waveforms decoded from parallel input data, the AD5546/AD5556 handle equally well low frequency ac reference signals for signal attenuation, channel equalization, and waveform generation applications. The maximum signal range can be up to ±18 V (see Figure 22).

## SYSTEM CALIBRATION

The initial accuracy of the system can be adjusted by trimming the voltage reference ADR0x with a digital potentiometer (see Figure 23). The AD5170 provides an OTP (one time programmable), 8-bit adjustment that is ideal and reliable for such calibration. The Analog Devices, Inc., OTP digital potentiometer comes with programmable software that simplifies the factory calibration process.

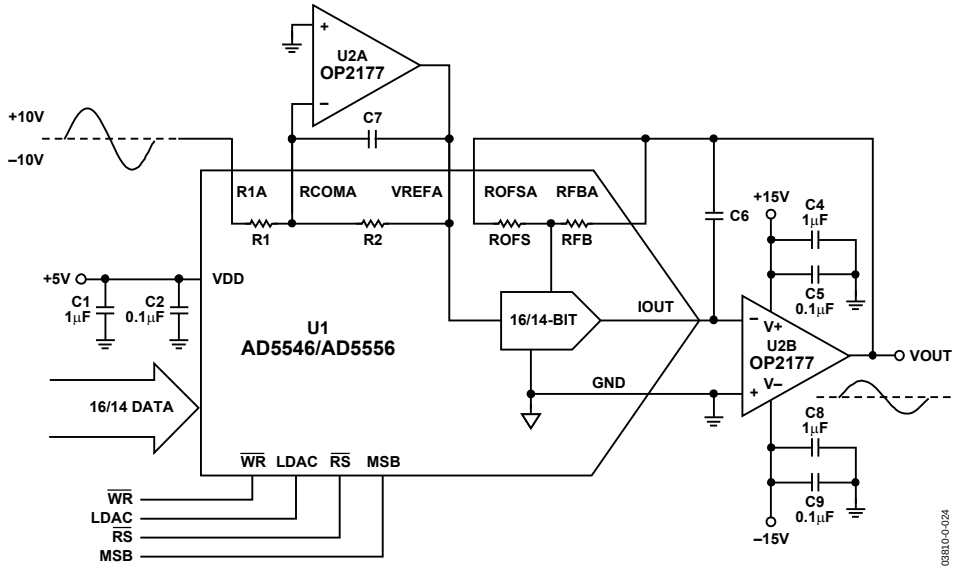


*Figure 22. Signal Attenuator with AC Reference*

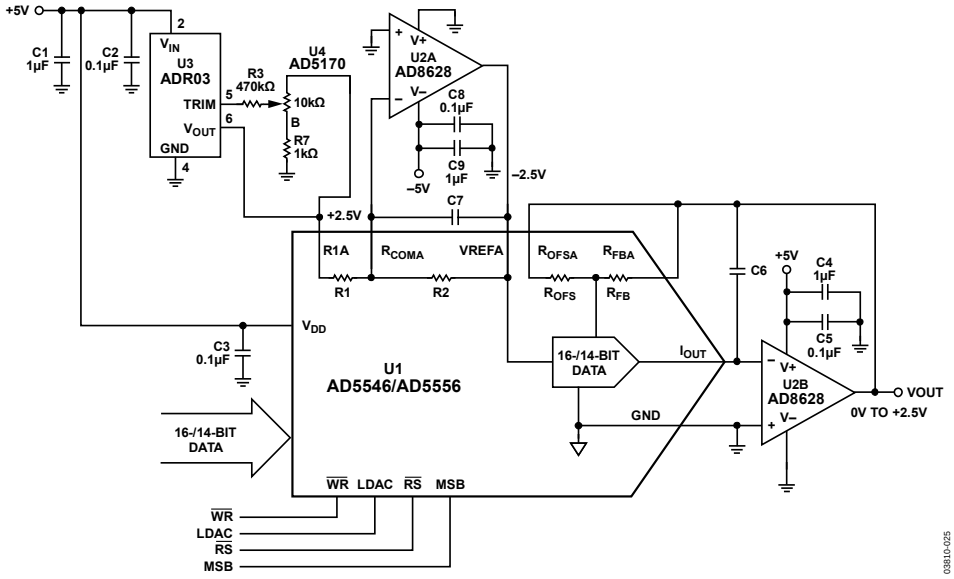


*Figure 23. Full Span Calibration*

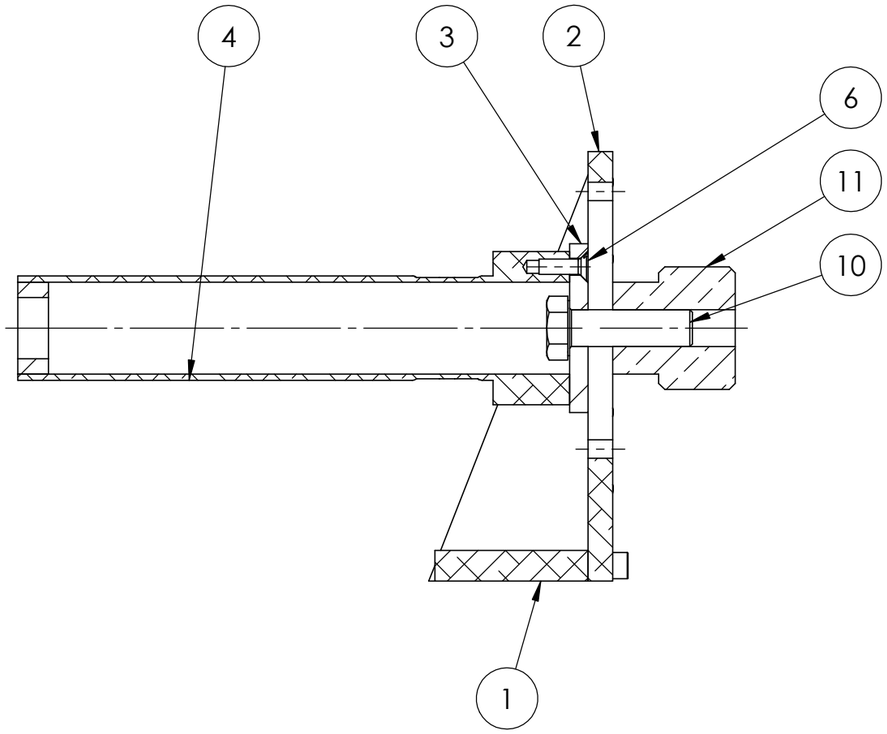


SECTION A-A

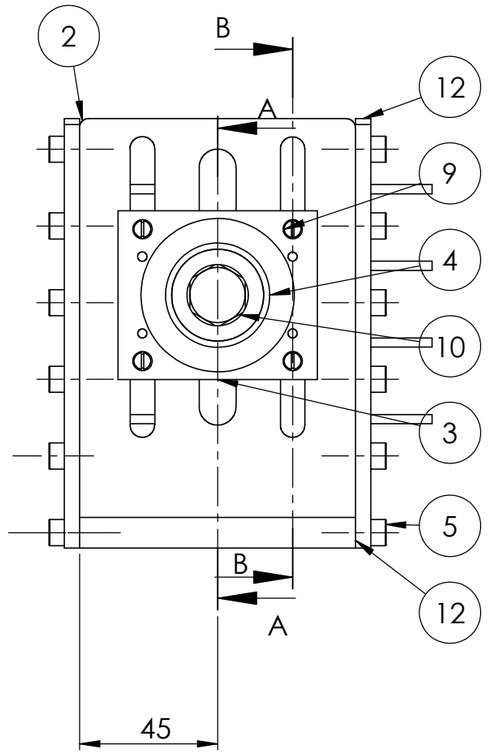


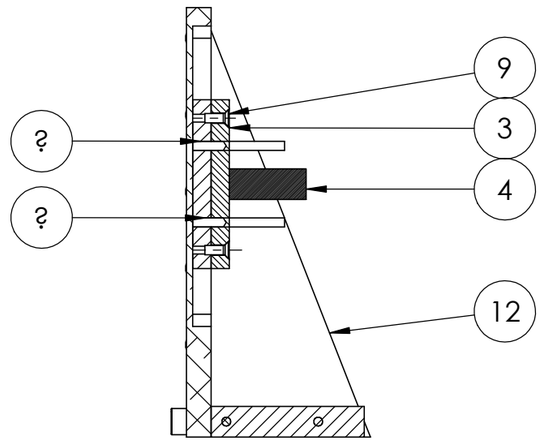


SECTION B-B

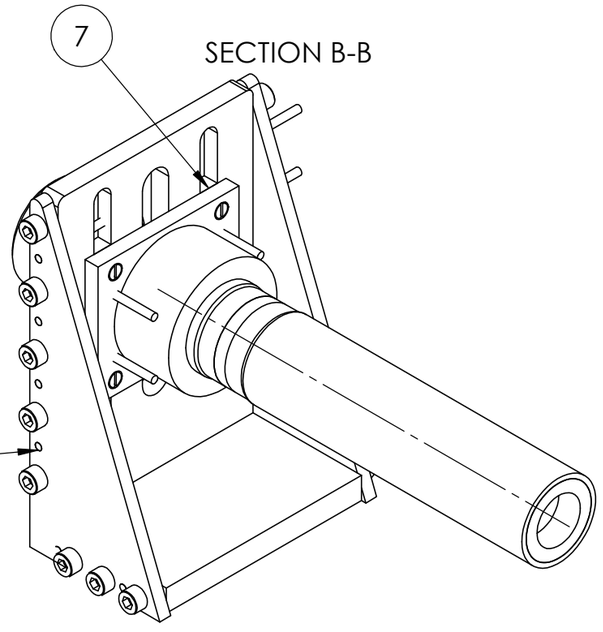


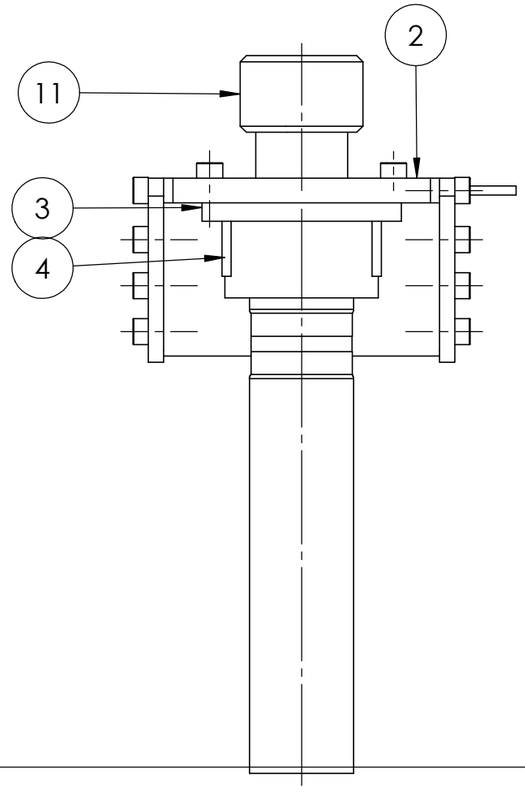


| ITEM NO. | PART NUMBER | QTY. |
|---|---|---|
| 1 | Base | 1 |
| 2 | Backplate | 1 |
| 3 | Vertical height plate | 1 |
| 4 | Strain bar | 1 |
| 5 | ISO 4762 M5 x 12 --- 12N | 20 |
| 6 | ISO 2009 - M5 x 16 --- 16N | 5 |
| 7 | Guide | 2 |
| 8 | Pin | 16 |
| 9 | ISO 2009 - M3 x 8 --- 8N | 4 |
| 10 | ISO 8676 - M12x1.5 x 40-N | 1 |
| 11 | Custon nut | 1 |
| 12 | Steel gusset | 2 |
| 13 | Spacer ring | 1 |

| | | | | |
|---|---|---|---|---|
| A3 Landscape | University of Cape Town<br>Department of Mechanical Engineering | | | |
| | Title:<br>Thumb dyn 2 | | | |
| Assembly Drawing | Scale:<br>1:2 | Date:<br>2015/05/27 | Sheet1 | of<br>1 |
| | Drawn By: | | Drawing Number | |

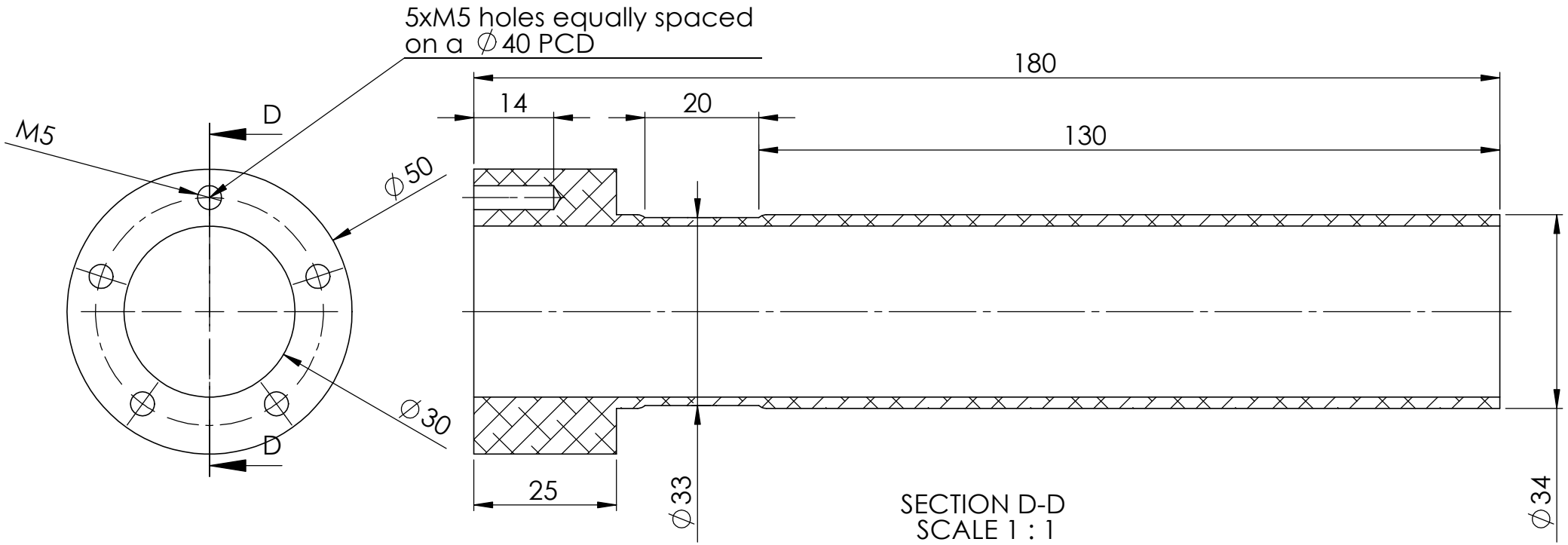


| | | | | |
|---|---|---|---|---|
| A4 Landscape | University of Cape Town<br>Department of Mechanical Engineering | | | |
| | Title:<br>Strain bar | | | |
| Part Finish | Scale:<br>1:2 | Date:<br>2015/05/27 | Sheet1 | of<br>1 |
| Material: | Drawn By: | | Drawing Number | |

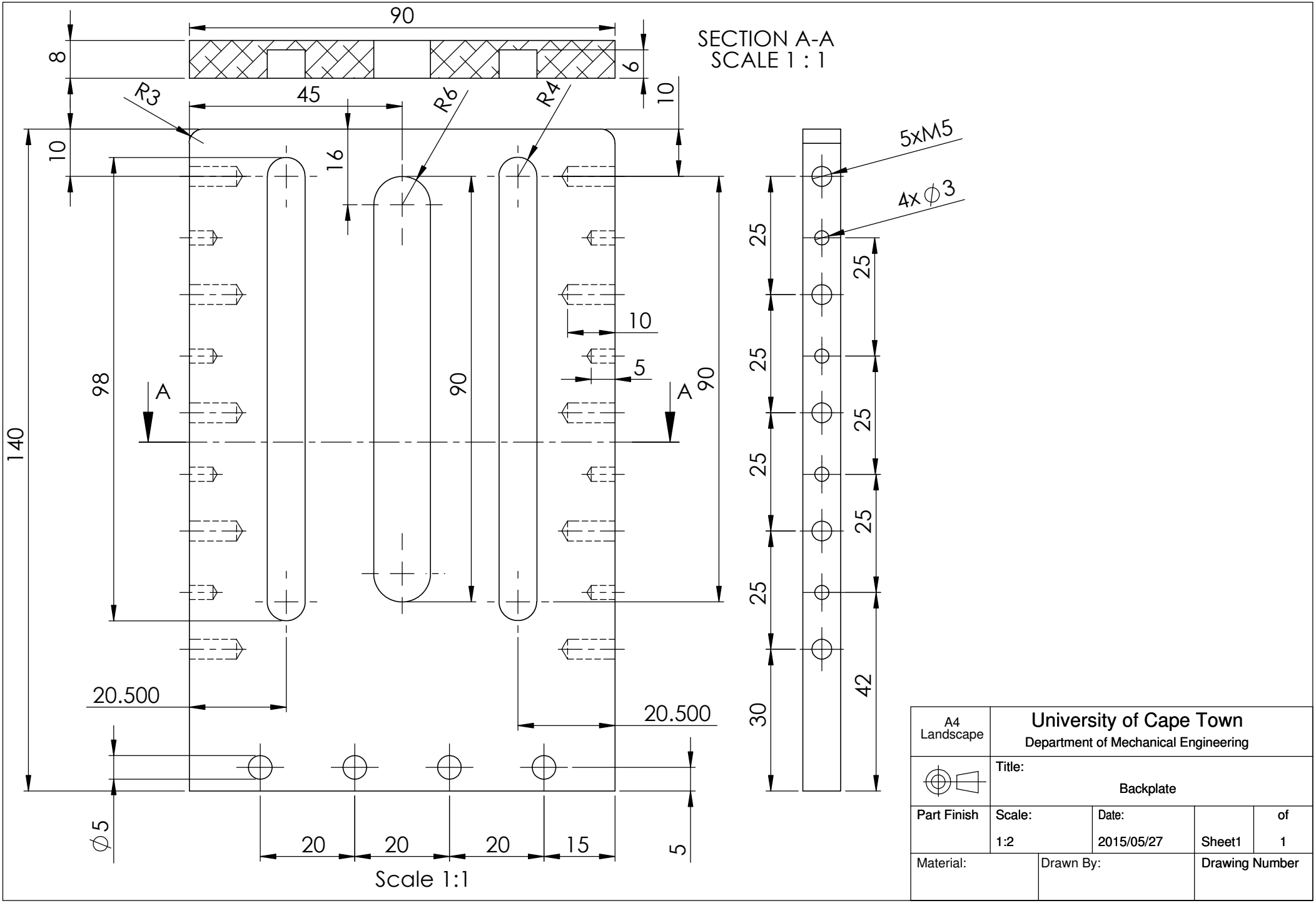


| | | | | |
|---|---|---|---|---|
| A4 Landscape | University of Cape Town<br>Department of Mechanical Engineering | | | |
| | Title:<br>Backplate | | | |
| Part Finish | Scale:<br>1:2 | Date:<br>2015/05/27 | Sheet1 | of<br>1 |
| Material: | Drawn By: | | Drawing Number | |

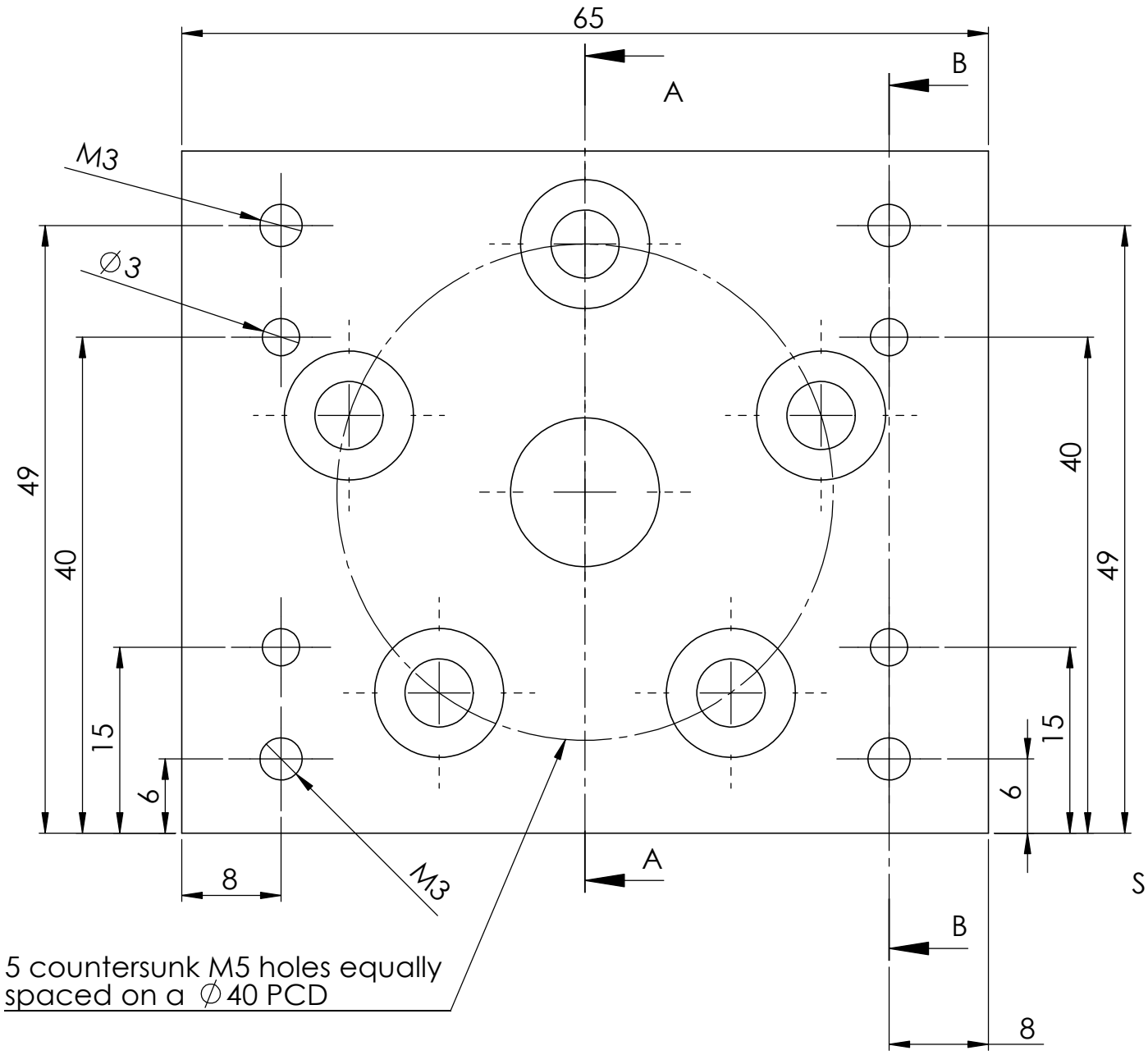


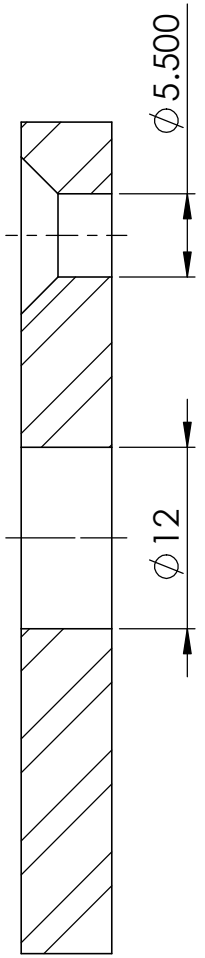


SECTION A-A

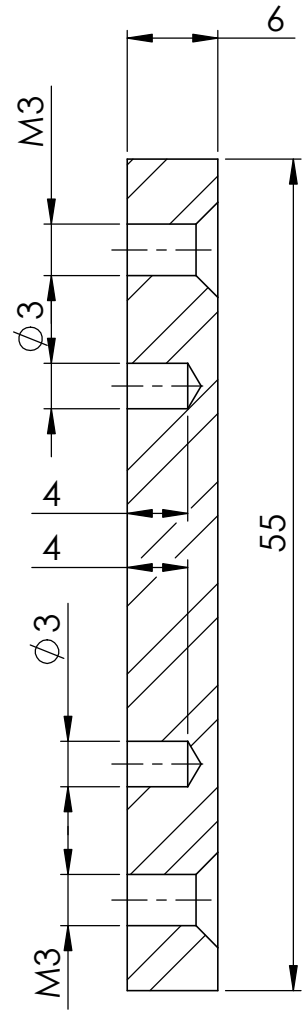


SECTION B-B

| | | | | |
|---|---|---|---|---|
| A4 Landscape | University of Cape Town<br>Department of Mechanical Engineering | | | |
| | Title:<br>Vertical height plate | | | |
| Part Finish | Scale:<br>2:1 | Date:<br>2015/05/27 | Sheet1 | of<br>1 |
| Material: | Drawn By: | | Drawing Number | |

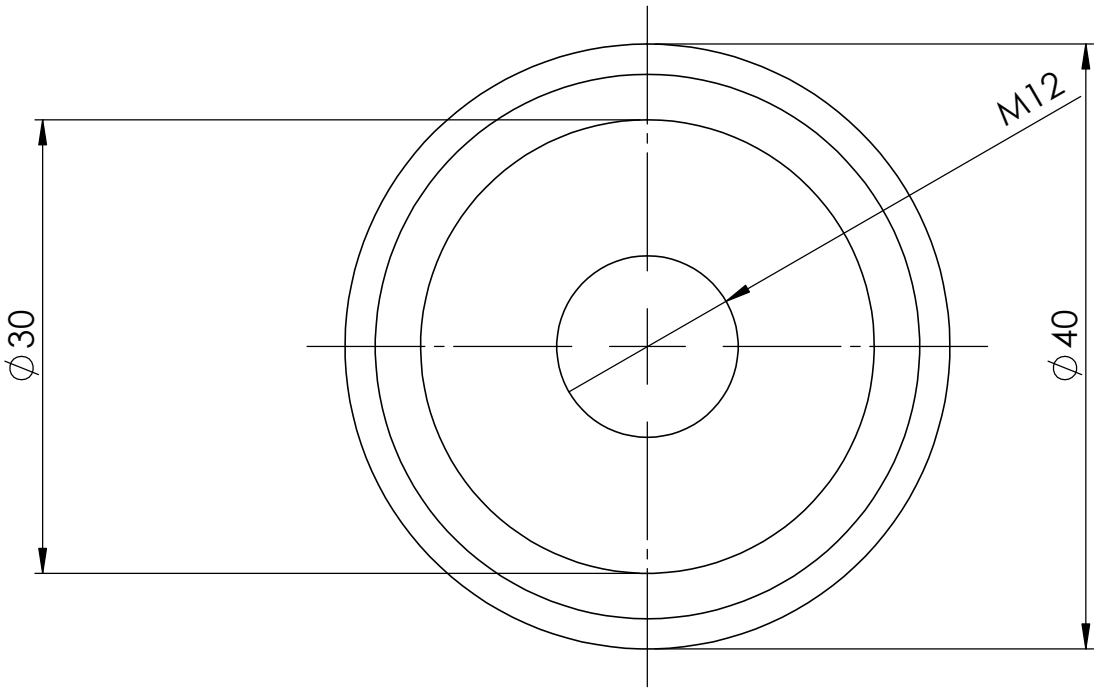


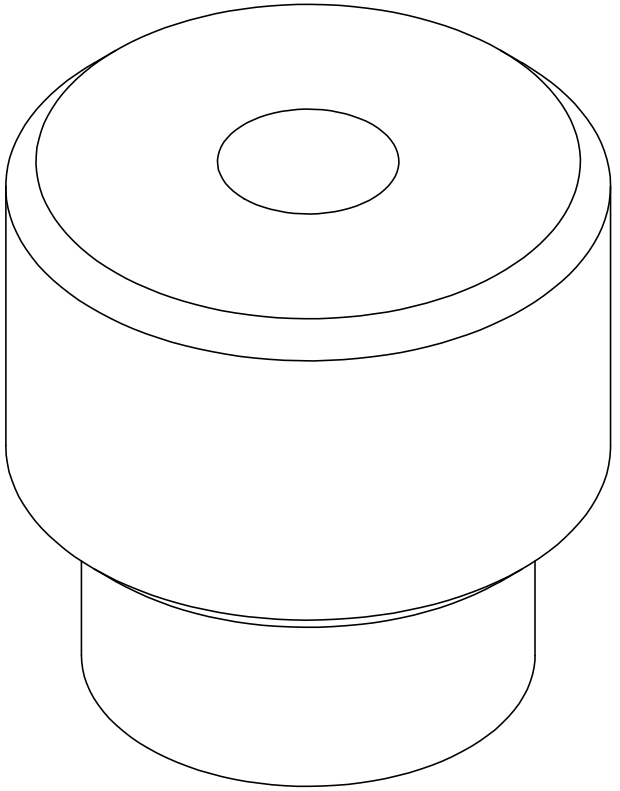

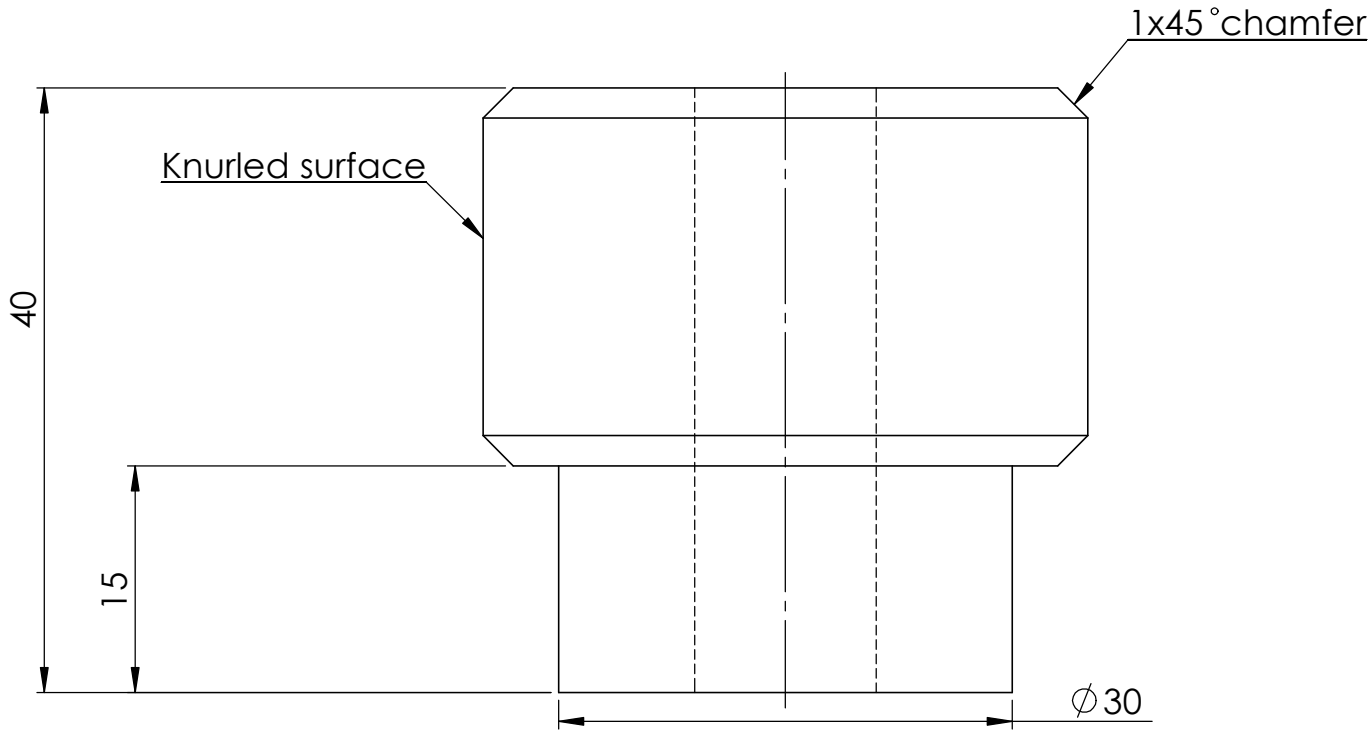


| | | | | |
|---|---|---|---|---|
| A4 Landscape | University of Cape Town<br>Department of Mechanical Engineering | | | |
| | Title:<br>Custon nut | | | |
| Part Finish | Scale:<br>2:1 | Date:<br>2015/05/27 | Sheet1 | of<br>1 |
| Material: | Drawn By: | | Drawing Number | |

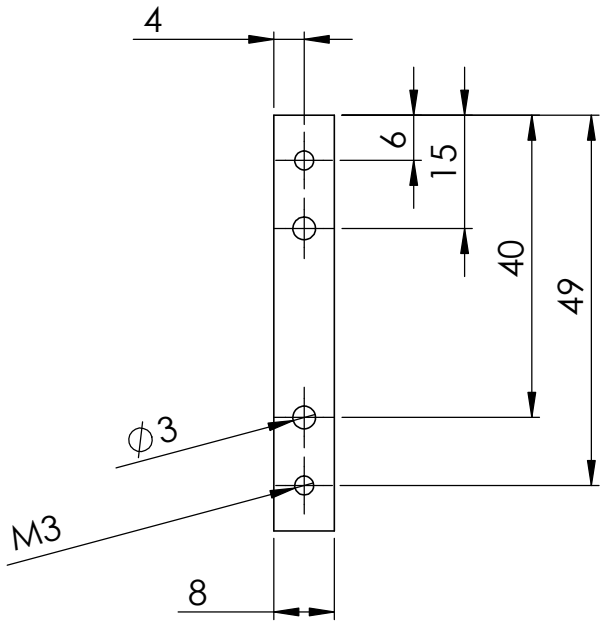


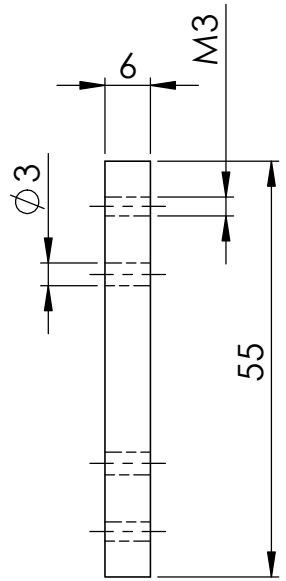


| | | | | |
|---|---|---|---|---|
| A4 Landscape | University of Cape Town<br>Department of Mechanical Engineering | | | |
| | Title:<br>Guide | | | |
| Part Finish | Scale:<br>1:1 | Date:<br>2015/05/27 | Sheet1 | of<br>1 |
| Material: | Drawn By: | | Drawing Number | |

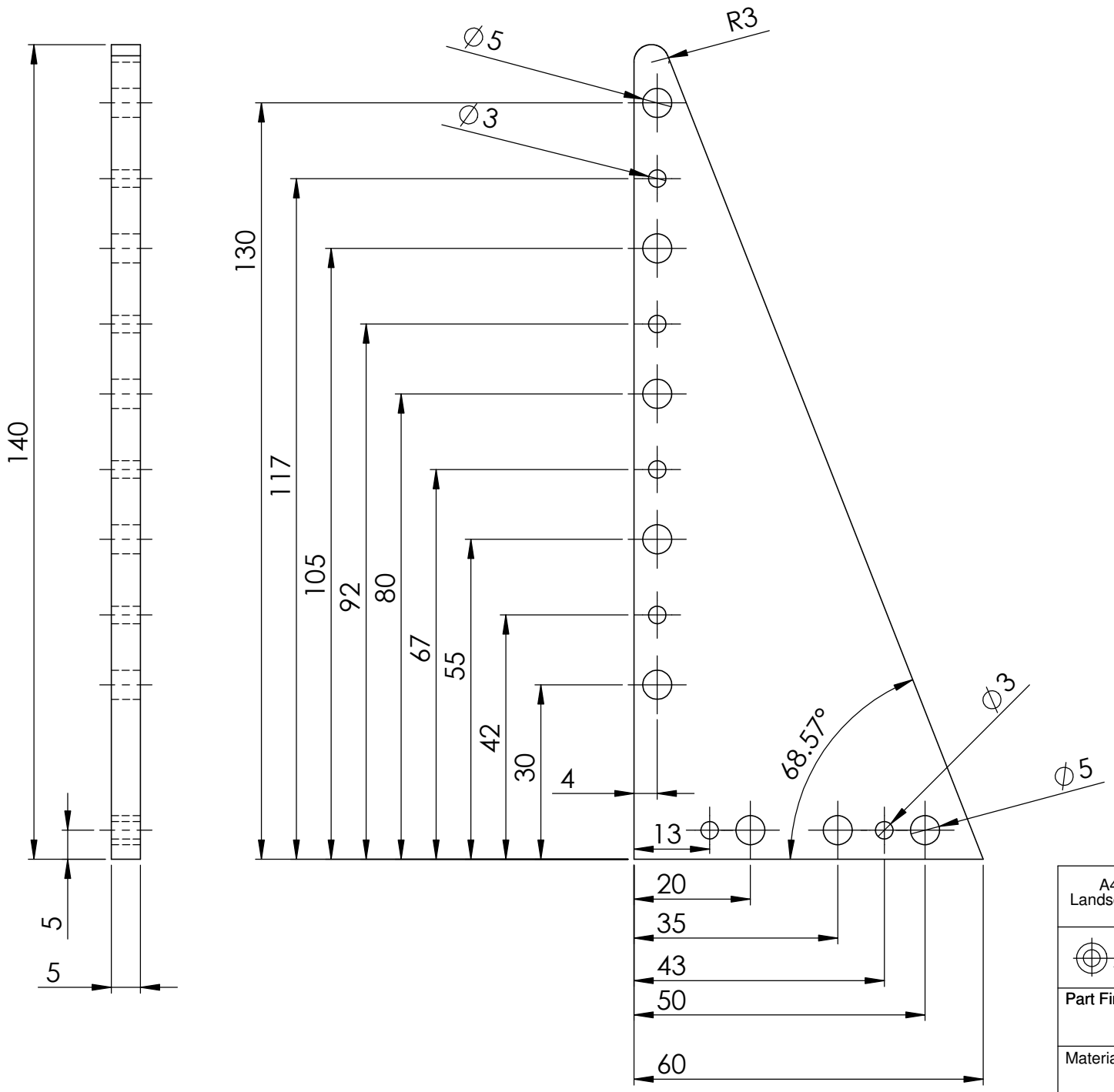


| | | | | |
|---|---|---|---|---|
| A4 Landscape | University of Cape Town<br>Department of Mechanical Engineering | | | |
| | Title:<br>Steel gusset | | | |
| Part Finish | Scale:<br>1:2 | Date:<br>2015/05/27 | Sheet1 | of<br>1 |
| Material: | Drawn By: | | Drawing Number | |

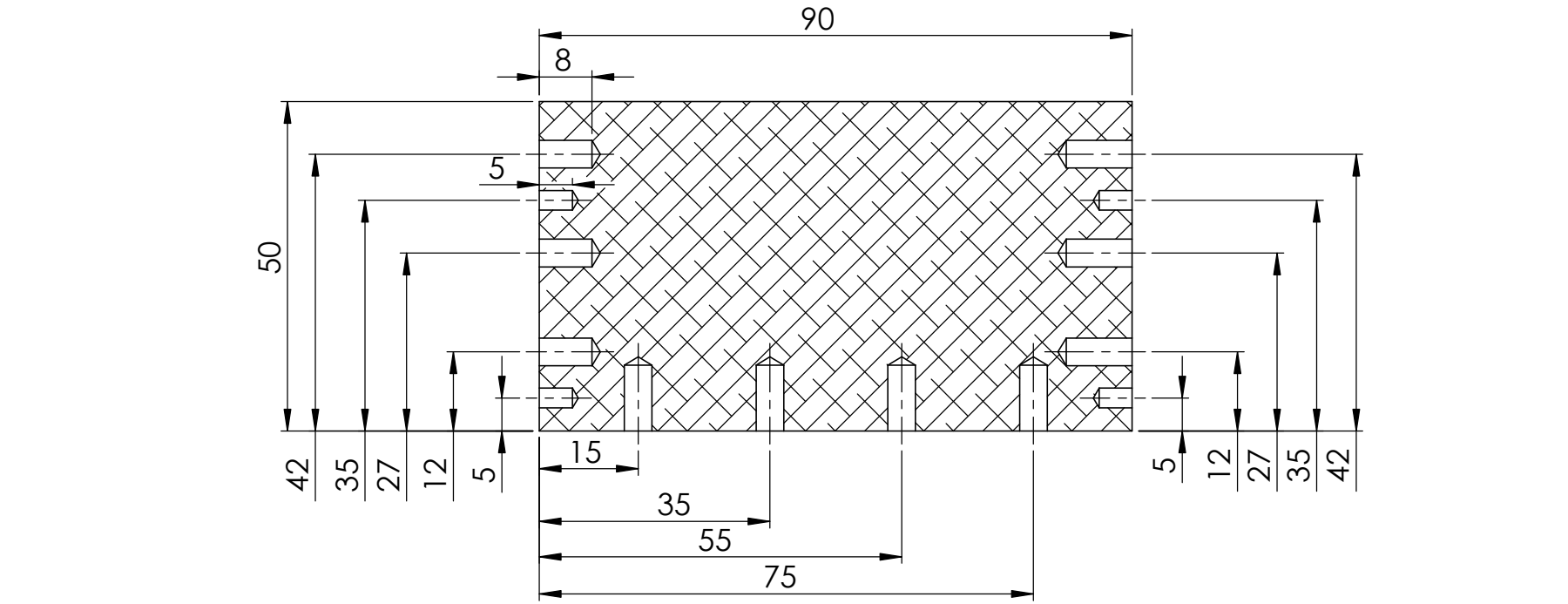


SECTION A-A
SCALE 1 : 1

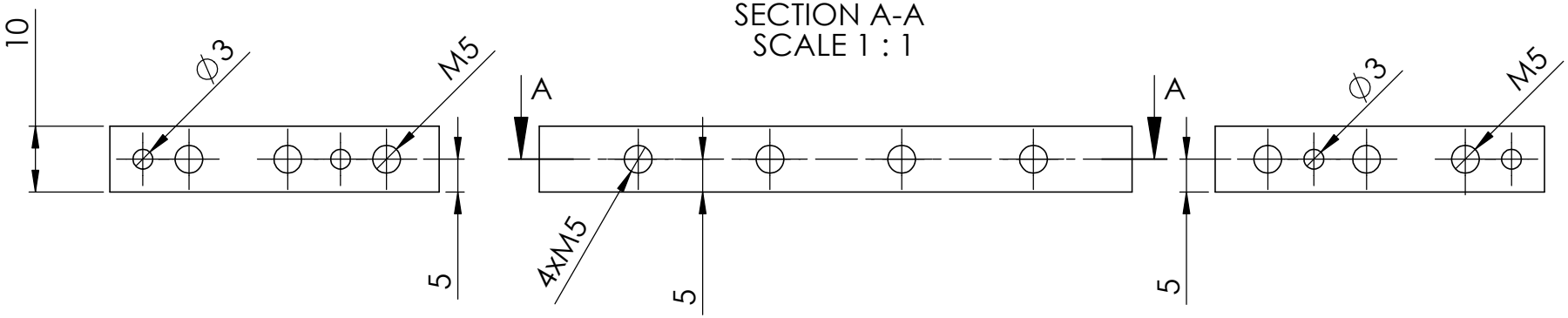


| | | | | |
|---|---|---|---|---|
| A4 Landscape | University of Cape Town<br>Department of Mechanical Engineering | | | |
| | Title:<br>Base | | | |
| Part Finish | Scale:<br>2:1 | Date:<br>2015/05/27 | Sheet1 | of<br>1 |
| Material: | Drawn By: | | Drawing Number | |

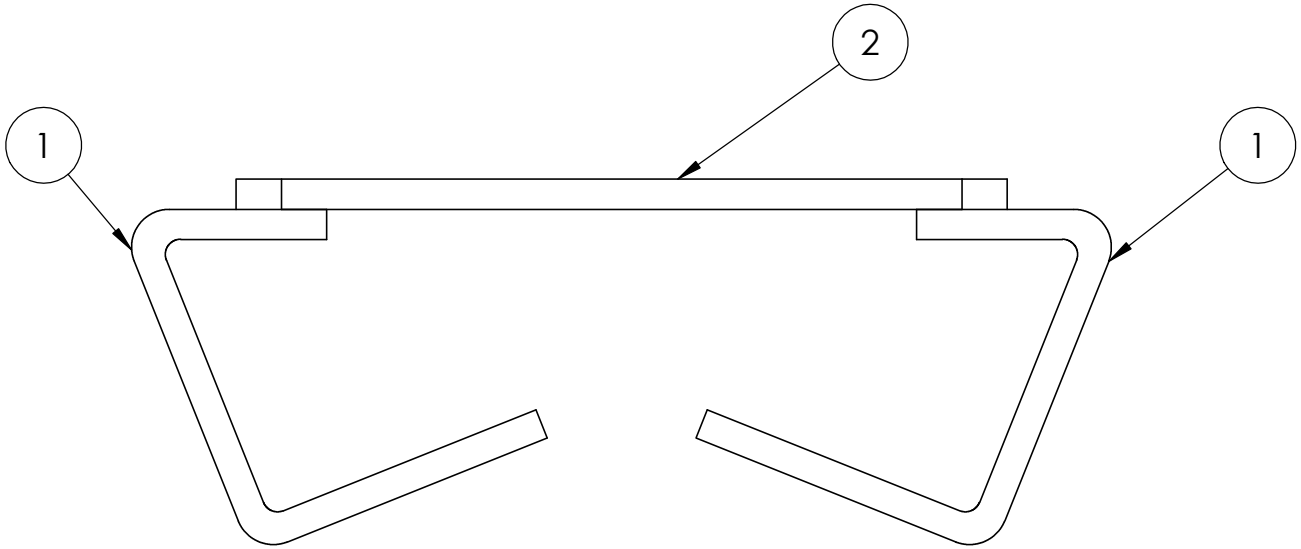


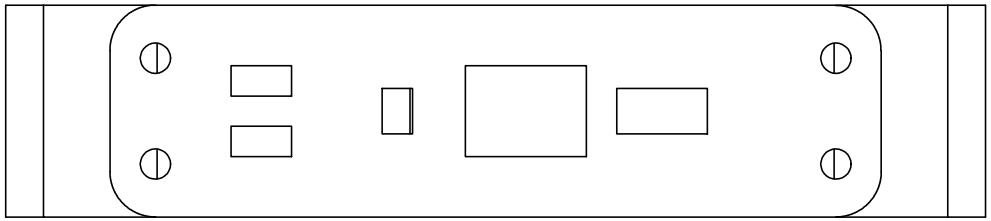

| ITEM NO. | PART NUMBER | QTY. |
|---|---|---|
| 1 | Finger holder | 2 |
| 2 | Strain board 2011 | 1 |

| | | | | |
|---|---|---|---|---|
| A4 Landscape | University of Cape Town<br>Department of Mechanical Engineering | | | |
| | Title:<br>Assem1 | | | |
| Assembly Drawing | Scale:<br>2:1 | Date:<br>2015/05/29 | Sheet1 | of<br>1 |
| | Drawn By: | | Drawing Number | |

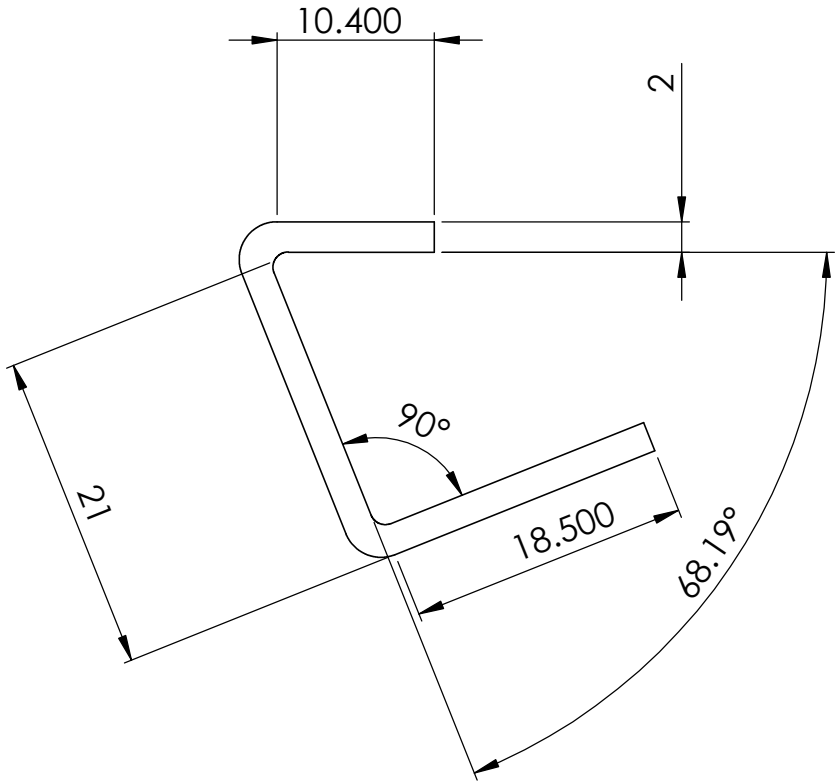


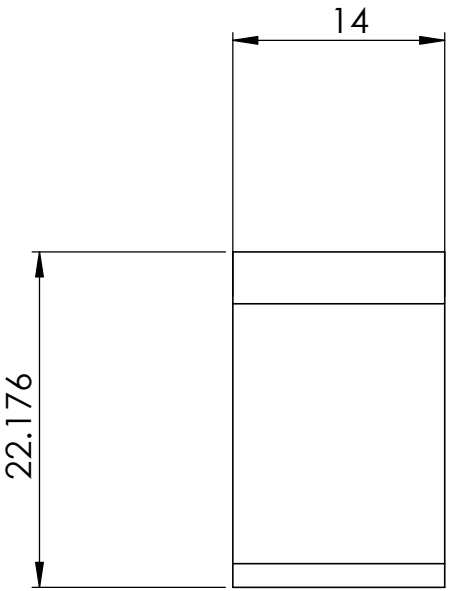


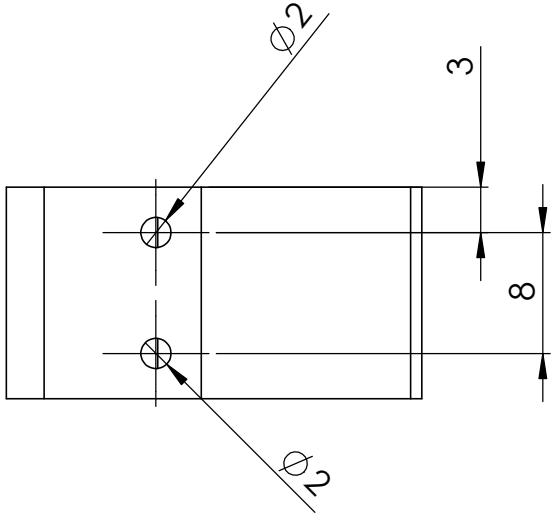


| | | | | |
|---|---|---|---|---|
| A4 Landscape | University of Cape Town<br>Department of Mechanical Engineering | | | |
| | Title:<br>Finger holder | | | |
| Part Finish | Scale:<br>2:1 | Date:<br>2015/05/27 | Sheet1 | of<br>1 |
| Material: | Drawn By: | | Drawing Number | |

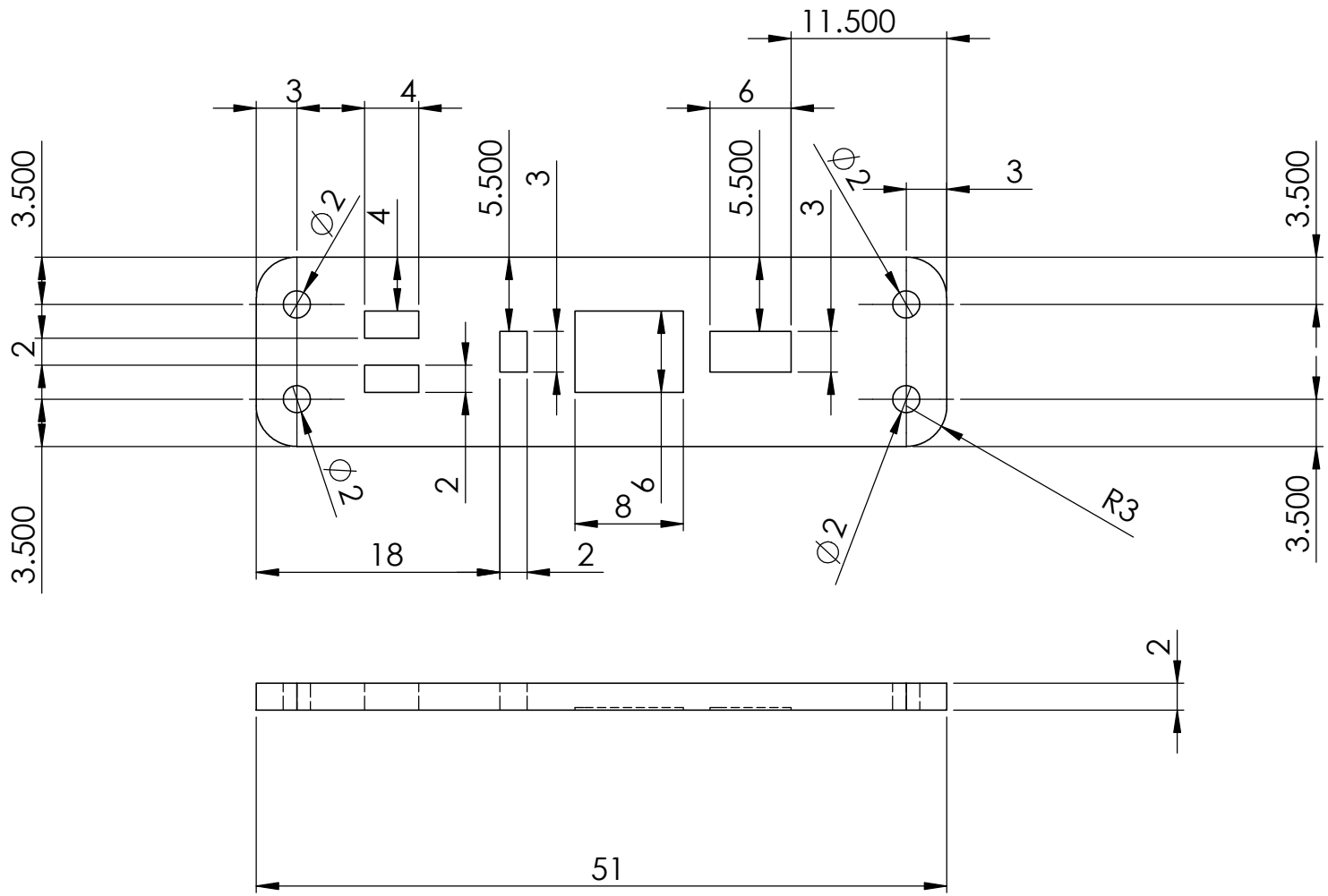


| | | | | |
|---|---|---|---|---|
| A4 Landscape | University of Cape Town<br>Department of Mechanical Engineering | | | |
| | Title:<br>Strain gauge board | | | |
| Part Finish | Scale:<br>2:1 | Date:<br>2015/05/27 | Sheet1 | of<br>1 |
| Material: | Drawn By: | | Drawing Number | |

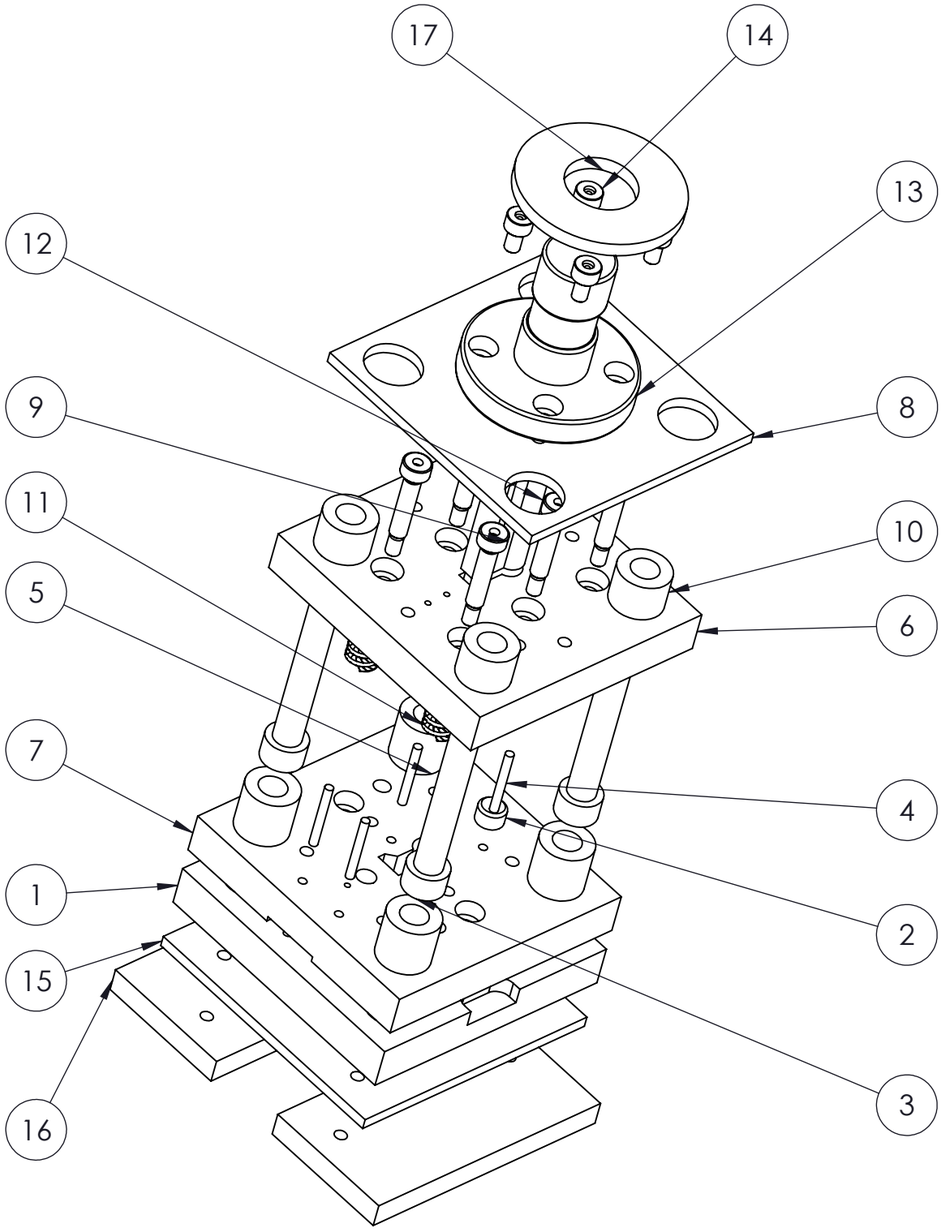


| ITEM NO. | PART NUMBER | MATERIAL | QTY. |
|---|---|---|---|
| 17 | Spacer for part 9 | Aluminium | 1 |
| 16 | Part1 | K110 | 2 |
| 15 | Part 2 | K110 | 1 |
| 14 | Shoulder Small | | 4 |
| 13 | Part 11 | K110 | 1 |
| 12 | Part 9 | K110 | 1 |
| 11 | Spring Final | | 6 |
| 10 | Brass Shoulder | Brass | 4 |
| 9 | Shoulder Final | Brass | 6 |
| 8 | Part 10 | K110 | 1 |
| 7 | Part 5 | K110 | 1 |
| 6 | Part 6 | K110 | 1 |
| 5 | Brass Shoulder Tall | Brass | 4 |
| 4 | Pin | | 6 |
| 3 | Support Poles | | 4 |
| 2 | Brass Pin | Brass | 1 |
| 1 | Part3 | K110 | 1 |

| | | | |
|---|---|---|---|
| A3 Landscape | University of Cape Town<br>Department of Mechanical Engineering | | |
| | Title: Electrode Punch Assembly-EXPLODED! | | |
| Assembly Drawing | Scale: 1:5 | Date: 2014/07/08 | Sheet1 of 1 |
| | Drawn By: | Drawing Number: ELEC-PUNCH EXPLODED | |

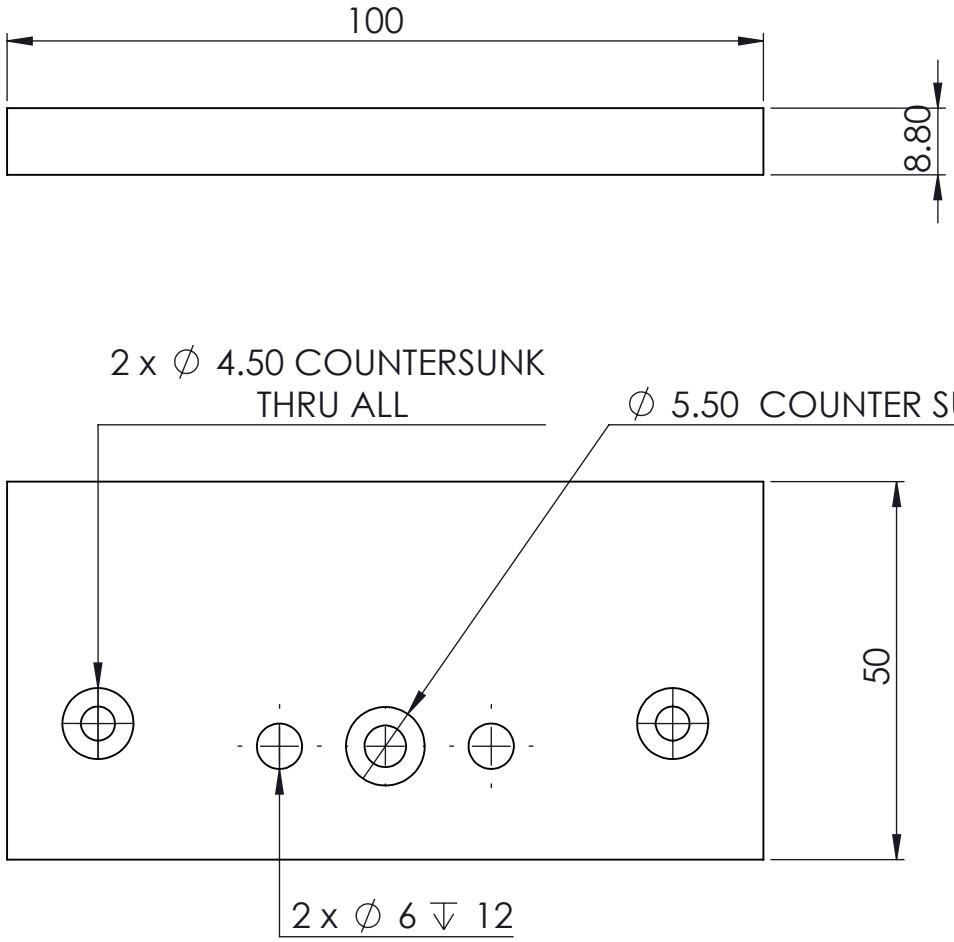


**SolidWorks Student Edition.**
**For Academic Use Only.**

| | | | | |
|---|---|---|---|---|
| A4 Landscape | University of Cape Town<br>Department of Mechanical Engineering | | | |
| | Title:<br>Part1 | | | |
| Part Finish | Scale:<br>1:1 | Date:<br>2014/07/08 | Sheet1 | of<br>1 |
| Material:<br>K110 | Drawn By: | | Drawing Number<br>ELEC-PUNCH_1 | |

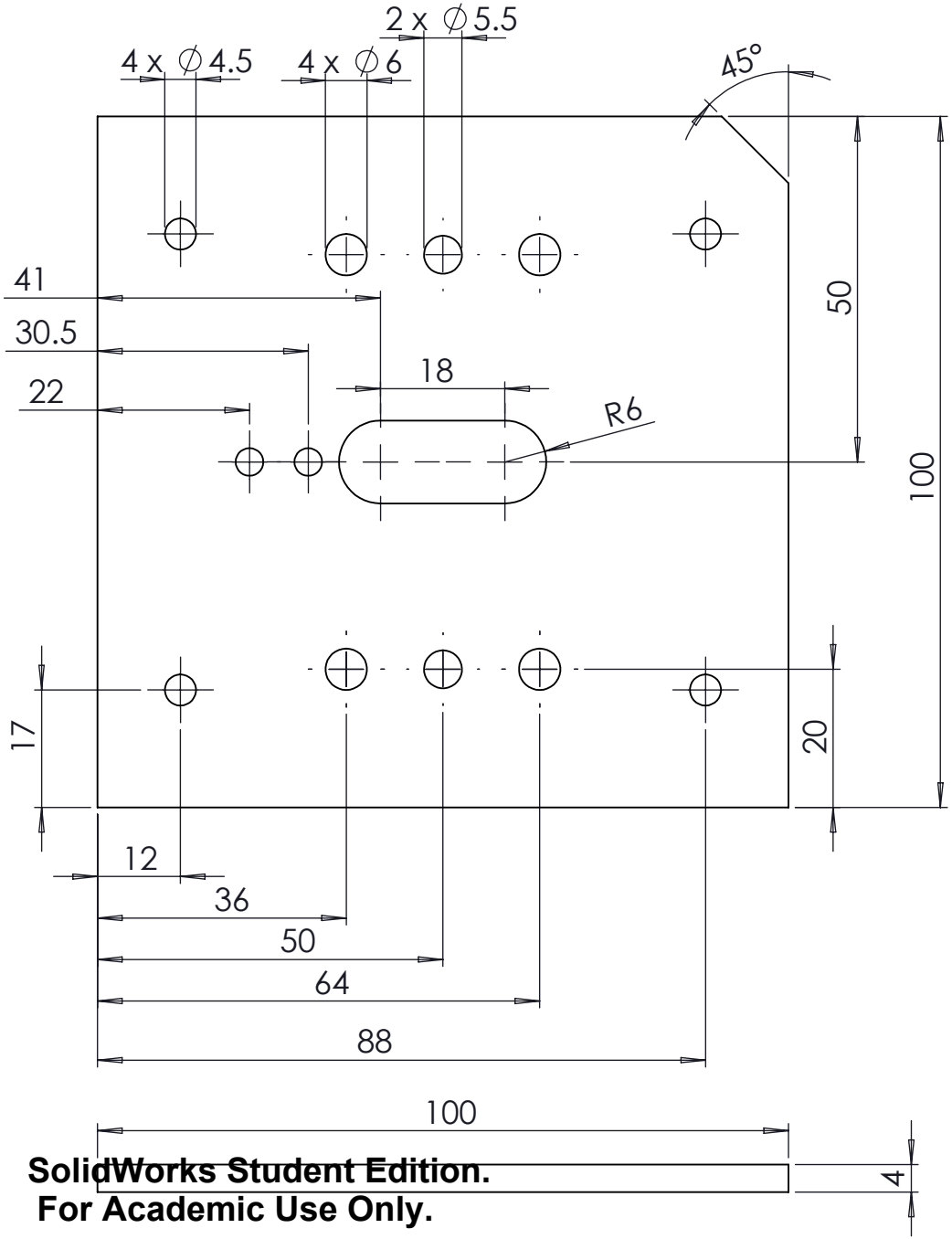


**SolidWorks Student Edition.**
**For Academic Use Only.**

| | | | | |
|---|---|---|---|---|
| A4 Landscape | University of Cape Town<br>Department of Mechanical Engineering | | | |
| | Title:<br>Part 2 | | | |
| Part Finish | Scale:<br>1:2 | Date:<br>2014/07/08 | Sheet1 | of<br>1 |
| Material:<br>K110 | Drawn By: | | Drawing Number<br>ELEC-PUNCH_2 | |

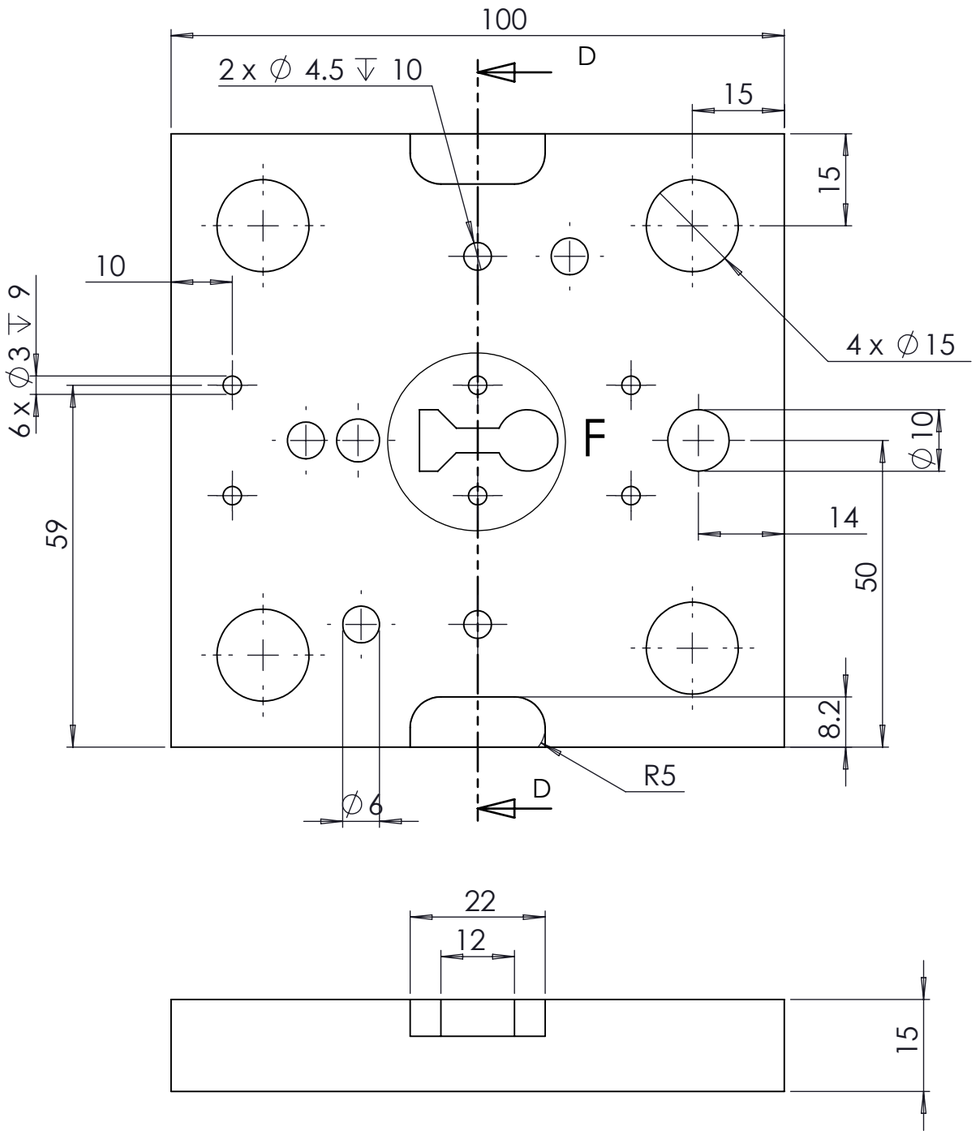


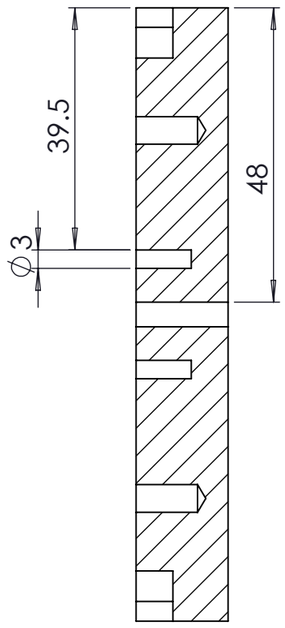


SECTION D-D

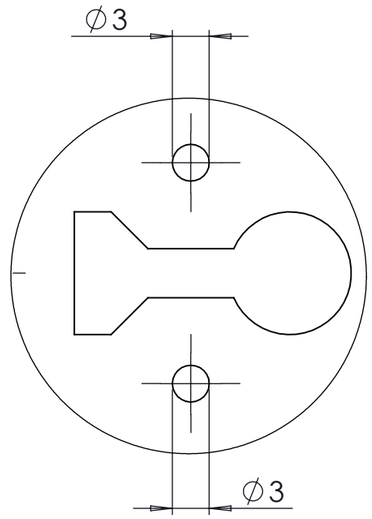


DETAIL F
SCALE 2 : 1

All Holes THRU unless stated otherwise

Please Refer to ELEC-PUNCH_9 for dimensions of centre mould

| | | | | |
|---|---|---|---|---|
| A3 Landscape | University of Cape Town<br>Department of Mechanical Engineering | | | |
| | Title:<br>Part 3 | | | |
| Part Finish | Scale:<br>1:1 | Date:<br>2014/07/08 | Sheet1 | of<br>1 |
| Material: | Drawn By: | | Drawing Number<br>ELEC-PUNCH_3 | |

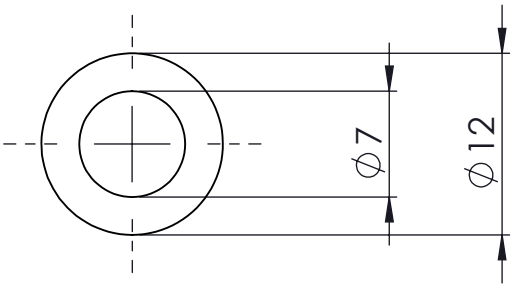


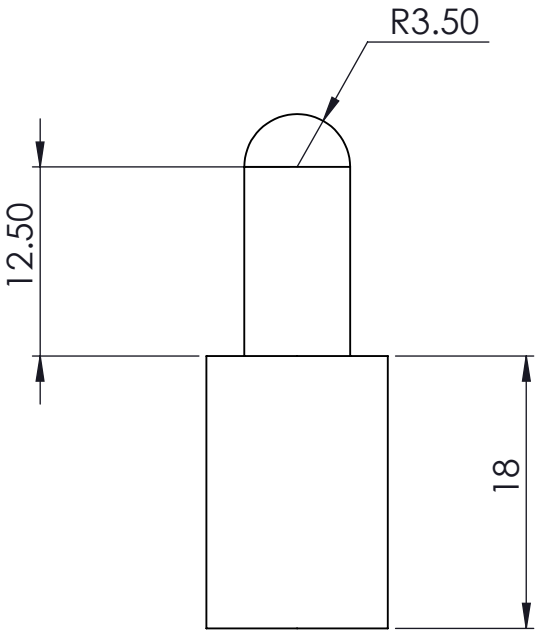


**SolidWorks Student Edition.**
**For Academic Use Only.**

| | | | | |
|---|---|---|---|---|
| A4 Portrait | University of Cape Town<br>Department of Mechanical Engineering | | | |
| | Title:<br>Black pin | | | |
| Part Finish | Scale:<br>2:1 | Date:<br>2014/07/08 | Sheet1 | of<br>1 |
| Material:<br>K110 | Drawn By: | | Drawing Number<br>ELEC_PUNCH_PIN | |

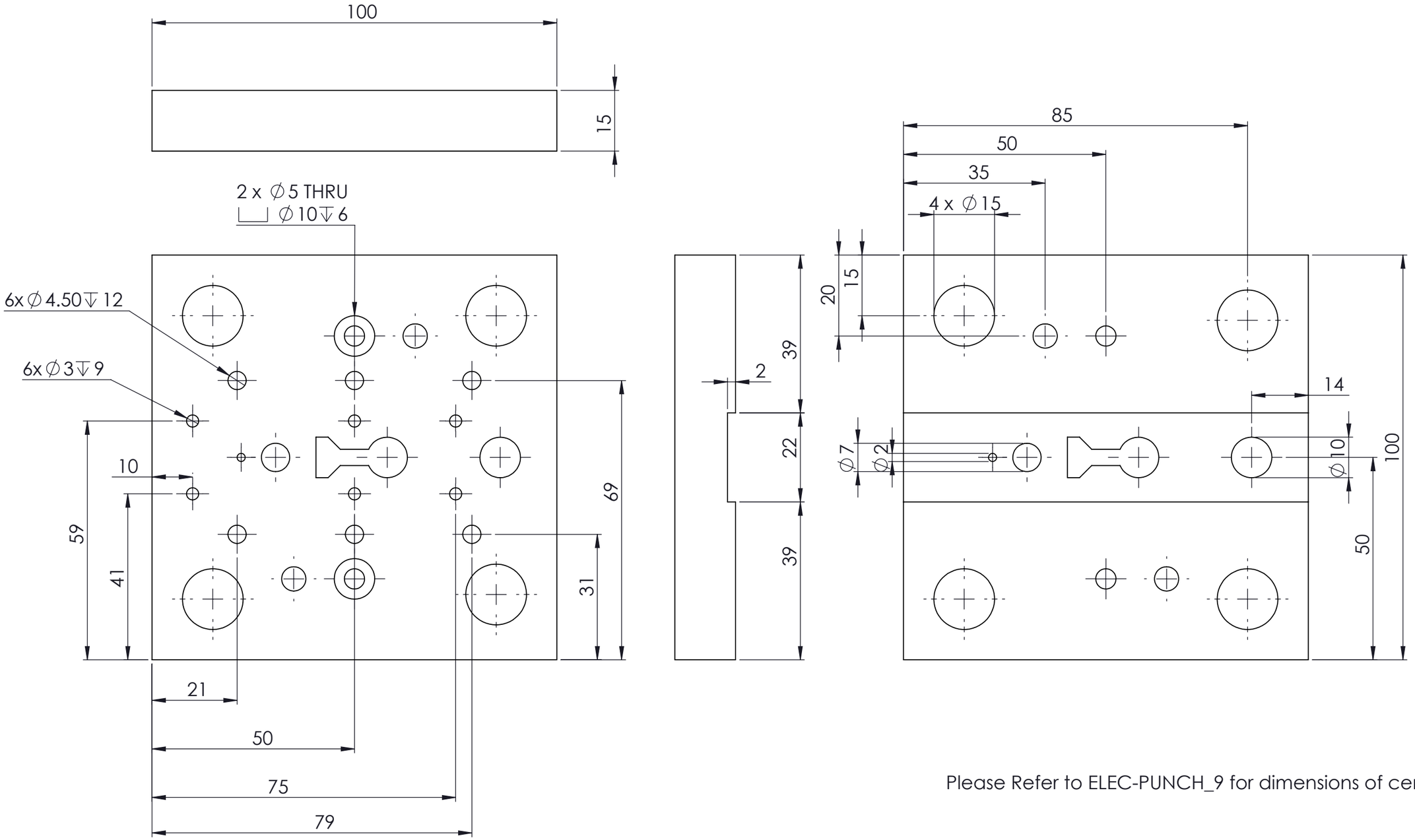


Please Refer to ELEC-PUNCH_9 for dimensions of centre mould

**SolidWorks Student Edition.**
**For Academic Use Only.**

| | | | | |
|---|---|---|---|---|
| A3 Landscape | University of Cape Town<br>Department of Mechanical Engineering | | | |
| | Title:<br>Part 5 | | | |
| Part Finish | Scale:<br>1:1 | Date:<br>2014/07/08 | Sheet1 | of<br>1 |
| Material:<br>K110 | Drawn By: | | Drawing Number<br>ELEC-PUNCH_5 | |

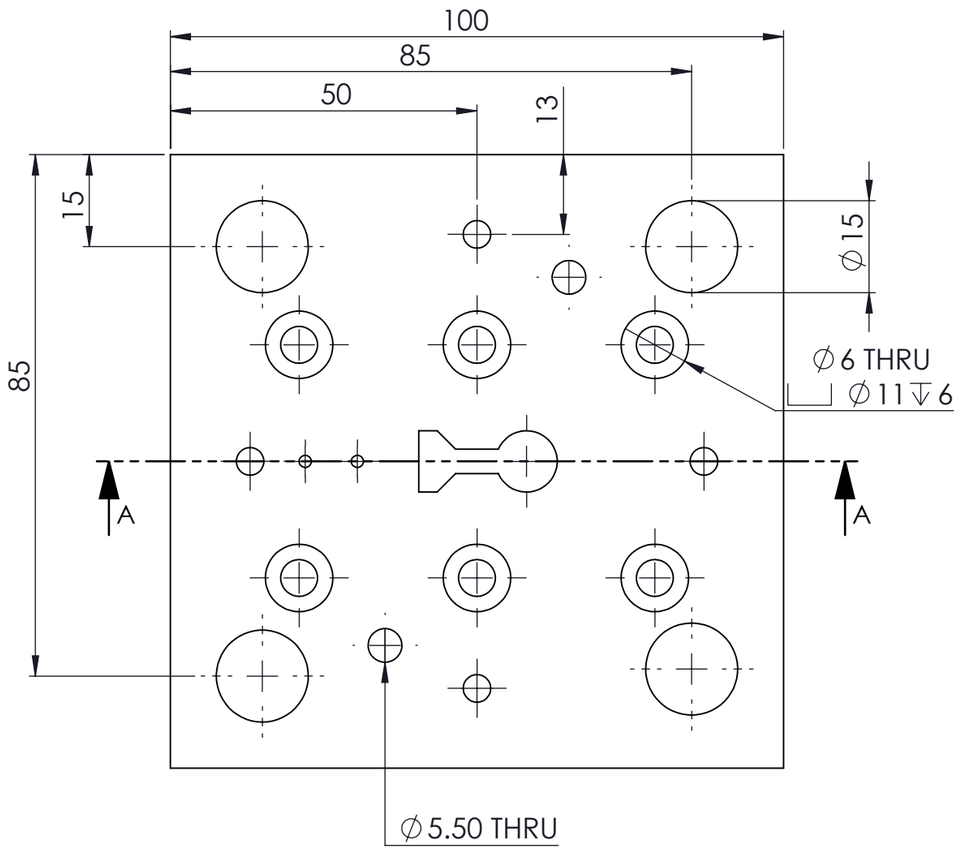


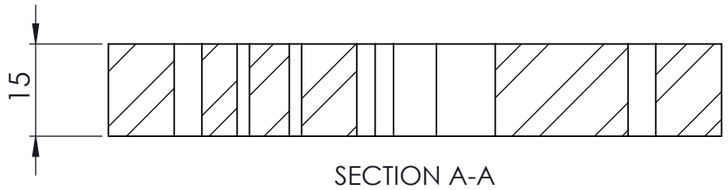


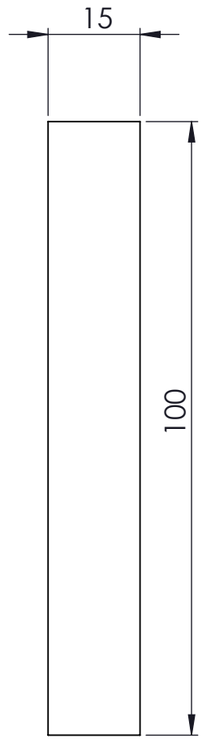


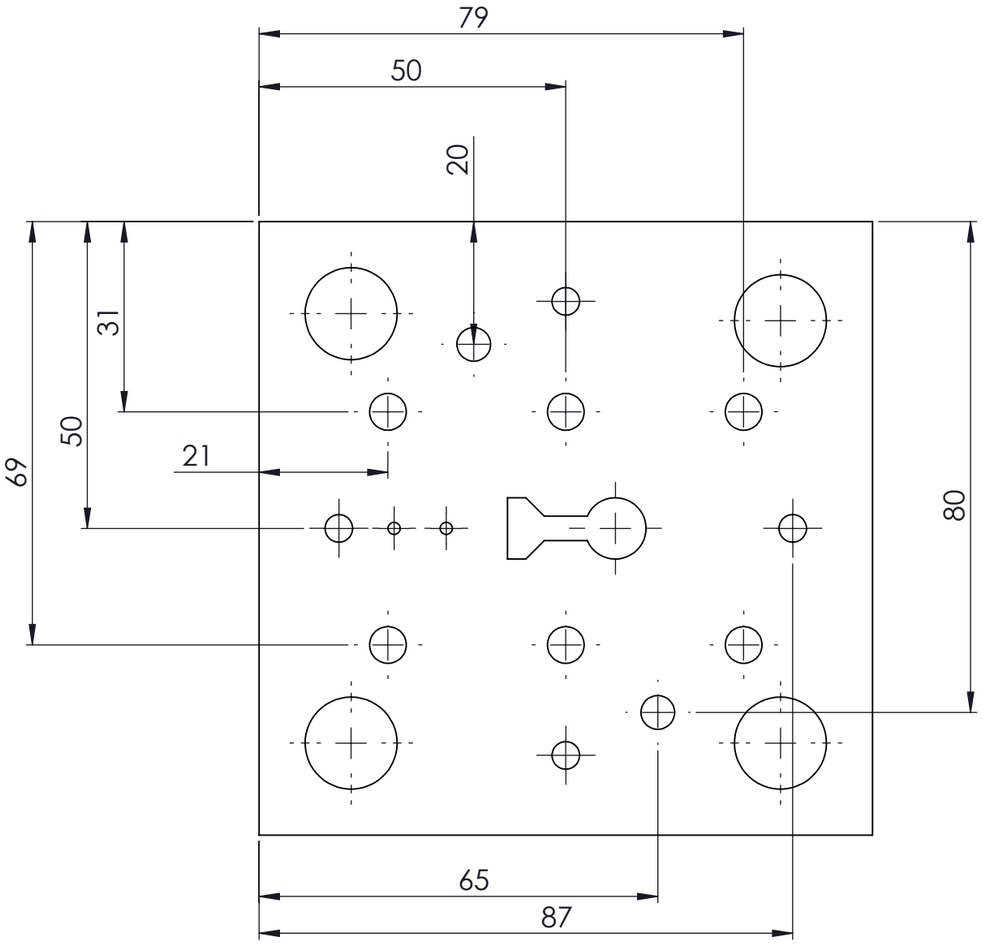


Please Refer to ELEC-PUNCH_9 for dimensions of centre mould

**SolidWorks Student Edition.**
**For Academic Use Only.**

| | | | | |
|---|---|---|---|---|
| A3 Landscape | University of Cape Town<br>Department of Mechanical Engineering | | | |
| | Title:<br>Part 6 | | | |
| Part Finish | Scale:<br>1:1 | Date:<br>2014/07/08 | Sheet1 | of<br>1 |
| Material:<br>K110 | Drawn By: | | Drawing Number<br>ELEC-PUNCH_6 | |

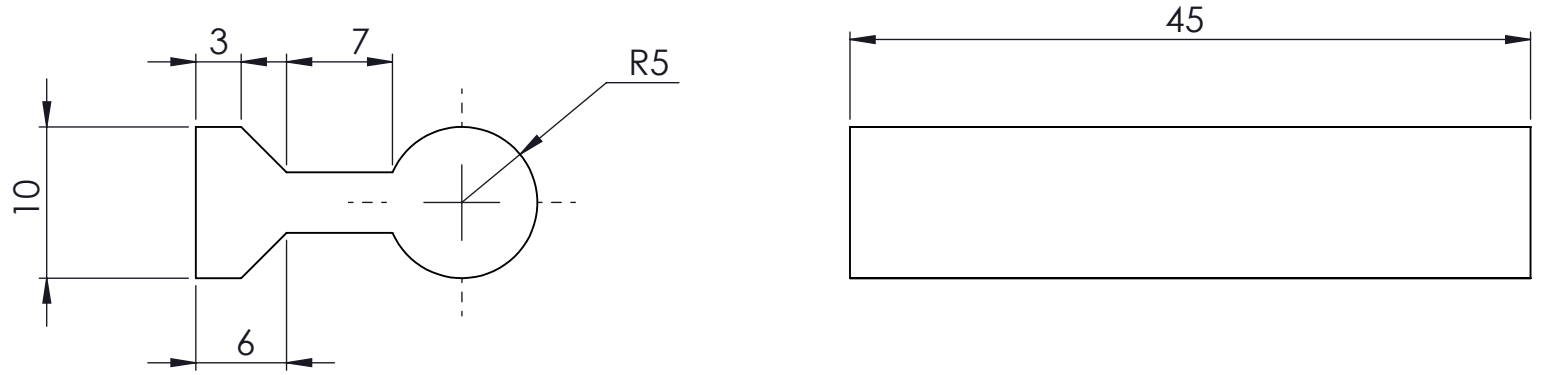


**SolidWorks Student Edition.**
**For Academic Use Only.**

| | | | | |
|---|---|---|---|---|
| A4 Landscape | University of Cape Town<br>Department of Mechanical Engineering | | | |
| | Title:<br>Part 9 | | | |
| Part Finish | Scale:<br>2:1 | Date:<br>2014/07/08 | Sheet1 | of<br>1 |
| Material:<br>K110 | Drawn By: | | Drawing Number<br>ELEC-PUNCH_9 | |

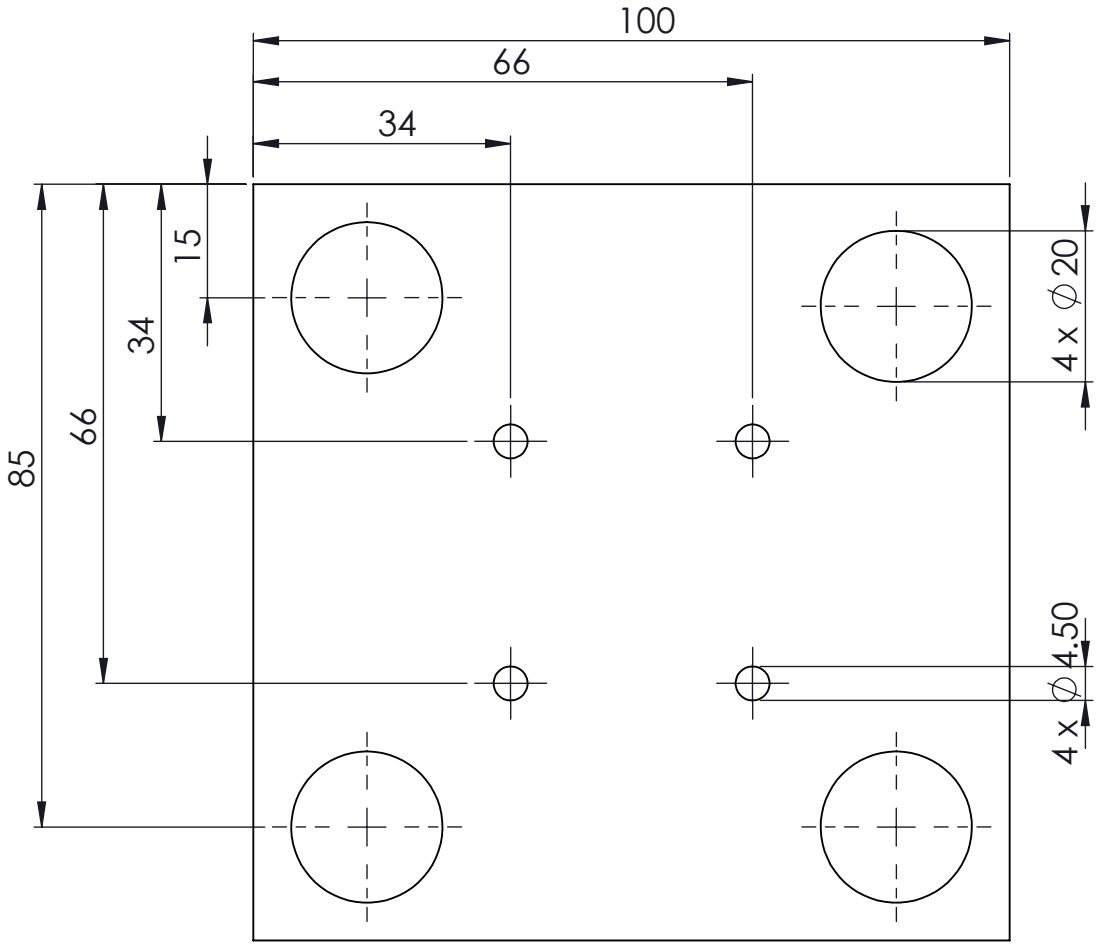


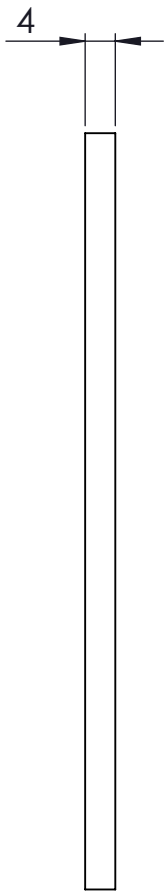


**SolidWorks Student Edition.**
**For Academic Use Only.**

| | | | | |
|---|---|---|---|---|
| A4 Landscape | University of Cape Town<br>Department of Mechanical Engineering | | | |
| | Title:<br>Part 10 | | | |
| Assembly Drawing | Scale:<br>1:2 | Date:<br>2014/07/08 | Sheet1 | of<br>1 |
| | Drawn By: | | Drawing Number<br>ELEC-PUNCH_10 | |

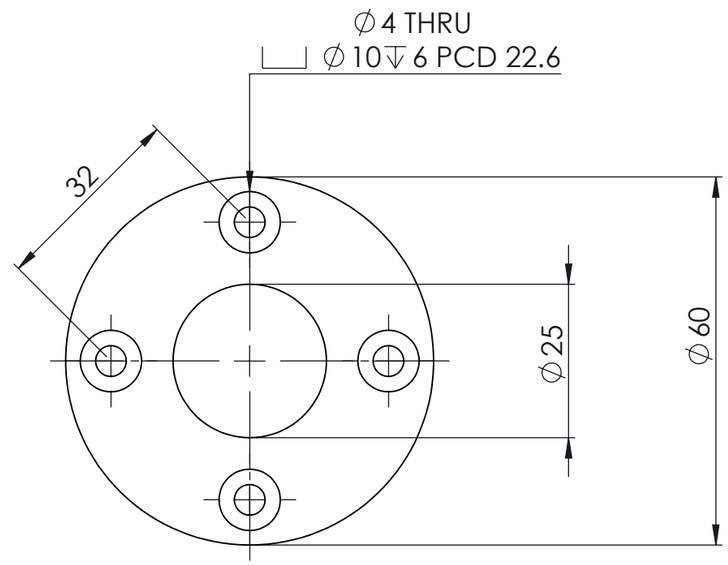


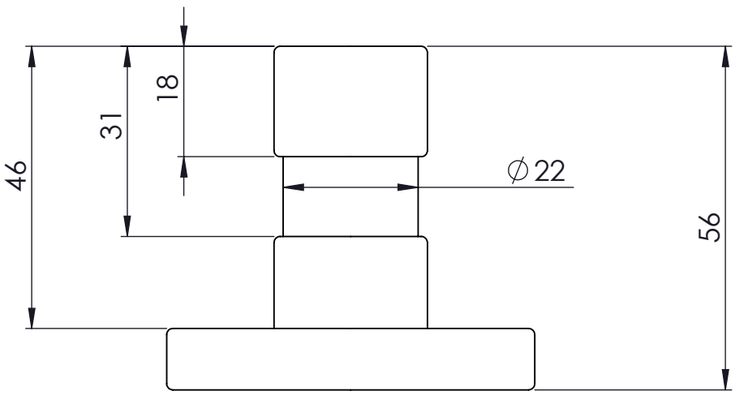


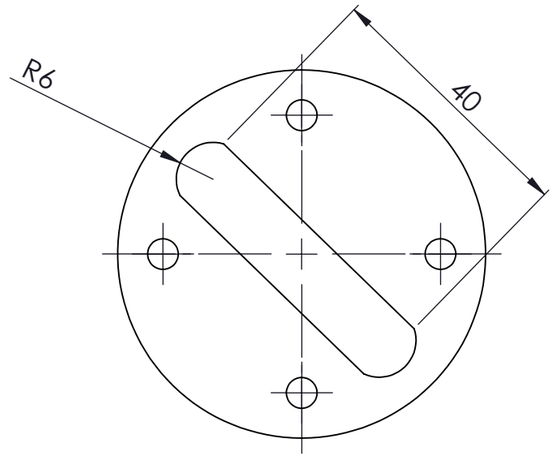


Fillet all edges by 1mm

| | | | | |
|---|---|---|---|---|
| A3 Landscape | University of Cape Town<br>Department of Mechanical Engineering | | | |
| | Title:<br>Part 11 | | | |
| Part Finish | Scale:<br>1:2 | Date:<br>2014/07/08 | Sheet1 | of<br>1 |
| Material:<br>K110 | Drawn By: | | Drawing Number<br>ELEC-PUNCH-PART 11 | |